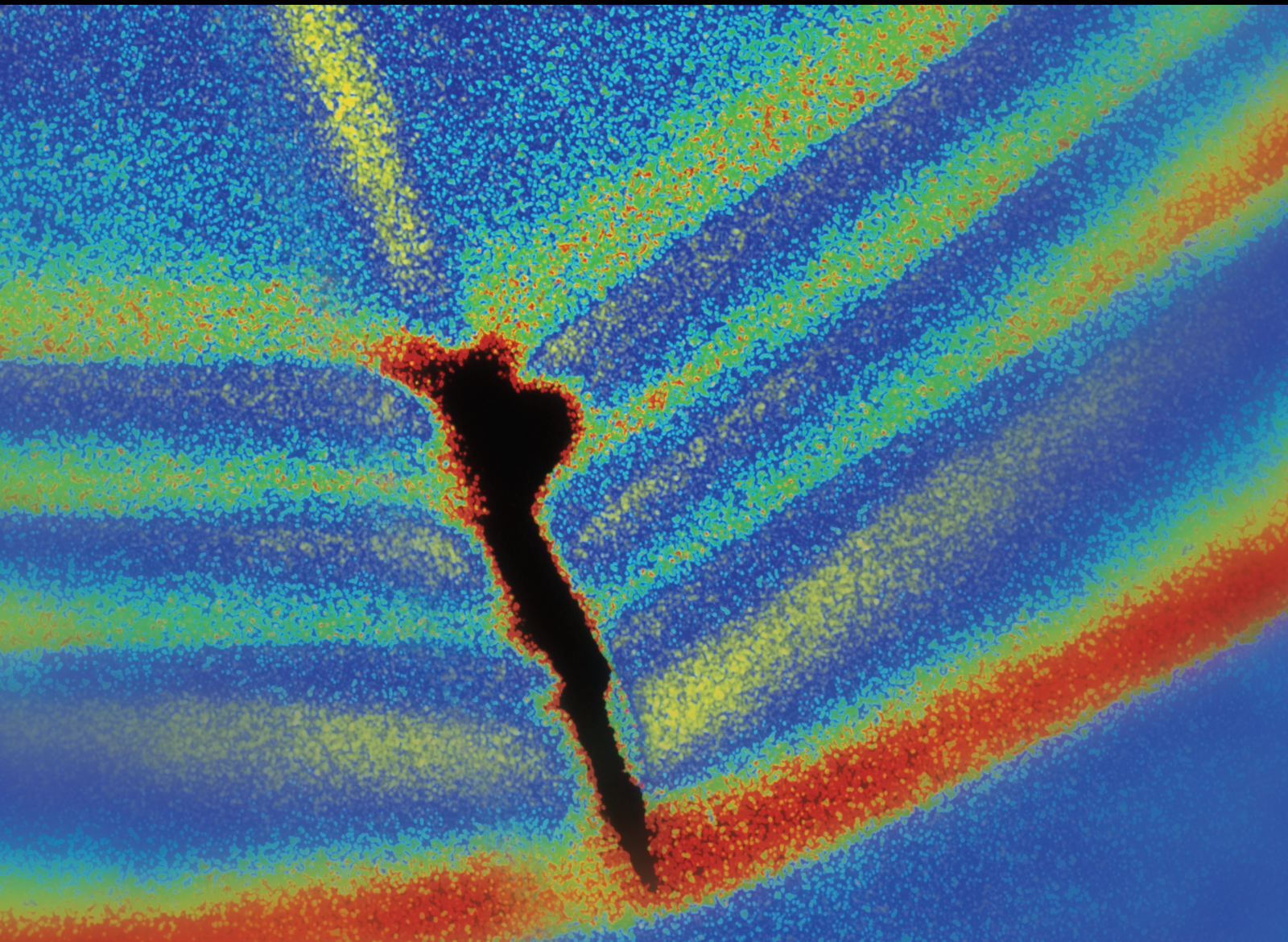


Vibration Control Techniques for Dynamic Response Mitigation of Civil Structures under Multiple Hazards

Lead Guest Editor: Said Elias

Guest Editors: Rajesh Rupakhety and Vasant Matsagar





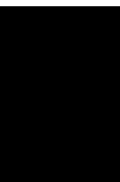
**Vibration Control Techniques for Dynamic
Response Mitigation of Civil Structures under
Multiple Hazards**

Shock and Vibration

**Vibration Control Techniques for
Dynamic Response Mitigation of Civil
Structures under Multiple Hazards**

Lead Guest Editor: Said Elias

Guest Editors: Rajesh Rupakhety and Vasant
Matsagar



Copyright © 2021 Hindawi Limited. All rights reserved.

This is a special issue published in “Shock and Vibration.” All articles are open access articles distributed under the Creative Commons Attribution License, which permits unrestricted use, distribution, and reproduction in any medium, provided the original work is properly cited.

Chief Editor

Huu-Tai Thai , Australia

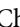
Associate Editors

Ivo Calìo , Italy
Nawawi Chouw , New Zealand
Longjun Dong , China
Farzad Ebrahimi , Iran
Mickaël Lallart , France
Vadim V. Silberschmidt , United Kingdom
Mario Terzo , Italy
Angelo Marcelo Tusset , Brazil

Academic Editors

Omid A. Yamini , Iran
Maher Abdelghani, Tunisia
Haim Abramovich , Israel
Desmond Adair , Kazakhstan
Manuel Aenlle Lopez , Spain
Brij N. Agrawal, USA
Ehsan Ahmadi, United Kingdom
Felix Albu , Romania
Marco Alfano, Italy
Sara Amoroso, Italy
Huaming An, China
P. Antonaci , Italy
José V. Araújo dos Santos , Portugal
Lutz Auersch , Germany
Matteo Aureli , USA
Azwan I. Azmi , Malaysia
Antonio Batista , Brazil
Mattia Battarra, Italy
Marco Belloli, Italy
Francisco Beltran-Carbajal , Mexico
Denis Benasciutti, Italy
Marta Berardengo , Italy
Sébastien Besset, France
Giosuè Boscato , Italy
Fabio Botta , Italy
Giuseppe Brandonisio , Italy
Francesco Bucchi , Italy
Rafał Burdzik , Poland
Salvatore Caddemi , Italy
Wahyu Caesarendra , Brunei Darussalam
Baoping Cai, China
Sandro Carbonari , Italy
Cristina Castejón , Spain

Nicola Caterino , Italy
Gabriele Cazzulani , Italy
Athanasios Chasalevris , Greece
Guoda Chen , China
Xavier Chimentin , France
Simone Cinquemani , Italy
Marco Civera , Italy
Marco Cocconcelli , Italy
Alvaro Cunha , Portugal
Giorgio Dalpiaz , Italy
Thanh-Phong Dao , Vietnam
Arka Jyoti Das , India
Raj Das, Australia
Silvio L.T. De Souza , Brazil
Xiaowei Deng , Hong Kong
Dario Di Maio , The Netherlands
Raffaella Di Sante , Italy
Luigi Di Sarno, Italy
Enrique Lopez Droguett , Chile
Mădălina Dumitriu, Romania
Sami El-Borgi , Qatar
Mohammad Elahinia , USA
Said Elias , Iceland
Selçuk Erkaya , Turkey
Gaoliang Fang , Canada
Fiorenzo A. Fazzolari , United Kingdom
Luis A. Felipe-Sese , Spain
Matteo Filippi , Italy
Piotr Fołga , Poland
Paola Forte , Italy
Francesco Franco , Italy
Juan C. G. Prada , Spain
Roman Gabl , United Kingdom
Pedro Galvín , Spain
Jinqiang Gan , China
Cong Gao , China
Arturo García García-Perez, Mexico
Rozaimi Ghazali , Malaysia
Marco Gherlone , Italy
Anindya Ghoshal , USA
Gilbert R. Gillich , Romania
Antonio Giuffrida , Italy
Annalisa Greco , Italy
Jiajie Guo, China

Amal Hajjaj , United Kingdom
Mohammad A. Hariri-Ardebili , USA
Seyed M. Hashemi , Canada
Xue-qi He, China
Agustin Herrera-May , Mexico
M.I. Herreros , Spain
Duc-Duy Ho , Vietnam
Hamid Hosano , Japan
Jin Huang , China
Ahmed Ibrahim , USA
Bernard W. Ikuu, Kenya
Xingxing Jiang , China
Jiang Jin , China
Xiaohang Jin, China
MOUSTAFA KASSEM , Malaysia
Shao-Bo Kang , China
Yuri S. Karinski , Israel
Andrzej Katunin , Poland
Manoj Khandelwal, Australia
Denise-Penelope Kontoni , Greece
Mohammadreza Koopialipour, Iran
Georges Kouroussis , Belgium
Genadijus Kulvietis, Lithuania
Pradeep Kundu , USA
Luca Landi , Italy
Moon G. Lee , Republic of Korea
Trupti Ranjan Lenka , India
Arcanjo Lenzi, Brazil
Marco Lepidi , Italy
Jinhua Li , China
Shuang Li , China
Zhixiong Li , China
Xihui Liang , Canada
Tzu-Kang Lin , Taiwan
Jinxin Liu , China
Ruonan Liu, China
Xiuquan Liu, China
Siliang Lu, China
Yixiang Lu , China
R. Luo , China
Tianshou Ma , China
Nuno M. Maia , Portugal
Abdollah Malekjafarian , Ireland
Stefano Manzoni , Italy


Stefano Marchesiello , Italy
Francesco S. Marulo, Italy
Traian Mazilu , Romania
Vittorio Memmolo , Italy
Jean-Mathieu Mencik , France
Laurent Mevel , France
Letícia Fleck Fadel Miguel , Brazil
FuRen Ming , China
Fabio Minghini , Italy
Marco Miniaci , USA
Mahdi Mohammadpour , United Kingdom
Rui Moreira , Portugal
Emiliano Mucchi , Italy
Peter Múčka , Slovakia
Fehmi Najar, Tunisia
M. Z. Naser, USA
Amr A. Nassr, Egypt
Sundararajan Natarajan , India
Toshiaki Natsuki, Japan
Miguel Neves , Portugal
Sy Dzung Nguyen , Republic of Korea
Trung Nguyen-Thoi , Vietnam
Gianni Niccolini, Italy
Rodrigo Nicoletti , Brazil
Bin Niu , China
Leilei Niu, China
Yan Niu , China
Lucio Olivares, Italy
Erkan Oterkus, United Kingdom
Roberto Palma , Spain
Junhong Park , Republic of Korea
Francesco Pellicano , Italy
Paolo Pennacchi , Italy
Giuseppe Petrone , Italy
Evgeny Petrov, United Kingdom
Franck Poisson , France
Luca Pugi , Italy
Yi Qin , China
Virginio Quaglini , Italy
Mohammad Rafiee , Canada
Carlo Rainieri , Italy
Vasudevan Rajamohan , India
Ricardo A. Ramirez-Mendoza , Mexico
José J. Rangel-Magdaleno , Mexico

Didier Rémond , France
Dario Richiedi , Italy
Fabio Rizzo, Italy
Carlo Rosso , Italy
Riccardo Rubini , Italy
Salvatore Russo , Italy
Giuseppe Ruta , Italy
Edoardo Sabbioni , Italy
Pouyan Roodgar Saffari , Iran
Filippo Santucci de Magistris , Italy
Fabrizio Scozzese , Italy
Abdullah Seçgin, Turkey
Roger Serra , France
S. Mahdi Seyed-Kolbadi, Iran
Yujie Shen, China
Bao-Jun Shi , China
Chengzhi Shi , USA
Gerardo Silva-Navarro , Mexico
Marcos Silveira , Brazil
Kumar V. Singh , USA
Jean-Jacques Sinou , France
Isabelle Sochet , France
Alba Sofi , Italy
Jussi Sopanen , Finland
Stefano Sorace , Italy
Andrea Spaggiari , Italy
Lei Su , China
Shuaishuai Sun , Australia
Fidelis Tawiah Suorineni , Kazakhstan
Cecilia Surace , Italy
Tomasz Szolc, Poland
Iacopo Tamellini , Italy
Zhuhua Tan, China
Gang Tang , China
Chao Tao, China
Tianyou Tao, China
Marco Tarabini , Italy
Hamid Toopchi-Nezhad , Iran
Carlo Trigona, Italy
Federica Tubino , Italy
Nerio Tullini , Italy
Nicolò Vaiana , Italy
Marcello Vanali , Italy
Christian Vanhille , Spain

Dr. Govind Vashishtha, Poland
F. Viadero, Spain
M. Ahmer Wadee , United Kingdom
C. M. Wang , Australia
Gaoxin Wang , China
Huiqi Wang , China
Pengfei Wang , China
Weiqiang Wang, Australia
Xian-Bo Wang, China
YuRen Wang , China
Wai-on Wong , Hong Kong
Yuanping XU , China
Biao Xiang, China
Qilong Xue , China
Xin Xue , China
Diansen Yang , China
Jie Yang , Australia
Chang-Ping Yi , Sweden
Nicolo Zampieri , Italy
Chao-Ping Zang , China
Enrico Zappino , Italy
Guo-Qing Zhang , China
Shaojian Zhang , China
Yongfang Zhang , China
Yaobing Zhao , China
Zhipeng Zhao, Japan
Changjie Zheng , China
Chuanbo Zhou , China
Hongwei Zhou, China
Hongyuan Zhou , China
Jiaxi Zhou , China
Yunlai Zhou, China
Radoslaw Zimroz , Poland


Contents

Seismic Test and Simulation of Spring Vibration Isolated Foundation for Turbo-Generator

Dong An  and Tianwang Liu

Research Article (16 pages), Article ID 8884920, Volume 2021 (2021)

Multihazard Response Control of Base-Isolated Buildings under Bidirectional Dynamic Excitation

Daniel H. Zelleke , Sandip K. Saha , and Vasant A. Matsagar 


Research Article (24 pages), Article ID 8830460, Volume 2020 (2020)

Development of Rocking Isolation for Response Mitigation of Elevated Water Tanks under Seismic and Wind Hazards

Hassan Alemzadeh, Hamzeh Shakib , and Mohammad Khanmohammadi

Research Article (26 pages), Article ID 5498298, Volume 2020 (2020)

Development of a Frequency-Adjustable Tuned Mass Damper (FATMD) for Structural Vibration Control

Huaguo Gao, Congbao Wang, Chen Huang, Wenlong Shi, and Linsheng Huo 



Research Article (16 pages), Article ID 9605028, Volume 2020 (2020)

Effectiveness of Friction Dampers in Seismic and Wind Response Control of Connected Adjacent Steel Buildings

Anshul Malhotra, Tathagata Roy , and Vasant Matsagar 


Research Article (21 pages), Article ID 8304359, Volume 2020 (2020)

Unified Shear-Flexural Model for Vibration Control of Buildings Using Passive Dynamic Absorbers

Hugo Hernández-Barrios , Iván F. Huergo, Carlos Arce-León , and Carlos M. Patlán


Research Article (25 pages), Article ID 8810482, Volume 2020 (2020)

Energy Response Analysis of Continuous Beam Bridges with Friction Pendulum Bearing by Multihazard Source Excitations

Bing Li, Bin Wang , Shaohua Wang, and Xiao Wu

Research Article (17 pages), Article ID 3724835, Volume 2020 (2020)

Mitigating Large Vibrations of Stayed Cables in Wind and Rain Hazards

Hung Vo-Duy and Cung H. Nguyen 

Research Article (10 pages), Article ID 5845712, Volume 2020 (2020)

Research Article

Seismic Test and Simulation of Spring Vibration Isolated Foundation for Turbo-Generator

Dong An  and Tianwang Liu

School of Civil Engineering, North China University of Technology, Beijing 100144, China

Correspondence should be addressed to Dong An; hadesloveln@163.com

Received 14 July 2020; Revised 15 December 2020; Accepted 20 February 2021; Published 3 March 2021

Academic Editor: Dr Vasant Matsagar

Copyright © 2021 Dong An and Tianwang Liu. This is an open access article distributed under the Creative Commons Attribution License, which permits unrestricted use, distribution, and reproduction in any medium, provided the original work is properly cited.

The 1 : 8 model of turbo-generator vibration isolated foundation of common islands in nuclear plants was established for vibration characteristic tests and pseudodynamic experiments. The finite element model was established by SeismoStruct for time-history analysis. Frequencies, modal shapes and seismic responses, deformation curves, and spring deformations were compared and analyzed. Results from tests and experiments show that the natural frequencies of spring vibration isolation foundation are lower than those of common frame foundations and the vertical frequencies are far from the working disturbance frequency of the turbo-generator units. The spring vibration isolation device can reduce the acceleration response of the TG (turbo-generator) deck and redistribute the horizontal earthquake action of the foundation according to the stiffness to give full play to the seismic capacity of the columns. The errors of natural vibration frequencies and maximum seismic response are approximately 15% and 10%, respectively, and the simulation results are in good agreement with the test and experiment data. The proportion and distribution of spring deformation are close, and the test study shows the convenient and precise realization of the simulation. Results of seismic experiments and numerical simulations show that the foundation design meets the standard of the “Code for Seismic Design of Buildings” in China, which realizes the goal of spring vibration isolation and seismic resistance. The foundation design is also reasonable, safe, and reliable.

1. Introduction

The statistics [1] reveal that more than 40 nuclear power units in mainland China have entered commercial operation, approximately 20 units are under construction, and additional units are ready to be built or are being planned. Figure 1 shows the distribution of nuclear power plants in mainland China. Turbo-generator (TG) is the “heart” of power plants and even power systems. TG is the core component either in thermal power or nuclear power. As the structure of nuclear power conventional island carrying the entire TG unit, the turbine foundation not only bears huge equipment weight but also handles the dynamic load of the turbine. Figure 2 is a typical conventional turbine foundation [2]. The use of a half-speed TG will inevitably increase with the development of nuclear power design autonomy and large-scale unit power. However, its 25 Hz operating frequency is close to the vertical basic frequency of common

frame foundation, which is prone to produce the “resonance” effect that is not conducive to unit operation.

Spring isolation technology was first applied to TG more than 50 years ago. Researchers [3] found there are two strategies to reduce the seismic response of turbine foundations: one is to reduce the fundamental frequency of the structure, and the other is to improve the damping of the system. The spring vibration isolation system, which separates the TG deck and the column, can satisfy the two aforementioned points. This system not only substantially reduces the vertical natural frequency but also adjusts the damping of the entire system appropriately. Although many engineering examples of spring vibration isolation foundation are found abroad, no real systematic theoretical or experimental study, which is limited to the actual measurement of TG on the working state [4], is unavailable. However, the use of spring vibration isolation foundation in conventional nuclear power island has no precedent at that



FIGURE 1: Nuclear power plants in China.

time in China. Thus, effectively executing design selection, theoretical analysis, experimental research, and field testing is necessary. Chinese experts and scholars conducted numerous studies. Luo et al. [3] discussed the seismic performance of three examples using the spring vibration isolation foundation and obtained similar conclusions despite differences in the foundation model, calculation program, calculation assumption, and calculation method. Spring vibration isolation foundation can also reduce the basic frequency of turbine foundations, and the use of dampers to improve the damping ratio of the system can effectively reduce the seismic responses. Zhu and Chen [5] established the dynamic equation of the spring vibration isolation system and conducted the finite element analysis. The results reveal that the spring vibration isolation damping element can advance the basic frequency of the entire

structure system and reduce the probability of resonance under the working frequency. Song et al. [6] conducted a series of studies on the foundation selection, design criteria, vibration analysis, and field test of the first Ling'ao Phase II half-speed machine with spring vibration isolation foundation in China. The results show that the vertical first-order frequency of the spring foundation is far less than the working frequency of the half-speed unit which has effective dynamic characteristics. The acceleration response of the TG deck can be reduced by spring vibration isolation, and the foundation has a good seismic performance. The application of spring vibration isolation foundation in conventional nuclear power island has been successful. The experimental research is a necessary verification and an important supplement for theoretical analysis and field measurement. Shao et al. [4, 7] conducted the first comprehensive model test on

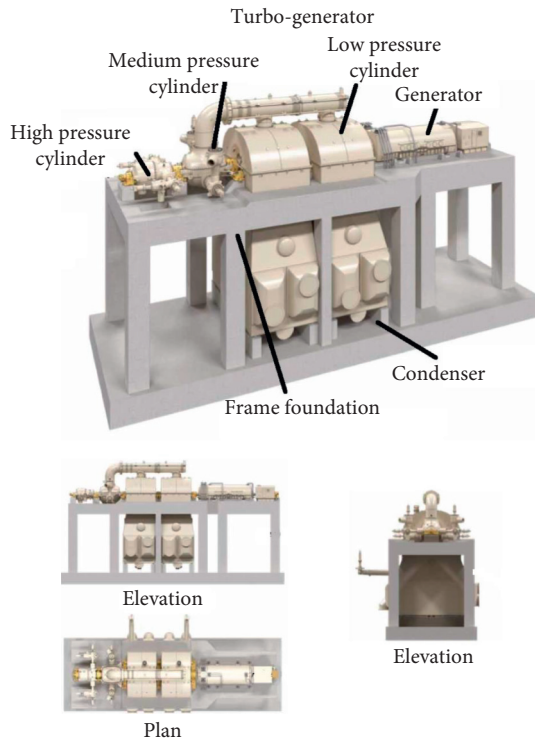


FIGURE 2: Concrete foundations for turbine generators (HP-IP-LP-LP with bottom exhaust).

spring vibration isolation foundations of TG unit. The test results show that the spring vibration isolation improves the seismic performance of the foundation, and the increase in the damping ratio is beneficial to the improvement of the seismic performance. Considering dynamic characteristics, the overall calculation model is close to the test results. The spring vibration isolation foundation is the best choice for a half-speed TG with a working frequency of 25 Hz. Researchers tended to provide additional attention to the influence of dynamic characteristics of turbine foundation on TG deck vibration and performed numerous investigations have done a considering common or spring foundation [8–12]. With the application of spring isolation technology and additional advanced research methods, Li et al.[12] built a TG deck and spring isolation foundation combined vibration test bench. Particularly, the influence of spring isolation foundation on TG deck vibration is investigated. A 300 MW turbine-generator-foundation system is analyzed under earthquakes [13]. A new seismic isolation system based on spring tube braces was studied [14]. Hur and Park [15] evaluated the applicability of seismic isolation devices under seismic loads.

The TG foundation has the following characteristics. (1) Installed capacity and number of cylinders affect the TG deck condition of the unit. Thus, selecting the foundation and allocating the unit to meet the dynamic characteristics of the TG deck operation are necessary. (2) Technological requirements of different manufacturers lead to different shapes of the foundation structure or different parts of the location. (3) The structure of the foundation is complex, the

weight of the upper structure and equipment is huge, and the size of the TG deck beam is large. Meanwhile, the space occupied by the lower condenser is large. However, the size of the column is relatively small. The difference of foundations in the TG foundation model experiments [4, 16–20] is considerably large. Therefore, examining the difference separately is necessary. Especially for spring vibration isolation foundation, the overall dynamic characteristics of the foundation will change markedly when the spring vibration isolator is placed at the top of the column. The Code for Seismic Design of Buildings (2016) [21] stipulates that “when a complex structure adopts vibration isolation design, the design scheme shall be determined after model test.”

The seismic performance of spring vibration isolation foundations of TG units is studied in this paper through physical modelling and numerical simulation. First, the 1 : 8 spring vibration isolation foundation model of the TG unit is designed and manufactured following similarity theory. The basic frequency and mode shape of the foundation are obtained by the natural characteristic test. Then, the current codes in China and the requirements of manufacturers indicate that the acceleration time history of 7-degree fortification earthquake is input, and the seismic performance under the horizontal earthquake action of the foundation is studied by pseudodynamic experiments. Simultaneously, the finite element software SeismoStruct is used to simulate the spring foundation, and the simulation results are compared with the experimental results. Finally, the evaluation of the seismic performance of the foundation and the suggestions of similar tests are given to guide for the design and test loading of this kind of structure.

2. Experimental Investigation

2.1. Model Design and Fabrication. Adopting the frame structure, the scale ratio of the turbine spring vibration isolation foundation model is 1 : 8. The plan and section of the model are shown in Figure 3, the dimensions indicated in the figure are in millimeters, and the model similarity [22] is presented in Table 1. The model material is similar to the prototype of the practical project. The longitudinal reinforcement of the beam, column, and slab is HRB400, the stirrup is HPB300, and the concrete strength grade is C40. The abovementioned grades are Chinese code values. The reinforcement ratio of the foundation model is similar to that of the prototype. The principle of quality similarity indicates that the quality of equipment used in TGs is simulated by cast iron block, and the position of the mass block is consistent with that of equipment. The concrete base plate is anchored to the laboratory floor by foot bolts. The concrete construction of the whole foundation structure is divided into five parts. The five parts are as follows: the base plate, the column and one-story platform, the column and two-story platform, the upper part of the column, and the TG deck. The spring vibration isolation device is installed after the upper part of the column has been constructed. The completed model used in natural characteristic tests and seismic experiments is shown in Figure 4. The stiffness of

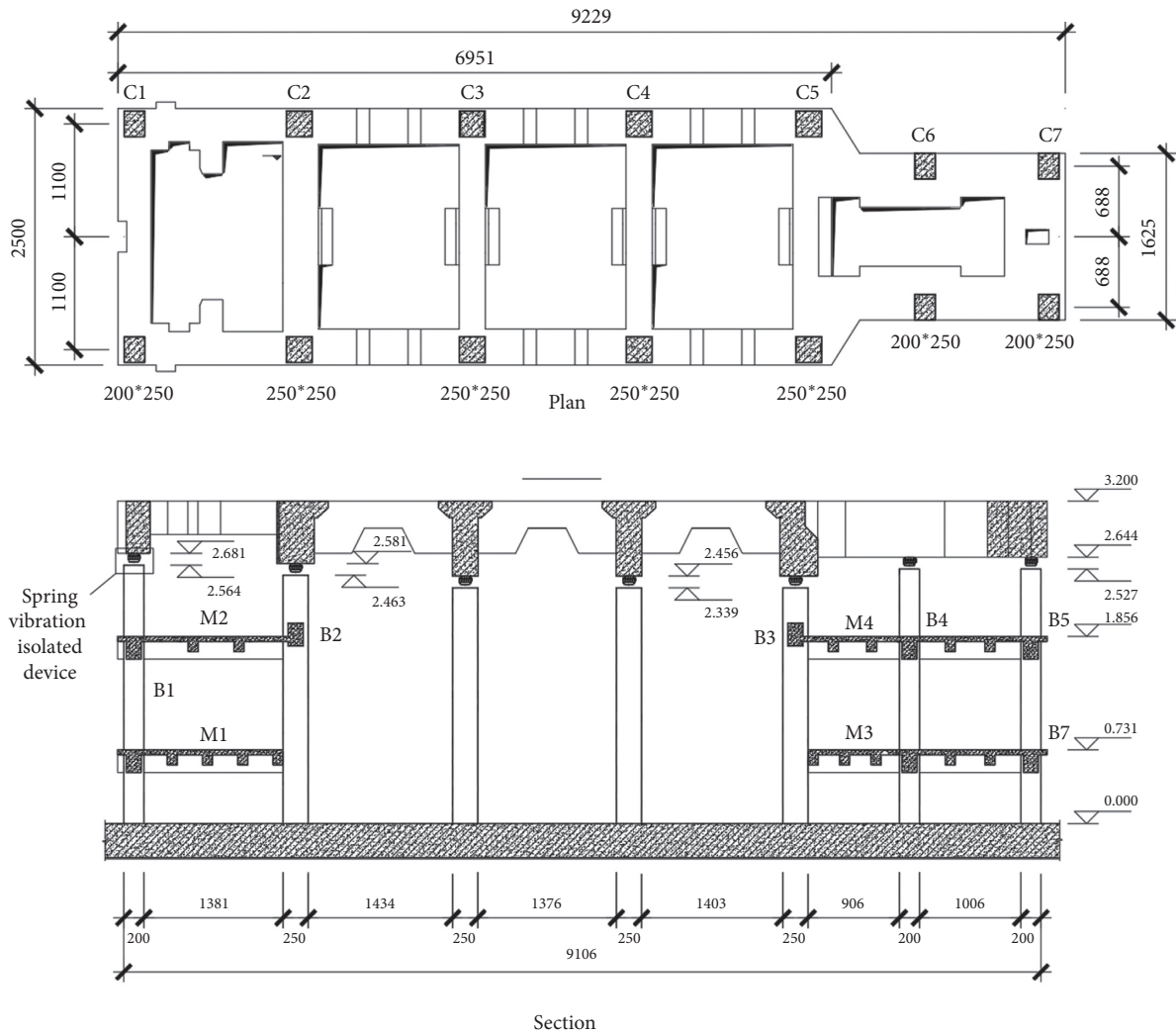


FIGURE 3: Layout drawing of test model (mm).

TABLE 1: Similarity relation of scale model.

Length	Coefficient
Geometry size	1 : 8
Modulus of elasticity	1 : 1
Density	1 : 1
Force (gravity, horizontal resistance)	1 : 8
Stiffness	1 : 8
Mass	1 : 512
Time (period)	1 : 8
Frequency	8 : 1
Acceleration	8 : 1
Displacement	1 : 8

each spring isolated device installed in the model is shown in Table 2.

2.2. Natural Vibration Characteristic Test

2.2.1. Instrumentation. The dynamic signal analyzer, data acquisition, and modal analysis software used in the self-

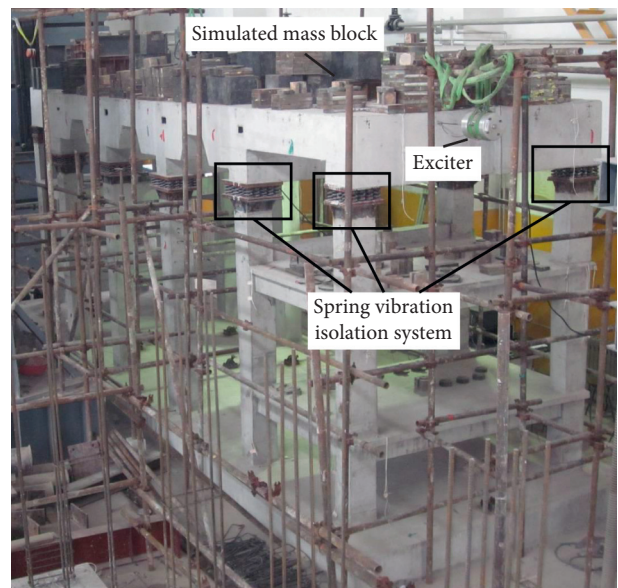


FIGURE 4: Photo of the experimental model.

TABLE 2: Stiffness of spring isolated device (kN/mm).

Column number		C1	C2	C3/C4/C5	C6	C7
Spring stiffness	Vertical	30.96	59.09	52.44	36.34	20.89
	Horizontal	16.01	29.74	25.44	20.24	11.36

vibration characteristic test are all from Belgium LMS International Company. Acceleration and force transducers were obtained from PCB Company in the United States.

2.2.2. Test Method. The multipoint spatial excitation multipoint three-dimensional measurement method was used to test the self-vibration characteristics of the model. Three excitation points were selected as horizontal transverse (X direction), horizontal longitudinal (Y direction), and vertical (Z direction) excitation points to exert excitation force on the model, and the responses of several measurement points selected in accordance with the characteristics of the model in three directions were measured. One of the exciters, which has a horizontal longitudinal direction (Y direction), is shown in Figure 4.

2.2.3. Layout of Measuring Points. Under the condition that the excitation energy is distributed throughout the foundation, the measurement points are arranged, and the excitation measurement model is established. Figure 5 shows that the excitation points of nos. 30, 3, and 15 are X , Y , and Z directions, respectively.

2.3. Pseudodynamic Test

2.3.1. Test Setup. Pseudodynamic test is suitable for large-scale model tests. Actuators are used to exert effects on the model. Therefore, the influence of the applied effect is similar to that of the real earthquake. Turbine generator with its foundation can be modeled as a single degree of freedom (SDOF) [23]. Single point loading is adopted in this paper. The natural frequencies of the two horizontal principal axes of the spring isolation foundation studied in this paper are remarkably close. Exerting seismic action on the spring isolation foundation in two directions is necessary; that is, the seismic test is divided into longitudinal and horizontal directions.

2.3.2. Loading System. Pseudodynamic test is a computer-actuator online test. The rated load of the horizontal hydraulic servo actuator used in this paper is 500 kN and the stroke is 250 mm. Gravity effect is generally neglected in conventional dynamic characteristic tests. However, in the pseudodynamic test of spring vibration isolation foundation, the gravity effect will influence the vertical deformation of spring. Therefore, a vertical preloading hydraulic system is added to the pseudodynamic test device in this paper to simulate the gravity effect. The test loading device and field are shown in Figures 6 and 7.

2.3.3. Measurement Scheme. Linear variable differential displacement transducers are arranged on the intermediate platform (one and two stories), column top, and beam and column joints of the intermediate platform to measure the displacement of the model in real-time during the pseudodynamic test. The displacement sensor number is shown in Figure 3.

2.3.4. Selection of Seismic Waves. The fortification intensity of the project is 7 degree of China code, the basic design acceleration is 0.1 g, and the earthquake is divided into the first group and the site category II. First, two typical strong earthquake records were selected following the requirements of the manufacturer, namely, Imperial Valley (USA, 1979) and Alaska (USA, 2002). Then, the code response spectrum was used as the target spectrum, and an artificial seismic wave was generated iteratively. Each seismic wave was loaded in two directions. The digital seismic acceleration time history was adjusted in accordance with the fortification intensity, and its peak value is adjusted to 0.1 g, which is the basic acceleration of 7-degree fortification earthquake. The seismic wave and its response spectrum used in the pseudodynamic test are, respectively, shown in Figures 8 and 9. According to the different directions of the input seismic wave, the pseudodynamic test can be divided into six working conditions, as shown in Table 3.

2.3.5. Parameters. Table 4 lists the test parameters used in the pseudodynamic test.

3. Finite Element Analysis

SeismoStruct is used in this study to simulate the seismic response of foundation model structures. The program can consider geometric and material nonlinearities to conduct structural time-history and IDA analyses.

3.1. Material Model and Element Type. The material parameters of concrete and steel bar used in the numerical simulation agree with those of the test. Reinforced Menegotto-Pinto model [24] is adopted for the constitutive relationship of steel bars, which is suitable for repeated loading. The concrete adopts the nonlinear constitutive model of concrete [25]. The section of beam and column is simplified following the test drawings and individual positions. The section can define the diameter, position, and number of longitudinal reinforcement and stirrups. InfrmDB element based on displacement is used in the beam-column element. The number of the cross-section fibers is 150, and the shape of cross-section is slightly different. Rayleigh damping is adopted, and the damping ratio is 0.05. The link element is used to simulate the spring vibration isolation device, and a linear model is used. The horizontal and vertical stiffness are consistent with the spring vibration isolation device used in the experimental model. Additional mass is consistent with the position and size of cast iron mass block in the test. According to the

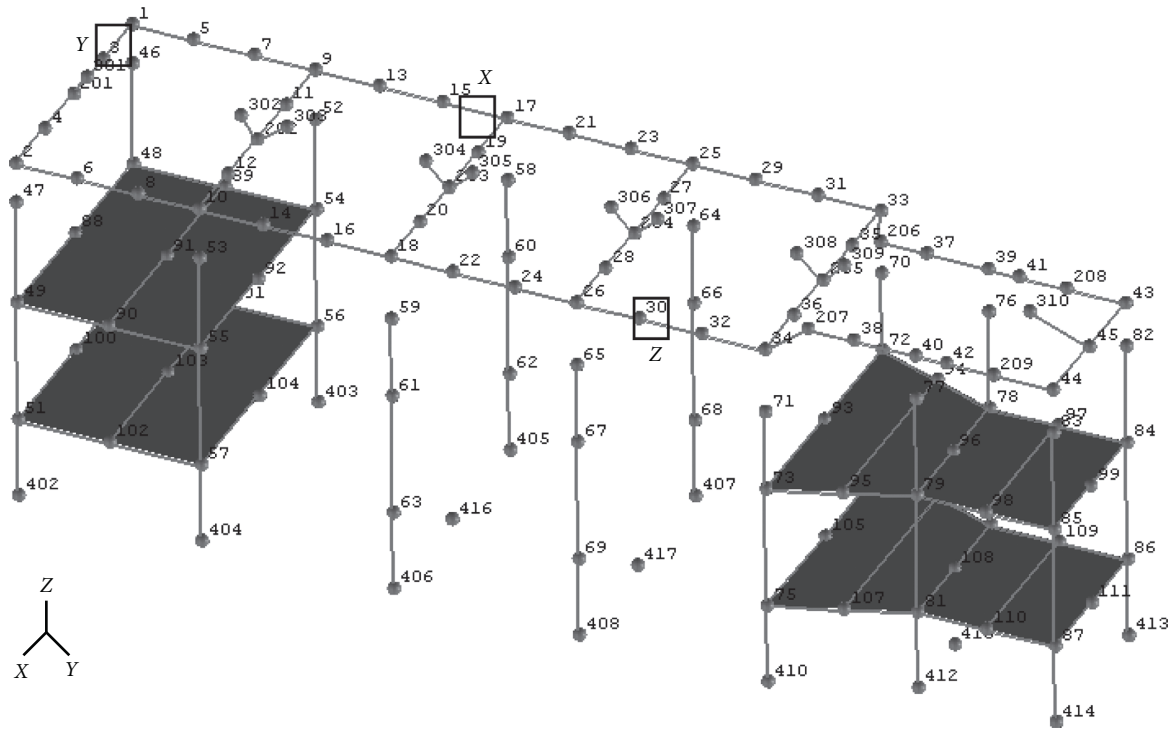


FIGURE 5: Distribution of measuring points for self-vibration test.

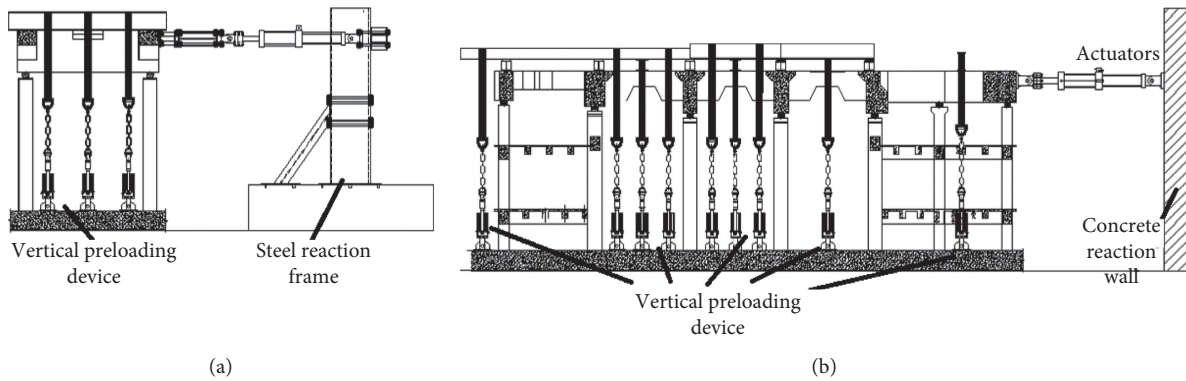


FIGURE 6: Loading system for pseudodynamic experiment. (a) Transverse loading. (b) Longitudinal loading.

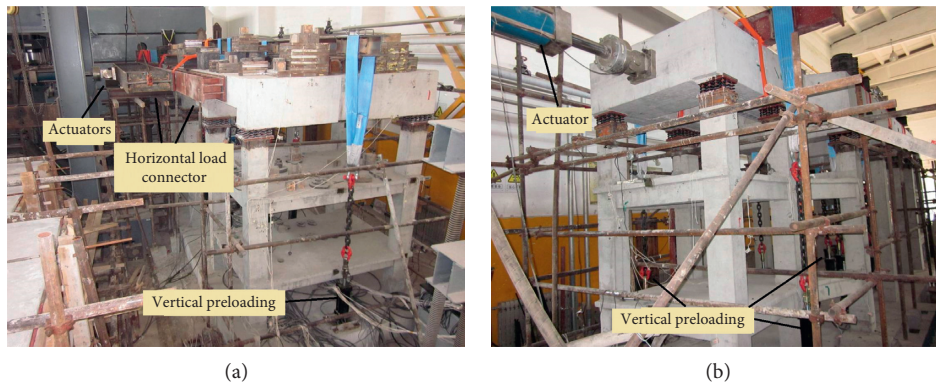


FIGURE 7: Photo of pseudodynamic experiment. (a) Transverse loading. (b) Longitudinal loading.

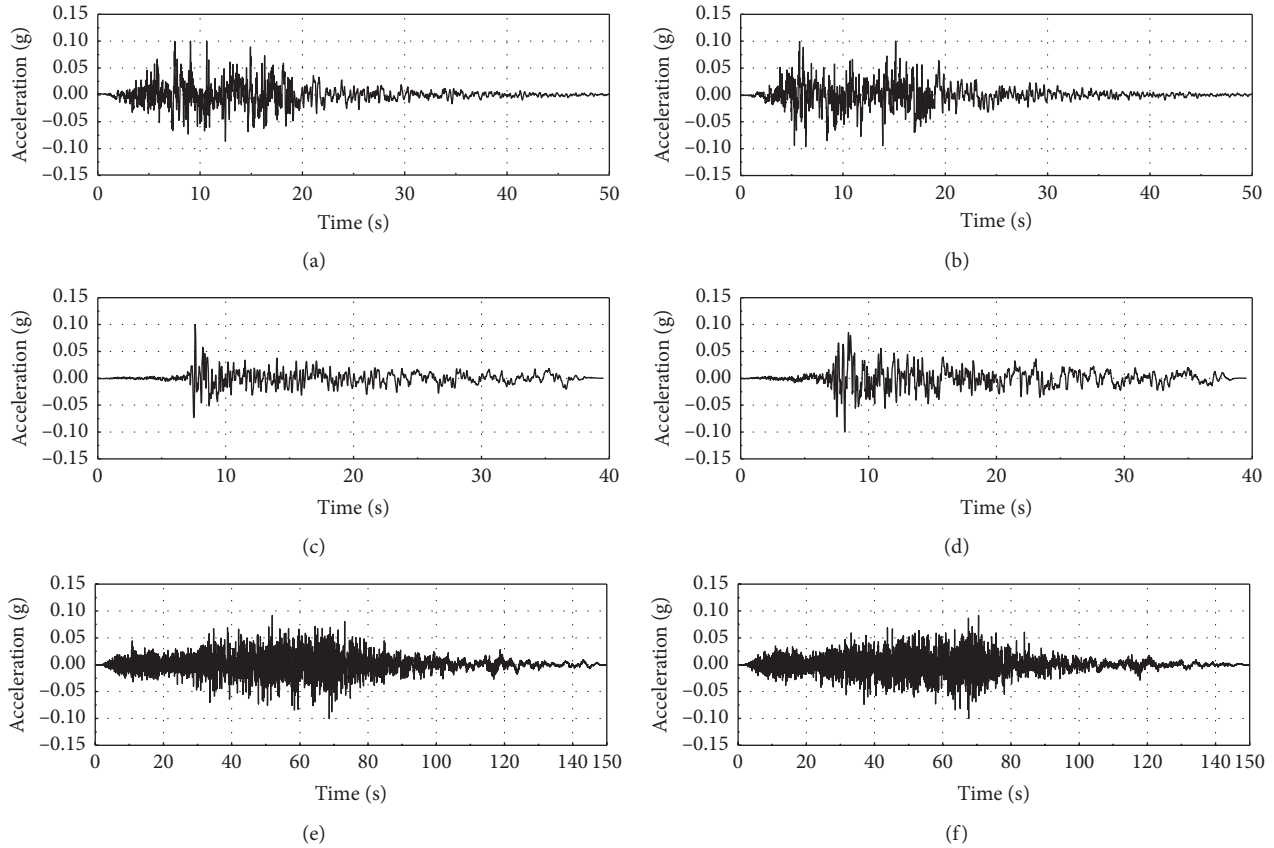


FIGURE 8: Earthquake acceleration time-history curves of intensity 7 fortification. (a) Synthesized (transverse input). (b) Synthesized (longitudinal input). (c) Imperial Valley (transverse input). (d) Imperial Valley (longitudinal input). (e) Alaska (transverse input). (f) Alaska (longitudinal input).

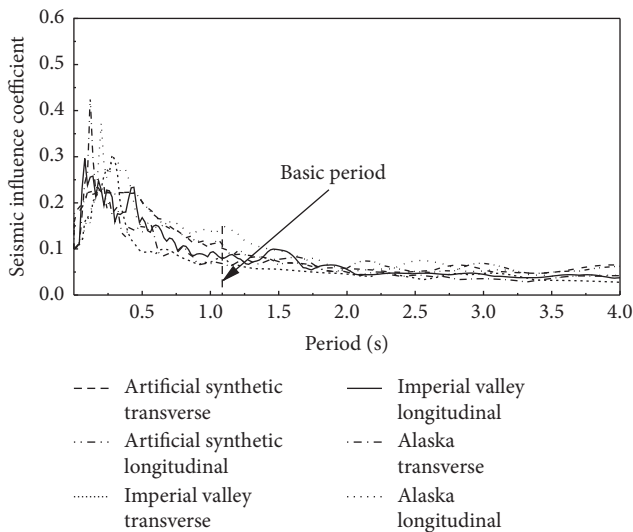


FIGURE 9: Response spectra of acceleration applied in pseudodynamic experiments.

TABLE 3: Experimental conditions (7-degree fortification).

Earthquake type	Direction	Number
Artificial synthetic	Transverse	Condition 1
	Longitudinal	Condition 2
Imperial Valley	Transverse	Condition 3
	Longitudinal	Condition 4
Alaska	Transverse	Condition 5
	Longitudinal	Condition 6

TABLE 4: Experiment parameters.

Parameter	Value	
Time step (s)	0.00125	
Loading speed (s)	10.0	
Equivalent mass (kg)	26728	
Vertical preload (kN)	1680	
Damping ratio (/)	0.05	
Initial stiffness (10^3 kN/m)	Transverse	48.4
	Longitudinal	50.0

above selection, the SeismoStruct model of the TG spring foundation in this paper is shown in Figure 10. The figure reveals the division and approximate size of beam-column section elements. Green squares, blue squares, gray squares,

and green arrows, respectively, denote additional mass, spring elements, column bottom consolidation, and the location and direction of ground motion input (taking longitudinal as an example).

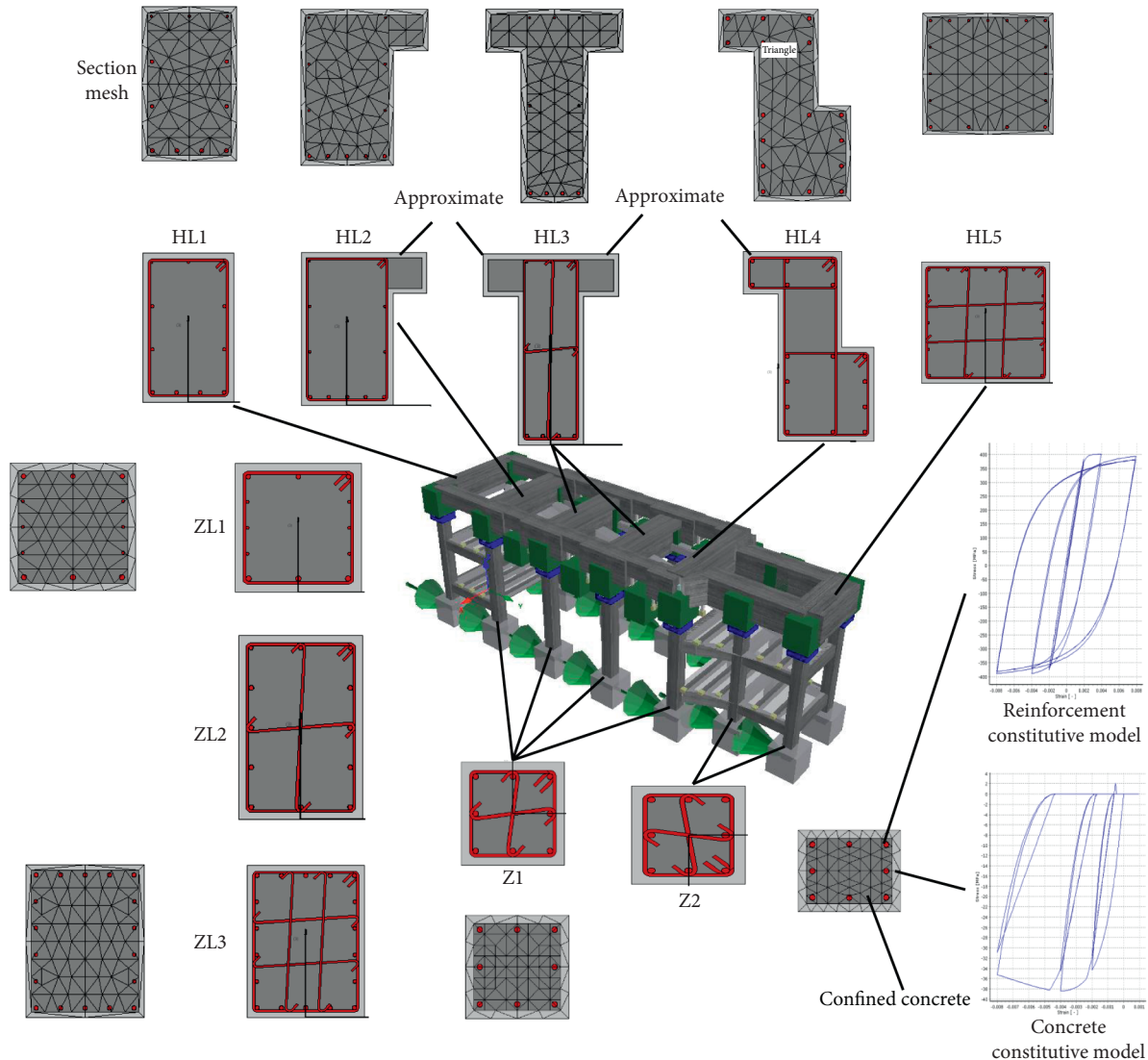


FIGURE 10: Model established by SeismoStruct and section mesh.

3.2. Ground Motion Input. In the pseudodynamic test, the foundation model is approximated as an equivalent single degree of freedom system because the equipment weight is concentrated on the TG deck, and the actuator acts on the elevation of the TG deck. SeismoStruct numerical simulation does not need to make this approximation. The input position of earthquake motion is directly at the bottom of the column.

4. Results

4.1. Natural Vibration Characteristics

4.1.1. Natural Frequency. The frequency results obtained from the natural vibration test are converted to the prototype according to the similarity ratio. This paper mainly compares the results of the modal test and numerical simulation. Two methods are used for numerical simulation: one is the SeismoStruct model, and the other is the

STARDYNE program adopted by the manufacturer, which uses the bar element. Among these methods, the calculation model of STARDYNE is divided into the top deck model (without considering the structure below the vibration isolation device) and overall model (TG deck and substructure considering the column and the intermediate platform). Table 5 compares the natural frequencies of the experimental and numerical results. The first six frequencies and modal shapes reveal that the test results are in good agreement with that of numerical simulation, and the error is small, which shows that the numerical simulation is reasonable. In the first six orders, the results of the low-order model test are smaller than those of the numerical simulation, while the results of the high-order model test are large. This result indicates that the numerical simulation regards the end of the column as consolidation, which improves the stiffness of the entire structure, thereby resulting in the vibration of the TG deck. Moreover, the results of numerical simulation are large and involve the

TABLE 5: Contrast of natural frequencies (Hz).

Mode shape characteristics	Test	Numerical simulation			
		SeismoStruct	Top deck	STAR DYNE TG deck and substructure	
Transverse translation	0.92	1.06 (15%)	1.06 (15%)	1.04 (13%)	
Longitudinal translation	1.01	1.15 (14%)	1.12 (11%)	1.09 (8%)	
Translation torsion	1.23	1.34 (9%)	1.37 (11%)	1.34 (9%)	
Vertical bending	3.48	3.26 (−6%)	3.26 (−6%)	3.25 (−7%)	
Vertical swing	Transverse	3.57	2.77 (−22%)	3.04 (−15%)	3.04 (−15%)
	Longitudinal	\	3.07 (\)	4.34 (\)	4.47 (\)

Note. In parentheses, the percentage of deviation between numerical model and test results is given.

vibration of the column, and the results of numerical simulation are smaller. Overall, the STAR DYNE model is closest to the experimental results. The results show that the natural frequencies of spring vibration isolation foundation are low, and the vertical natural frequencies are far away from the unit operating disturbance frequency (25 Hz).

4.1.2. Mode Shape. Figure 11 is the modal shape diagram of the model. The test results are listed on the left, the overall model results of STAR DYNE are listed in the middle, and the results of the SeismoStruct model are listed on the right (no additional mass and spring elements are shown). The first six vibration modes of the model are the entire vibration of the platform plate, which shows that the spring vibration isolation device can separate the foundation platform plate from the column and achieve a certain degree of dynamic decoupling. Thus, the dynamic transmission from the platform plate to the column can be reduced during the operation of the unit.

4.2. Seismic Test

4.2.1. Seismic Response. Seismic responses obtained from pseudodynamic experiments applied to the foundation are transformed into prototype results according to the similarity ratio of the model and prototype. Table 6 lists the maximum values and comparisons between the experiment and the simulation results of the foundation seismic response under various conditions. SeismoStruct is used to simulate the seismic response, and the error of the test results is approximately 10%. Combining with the discussion of 3.1.1 natural frequency, the stiffness of the model established by numerical simulation is larger than that of the experimental model, especially the connection between spring vibration isolation device and column and top deck. From the viewpoint of restoring force and displacement, the simulation results are approximately 15% larger than the experimental results, which is consistent with the analysis of self-vibration characteristics.

The requirements of the seismic code indicate that the structural joint between the foundation slab and the plant structure shall be taken as 1.2 times of the maximum displacement of the TG deck, which shall not be less than 200 mm. The test results show that 1.2 times of the maximum displacement of the foundation slab is less than

200 mm. Thus, increasing the structural joint here is unnecessary.

The magnification factor of foundation (maximum response acceleration divides maximum input acceleration) is only 0.91 when 7-degree fortification earthquake is the input. This factor appearing in working condition 5 is small in other working conditions. The horizontal stiffness of the spring vibration isolation foundation is substantially lower than that of the rigid common foundation. The first-order natural frequency test value is 0.92 Hz (period 1.09 s), the calculated value is 1.04 Hz (period 0.96 s), and the predominant period is 0.35 s away from the site. This finding shows that the spring vibration isolation device prolongs the natural vibration period of the foundation, and the seismic influence coefficient (amplification coefficient) enters the less valuable part of the response spectrum. Spring vibration isolation devices elevate the seismic performance of the foundation.

4.2.2. Seismic Force Response. Figure 12 shows the force seismic response time history under each condition.

4.2.3. Seismic Displacement Response. Figure 13 shows a comparison of the displacement seismic response between the test and the simulation under each condition. The trend of the time-history curves of the two methods is identical and the size is close. In case 1, the test is almost the same as the first 20 s of the simulation, and the test curve deviates after 20 s. Moreover, residual after the test is still observed, which indicates the presence of gap between the foundation and the transverse loading device. Follow-up experiments corrected this problem, and no similar situation occurs again. The trend and size of displacement time-history curve in the three conditions of transverse loading are relatively consistent. This finding shows that the numerical simulation is correct and can simulate the displacement response and deformation of the foundation. When the curve is loaded longitudinally, the results of simulation are larger than those of experiments, such as 10–20 s in condition 2, 10–15 s in condition 4, and 50–55 s and 80–90 s in condition 6.

4.2.4. Deformation Analysis. Figure 14 shows the maximum response of seismic displacement at different locations of the foundation under experiment condition and numerical





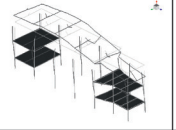
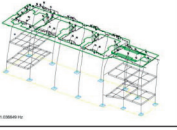
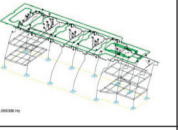
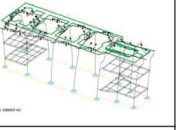
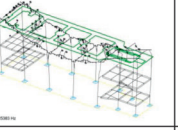
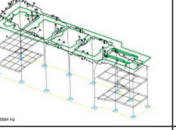
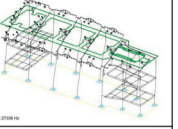
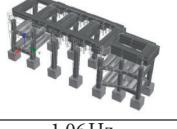
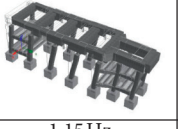
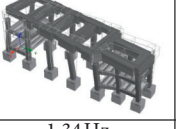



Mode shape	Transverse translation	Longitudinal translation	Translation torsion	Vertical bending	Vertical swing-transverse	Vertical swing-longitudinal
Test						/
	0.92Hz	1.01 Hz	1.23 Hz	3.48 Hz	3.57 Hz	/
STARDYNE						
	1.04Hz	1.09Hz	1.34Hz	3.25 Hz	3.04Hz	4.47Hz
Seismostruct						
	1.06Hz	1.15Hz	1.34Hz	3.01 Hz	2.77 Hz	3.07Hz

FIGURE 11: Modal shape contrast of test and simulation.

TABLE 6: Max values of seismic response.

	Seismic experiments				SeismoStruct simulation			
	Displacement (mm)	Acceleration (m/s^2)	Velocity (m/s)	Restoring force (kN)	Displacement (mm)	Acceleration (m/s^2)	Velocity (m/s)	Restoring force (kN)
1	37.17	0.64	0.13	8484	32.55 (12%)	0.60 (6%)	0.12 (8%)	9948 (-17%)
2	32.60	0.69	0.14	9485	35.78 (-10%)	0.77 (-12%)	0.17 (-21%)	9636 (-2%)
3	25.99	0.52	0.11	7081	24.67 (5%)	0.45 (13%)	0.10 (9%)	7727 (-9%)
4	47.43	0.91	0.19	12367	48.59 (-2%)	0.93 (-2%)	0.21 (-11%)	14444 (-17%)
5	41.77	0.73	0.16	9734	37.25 (11%)	0.59 (19%)	0.13 (19%)	9585 (2%)
6	39.14	0.75	0.16	10266	37.84 (3%)	0.85 (-13%)	0.18 (-13%)	12888 (-26%)

Note. In parentheses, the percentage of deviation between test and simulation results is shown. The positive value indicates that the test results are larger than the simulation results.

simulation. The measurement points of displacement are arranged from bottom to top on each column, two intermediate platforms, column tops and top deck. The section of C2 column and M1/M2 platform is taken as an example for transverse loading, while C7 column and M3/M4 platform are taken as examples for longitudinal loading. Among these examples, B6 and B7 are the measuring points of one-story platform beam, B2 and B5 are the measuring points of two-story platform beam, B2 and B6 are the transverse measuring points, and B5 and B7 are the longitudinal measuring points. The figure shows that the deformation at each position of the foundation is linear, which conforms to the pseudodynamic experimental hypothesis of single degree of freedom. The experimental and simulated deformation curves of the foundation are basically the same under transverse loading. The deformation of the upper part of the column in case 1 and 5 is larger than that in other cases. This phenomenon may be due to the decrease in rigidity caused by the separate pouring of the section. The loading position of the actuator under longitudinal loading is far from the displacement measurement position. The deformation along the height of the foundation is linear after applying seismic action, and the test deformation curve is smoother. The upper part is free in

the numerical simulation, and the stiffness ratio is the main factor of deformation. The constraint of the one- and two-story platforms induces the deformation curve on the break point, and the simulation curve shows that the spring deformation is large.

4.2.5. *Spring Deformation.* The largest difference between spring and rigid common foundations lies in the spring isolation device that separates the column from the top deck, which will inevitably lead to different displacements of columns in frame foundation under horizontal earthquake action. Figure 15 is a comparison of the top displacement of each column and that of the top deck under the action of artificial synthetic wave, typical record Imperial Valley, and Alaska which are 7-degree fortification earthquakes under lateral loading. The first half is the experimental results, and the second half is the simulation results. The displacement connection at the top of the column to the spring isolator at the top of the base C2/C3/C4/C5/C6 column has large stiffness; therefore, the deformation of the spring is small, which shows the large displacement of the column. The maximum displacement of the top of the column appears in

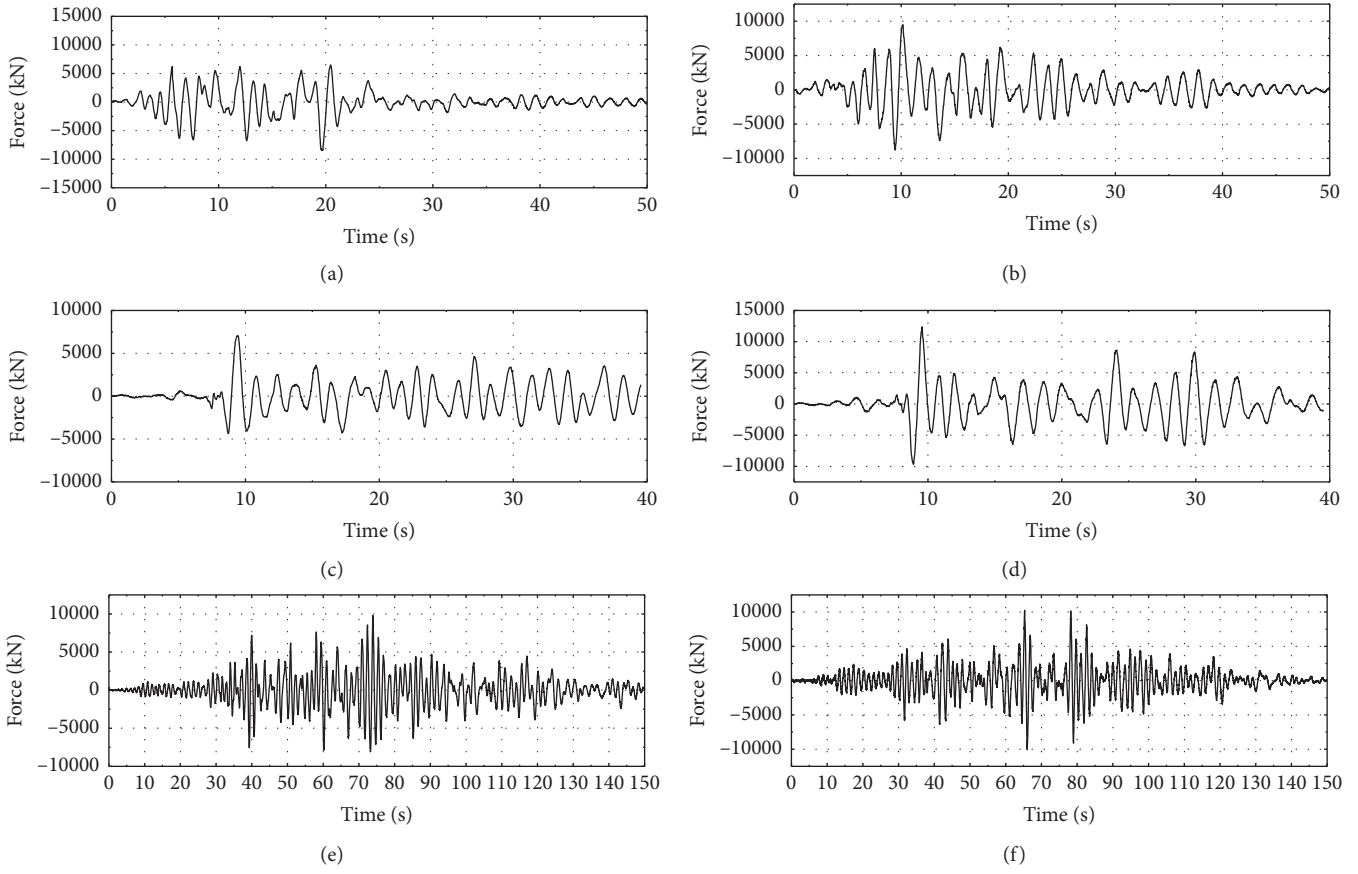


FIGURE 12: Force seismic response time-history curves. (a) Artificial synthetic-condition 1-transverse. (b) Artificial synthetic-condition 2-longitudinal. (c) Imperial Valley-condition 3-transverse. (d) Imperial Valley-condition 4-longitudinal. (e) Alaska-condition 5-transverse. (f) Alaska-condition 6-longitudinal.

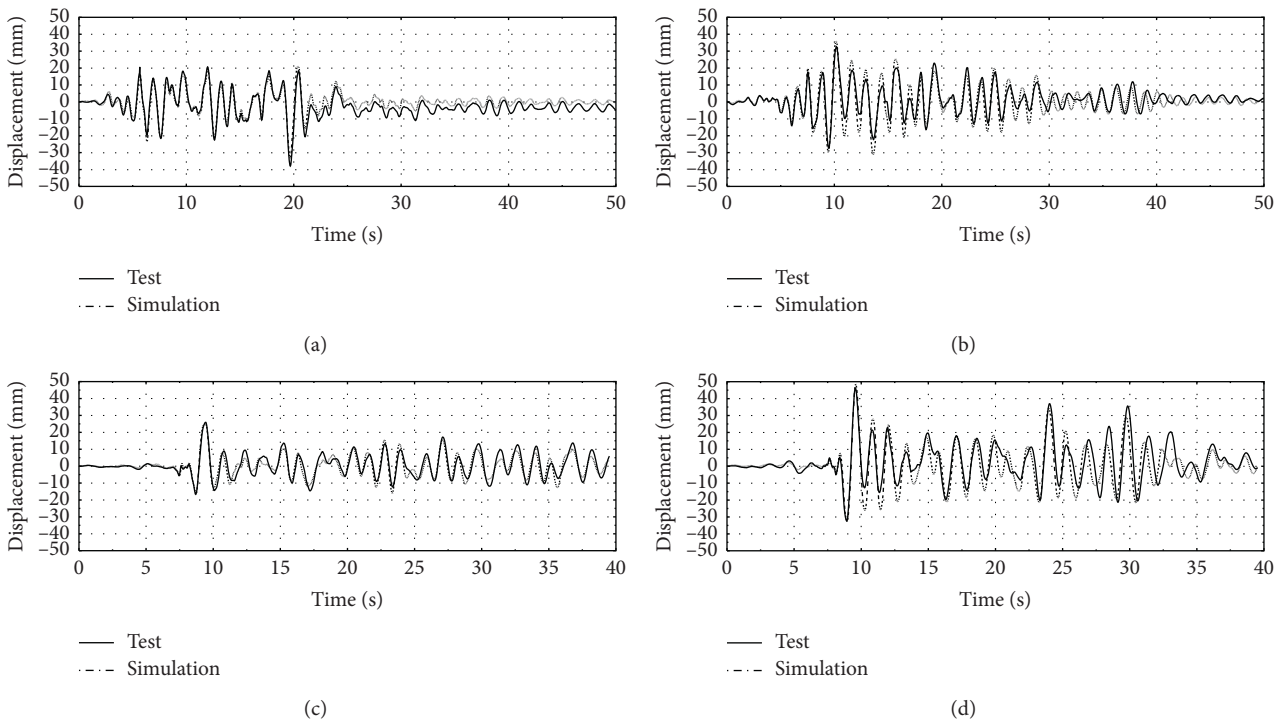


FIGURE 13: Continued.

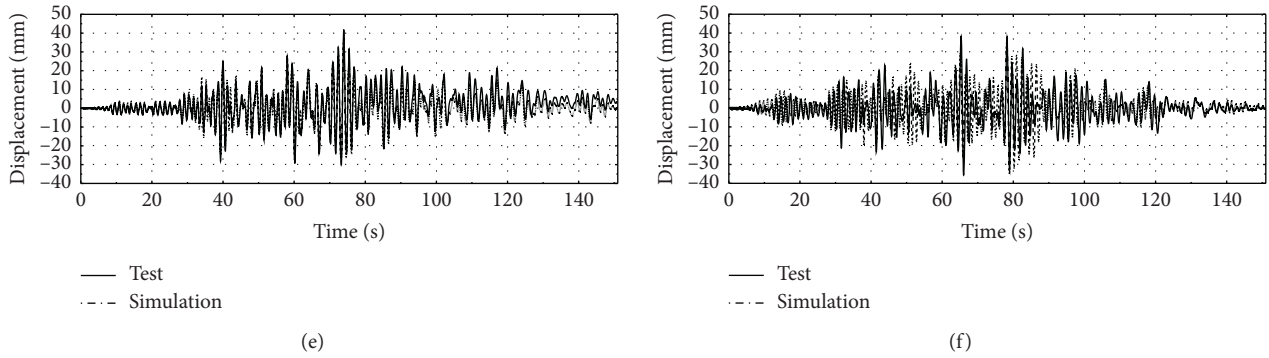


FIGURE 13: Displacement seismic response contrast between experiments and simulations. (a) Artificial synthetic-condition 1-transverse. (b) Artificial synthetic-condition 2-longitudinal. (c) Imperial Valley-condition 3-transverse. (d) Imperial Valley-condition 4-longitudinal. (e) Alaska-condition 5-transverse. (f) Alaska-condition 6-longitudinal.

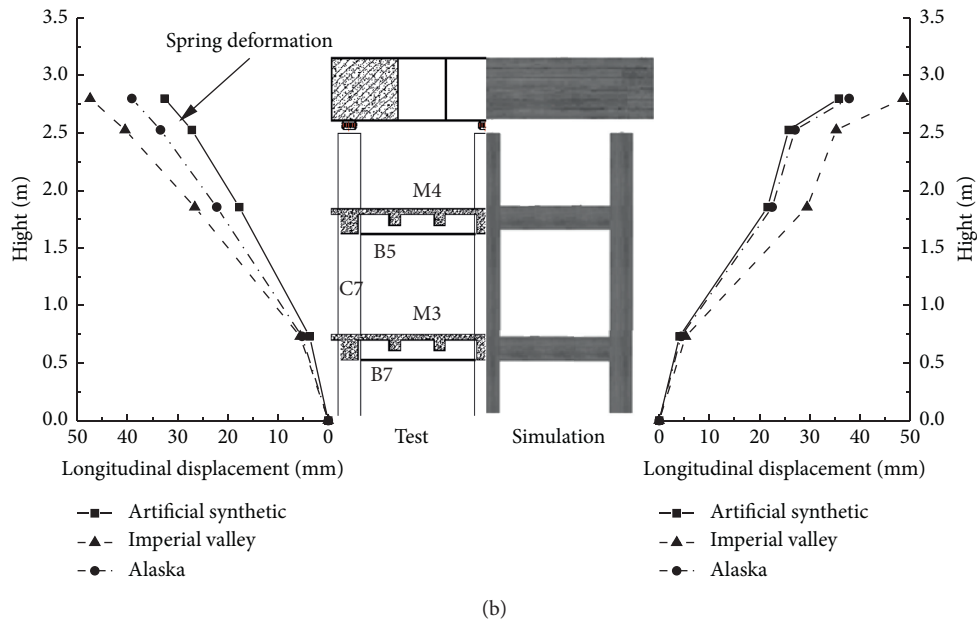
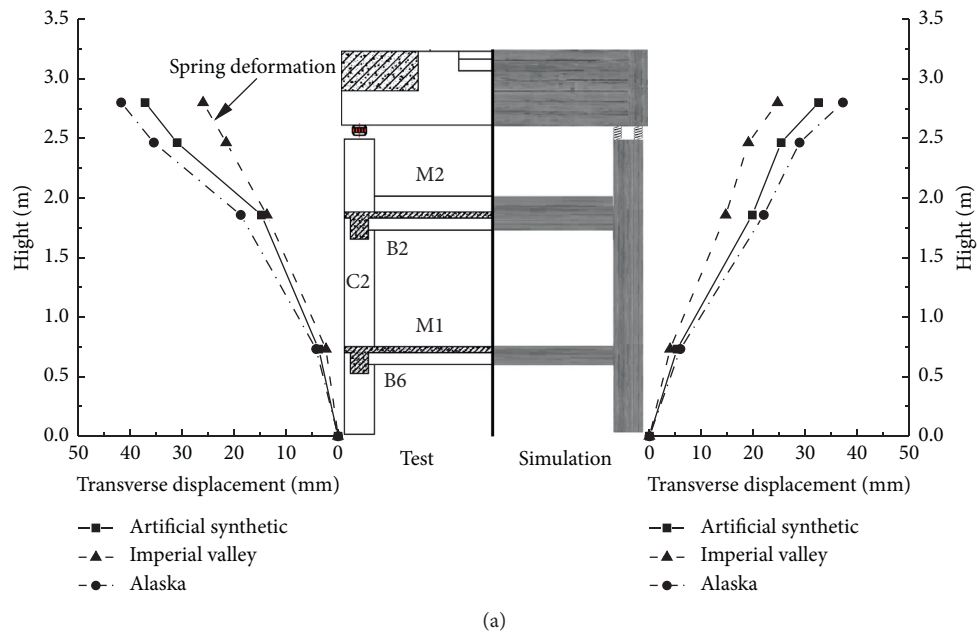


FIGURE 14: Displacement response contrast of different location. (a) Transverse loading. (b) Longitudinal loading.

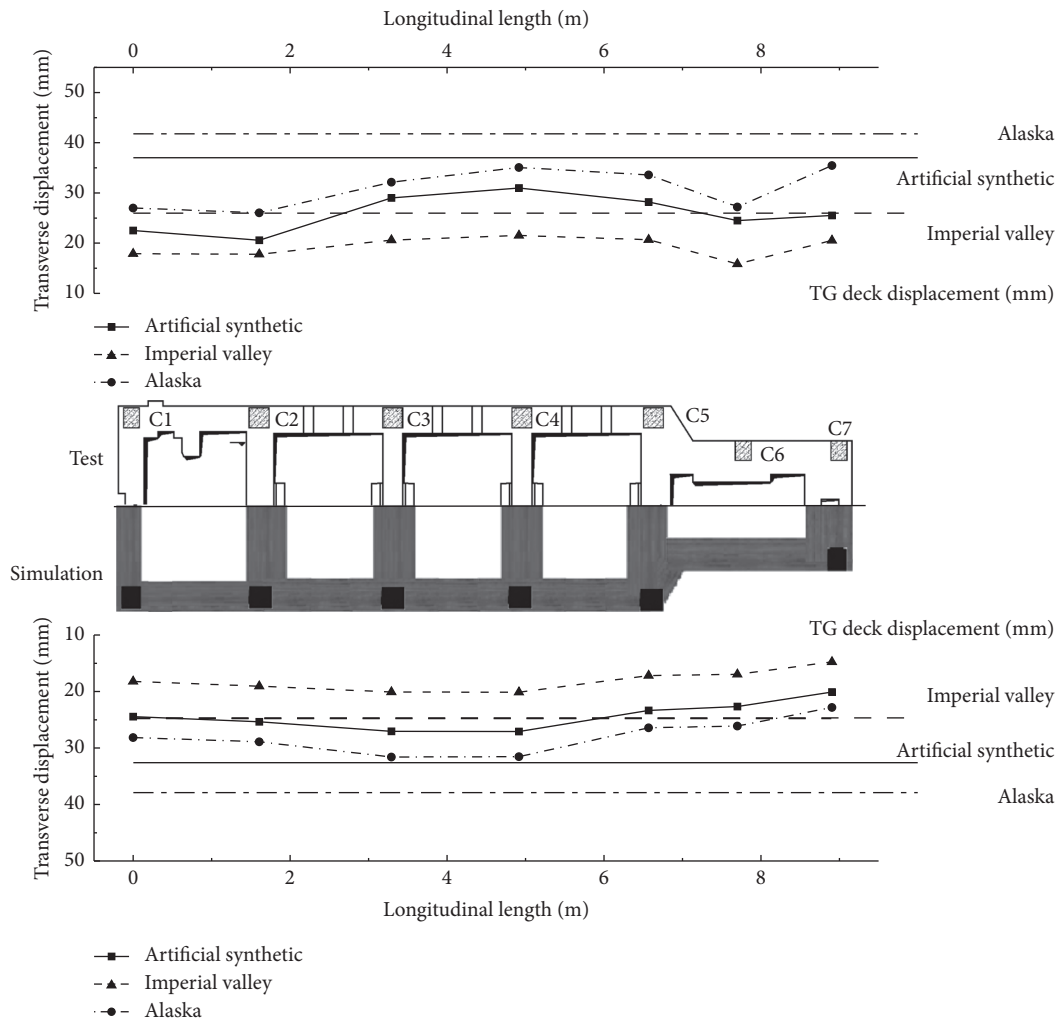


FIGURE 15: Displacement seismic response contrast of TG deck and column top.

C3 and C4 between the two low pressure cylinders in each condition. This phenomenon is due to the absence of other connections between the column and the entire structure except through the spring vibration isolator and the top deck, and the stiffness of the column is lower than that of other columns. Under the experimental conditions, the displacement of C7 column at the end of the high-pressure cylinder of the foundation is large, and the breaking point of the connecting line appears at C6. This situation is absent in the simulation possibly because the rigid center of the foundation platform does not coincide with the center of mass, and the longitudinal dimension is large. Moreover, the foundation demonstrates a small amount of torsion under lateral loading.

Table 7 shows the comparison between the maximum displacement of the top deck and that of the spring obtained by the test and simulation under various conditions. The dimensions of C3 and C4 columns are the same, and the horizontal stiffness of the top spring isolator is similar. The spring deformation should be equal regardless of pseudo-dynamic experiment of the top deck loading or the numerical simulation of the bottom loading of the column. The

data in Table 7 only prove this point. The proportion of the spring deformation at the top of C3 and C4 is completely equal when the vertical loading is applied. The foundation model is slightly twisted when the vertical loading is applied, and the two are still remarkably close. The top displacement of the column from the spring deformation is different because the stiffness of each column and the corresponding spring isolator is different. However, the spring deformation accounts for approximately 20% of the displacement ratio of the platform plate, and some deformations exceed 40%. Deformation values are distributed inversely according to the stiffness of columns and springs. The top displacement of columns with small and large stiffness is respectively large and small. The existence of spring vibration isolation device redistributes the seismic action of columns, induces uniform force of columns, gives full play to the resistance of each column, and improves the seismic performance of the foundation.

4.2.6. Comparison of Deck Displacements. Spring vibration isolation is an important part of the foundation structure.

TABLE 7: Spring deformation and displacement of TG deck (mm).

Earthquake type and condition	Direction	Method	Column number						
			C1	C2	C3	C4	C5	C6	C7
Artificial synthetic	T	Test	14.64 (39%)	16.60 (45%)	8.14 (22%)	6.16 (17%)	8.95 (24%)	12.68 (34%)	11.63 (31%)
		Simulation	8.09 (25%)	7.19 (22%)	5.50 (17%)	5.45 (17%)	9.20 (28%)	9.86 (30%)	12.47 (38%)
	L	Test	5.73 (18%)	6.11 (19%)	5.44 (17%)	5.41 (17%)	8.29 (25%)	8.81 (27%)	7.91 (24%)
Imperial Valley		Simulation	14.81 (41%)	12.12 (34%)	7.03 (20%)	7.00 (20%)	14.62 (41%)	14.63 (41%)	13.76 (38%)
	T	Test	8.08 (31%)	8.20 (32%)	5.39 (21%)	4.47 (17%)	5.32 (20%)	10.16 (39%)	5.44 (21%)
		Simulation	6.45 (26%)	5.62 (23%)	4.57 (19%)	4.53 (18%)	7.48 (30%)	7.70 (31%)	9.90 (40%)
Alaska	L	Test	7.52 (16%)	8.21 (17%)	6.94 (15%)	7.76 (16%)	11.99 (25%)	11.53 (24%)	11.35 (24%)
		Simulation	11.94 (25%)	13.29 (27%)	3.58 (7%)	3.22 (7%)	14.61 (30%)	15.23 (31%)	15.73 (32%)
	T	Test	14.97 (36%)	15.92 (38%)	9.83 (23%)	6.89 (16%)	8.38 (20%)	14.76 (35%)	6.49 (15%)
		Simulation	9.08 (24%)	8.34 (22%)	5.66 (15%)	5.70 (15%)	10.82 (29%)	11.13 (30%)	14.44 (39%)
	L	Test	7.53 (19%)	6.77 (17%)	6.40 (16%)	5.92 (15%)	5.70 (15%)	7.95 (20%)	7.57 (19%)
		Simulation	9.98 (26%)	10.78 (28%)	3.74 (10%)	3.62 (10%)	12.00 (32%)	12.99 (34%)	13.10 (35%)

Note. In parentheses, the ratio of spring deformation to top deck displacement is expressed in percentage. T means transverse and L means longitudinal.

TABLE 8: Deck displacements before and after isolation (mm).

Earthquake type	Number	After isolation	Before isolation
Artificial synthetic	Condition 1	32.55	5.52
	Condition 2	35.78	5.77
Imperial Valley	Condition 3	24.67	4.21
	Condition 4	48.59	8.22
Alaska	Condition 5	37.25	5.03
	Condition 6	37.84	4.75

Maintaining the numerical model, only the spring isolators are removed, and the concrete frame beams and columns are fixed. The seismic response of the foundation slab is studied under the same conditions. Table 8 shows the comparison between the maximum displacement of the TG deck before and after isolation using spring isolators. The maximum displacement of the TG deck before isolation is less than that after isolation. Although the spring isolator can help the natural frequency of the foundation structure in avoiding the vibration frequency of the machine, because of its small horizontal stiffness, the seismic response of the structure is larger under horizontal earthquakes.

5. Conclusions

A 1:8 scale spring vibration isolation foundation of a nuclear power conventional island TG unit, including self-vibration characteristic test, pseudodynamic seismic experiments, and finite element simulation, is studied comprehensively in this paper. The results are transformed to prototype according to the similarity principle, and the comparative analysis of the test and simulation is conducted. The main conclusions are as follows:

- (1) The first and second modes of the foundation are transverse and longitudinal translations with corresponding frequencies of 0.92 and 1.01 s. The results of the SeismoStruct model established in this paper are the same as those of the test. The first and second frequencies are 1.06 and 1.12 s, respectively. The overall model is closer to the test results. The results of natural vibration characteristics show that the natural frequency of spring vibration isolation foundation is low, and the vertical natural frequency is far away from the unit operating disturbance frequency (25 Hz).
- (2) In the pseudodynamic test, the maximum responses of acceleration, velocity, displacement, and restoring force of turbine foundation plate under 7-degree fortification earthquake are 0.91 m/s², 0.19 m/s, 47.42 mm, and 12367 kN, respectively; in numerical simulation, the maximum responses of acceleration, velocity, displacement, and restoring force of turbine foundation plate under 7-degree fortification earthquake are 0.93 m/s², 0.19 m/s, 48.59 mm, and 14444 kN, respectively.
- (3) Under the action of earthquake, the acceleration of the spring vibration isolation base plate is not

amplified, and the device can protect the steam turbine to reduce the impact of acceleration during earthquakes.

- (4) Vibration isolation spring is crucial in resisting earthquakes. The vibration isolation spring separates the column and platform, and the displacement of the top of the column is no longer equal. The horizontal seismic force on the entire foundation is adjusted by the spring vibration isolation device and redistributed to each column to give full play to the seismic capacity of each column.
- (5) Comparing the results with physical modelling and the numerical simulation, the foundation is simulated by the finite element method using SeismoStruct software. The error of natural vibration characteristic is approximately 15%. The maximum error of seismic response is approximately 10%, the trend of displacement seismic response curve is the same, and the magnitude is close. The approximation degree of the deformation curve at each position of the foundation is relatively high. The distribution of spring deformation is consistent, and the proportion of spring deformation to TG deck displacement is close. From the research object of this paper, the simulation effect is satisfactory and can meet the needs of the project.
- (6) The comparison results of the maximum displacement of the TG deck before isolation and after isolation reveal that the maximum displacement of the TG deck after isolation is approximately six times that of that before isolation based on the seismic test.
- (7) The result indicates that the foundation design meets the standard of “Code for Seismic Design of Buildings” in China and achieves the goal of spring vibration isolation and seismic resistance. According to the requirements of the seismic code, 1.2 times of the maximum displacement of the foundation slab is less than 200 mm.
- (8) The test process and results show that the loading mode of the seismic test has some influence on the seismic response of the structure, which needs further study in the future. Numerical simulation should be conducted in the future to supplement the research on the seismic performance of such structures.

Data Availability

The data used to support the findings of this study are available from the corresponding author upon request.

Conflicts of Interest

The authors declare that there are no conflicts of interest regarding the publication of this paper.

Acknowledgments

This work was supported by the Youth Talent Support Program of North China University of Technology. The authors deeply express sincere appreciation to them.

References

- [1] World Nuclear Association, *Nuclear Power in China [EB/OL]*, World Nuclear Association, London, UK, 2018, <http://www.world-nuclear.org>.
- [2] H. C. H. Liu, *Concrete Foundations for Turbine Generators: Analysis, Design, and Construction*, American Society of Civil Engineers (ASCE), Reston, VA, USA, 2018.
- [3] G. S. H. Luo, J. X. Fang, and J. Wang, "Aseismic performance of spring supported turbo-generator foundation," *Engineering Journal of Wuhan University*, vol. 42, no. S1, pp. 436–442, 2009.
- [4] X. Y. Shao, J. Z. H. Zhou, and X. J. Yin, "Research of model test of spring vibration isolated turbo-generator foundation-Test of dynamic characters," *Engineering Journal of Wuhan University*, vol. 44, no. S1, pp. 364–368, 2011.
- [5] T. Zhu and C. L. Chen, "Vibration isolation for frame foundation of a power machinery," *Journal of Vibration and Shock*, vol. 29, no. 02, pp. 121–124+225, 2010.
- [6] Y. Q. Song, X. Q. Zhou, and J. J. Wu, "Selection and design of spring foundation of half speed turbine generator for ling'ao Phase II NPP," *Nuclear Power Engineering*, vol. 32, no. S2, pp. 34–37, 2011.
- [7] X. Y. Shao, J. Z. H. Zhou, and X. J. Yin, "Research of model test of spring vibration isolated turbo-generator foundation-Pseudo-dynamic earthquake test," *Engineering Journal of Wuhan University*, vol. 44, no. S1, pp. 389–392, 2011.
- [8] D. Q. Mei, W. He, and Z. C. H. Chen, "Research on model test of frame foundation model for steam turbine-generator set," *Power Engineering*, vol. 21, no. 6, pp. 1523–1527, 2001.
- [9] Z. G. Wang, N. Sun, and X. B. Gao, "Modal analysis for a 1:10 model of turbine-dynamotor frame foundation," *Earthquake Engineering and Engineering Vibration*, vol. 25, no. 1, pp. 33–37, 2005.
- [10] L. G. Kang, X. W. Li, and Y. L. Xie, "Experimental research and analysis on dynamic characters of turbine-generator unit frame foundation," *Journal of Building Structures*, vol. 29, no. S1, pp. 20–26, 2008.
- [11] B. Y. Zhang, Q. J. Li, and W. Wang, "Experiment study on dynamic characteristics of spring vibration isolating foundation for large turbine-generator set," *Journal of Harbin Institute of Technology*, vol. 47, no. 4, pp. 37–43, 2015.
- [12] W. F. Li, X. J. Wang, and Q. Sun, "Design of a combined vibration test rig for shafting and spring vibration-isolated foundation of nuclear power half-speed unites," *Journal of Chinese Society of Power Engineering*, vol. 37, no. 11, pp. 890–894+944, 2017.
- [13] W. Liu and M. Novak, "Dynamic behaviour of turbine-generator-foundation systems," *Earthquake Engineering & Structural Dynamics*, vol. 24, no. 3, pp. 339–360, 1995.
- [14] V. Karayel, E. Yuksel, T. Gokce, and F. Sahin, "Uni-axial shaking table tests and validations of a seismic isolation system made of spring tube braces," *Soil Dynamics and Earthquake Engineering*, vol. 118, no. 3, pp. 35–46, 2019.
- [15] M.-W. Hur and T.-W. Park, "Performance evaluation of seismic isolation system by installation location in lighthouse structures," *Shock and Vibration*, vol. 2018, Article ID 5751623, 13 pages, 2018.
- [16] D. An, X. Sun, and T. J. Qu, "Modal analysis of experiment on model of spring vibration isolated turbine-generator foundation," *Journal of North China University of Technology*, vol. 24, no. 3, pp. 84–88, 2012.
- [17] T. J. Qu, K. Xiang, and X. J. Yin, "Pseudo-dynamic test of the anti-seismic performance of turbine generator foundation," *Earthquake Resistant Engineering and Retrofitting*, vol. 35, no. 1, pp. 115–119, 2013.
- [18] M. M. Zan and T. J. Qu, "Test of the vibration isolation efficiency of spring-supported turbo-generator foundation," *Journal of North China University of Technology*, vol. 27, no. 1, pp. 80–83, 2015.
- [19] X. G. Chen and T. J. Qu, "Modal test on the model of a foundation for 1000MW turbo-unit," *Journal of North China University of Technology*, vol. 29, no. 5, pp. 129–134, 2017.
- [20] D. An and T. J. Qu, "Seismic behavior of turbine-generator foundation under strong earthquake action in different directions," *Advances in Civil Engineering*, vol. 2018, Article ID 2506264, 10 pages, 2018.
- [21] S. Mohurd and M. Aqsiq, "Code for Seismic Design of Buildings": *GB50011-2010*, China Architecture and Building Press, Beijing, China, 2016 edition, 2016.
- [22] S. Kumar, Y. Itoh, K. Saizuka, and T. Usami, "Pseudodynamic testing of scaled models," *Journal of Structural Engineering*, vol. 123, no. 4, pp. 524–526, 1997.
- [23] S. Abdullah and N. H. A. Hamid, "Modelling of turbine-generator and foundation as single degree of freedom using ruaumoko programme," *International Journal of Engineering & Advanced Technology*, vol. 07, no. 01, pp. 18–31, 2012.
- [24] M. Menegotto and P. E. Pinto, "Method of analysis of cyclically loaded RC plane frames including changes in geometry and non-elastic behavior of elements under normal force and bending," *Preliminary Report, IABSE*, vol. 13, pp. 15–22, 1973.
- [25] J. B. Mander, M. J. N. Priestley, and R. Park, "Theoretical stress-strain model for confined concrete," *Journal of Structural Engineering*, vol. 114, no. 8, pp. 1804–1826, 1988.

Research Article

Multihazard Response Control of Base-Isolated Buildings under Bidirectional Dynamic Excitation

Daniel H. Zelleke ¹, Sandip K. Saha ², and Vasant A. Matsagar ¹

¹Multi-Hazard Protective Structures (MHPS) Laboratory, Department of Civil Engineering, Indian Institute of Technology (IIT) Delhi, Hauz Khas, New Delhi 110016, India

²School of Engineering, Indian Institute of Technology (IIT) Mandi, Kamand, Mandi 175005, India

Correspondence should be addressed to Vasant A. Matsagar; matsagar@civil.iitd.ac.in

Received 21 June 2020; Revised 7 September 2020; Accepted 4 November 2020; Published 21 December 2020

Academic Editor: Franck Poisson

Copyright © 2020 Daniel H. Zelleke et al. This is an open access article distributed under the Creative Commons Attribution License, which permits unrestricted use, distribution, and reproduction in any medium, provided the original work is properly cited.

The issues of safety and posthazard functionality of structures under multihazard scenarios are some of the significant challenges in the current dynamic and rapidly growing urban environment. In this paper, multistory base-isolated buildings are investigated under the independent multihazard scenario of earthquake and blast-induced ground motion (BIGM). Multistory building models equipped with five different types of isolation systems, namely, the laminated rubber bearing (LRB), lead-rubber bearing (N-Z system), pure friction (PF) system, friction pendulum system (FPS), and resilient-friction base isolator (R-FBI) are assessed under bidirectional multihazard excitations. The suitability of the isolation systems and their key parameters in protecting multistory buildings is evaluated. Furthermore, the influence of the superstructure characteristics, such as the superstructure damping and the number of stories, is also assessed. The effect of bidirectional hazards on fixed-base buildings is also presented for comparison. The key response quantities of base-isolated buildings are presented and compared for different isolation systems. Parametric investigations are also conducted, and the trends of the response quantities are presented to study the influence of important parameters of isolation systems in protecting the buildings under the multihazard scenario of earthquake and BIGM. The results of the investigation show that the behaviors of the buildings equipped with various isolation systems are different for the two hazards. Moreover, the influences of the key parameters of the isolation systems are found to be different for various hazards. Therefore, the selection of design parameters of isolation systems shall be made with due consideration of the influence of multiple hazards. Additionally, the influence of the properties of the superstructure, such as the number of stories and the damping of the superstructure, on the behavior of the base-isolated buildings under the multihazard loading, is presented.

1. Introduction

Earthquakes have been and remain to be one of the prominent threats to the safety and serviceability of civil engineering structures and infrastructure systems. Numerous strategies have been proposed, researched, and implemented for seismic protection of structures [1–4]. The use of structural response control strategies has been proven to be an effective approach. Base isolation is an effective strategy to protect structures, the inhabitants of the structures, and the contents housed within the structures against the undesirable effects of earthquakes. It reduces the earthquake force imparted on the superstructure by increasing the

fundamental time period of the structure and dissipating the earthquake energy [5, 6]. Various types of base isolation strategies, such as the elastomeric type bearings, sliding bearings, and rolling bearings, have been proposed [6]. Also, different active and semiactive seismic isolation strategies have attracted researchers' attention in recent years [7–10].

Structures, including those equipped with base isolation systems, are also likely to be subjected to other hazards in their service life, which necessitates the consideration of various types of loadings in the design of structures. Despite the significant socioeconomic impact caused by various natural and human-made hazards [11, 12], such as blast, impact, earthquake, tsunami, and wind, less attention is

devoted on research and development to understand the behavior of structures under multiple hazards and to devise design strategies thereof. Additionally, the risk associated with the reduced safety and serviceability of key infrastructures, categorized as lifeline structures, such as hospitals, bridges, power plants, data centers, and communication centers, is paramount. Therefore, it is crucial to design structures, especially the critical infrastructures, by considering all the hazards likely to affect safety and serviceability. There is limited research on the use of the multihazard approach in the performance assessment and design of structures. For instance, Messervey et al. [13], Gardoni and LaFave [12], Mahmoud and Chulahwat [14], Venanzi et al. [15], and Roy and Matsagar [16, 17] have conducted studies on the multihazard protection of structures.

Although base isolation is an effective strategy to mitigate the adverse effects of earthquakes, its efficacy in protecting structures under multihazard loading is not explored adequately. Most of the studies on the base-isolated structures also focus on earthquake protection, and therefore, there are limited studies that are conducted on the performance assessment of base-isolated structures under other hazards, such as wind and blast. Some of the attempts to investigate the behavior of base-isolated structures under wind loading include the studies conducted by Henderson and Novak [18, 19]. They have conducted theoretical and experimental studies to assess the response of the base-isolated buildings under wind loading, wherein the theoretical and experimental results are compared. Chen and Ahmadi [20] have evaluated the sensitivity of structures isolated by the laminated rubber bearing (LRB), high damping rubber bearing (HDRB), and resilient-rubber bearing (R-FBI) to wind loading. Furthermore, Kareem [21] has studied the dynamic response of base-isolated buildings with passive dampers under wind loading. Later, Liang et al. [22] have assessed the habitability of base-isolated buildings under fluctuating wind load. Recently, a probabilistic investigation on the response of tall base-isolated buildings under wind loading has been reported by Feng and Chen [23].

The response of base-isolated structures under surface blast has been assessed by some researchers. Zhang and Phillips [24, 25] have studied the performance of a multistory base-isolated building with and without passive supplemental dampers in suppressing the vibration response of the building exposed to blast loading. Also, Kangda and Bakre [26] have assessed the response of base-isolated structures subjected to surface blast and concluded that base isolation could be effective in mitigating the blast response quantities, such as the peak story displacement, story drift, and root mean square (RMS) absolute acceleration. The performance of base-isolated buildings under blast-induced ground motion (BIGM) has also captured attention in the recent times. Mondal et al. [27, 28] have studied the response of buildings isolated by lead-rubber bearing (N-Z system) under BIGM. Further, the performance of a base isolation system equipped with shape-memory alloy in protecting

buildings under BIGM has been studied by Mondal et al. [29]. Furthermore, the use of various base isolation systems in protecting buildings against blast-induced ground motions has been discussed by Mondal et al. [30]. The findings of the investigations reveal that base isolation can be beneficial to control the vibration response of buildings under blast-induced ground motions. The performance of base isolation strategies for the vibration response control of buildings under other nonseismic hazards, such as train-induced vibrations, has also been explored [31–33]. The available limited literature on the implementation of base isolation for the vibration response control of buildings under different types of excitations indicate the potential benefit of the strategy in mitigating the adverse effects of various types of hazards. Notwithstanding the vibration protection potential of base isolation systems, base-isolated buildings could be influenced differently under distinct types of hazards. Therefore, it is necessary to consider the multihazard approach to satisfy safety and serviceability design requirements for base-isolated buildings that are likely to be subjected to different types of loading. However, there are no studies which investigate the behavior of base-isolated buildings subjected to both earthquakes and blast-induced ground motions. In addition, the influence of the key parameters of the base isolation systems on the efficacy of the response mitigation under the multihazard scenario of earthquake and BIGM has not been explored.

Therefore, it would be essential to investigate and unveil the performance of buildings equipped with the laminated rubber bearing (LRB), lead-rubber bearing (N-Z system), pure friction (PF) system, friction pendulum system (FPS), and resilient-friction base isolator (R-FBI) under the multihazard scenario of earthquake and blast-induced ground motion. Consequently, the behavior of buildings equipped with various base isolation systems is assessed under multihazard loading in this paper. The main objectives of this study include the following: (a) to assess the performance of base-isolated buildings under bidirectional near-fault (NF) earthquake ground motions, far-fault (FF) earthquake ground motions, and blast-induced ground motions (BIGMs), (b) to evaluate the effect of the characteristic parameters of the five base isolation systems, considered herein, on the behavior of base-isolated buildings under different hazards, and (c) to study the effect of the properties of the superstructure on the multihazard response of base-isolated buildings.

2. Modeling of a Base-Isolated Building under Bidirectional Excitation

The schematic diagram and idealized model of the base-isolated building considered in this investigation are depicted in Figure 1. The three-dimensional model of the base-isolated building portrayed in the figure shows the orientation of the building, the location of the isolators, the superstructure properties, and the base excitation. The mathematical modeling of the base-isolated building

under bidirectional base excitation is described as follows.

2.1. Governing Equations of Motion. The governing equations of motion of the base-isolated building, subjected to ground acceleration, are derived under the assumption that the superstructure remains in the elastic range. Furthermore, it is considered that the floors are infinitely rigid, the beams and columns are axially inextensible, the building is symmetric in both X and Y directions, and the torsional response of the building is neglected. Accordingly, two degrees of freedom, lateral displacements in X and Y directions, at each floor and base mass levels are considered in the formulation of the equations of motion. The matrix form of the governing equations of motion of the base-isolated building under bidirectional base excitation is given as

$$\overline{\mathbf{M}}\ddot{\mathbf{X}} + \overline{\mathbf{C}}\dot{\mathbf{X}} + \overline{\mathbf{K}}\mathbf{X} + \bar{\mathbf{f}} = -\overline{\mathbf{M}}\bar{\mathbf{r}}\ddot{\mathbf{U}}_g, \quad (1)$$

where $\overline{\mathbf{M}}$, $\overline{\mathbf{C}}$, and $\overline{\mathbf{K}}$, respectively, are the mass, damping, and stiffness matrices of the base-isolated building. These structural property matrices are given as

$$\begin{aligned} \overline{\mathbf{M}} &= \begin{bmatrix} m_b & \mathbf{0} & \mathbf{0} & \mathbf{0} \\ \mathbf{0}^T & \mathbf{M}_s & \mathbf{0}^T & \mathbf{0} \\ 0 & \mathbf{0} & m_b & \mathbf{0} \\ \mathbf{0}^T & \mathbf{0} & \mathbf{0}^T & \mathbf{M}_s \end{bmatrix}, \\ \overline{\mathbf{C}} &= \begin{bmatrix} 0 & c_{1x}\mathbf{r}^b & 0 & \mathbf{0} \\ \mathbf{0}^T & \mathbf{C}_{sx} & \mathbf{0}^T & \mathbf{0} \\ 0 & \mathbf{0} & 0 & c_{1y}\mathbf{r}^b \\ \mathbf{0}^T & \mathbf{0} & \mathbf{0}^T & \mathbf{C}_{sy} \end{bmatrix}, \\ \overline{\mathbf{K}} &= \begin{bmatrix} 0 & k_{1x}\mathbf{r}^b & 0 & \mathbf{0} \\ \mathbf{0}^T & \mathbf{K}_{sx} & \mathbf{0}^T & \mathbf{0} \\ 0 & \mathbf{0} & 0 & k_{1y}\mathbf{r}^b \\ \mathbf{0}^T & \mathbf{0} & \mathbf{0}^T & \mathbf{K}_{sy} \end{bmatrix}, \end{aligned} \quad (2)$$

where $\mathbf{M}_s = \text{diag}[m_1, m_2, \dots, m_j, \dots, m_N]$ is the superstructure mass matrix of size N ; N is the number of stories; m_j is the mass of the j^{th} floor; m_b is the base mass; \mathbf{C}_{sx} and \mathbf{K}_{sx} , respectively, are the damping and the stiffness matrices of the superstructure in the X direction; \mathbf{C}_{sy} and \mathbf{K}_{sy} , respectively, are the damping and the stiffness matrices of the superstructure in the Y direction; c_{1x} and c_{1y} are the damping constants of the first story of the building in X and Y directions, respectively; k_{1x} and k_{1y} are the stiffnesses of the first story of the building in X and Y directions, respectively; $\mathbf{r}^b = \{1, 0, 0, \dots, 0\}$ is a row vector of size N ; $\mathbf{0} = \{0, 0, \dots, 0\}$ is a row vector of size N ; and $\mathbf{0}$ is a null matrix of size $N \times N$.

Furthermore, the vectors of displacements, velocities, and accelerations of the base-isolated building, $\overline{\mathbf{X}}$, $\dot{\overline{\mathbf{X}}}$, and $\ddot{\overline{\mathbf{X}}}$, respectively, the vector of the restoring forces in the isolator,

$\bar{\mathbf{f}}$, the vector of ground accelerations, $\ddot{\mathbf{U}}_g$, and the matrix of influence coefficients, $\bar{\mathbf{r}}$, are given as follows.

$$\begin{aligned} \overline{\mathbf{X}} &= \{x_b, \mathbf{X}_s^T, y_b, \mathbf{Y}_s^T\}^T, \\ \dot{\overline{\mathbf{X}}} &= \{\dot{x}_b, \dot{\mathbf{X}}_s^T, \dot{y}_b, \dot{\mathbf{Y}}_s^T\}^T, \\ \ddot{\overline{\mathbf{X}}} &= \{\ddot{x}_b, \ddot{\mathbf{X}}_s^T, \ddot{y}_b, \ddot{\mathbf{Y}}_s^T\}^T, \\ \bar{\mathbf{f}} &= \{-f_{bx}, \mathbf{0}, -f_{by}, \mathbf{0}\}^T, \\ \ddot{\mathbf{U}}_g &= \{\ddot{x}_g, (\ddot{x}_g + \ddot{x}_b), \ddot{y}_g, (\ddot{y}_g + \ddot{y}_b)\}^T, \\ \bar{\mathbf{r}} &= \begin{bmatrix} 1 & 0 & 0 & 0 \\ \mathbf{0}^T & \mathbf{r} & \mathbf{0}^T & \mathbf{0}^T \\ 0 & 0 & 1 & 0 \\ \mathbf{0}^T & \mathbf{0}^T & \mathbf{0}^T & \mathbf{r} \end{bmatrix}, \end{aligned} \quad (3)$$

where x_b and y_b , respectively, are the displacements of the base mass relative to the ground in X and Y directions; \dot{x}_b and \dot{y}_b , respectively, are the velocities of the base mass relative to the ground in X and Y directions; \ddot{x}_b and \ddot{y}_b , respectively, are the accelerations of the base mass relative to the ground in X and Y directions; $\mathbf{X}_s = \{x_1, x_2, \dots, x_N\}^T$ and $\mathbf{Y}_s = \{y_1, y_2, \dots, y_N\}^T$, respectively, are the vectors of floor displacements in X and Y directions; $\dot{\mathbf{X}}_s$ and $\dot{\mathbf{Y}}_s$, respectively, are the vectors of floor velocities in X and Y directions; $\ddot{\mathbf{X}}_s$ and $\ddot{\mathbf{Y}}_s$, respectively, are the vectors of floor accelerations in X and Y directions; f_{bx} and f_{by} , respectively, are the X and Y components of the force acting on the base isolators; \ddot{x}_g and \ddot{y}_g are the ground accelerations in X and Y directions, respectively; and $\mathbf{r} = \{1, 1, \dots, 1\}^T$ is a column vector of influence coefficients of size N . The solution of the governing equations of motion is obtained numerically using state-space formulation.

2.2. Mathematical Modeling of Base Isolators under Bidirectional Excitation. In this study, the multihazard response of multistory buildings isolated by elastomeric and sliding bearings are studied. Two elastomeric bearings, the laminated rubber bearing (LRB) and lead-rubber bearing (N-Z system), are used; whereas, the three types of sliding bearings investigated are the pure friction (PF) system, friction pendulum system (FPS), and resilient-friction base isolator (R-FBI). The mathematical modeling of the base isolation bearings is realized by considering their characteristic parameters. The LRB is mathematically represented using the isolation time period (T_b) and the isolation damping ratio (ξ_b), whereas the N-Z system is modeled using the isolation time period (T_b), the isolation damping ratio (ξ_b), the yield displacement (q), and normalized yield strength (F_0). The PF system is characterized using the friction coefficient (μ_b), and the isolation time period (T_b) and the friction coefficient (μ_b) are used to model the FPS. Furthermore, the isolation time period (T_b), the friction coefficient (μ_b), and the isolation damping ratio (ξ_b) are used to model the R-FBI. The LRB is a linear isolation system, and the restoring forces of the bearing in X and Y directions can be obtained as

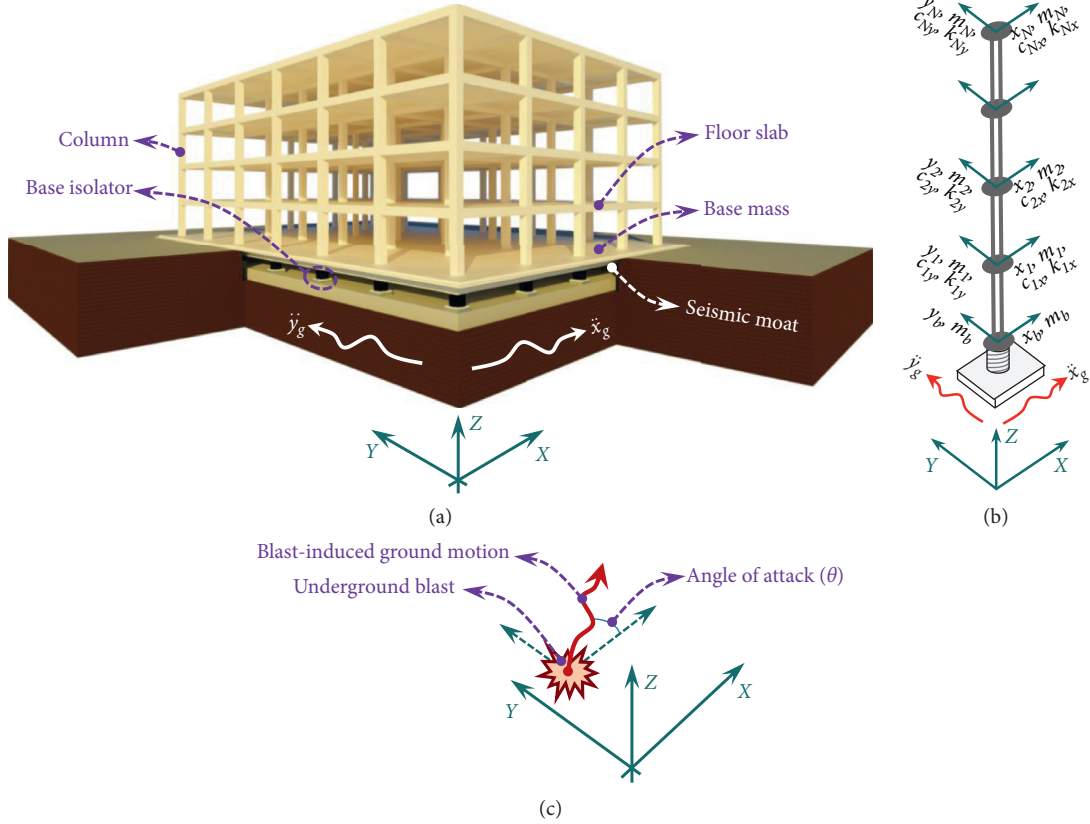


FIGURE 1: Base-isolated building subjected to bidirectional base excitation: (a) schematic diagram, (b) idealized model, and (c) blast-induced ground motion (BIGM).

$$\begin{aligned} f_{bx} &= c_b \dot{x}_b + k_b x_b, \\ f_{by} &= c_b \dot{y}_b + k_b y_b, \end{aligned} \quad (4)$$

where $c_b = 2\xi_b M_t \omega_b$ is the isolation damping coefficient; $k_b = M_t (2\pi/T_b)^2$ is the isolation stiffness; ω_b is the angular frequency of the isolation system; and $M_t = m_b + \sum_{j=1}^N m_j$ is the total mass of the base-isolated building.

The N-Z system, PF system, FPS, and R-FBI are non-linear isolators, and their force-deformation behaviors are mathematically modeled with and without considering the bidirectional interaction. The restoring forces in the isolation system acting in X and Y directions, respectively, can be obtained as

$$f_{bx} = c_b \dot{x}_b + \alpha k_i x_b + (1 - \alpha) F_y h_x, \quad (5a)$$

$$f_{by} = c_b \dot{y}_b + \alpha k_i y_b + (1 - \alpha) F_y h_y, \quad (5b)$$

where $k_i = F_y/q$ is the initial stiffness of the isolator and $\alpha = k_b/k_i$ is the postyield to preyield stiffness ratio of the isolator. Furthermore, the nondimensional hysteretic displacement components, h_x and h_y , are evaluated using a set of nonlinear differential equations proposed by Wen [34, 35] and Park et al. [36], respectively, for hysteretic behavior without and with bidirectional interaction. Without accounting for the bidirectional interaction, the values of h_x and h_y can be obtained using the following equations:

$$q \dot{h}_x = A \dot{x}_b + \beta |\dot{x}_b| h_x |h_x|^{n-1} - \tau \dot{x}_b |h_x|^n, \quad (6a)$$

$$q \dot{h}_y = A \dot{y}_b + \beta |\dot{y}_b| h_y |h_y|^{n-1} - \tau \dot{y}_b |h_y|^n. \quad (6b)$$

On the contrary, considering the bidirectional interaction, h_x and h_y can be evaluated based on the following equation:

$$q \begin{Bmatrix} \dot{h}_x \\ \dot{h}_y \end{Bmatrix} = \begin{bmatrix} A - \beta \text{sgn}(\dot{x}_b) h_x |h_x|^{n-1} - \tau |h_x|^n & -\beta \text{sgn}(\dot{y}_b) h_x |h_y|^{n-1} - \tau h_x h_y \\ -\beta \text{sgn}(\dot{x}_b) h_y |h_x|^{n-1} - \tau h_x h_y & A - \beta \text{sgn}(\dot{y}_b) h_y |h_y|^{n-1} - \tau |h_y|^n \end{bmatrix} \begin{Bmatrix} \dot{x}_b \\ \dot{y}_b \end{Bmatrix}, \quad (7)$$

where $n=2$ is a parameter used to characterize the smoothness of the nonlinear force-deformation curve of the

isolation system, and $\text{sgn}()$ represents the signum function. The values of the dimensionless parameters A , β , and τ ,

TABLE 1: Properties of the superstructure and isolation systems of base-isolated buildings.

Component of base-isolated buildings	Parameter	Unit	Values/range of the parameter used in the study		
Superstructure	Mass of each floor, m_j	kg	1,427,100		
	Base mass, m_b	kg	1,427,100		
	Damping ratio, ξ_s	—	0.02–0.08		
	Fundamental time period, T^*	s	0.1, 0.2, 0.4, 0.6, and 0.8		
	Height of each story, H	m	3.5		
Base isolation system	N-Z system	Isolation time period, T_b	s	2.5	
		Isolation damping ratio, ξ_b	—	0.05–0.15	
		Normalized yield strength, F_0	—	0.025–0.2	
		Yield displacement, q	cm	2.5	
		Isolation time period, T_b	s	2, 2.5, 3, and 3.5	
	LRB	Isolation damping ratio, ξ_b	—	0.025–0.25	
		PF system	Friction coefficient, μ_b	—	0.025–0.2
			Yield displacement, q	cm	0.025
	FPS	Isolation time period, T_b	s	2, 2.5, 3, and 3.5	
		Friction coefficient, μ_b	—	0.025–0.25	
		Yield displacement, q	cm	0.025	
	R-FBI	Isolation time period, T_b	s	2.5	
		Isolation damping ratio, ξ_b	—	0.05–0.15	
		Friction coefficient, μ_b	—	0.025–0.2	
		Yield displacement, q	cm	0.025	

*The values are given for the fixed-base models of 1, 2, 4, 6, and 8 story buildings, respectively.

respectively, are given as 1, 0.5, and 0.5 for the N-Z system [37]; whereas, the values of A , β , and τ , respectively, are given as 1, 0.1, and 0.9 for the PF system, FPS, and R-FBI [38]. Also, the value of the yield displacement, q , is taken as 2.5 cm for the N-Z system [39], whereas $q=0.25$ mm is used for sliding isolation systems. Additionally, the damping ratio of the PF system, the postyield stiffness of the PF system, and the damping ratio of the FPS are taken as 0. The yield strength of the N-Z system is evaluated as $F_y = F_0 W_t$, where F_0 and W_t , respectively, are the normalized yield strength of the isolation bearing and the total weight of the base-isolated building. The yield strength of the PF system, FPS, and R-FBI is evaluated as $F_y = \mu_b W_t$, where μ_b is the friction coefficient of the isolation system.

3. Numerical Study

Base-isolated buildings are studied under bidirectional multihazard excitations. The buildings are isolated using five types of base isolation systems, and the behavior of the isolated buildings is assessed under near-fault (NF) earthquakes, far-fault (FF) earthquakes, and blast-induced ground motion (BIGM). The schematic diagram and the idealized model of the base-isolated building studied in this paper are portrayed in Figures 1(a) and 1(b). The masses of all the floors of the building and the base mass are considered to be equal ($m_j = m_b = m$). Also, the lateral stiffnesses of all stories are equal for both X and Y directions. The Rayleigh method is used to construct the damping matrix of the superstructure where the damping ratio of the superstructure (ξ_s) is considered to be 5%. Five building models having different number of stories are studied. The different values of the number of stories of the five buildings are 1, 2, 4, 6, and 8; whereas the fundamental time period (T) values for fixed-base buildings are 0.1 s, 0.2 s, 0.4 s, 0.6 s, and 0.8 s,

respectively. Furthermore, the story height (H) of 3.5 m is considered for all the buildings. A summary of the properties of the superstructure and five base isolation systems used in this study is presented in Table 1.

In numerical investigations, the performances of the buildings equipped with five base isolation systems are assessed by studying different response quantities under NF earthquakes, FF earthquakes, and BIGMs. The response quantities, in X and Y directions, that are evaluated and studied include the absolute top floor accelerations (\ddot{x}_N and \ddot{y}_N , respectively); top floor displacements (x_N and y_N , respectively), relative to the ground; isolator displacements (x_b and y_b , respectively), relative to the ground; normalized base shears (V_x^n and V_y^n , respectively); total superstructure drift ratio (Δ_{total}^x and Δ_{total}^y , respectively); and maximum interstory drift ratio ($\text{Max}(\Delta_j^x)$ and $\text{Max}(\Delta_j^y)$, respectively). The total superstructure drift ratio is obtained as the ratio of the total drift of the superstructure to the total height of the superstructure. Furthermore, the maximum interstory drift ratio is obtained as the maximum of the peak values of the interstory drift ratios of all the stories of the building. In addition, resultant top floor acceleration ($\ddot{\sigma}_N$), resultant top floor displacement (σ_N), resultant isolator displacement (σ_b), resultant normalized base shear (V_σ^n), resultant total superstructure drift ratio ($\Delta_{\text{total}}^\sigma$), and resultant maximum interstory drift ratio ($\text{Max}(\Delta_j^\sigma)$) are also studied.

3.1. Bidirectional Multihazard Condition Considered in the Study. The current study focuses on the investigation of the multihazard behavior of base-isolated buildings under bidirectional base excitations of different types. The near-fault (NF) earthquake ground motions, far-fault (FF) earthquake ground motions, and blast-induced ground motions (BIGMs) are imparted on buildings isolated using various

TABLE 2: Details of the six bidirectional earthquake ground motions used in the study.

Sl. no.	Earthquake event	Date of event	R_{rup} (km)	Record (NF/FF)	Notation	Component	Direction	PGA (g)
1	Imperial Valley	Oct 15, 1979	3.95	Array #5 (NF)	IV1979	Normal (N)	X	0.37
						Parallel (P)	Y	0.55
2	Loma Prieta	Oct 18, 1989	3.88	LGPC (NF)	LP1989	Normal (N)	X	0.57
						Parallel (P)	Y	0.61
3	Northridge	Jan 17, 1994	5.30	Sylmar (NF)	NR1994	Normal (N)	X	0.73
						Parallel (P)	Y	0.59
4	Imperial Valley	Oct 15, 1979	22.03	Delta (FF)	IV1979F	Normal (N)	X	0.24
						Parallel (P)	Y	0.35
5	Loma Prieta	Oct 18, 1989	24.82	HDA (FF)	LP1989F	Normal (N)	X	0.27
						Parallel (P)	Y	0.28
6	Northridge	Jan 17, 1994	23.41	Century City (FF)	NR1994F	Normal (N)	X	0.26
						Parallel (P)	Y	0.22

base isolation systems. Six recorded bidirectional earthquake ground motion records are used in this investigation. Three of the six earthquake ground motion records (a) the 1979 Imperial Valley with the closest distance to rupture plane, R_{rup} , of 3.95 km (IV1979); (b) the 1989 Loma Prieta, $R_{rup} = 3.88$ km (LP1989); and (c) the 1994 Northridge, $R_{rup} = 5.3$ km (NR1994) are near-fault earthquake ground motions. The remaining three earthquake ground motion records (a) the 1979 Imperial Valley, $R_{rup} = 22.03$ km (IV1979F); (b) the 1989 Loma Prieta, $R_{rup} = 24.82$ km (LP1989F); and (c) the 1994 Northridge, $R_{rup} = 23.41$ km (NR1994F) are far-fault earthquake ground motions. Table 2 provides the date of the event, the recording station, the closest distance to rupture plane, the peak ground acceleration (PGA) in gravitation acceleration (g) unit, and other relevant details of the earthquake ground motion data. In the table, the two components of each of the six earthquake events are presented, which are applied as base excitations in the X direction (\ddot{x}_g) and Y direction (\ddot{y}_g) simultaneously.

The extent of ground vibration due to blast is influenced by various parameters, such as the type of the explosive, the weight of the explosive, the type of the ground medium, and the distance to the charge. In this study, the blast-induced ground motion is represented mathematically using the function proposed by Carvalho and Battista [40]. The exponentially decaying BIGM acceleration, $\ddot{U}_g(t)$, that is imparted on the base-isolated buildings with an angle of attack (θ) measured from the X -axis (Figure 1(c)) can be evaluated as

$$\ddot{U}_g(t) = -\left(\frac{1}{t_d}\right)\ddot{u}_g e^{-(t/t_d)}, \quad (8)$$

where t is the time instant; $t_d = R/C_p$ is the arrival time; R is the distance to the charge; $\ddot{u}_g = 0.3607(Q/V)^{0.2872}(R/Q^{(1/3)})^{-1.3375}$ is the peak particle velocity (PPV) [41]; $C_p = \sqrt{E/\rho}$ is the velocity of wave propagation through the soil medium; E and ρ , respectively, are Young's modulus and the average density of the soil medium; V is the charge chamber volume in m^3 ; and Q is the weight of the equivalent trinitrotoluene (TNT) charge in kg.

The values of C_p , R , and V used in this study are 5280 m/s, 50 m, and 1000 m^3 , respectively, whereas the TNT charge

weight (Q) values of 50 t, 75 t, and 100 t are considered to evaluate BIGM acceleration. Additionally, the obtained BIGM acceleration is applied to the base-isolated buildings with angle of attack (θ) values of 0°, 15°, 30°, and 45°. For BIGM acceleration acting with an angle of attack θ from the X -axis, the X component of BIGM can be obtained as $\ddot{x}_g = \ddot{U}_g \cos(\theta)$, whereas the Y component can be computed as $\ddot{y}_g = \ddot{U}_g \sin(\theta)$. The time histories of the near-fault earthquakes, far-fault earthquakes, and BIGMs used in the study are presented in Figure 2, whereas the Fourier spectra of the three types of excitations are given in Figure 3.

3.2. Effect of Bidirectional Interaction. The two components of the considered earthquake ground motions and BIGMs are applied to the building as base excitations acting in X and Y directions simultaneously. The resultant response quantity can then be evaluated as $\psi_r = \sqrt{\psi_X^2 + \psi_Y^2}$, where ψ_r is the resultant value of any response quantity, ψ_X is the value of the response quantity in the X direction, and ψ_Y is the value of the response quantity in the Y direction.

For the linear base isolation system, laminated rubber bearing (LRB), the response of the building under bidirectional excitations can be obtained by evaluating the response of the building under the two components of the excitations applied in X and Y directions without special consideration of the bidirectional interaction at the isolation level. However, this approach may lead to incorrect results for the buildings isolated by nonlinear base isolation systems. When buildings isolated by nonlinear base isolators are subjected to bidirectional excitations, the force that is acting on the base isolators is derived from the excitations acting in both X and Y directions. Therefore, when the resultant force in the isolator equals the yield force, the postyield behavior of the isolation system is activated.

The X and Y components of the yield strength of the isolator are influenced by relative magnitudes of the isolator forces in X and Y directions. The relationship between the normalized yield strength (F_0), the normalized yield strength in the X direction (F_0^X), and the normalized yield strength in the Y direction (F_0^Y) is given as $(F_0)^2 = (F_0^X)^2 + (F_0^Y)^2$. The graphical representation of relationship between F_0^X , F_0^Y , and F_0 is depicted in Figure 4, as a function of the angle (direction) of the resultant isolator force measured from the X -axis (φ).

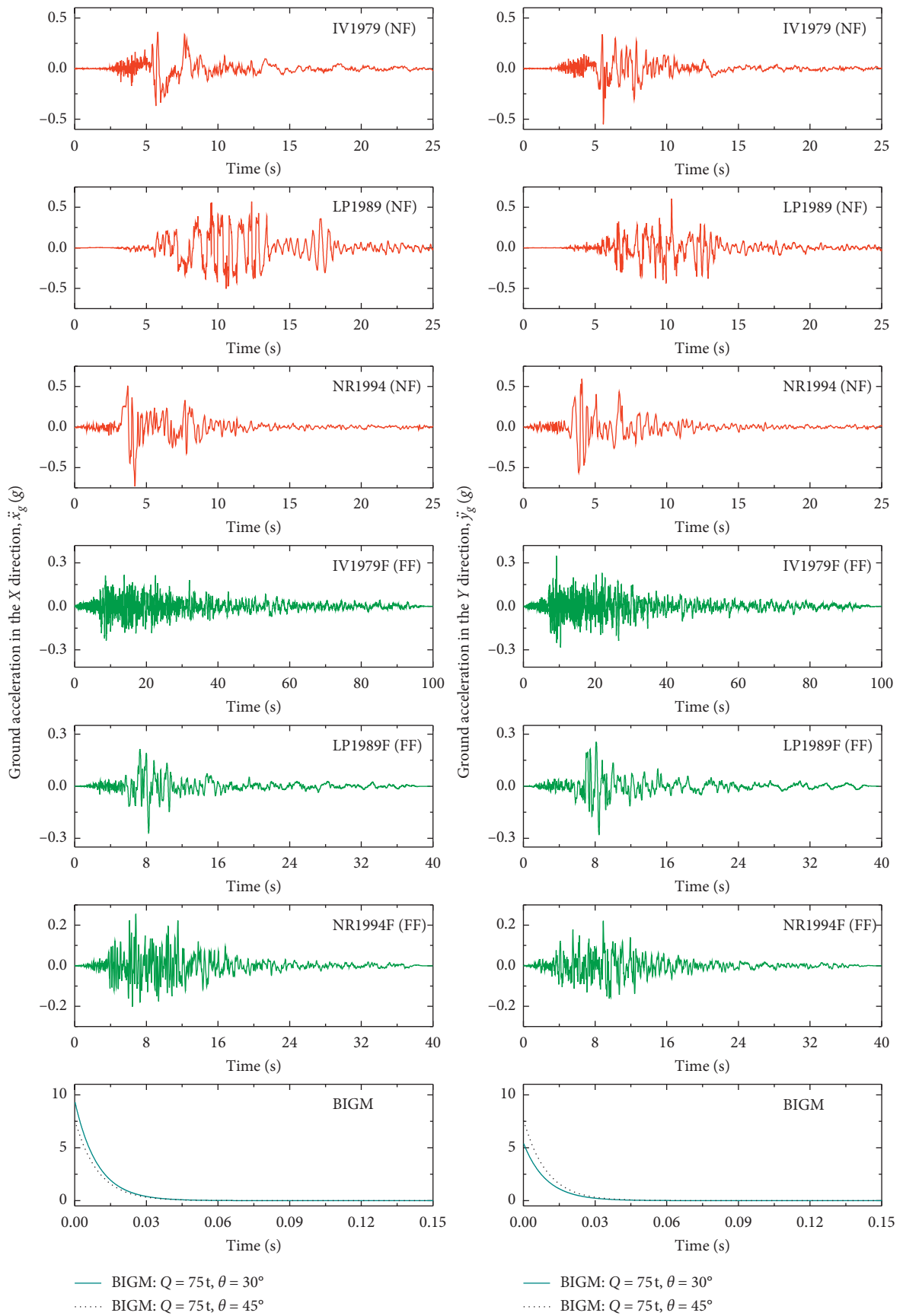


FIGURE 2: Time histories of NF earthquakes, FF earthquakes, and BIGMs used in the study.

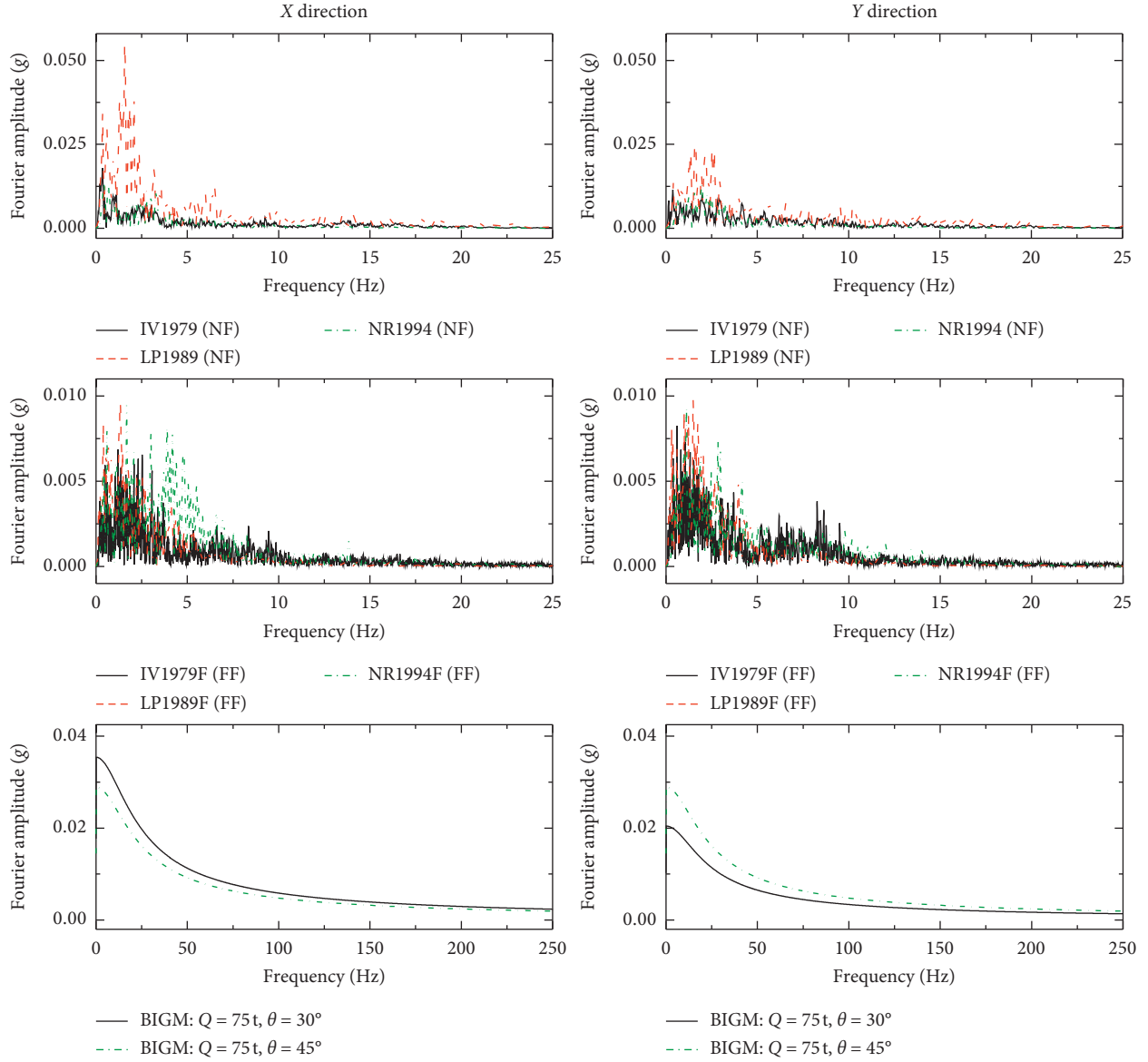


FIGURE 3: Fourier spectra of NF earthquakes, FF earthquakes, and BIGMs used in the study.

If the response of the building is evaluated independently for excitations acting in X and Y directions, it results in neglecting the effect of the bidirectional interaction. For example, the response of a four-story building with a fixed-base fundamental time period (T) of 0.4 s and a superstructure damping ratio (ξ_s) of 0.05 isolated by the FPS is presented in Figures 5 and 6. In Figure 5, the time histories of the top floor acceleration of the four-story building isolated by the FPS ($T_b = 2.5$ s and $\mu_b = 0.1$) with and without the consideration of bidirectional interaction are presented. Furthermore, the force-deformation plots of the FPS, with and without the consideration of bidirectional interaction under (a) LP1989, (b) LP1989F, and (c) BIGM, $Q = 75 t$ and $\theta = 30^\circ$, are shown in Figure 6. The time history plots and the force-deformation behavior depicted in Figures 5 and 6

show that the response obtained with and without the consideration of the bidirectional interaction are significantly different.

Therefore, a detailed comparative study is conducted for determining the degree to which the values of the different response quantities of base-isolated buildings are influenced due to the bidirectional interaction. The response quantities of the buildings isolated by the N-Z system, PF system, FPS, and R-FBI are studied under various bidirectional base excitations with and without the consideration of the bidirectional interaction. The percentage variation between the response quantities of the building with and without the consideration of the bidirectional interaction is evaluated as

$$\Delta\psi = \frac{(\psi_{\text{Int}} - \psi_{\text{NoInt}})}{\psi_{\text{NoInt}}} \times 100, \quad (9)$$

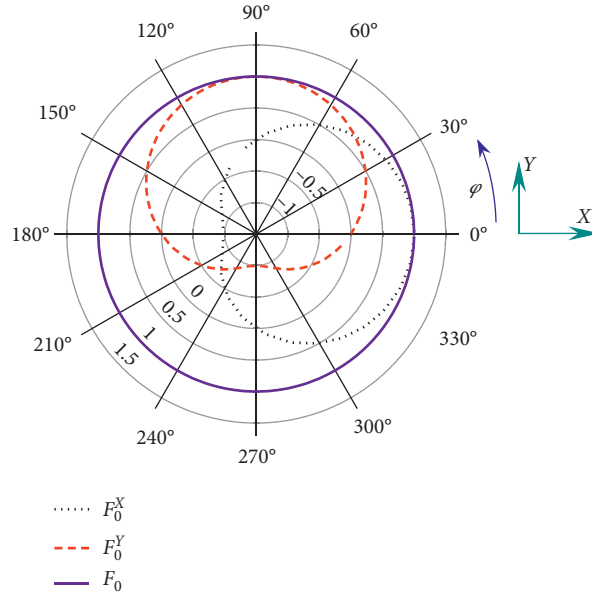


FIGURE 4: The relationship between the normalized yield strength of the isolator (F_0) and its components in X and Y directions (F_0^X and F_0^Y , respectively) for different directions (angle, φ , measured from the X -axis) of the resultant isolator force.

where $\Delta\psi$ is the percentage difference in a response quantity; ψ_{NoInt} is the peak value of the resultant response quantity when the bidirectional interaction is not considered; and ψ_{Int} is the peak value of the resultant response quantity when the bidirectional interaction is considered.

The values of $\Delta\psi$ corresponding to the resultant top floor acceleration, resultant isolator displacement, and resultant base shear of the four-story building equipped with four nonlinear isolators under NF earthquakes, FF earthquakes, and BIGMs are presented in Figure 7. It is shown in the figure that, for all cases, the resultant top floor acceleration and the resultant base shear are overestimated if the bidirectional interaction is neglected. On the contrary, the neglect of the bidirectional interaction is observed to result in the underestimation of the resultant isolator displacement response. The underestimation and overestimation of the response quantities arise because of the modeling approach that neglects the bidirectional interaction. When the bidirectional interaction is neglected, the isolation system is modeled in a way such that the postyield behavior is exhibited at a larger value of the normalized resultant isolator force than that of the case where the bidirectional interaction is considered. This results in the modeling of the isolation system with increased initial stiffness and reduced flexibility under bidirectional excitations. Consequently, a smaller value of resultant isolator displacement and larger values of resultant top floor acceleration and resultant base shear are obtained for the case where the bidirectional interaction is not considered.

The extent of the overestimation and underestimation of the response quantities varies depending on the excitation and the isolation system. For NF earthquake ground motions, the neglect of the bidirectional interaction results in the overestimation of the resultant top floor acceleration

and the resultant base shear by up to 44.5% and 31.9%, respectively. On the contrary, the resultant isolator displacement is underestimated by up to 32%. For FF earthquakes, the neglect of the bidirectional interaction resulted in the overestimation of the resultant top floor acceleration and the resultant base shear by up to 31.6% and 33.5%, respectively. Also, the resultant isolator displacement is underestimated by up to 81.2%. The resultant top floor acceleration and the resultant base shear are overestimated by up to 29.3% due to the neglect of the bidirectional interaction for the base-isolated buildings exposed to BIGMs. Furthermore, the resultant isolator displacement is underestimated by up to 27.6%. Consequently, it can be concluded that, when the bidirectional interaction is neglected, the resultant top floor acceleration and resultant base shear are overestimated, and the resultant isolator displacement is underestimated considerably under all three types of excitations. This influences the multihazard response of the base-isolated buildings significantly. Therefore, the bidirectional interaction should be considered to capture the behavior of base-isolated buildings under bidirectional NF earthquakes, FF earthquakes, and BIGMs with adequate accuracy.

3.3. Multihazard Response of Base-Isolated Buildings under Bidirectional Excitations. Four-story base-isolated buildings are studied under NF earthquakes, FF earthquakes, and BIGMs to understand the effect of the various base isolation systems on the behavior of the buildings under multihazard loading. The base-isolated buildings are subjected to bidirectional excitations, and their response quantities in X and

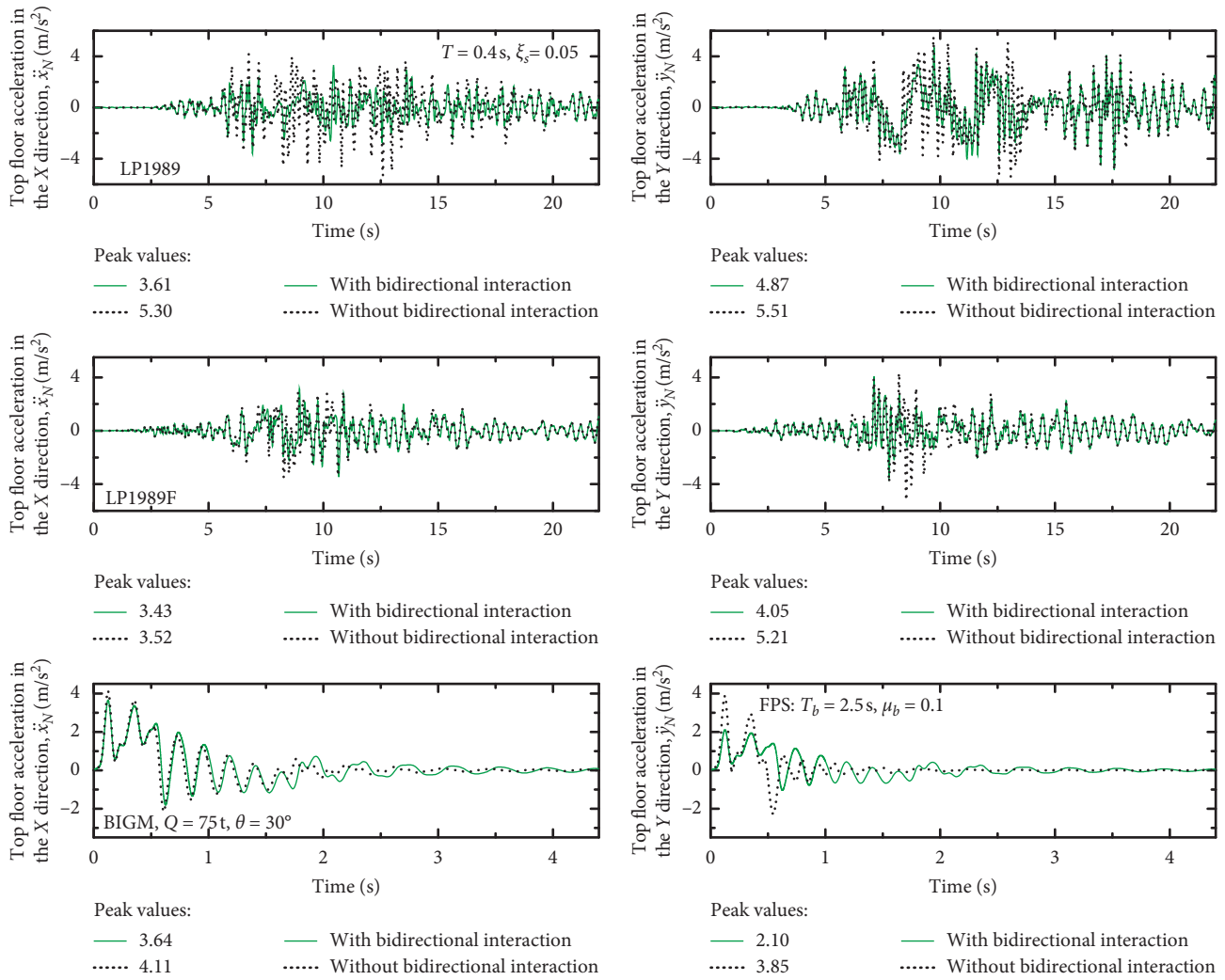


FIGURE 5: Top floor acceleration response history of a four-story base-isolated building with and without the consideration of bidirectional interaction.

Y directions and the resultant response quantities are investigated considering the bidirectional interaction.

3.3.1. Response of the Building Isolated by the N-Z System.

The trends of the peak values of the X component, Y component, and resultant response quantities (top floor acceleration and isolator displacement) of a four-story building equipped with the N-Z system are presented in Figure 8. The fixed-base fundamental time period (T) of the four-story building used in this investigation is 0.4 s, whereas a superstructure damping ratio (ξ_s) of 0.05 is considered. The isolation time period (T_b) of 2.5 s, yield displacement (q) of 2.5 cm, and isolation damping ratio (ξ_b) of 0.075 are used. Moreover, the normalized yield strength (F_0) of the N-Z system varied from 0.025 to 0.2.

The results presented in Figure 8 depict the influence of the normalized yield strength (F_0) of the N-Z system on the response quantities of the base-isolated building under NF earthquakes, FF earthquakes, and BIGMs. For NF earthquakes and FF earthquakes, the average trends of the

absolute top floor acceleration and the isolator displacement are also presented in the figure. The values of the response quantities for the fixed-base building are also presented for comparison. For all three types of excitations, the absolute top floor acceleration response of the building in X, Y, and resultant directions show a considerable reduction as compared to the fixed-base response (FBR). This reduction highlights the benefit of base isolation in suppressing the undesirable effect of NF earthquakes, FF earthquakes, and BIGMs.

The bidirectional response of the base-isolated building under BIGMs with different values of equivalent TNT charge weight (Q) and the angle of attack (θ) is also presented. The influence of Q on the response quantities is observed from the results obtained for BIGMs with a 30° angle of attack and equivalent TNT charge weight (Q) values of 50 t, 75 t, and 100 t. As expected, the response quantities are observed to be more for the higher value of TNT charge weight. In addition, the influence of the angle of attack is studied by taking BIGMs with 75 t equivalent

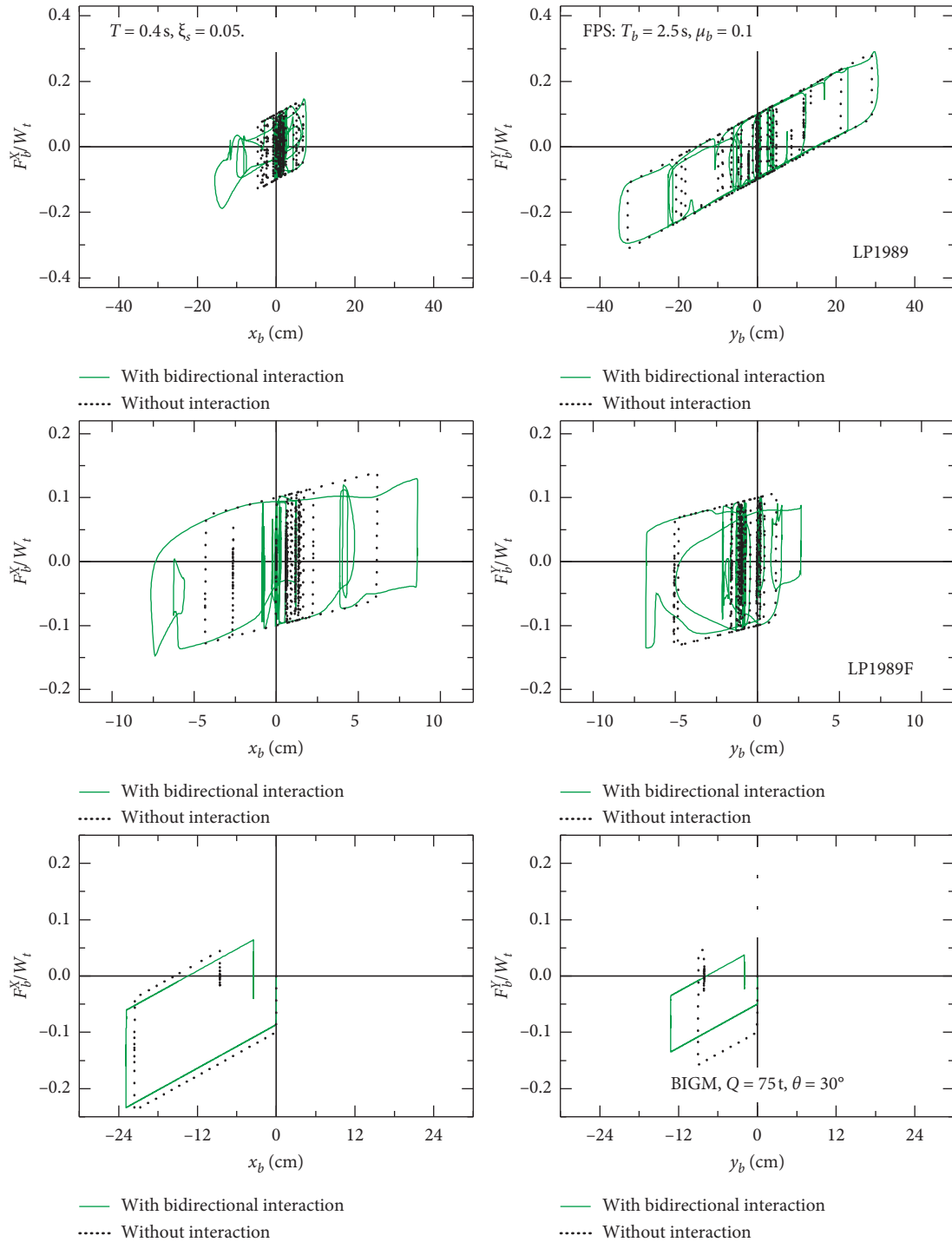


FIGURE 6: Force-deformation curve of the FPS system with and without the consideration of bidirectional interaction.

TNT charge weight and angle of attack (θ) values of 0° , 15° , 30° , and 45° . As the angle of attack increases, the response in the Y direction is observed to be increasing and the same in the X direction is observed to be decreasing. This is primarily because the building is symmetrical about X and Y axes, and the component of BIGM along the Y direction increases with an increasing angle of attack. The results presented in Figure 8 show that the top floor acceleration and isolator displacement response

quantities show a similar trend for different values of equivalent the TNT charge weight and angle of attack. Also, for the four-story building with similar properties in the X and Y directions, the resultant value of the response quantities under BIGMs having different values of the angle of attack are found to be the same. In addition, an increase in the normalized yield strength results in a decreasing trend of the resultant isolator displacement for the base-isolated buildings under all three types of

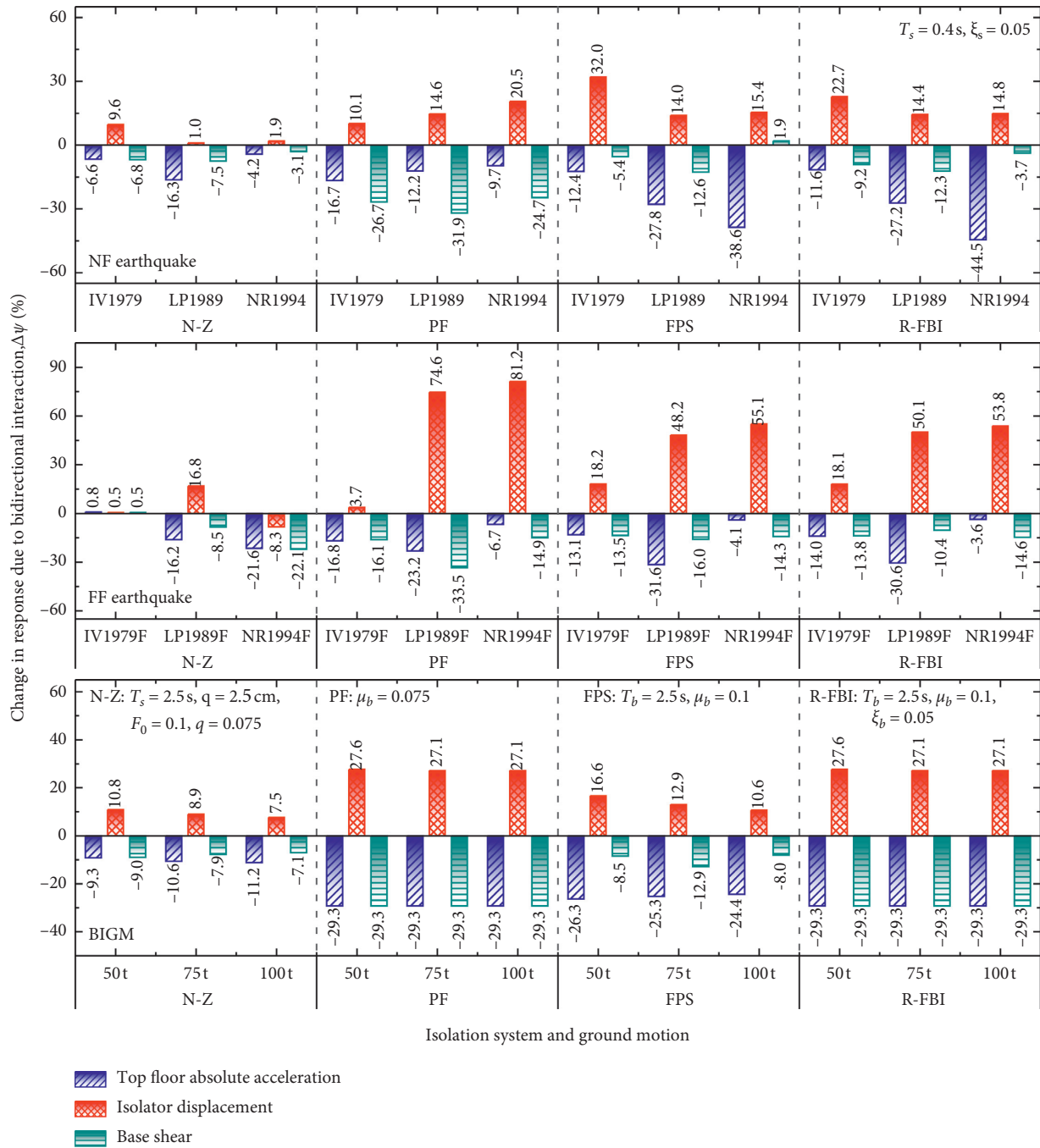


FIGURE 7: The effect of bidirectional interaction on the top floor acceleration, isolator displacement, and base shear response under earthquake and blast-induced ground motions.

excitations. On the contrary, the resultant top floor acceleration increases with the normalized yield strength for the base-isolated buildings under FF earthquake and BIGM. Furthermore, NF earthquakes result in an initial reduction of the resultant top floor acceleration, up to a certain value of the normalized yield strength of the isolator, and further increment of the normalized yield strength results in an increasing trend of the top floor acceleration.

To investigate the behavior of the base-isolated buildings further, under the multihazard scenario of earthquake and BIGM, the top floor acceleration, top floor displacement, isolator displacement, normalized base shear, total superstructure drift ratio, and maximum interstory drift ratio are evaluated under bidirectional NF earthquakes, FF earthquakes, and BIGMs. The X, Y, and resultant components of the response quantities are assessed for the buildings equipped with the N-Z system, LRB, PF system, FPS, and

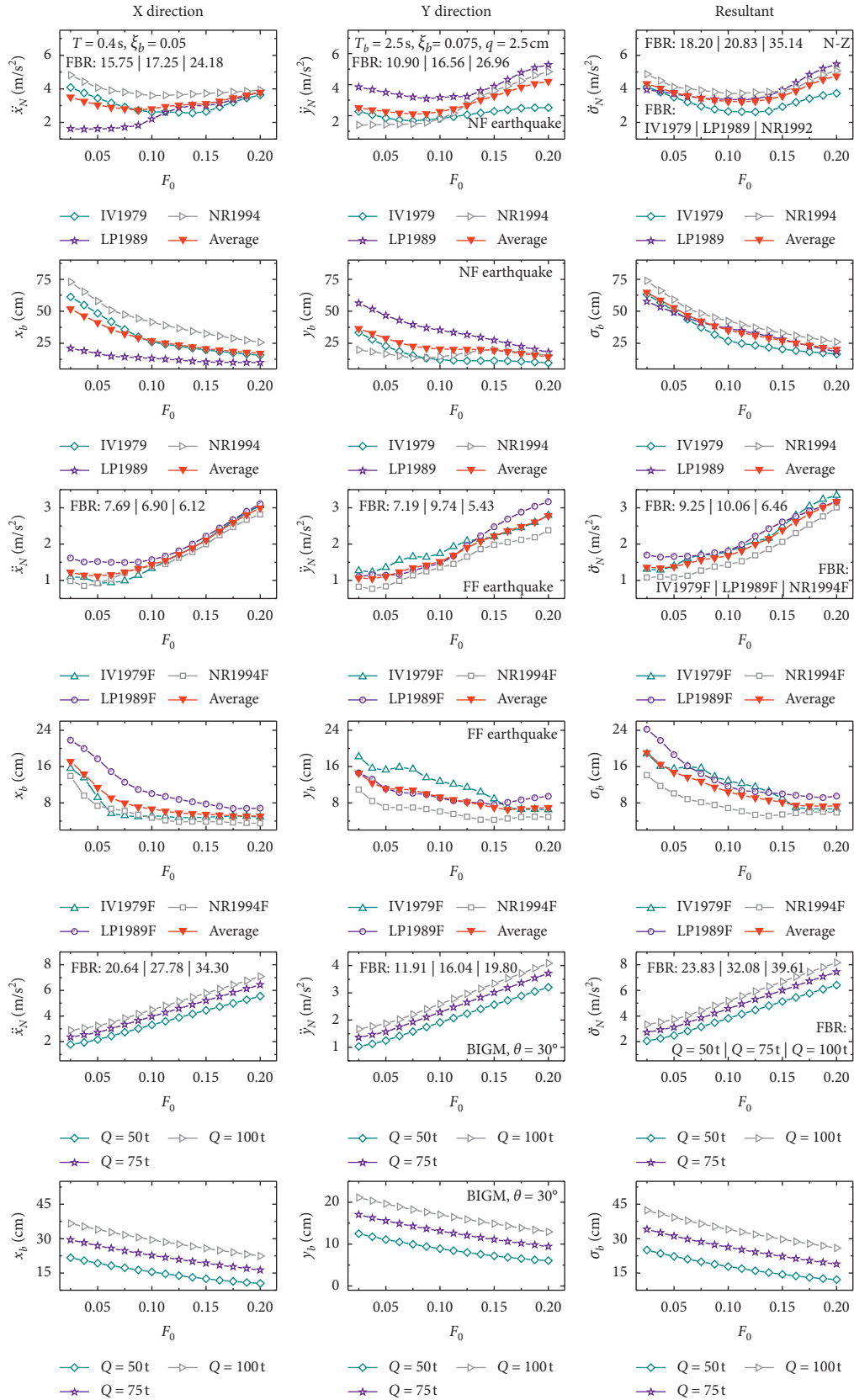


FIGURE 8: Continued.

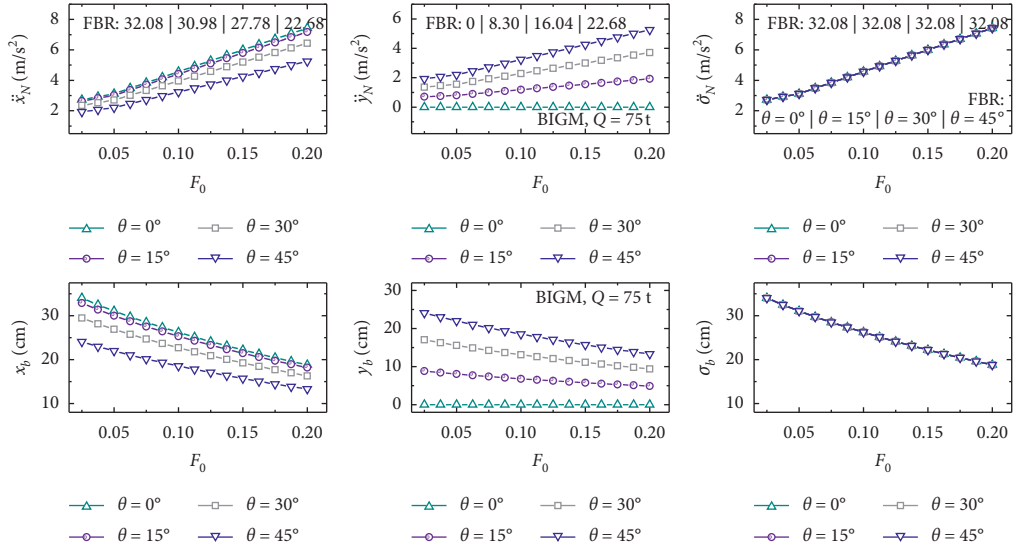


FIGURE 8: The response of a four-story building isolated by the N-Z system under NF earthquakes, FF earthquakes, and BIGMs.

R-FBI under multiple hazards. The average values of the response quantities obtained under IV1979, LP1989, and NR1994 earthquake ground motions are taken to obtain representative trends for the NF earthquake case. Similarly, the average values of the response quantities obtained under IV1979F, LP1989F, and NR1994F earthquake ground motions are taken to obtain representative trends for the FF earthquake case. The average response trends are obtained for the buildings isolated by the five base isolation systems under NF and FF earthquakes, which are then compared with the response trends obtained for the base-isolated buildings subjected to BIGM.

The comparison of the performance of the N-Z system ($T_b = 2.5$ s and $q = 2.5$ cm) under NF earthquake, FF earthquake, and BIGM is depicted in Figure 9 for the four-story building ($T = 0.4$ s and $\xi_s = 0.05$). The effect of the normalized yield strength (F_0) of the N-Z system on the resultant top floor acceleration ($\ddot{\sigma}_N$), resultant top floor displacement (σ_N), resultant isolator displacement (σ_b), resultant normalized base shear (V_σ^n), resultant total superstructure drift ratio (Δ_{total}^σ), and resultant maximum interstory drift ratio ($\text{Max}(\Delta_j^\sigma)$) is presented. The trends of the six response quantities obtained for the N-Z system with different isolation damping ratio (ξ_b) values are similar. For all three types of excitations, the resultant top floor displacement and resultant isolator displacement are observed to show reduction as the value of the normalized yield strength of the N-Z system (F_0) increases. On the contrary, the influence of the normalized yield strength on the resultant top floor acceleration, resultant normalized base shear, resultant total superstructure drift ratio, and resultant maximum interstory drift ratio is found to be different under NF earthquakes, FF earthquakes, and BIGMs. For the base-isolated building under NF earthquakes, an increase in the normalized yield strength of the N-Z system results in an initial reduction of the four response quantities. However, an increase in F_0 beyond the

value of about 0.13 results in an upsurge of the values of the resultant top floor acceleration, resultant normalized base shear, resultant total superstructure drift ratio, and resultant maximum interstory drift ratio. For the base-isolated building subjected to FF earthquake ground motions, an increase in the F_0 typically results in an increment of $\ddot{\sigma}_N$, V_σ^n , Δ_{total}^σ , and $\text{Max}(\Delta_j^\sigma)$, except for a relatively flat trend for small values of F_0 (up to 0.065) with isolation damping ratio, ξ_b , of 0.05 and 0.075. Furthermore, BIGM results in consistent increasing trends of $\ddot{\sigma}_N$, V_σ^n , Δ_{total}^σ , and $\text{Max}(\Delta_j^\sigma)$ for an increase in F_0 .

3.3.2. Response of the Building Isolated by LRB. The behavior of the building isolated by LRB under the three types of excitations is assessed considering different values of the isolation time period (T_b) and isolation damping ratio (ξ_b). The isolation damping ratio varied from 0.025 to 0.25, whereas four different values of the isolation time period (2 s, 2.5 s, 3 s, and 3.5 s) are considered. The influence of the isolation damping ratio on the response quantities of the four-story base-isolated building for the three types of excitations is depicted in Figure 10. The trends of the resultant top floor acceleration, resultant top floor displacement, resultant isolator displacement, resultant normalized base shear, resultant total superstructure drift ratio, and resultant maximum interstory drift ratio observed under earthquake excitation, for an increase in the isolation damping ratio, are similar. The values of the six response quantities reduce with an increase in the isolation damping ratio both under NF and FF earthquakes. For the building subjected to BIGM, the resultant normalized base shear, resultant total superstructure drift ratio, and resultant maximum interstory drift ratio show a relatively flat trend with an increase in the isolation damping ratio. On the contrary, an increase in the isolation damping ratio results in the reduction of the

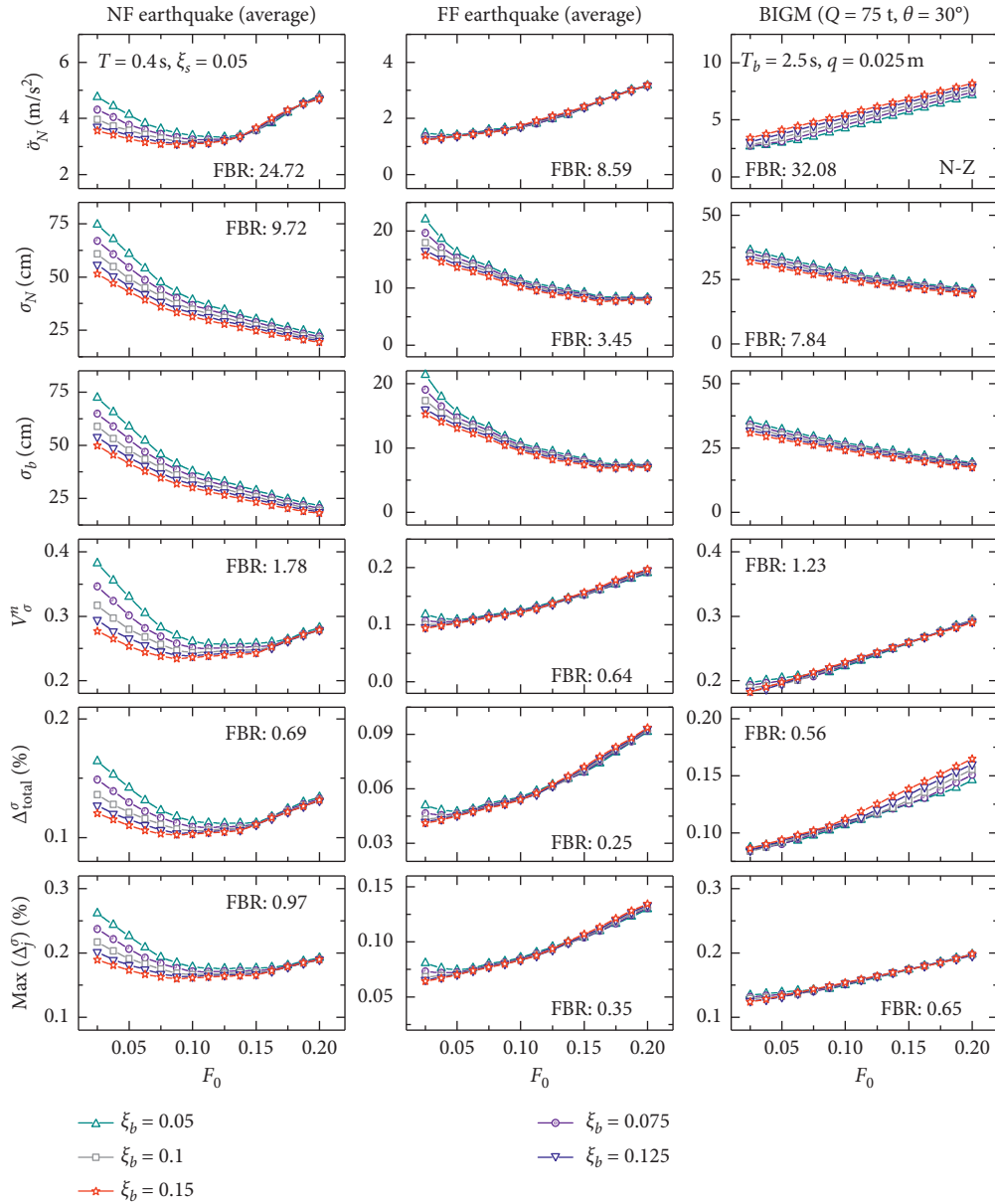


FIGURE 9: The effect of the normalized yield strength (F_0) and the isolation damping ratio (ξ_b) on the response of a four-story building isolated by the N-Z system under earthquake and BIGM.

resultant top floor displacement and resultant isolator displacement, whereas the resultant top floor acceleration increases with an increase in the isolation damping ratio.

3.3.3. Response of the Building Isolated by the PF System.

The performance of the PF system under NF earthquake, FF earthquake, and BIGM is evaluated by varying the friction coefficient of the isolation system (μ_b) from 0.025 to 0.25. The influence of the friction coefficient of the isolation system on the response quantities of the four-story base-isolated building under the three types of excitations is presented in Figure 11. The results plotted

in the figure show that the trends of the six response quantities are similar for NF earthquakes, FF earthquakes, and BIGMs. For all the three types of excitations, the top floor displacement and isolator displacement show a decreasing trend for an increase in the friction coefficient. Moreover, as the friction coefficient of the PF system increases, the top floor acceleration, base shear, total superstructure drift ratio, and maximum interstory drift ratio increase. Also, the comparison of the residual resultant isolator displacements of the building equipped with the PF system to that of the other isolation systems is presented in Table 3. Because the pure friction system lacks restoring capacity, the building isolated by the PF

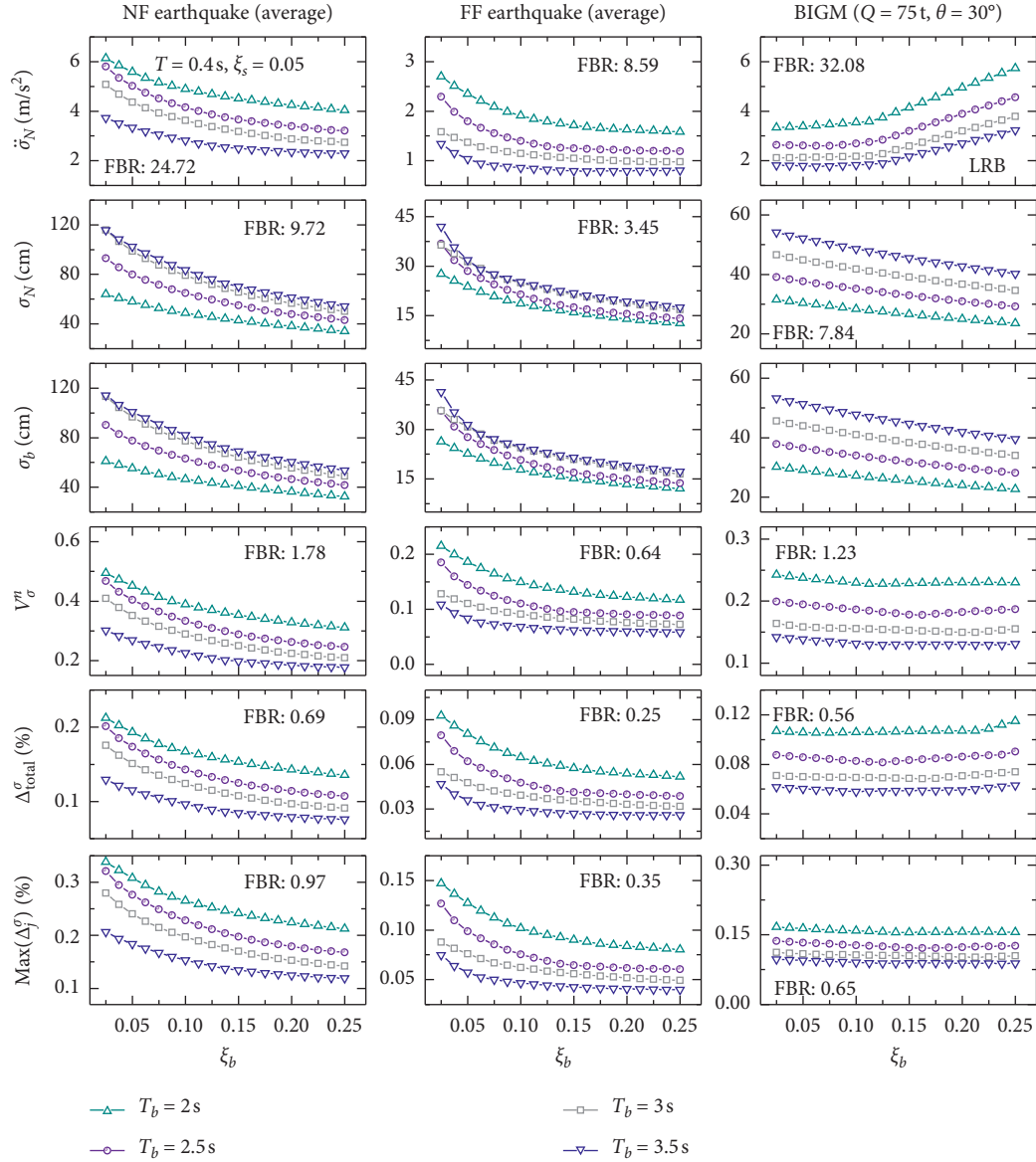


FIGURE 10: The effect of the isolation damping ratio (ξ_b) and the isolation time period (T_b) on the response of a four-story building isolated by LRB under earthquake and BIGM.

system is observed to be prone to large residual displacements under the three types of excitations.

3.3.4. Response of the Building Isolated by the FPS. The behavior of the four-story building isolated by the FPS under the independent multihazard scenario of earthquake and BIGM is presented in Figure 12. The isolation time period (T_b) values of 2 s, 2.5 s, 3 s, and 3.5 s are considered for the FPS, whereas the coefficient of friction of the isolation system (μ_b) is varied from 0.025 to 0.25. For small values of the friction coefficient of the FPS (i.e., approximately up to $\mu_b = 0.075$), the resultant top floor acceleration shows small reduction for an increase in μ_b under NF earthquakes, whereas the resultant top floor acceleration exhibits an increasing trend for an increase

in the friction coefficient of the FPS beyond 0.075. Under FF earthquake and BIGM, the resultant top floor acceleration shows a steady increase with an increase in μ_b . An increase in the friction coefficient of the FPS affects the resultant top floor displacement and resultant isolator displacement similarly. Both the response quantities reduce with an increase in the friction coefficient under NF earthquake, FF earthquake, and BIGM. Under NF earthquake, the resultant normalized base shear, resultant total superstructure drift ratio, and resultant maximum interstory drift ratio initially reduce with an increase in the friction coefficient of the isolator, and after a certain value of μ_b , the three response quantities start to show an increasing trend. For FF earthquake, the three response quantities show a small reduction for small values of the friction coefficient of the FPS ($\mu_b \leq 0.05$). For

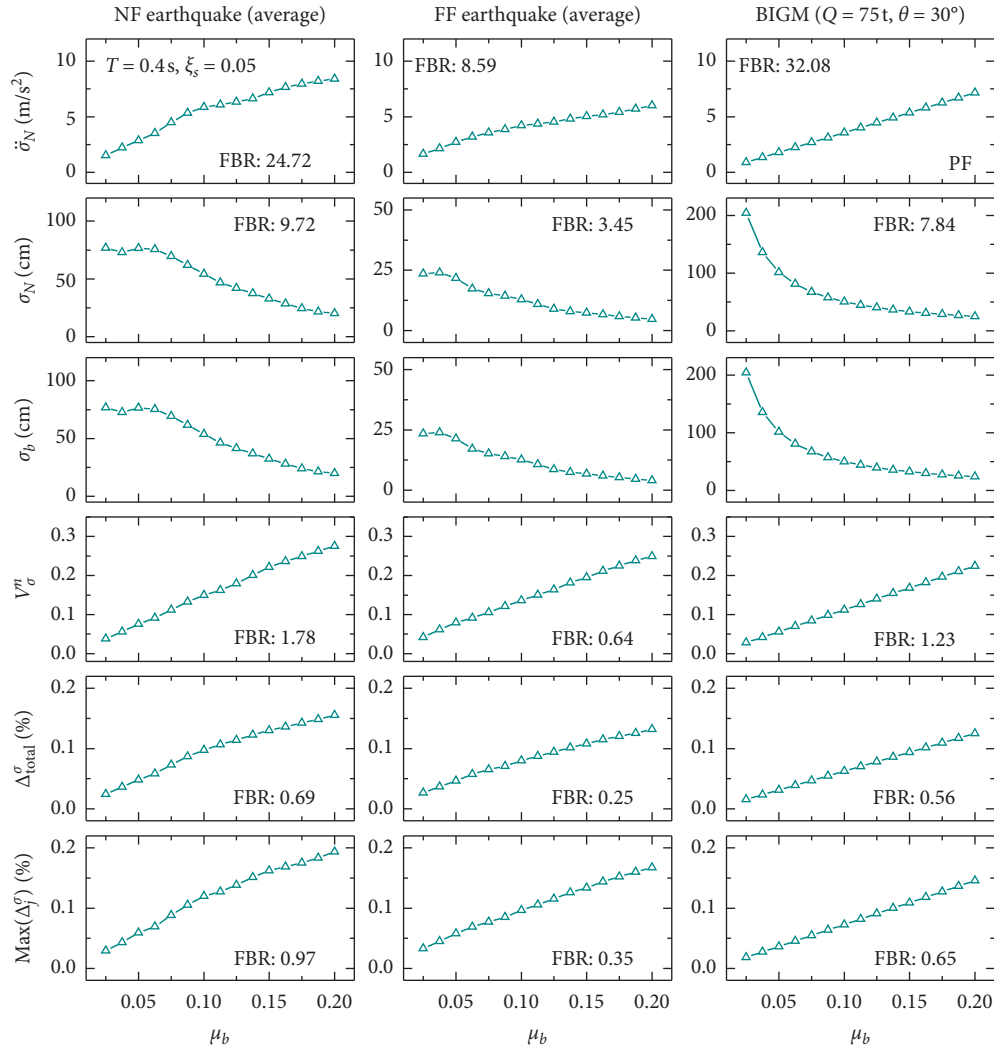


FIGURE 11: The response of a four-story building $T = 0.4$ s; $\xi_s = 0.05$ isolated by the PF system under NF earthquake, FF earthquake, and BIGM.

friction coefficient values beyond 0.05, the trends are reversed, and the three response quantities increase with an increase in μ_b . Moreover, an increase in μ_b results in a consistent increment of the resultant normalized base shear, resultant total superstructure drift ratio, and resultant maximum interstory drift ratio of the base-isolated building under BIGM.

3.3.5. Response of the Building Isolated by the R-FBI. The performance of the four-story building equipped with the R-FBI under NF earthquake, FF earthquake, and BIGM is portrayed in Figure 13. The isolation time period (T_b) of the R-FBI is taken as 2.5 s; the isolation damping ratio (ξ_b) values of 0.05, 0.075, 0.1, 0.125, and 0.15 are considered; and the coefficient of friction of the isolation system (μ_b) is varied from 0.025 to 0.2. The overall behavior of the building isolated by the R-FBI is similar to that of the building equipped with the FPS, except for a small difference in the trends of the resultant normalized base shear, resultant total superstructure drift ratio, and resultant

maximum interstory drift ratio under FF earthquakes. For the building equipped with the R-FBI subjected to FF earthquakes, an increase in the friction coefficient of the isolation system results in a consistent increment of the resultant normalized base shear, resultant total superstructure drift ratio, and resultant maximum interstory drift ratio.

For the building subjected to NF earthquakes, the top floor displacement, isolator displacement, normalized base shear, total superstructure drift ratio, and maximum interstory drift ratio are influenced significantly by the damping ratio of the R-FBI. For small values of the friction coefficient of the isolator, a larger isolation damping ratio results in smaller values of the five response quantities. However, as the friction coefficient of the R-FBI increases, the influence of the damping ratio of the isolation system diminishes. Moreover, the effect of the damping ratio of the R-FBI on the top floor acceleration is less under NF earthquakes, irrespective of the value of the friction coefficient. Under FF earthquakes, the top floor acceleration, normalized base shear, total

TABLE 3: Residual resultant isolator displacements of four-story base-isolated buildings under NF earthquakes, FF earthquakes, and BIGMs.

		Residual resultant isolator displacement for buildings ($T_s=0.4$ s, $\xi_s=0.05$) equipped with different isolation systems (cm)				
Excitation		LRB ($T_b=2$ s and $\xi_b=0.1$)	N-Z ($T_b=2$ s, $F_0=0.05$, and $\xi_b=0.1$)	PF ($\mu_b=0.05$)	FPS ($T_b=2$ s and $\mu_b=0.05$)	R-FBI ($T_b=2$ s, $\mu_b=0.05$, and $\xi_b=0.1$)
NF earthquake	IV1979	1.24	0.61	102.50	0.41	0.56
	LP1989	1.21	0.91	41.74	0.24	0.23
	NR1994	0.48	0.19	16.98	0.38	0.13
FF earthquake	IV1979F	0.62	0.12	11.63	0.62	0.60
	LP1989F	2.82	0.59	33.89	0.07	0.10
	NR1994F	0.66	0.51	5.19	0.55	0.53
BIGM	Q = 75 t; $\theta = 30^\circ$	0.06	0.02	101.32	2.26	1.88
	Q = 75 t; $\theta = 45^\circ$	0.06	0.02	101.32	2.26	1.88

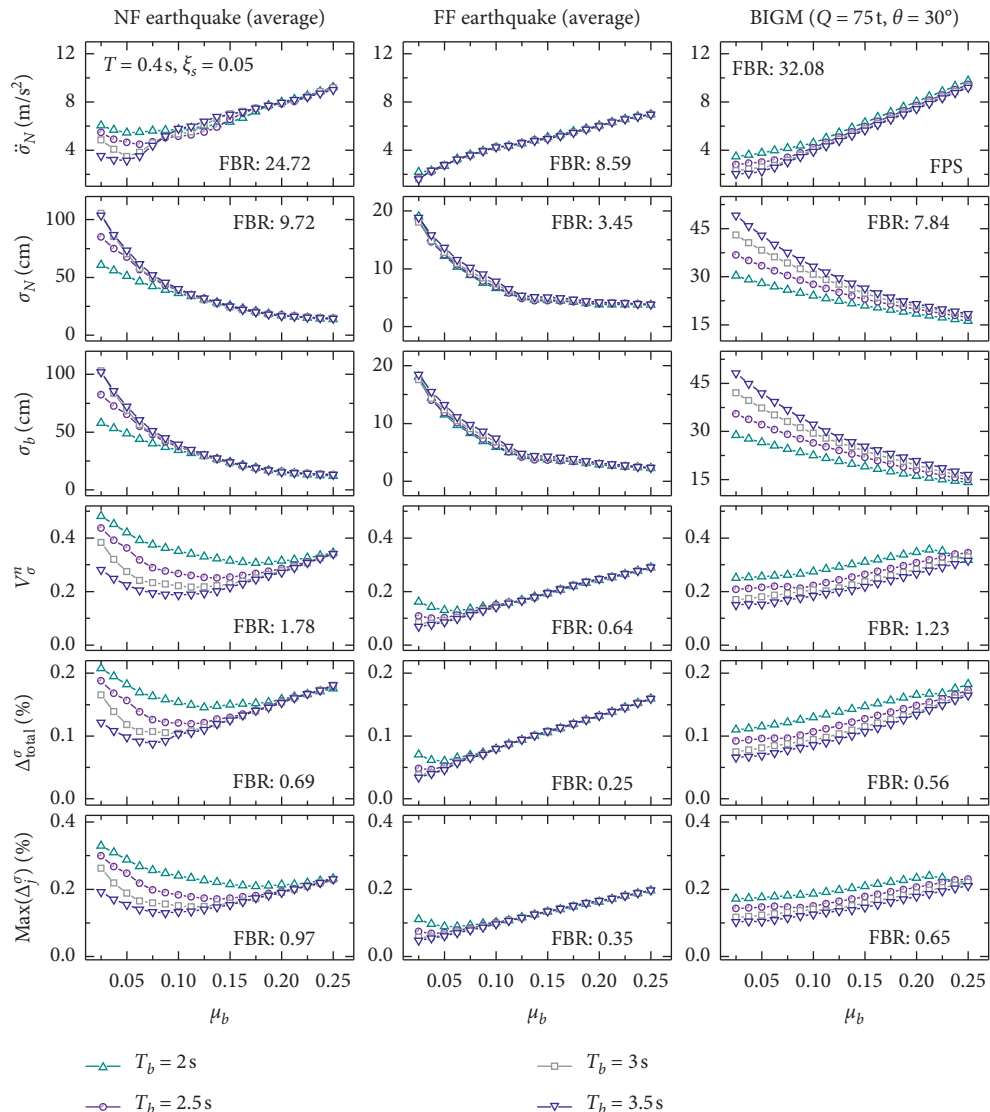


FIGURE 12: The effect of the friction coefficient of the isolator (μ_b) and the isolation time period (T_b) on the response of a four-story building isolated by the FPS under earthquake and BIGM.

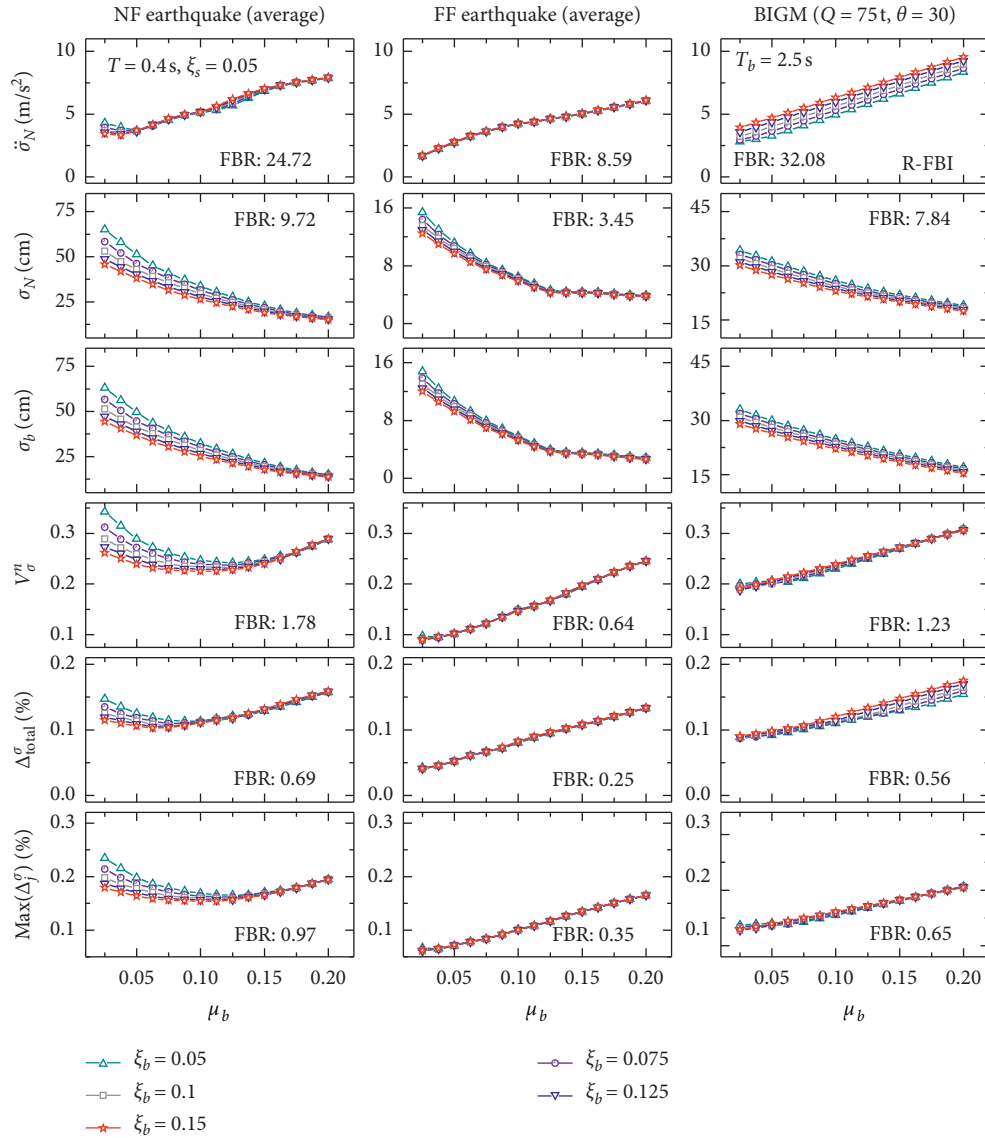


FIGURE 13: The effect of the friction coefficient of the isolator (μ_b) and the isolation damping ratio (ξ_b) on the response of a four-story building isolated by the R-FBI system under earthquake and BIGM.

superstructure drift ratio, and maximum interstory drift ratio are not influenced significantly by the damping ratio of the R-FBI. Similarly, the influence of the isolation damping on the normalized base shear and the maximum interstory drift ratio is small for the base-isolated building under BIGM. For the base-isolated building with small values of the friction coefficient of the R-FBI that is subjected to FF earthquakes and BIGMs, the top floor displacement and isolator displacement reduce as the damping ratio of the isolation system increase. On the contrary, the top floor acceleration and total superstructure drift ratio increase as the damping ratio increases for the base-isolated building under BIGM.

3.4. Influence of Superstructure Characteristics on Performance under Multihazard Scenario. The behavior of base-isolated buildings can be influenced by the characteristics of

the superstructure, such as the flexibility and damping of the superstructure. Therefore, the effect of the characteristics of the superstructure on the response of base-isolated buildings is assessed under NF earthquake, FF earthquake, and BIGM considering the bidirectional interaction. The influence of the flexibility of the superstructure is studied by quantifying the different response quantities of base-isolated buildings with different number of stories (N), i.e., 1, 2, 4, 6, and 8 stories. The values of the fundamental time period (T) for the fixed-base models of the buildings with 1, 2, 4, 6, and 8 stories, respectively, are considered as 0.1 s, 0.2 s, 0.4 s, 0.6 s, and 0.8 s, whereas the superstructure damping ratio for all the building models is considered to be 0.05. Five types of base isolation systems, the LRB ($T_b = 2.5$ s), N-Z system ($T_b = 2.5$ s, $\xi_b = 0.05$, and $q = 2.5$ cm), PF, FPS ($T_b = 2.5$ s), and R-FBI ($T_b = 2.5$ s and $\xi_b = 0.05$), are used to isolate the buildings having different number of stories. The effect of the number of stories on the trends of the resultant top floor

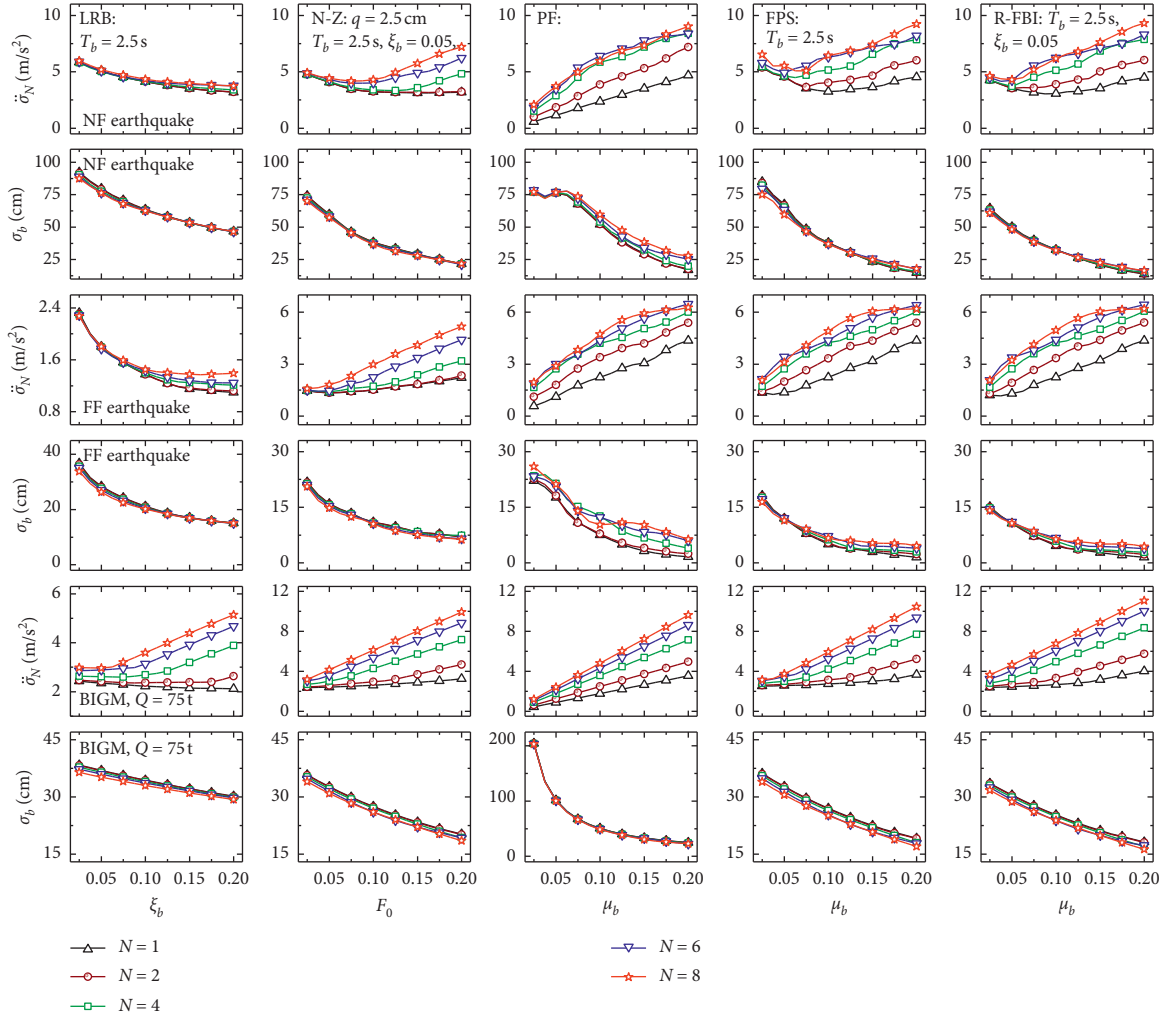


FIGURE 14: The effect of the number of stories on the top floor acceleration and isolator displacement of base-isolated buildings under NF earthquake, FF earthquake, and BIGM.

acceleration and resultant isolator displacement of the base-isolated buildings under NF earthquake, FF earthquake, and BIGM is presented in Figure 14. Under the three types of excitations, the trends of the resultant isolator displacements of the buildings equipped with five base isolators are observed to be identical for buildings having different number of stories. Additionally, similar trends of the resultant top floor acceleration are exhibited by base-isolated buildings having different number of stories. Though, the number of stories of the base-isolated buildings significantly influences the value of the top floor acceleration of the building under NF earthquake, FF earthquake, and BIGM. For all base-isolated buildings under all three types of excitations, the top floor acceleration increases with an increase in the number of stories. Moreover, the influence of the number of stories on the top floor acceleration is found to be prominent for larger values of the damping ratio of LRB, larger values of the normalized yield strength of the N-Z system, and larger values of the friction coefficients of the PF system, FPS, and R-FBI. On the contrary, it is observed that the number of stories of the building typically has less

influence on the values of the isolator displacements of the buildings isolated by the LRB, N-Z system, PF system, FPS, and R-FBI under three types of excitations.

The influence of the relative flexibility of the superstructure in X and Y directions is also studied. The ratio of the lateral stiffness of the columns of each story of the building in the Y direction to that of the X direction ($k_{j,Y}/k_{j,X}$) values of 1, 1.2, 1.4, 1.6, and 1.8 is considered. A four-story base-isolated building with a fixed-base fundamental time period of 0.4 s, in the X direction, is studied by using the different values of $k_{j,Y}/k_{j,X}$, under the multihazard scenario of earthquakes (NF earthquake and FF earthquake) and BIGMs. The trends of the resultant top floor acceleration and resultant isolator displacement of four-story base-isolated buildings with different values of $k_{j,Y}/k_{j,X}$ are depicted in Figure 15. The figure shows that the values of the resultant isolator displacements are not influenced significantly by $k_{j,Y}/k_{j,X}$ for the buildings isolated by the LRB, N-Z system, PF system, FPS, and R-FBI under three types of excitations. Also, a larger value of $k_{j,Y}/k_{j,X}$ is observed to result in a reduced value of resultant top floor acceleration, especially

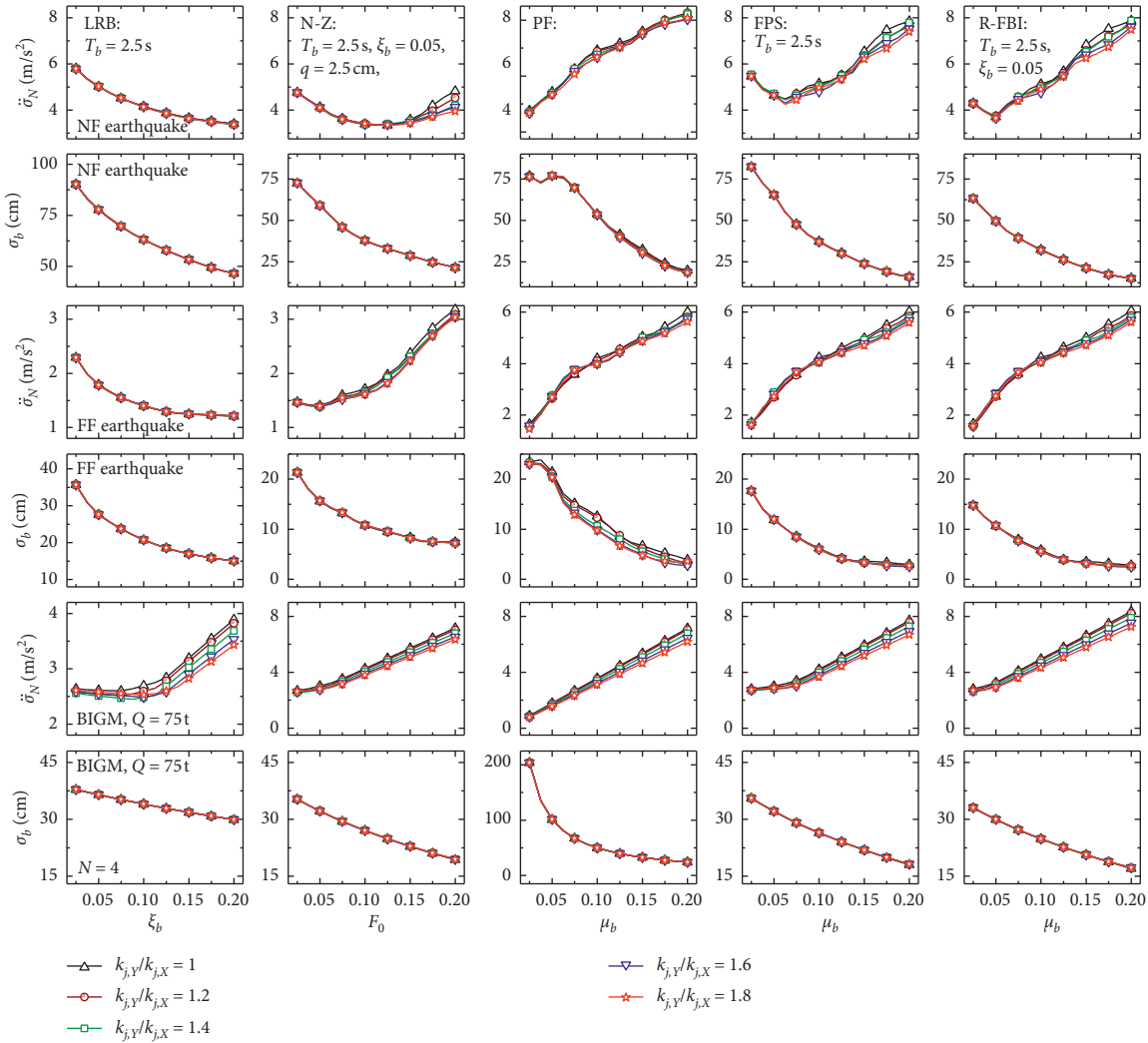


FIGURE 15: The effect of $k_{j,y}/k_{j,x}$ on the response of four-story base-isolated buildings under NF earthquake, FF earthquake, and BIGM.

for the buildings subjected to BIGM. However, the trends of the resultant top floor acceleration and the resultant isolator displacement obtained for different values of $k_{j,y}/k_{j,x}$ are the same. Therefore, it can be concluded that the relative flexibility of the superstructure in X and Y directions does not influence the behavior of the symmetrical building under NF earthquakes, FF earthquakes, and BIGMs.

The effect of the damping of the superstructure is evaluated by investigating the response of the four-story base-isolated building considering ξ_s values of 2%, 3.5%, 5%, 6.5%, and 8%. It may be worth mentioning that small structural damping ratio (i.e., 2% or 3.5%) may not be feasible for fixed-base multistory buildings when nonlinear deformation is considered. However, for base-isolated buildings, small values of superstructure damping can reasonably be considered because the superstructure is

prominently expected to behave elastically. The resultant top floor acceleration and resultant isolator displacement of the building isolated by the LRB, N-Z system, PF system, FPS, and R-FBI, under NF earthquake, FF earthquake, and BIGM, are obtained, and the trends are plotted in Figure 16. It is observed that superstructure damping does not affect the trends of the resultant top floor acceleration and resultant isolator displacement of the buildings isolated by four base isolation systems. Additionally, it is observed that the superstructure damping ratio does not influence the value of the isolator displacement for the buildings isolated by five base isolation systems under all three types of dynamic base excitations. However, although the trends of the top floor acceleration are the same, the results presented in Figure 16 show that a larger superstructure damping ratio typically results in a smaller value of top floor

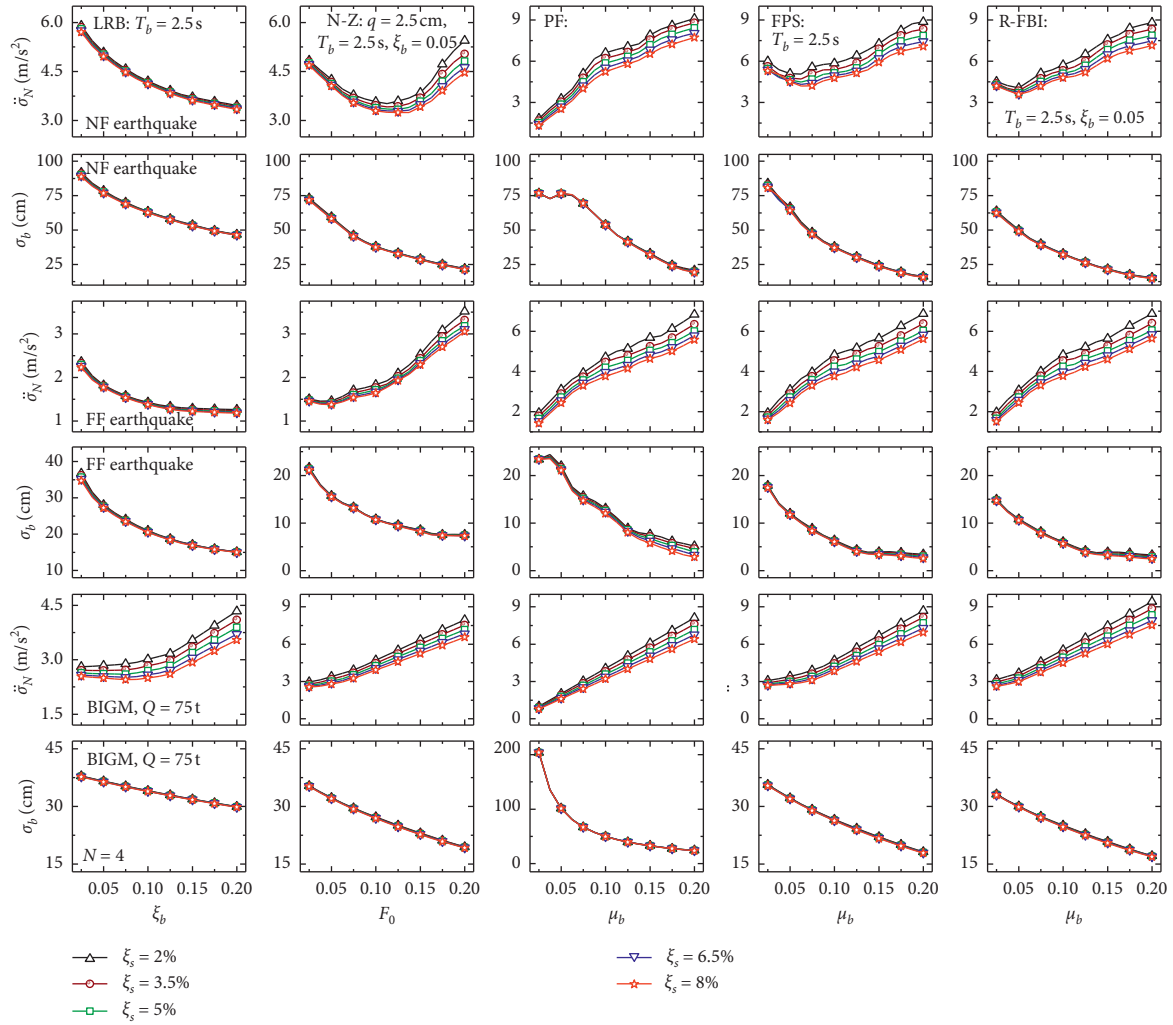


FIGURE 16: The effect of the superstructure damping on the response of the four-story base-isolated buildings under NF earthquake, FF earthquake, and BIGM.

acceleration. Therefore, based on the observations, it can be concluded that the superstructure characteristics have less influence on the behavior of the base-isolated buildings under the multihazard loading scenario of earthquakes (NF earthquakes and FF earthquakes) and BIGMs, as compared to the properties of the base isolators.

4. Conclusions

This study presents an investigation of the behavior of multi-story buildings isolated by various types of elastomeric and sliding base isolation systems under multihazard loading. The multihazard scenario of earthquakes (near-fault and far-fault earthquake) and blast-induced ground motion (BIGM) is considered, wherein the bidirectional effects of the hazards are taken into account. The influence of the selection of different values of the parameters of isolators on the key response quantities of the buildings, such as the top floor acceleration, top floor displacement, isolator displacement, base shear, interstory drift ratio, and total superstructure drift ratio, are assessed under the multihazard scenario. Furthermore, the influence of the

properties of the superstructure (superstructure flexibility and superstructure damping ratio) on the behavior of the base-isolated buildings under multihazard loading is assessed. Based on the findings of the extensive numerical studies, it is concluded that base-isolated buildings behave differently under the near-fault earthquake, far-fault earthquake, and blast-induced ground motion. Consequently, the design of the isolation systems and the selection of suitable parameters thereof shall be done cautiously, accounting for the effects of both types of hazards considered on the buildings. The specific conclusions of the study are listed as follows:

- (1) Although the base isolation technology can help in protecting buildings from three types of dynamic base excitations (NF earthquakes, FF earthquakes, and BIGMs), the base-isolated buildings behave differently under different multiple hazards.
- (2) The response quantities of the base-isolated buildings obtained with and without the consideration of bidirectional interaction are significantly different. The resultant isolator displacement is

underestimated, and the resultant top floor acceleration and resultant base shear are overestimated when the bidirectional interaction is neglected.

- (3) For the building isolated by LRB, an increase in ξ_b results in the reduction of all the six response quantities of the building under NF and FF earthquakes. However, the acceleration response increases with ξ_b for the building subjected to BIGM.
- (4) For the N-Z system, an increase in F_0 results in an initial reduction followed by an increase in the top floor acceleration, base shear, interstory drift, and total superstructure drift of the base-isolated building under NF earthquakes. On the contrary, all the four response quantities consistently increase with F_0 for BIGM.
- (5) The trends of the response quantities of the building isolated by the PF system observed under NF earthquakes, FF earthquakes, and BIGMs are similar.
- (6) For the buildings isolated by the FPS and R-FBI, the trends of the top floor displacement and the isolator displacement show a reducing trend for an increase in the value of μ_b under NF earthquakes, FF earthquakes, and BIGMs. However, the influence of the friction coefficient of the FPS on the trends of the top floor acceleration, base shear, interstory drift, and total superstructure drift is different for the three types of excitations.
- (7) Under NF earthquakes, FF earthquakes, and BIGMs, the trends of the top floor acceleration and the isolator displacement are similar for the base-isolated buildings with different number of stories (i.e., $N = 1, 2, 4, 6, 8$). Furthermore, the relative flexibility of the superstructure in X and Y directions does not influence the behavior of the building for all three types of dynamic base excitations, NF earthquakes, FF earthquakes, and BIGMs.
- (8) Superstructure damping does not influence the trends of the top floor acceleration and the isolator displacement under NF earthquakes, FF earthquakes, and BIGMs, for the considered range of isolator parameters.
- (9) The behavior of base-isolated buildings, under multihazard loading scenario of earthquakes and BIGMs, is influenced more by the properties of base isolators as compared to that of the superstructure.

Data Availability

The data used to support the findings of this study are available from the corresponding author upon request.

Conflicts of Interest

The authors declare that they have no conflicts of interest.

References

- [1] V. A. Zayas, S. S. Low, and S. A. Mahin, "A simple pendulum technique for achieving seismic isolation," *Earthquake Spectra*, vol. 6, no. 2, pp. 317–333, 1990.
- [2] T. T. Soong and B. F. Spencer Jr., "Active, semi-active and hybrid control of structures," in *Proceedings of the Twelfth World Conference on Earthquake Engineering*, Auckland, New Zealand, February 2000.
- [3] M. H. Stanikzai, S. Elias, V. A. Matsagar, and A. K. Jain, "Seismic response control of base-isolated buildings using multiple tuned mass dampers," *The Structural Design Of Tall And Special Buildings*, vol. 28, p. e1576, 2018.
- [4] R. Rupakhety, S. Elias, and S. Olafsson, "Shared tuned mass dampers for mitigation of seismic pounding," *Applied Sciences*, vol. 10, no. 6, p. 1918, 2020.
- [5] J. M. Kelly, "Aseismic base isolation: review and bibliography," *Soil Dynamics and Earthquake Engineering*, vol. 5, no. 3, pp. 202–216, 1986.
- [6] R. S. Jangid and T. K. Datta, "Seismic behaviour of base-isolated buildings: a state-of-the art review," in *Proceedings of the Institution of Civil Engineers-Structures and Buildings*, vol. 110, no. 2, pp. 186–203, 1995.
- [7] C.-M. Chang and B. F. Spencer, "Active base isolation of buildings subjected to seismic excitations," *Earthquake Engineering & Structural Dynamics*, vol. 39, no. 13, pp. 1493–1512, 2010.
- [8] Y. Peng, L. Ding, and J. Chen, "Performance evaluation of base-isolated structures with sliding hydromagnetic bearings," *Structural Control and Health Monitoring*, vol. 26, no. 1, p. e2278, 2018.
- [9] R. Rabiee and Y. Chae, "Adaptive base isolation system to achieve structural resiliency under both short- and long-period earthquake ground motions," *Journal of Intelligent Material Systems and Structures*, vol. 30, no. 1, pp. 16–31, 2018.
- [10] Y. Peng and T. Huang, "Sliding implant-magnetic bearing for adaptive seismic mitigation of base-isolated structures," *Structural Control and Health Monitoring*, vol. 26, no. 10, 2019.
- [11] P. Gardoni, C. Murphy, and A. Rowell, *Risk Analysis of Natural Hazards: Interdisciplinary Challenges and Integrated Solutions*, Springer, Berlin, Germany, 2016.
- [12] P. Gardoni and J. M. LaFave, *Multi-Hazard Approaches to Civil Infrastructure Engineering*, Springer, Berlin, Germany, 2016.
- [13] T. B. Messervey, D. Zangani, and S. Casciati, "Smart high-performance materials for the multi-hazard protection of civil infrastructure," *Safety And Security Engineering III*, vol. 108, 2009.
- [14] H. Mahmoud and A. Chulahwat, "Multi-hazard multi-objective optimization of building systems with isolated floors under seismic and wind demands," In P. Gardoni, J. LaFave. (eds) *Multi-hazard Approaches to Civil Infrastructure Engineering*. Springer, Cham, Switzerland, 2016.
- [15] I. Venanzi, O. Lavan, L. Ierimonti, and S. Fabrizi, "Multi-hazard loss analysis of tall buildings under wind and seismic loads," *Structure and Infrastructure Engineering*, vol. 14, no. 10, pp. 1295–1311, 2018.
- [16] T. Roy and V. Matsagar, "Effectiveness of passive response control devices in buildings under earthquake and wind during design life," *Structure and Infrastructure Engineering*, vol. 15, no. 2, pp. 252–268, 2019.

- [17] T. Roy and V. Matsagar, "Probabilistic assessment of steel buildings installed with passive control devices under multi-hazard scenario of earthquake and wind," *Structural Safety*, vol. 85, p. 101955, 2020.
- [18] P. Henderson and M. Novak, "Response of base-isolated buildings to wind loading," *Earthquake Engineering & Structural Dynamics*, vol. 18, no. 8, pp. 1201–1217, 1989.
- [19] P. Henderson and M. Novak, "Wind effects on base isolated buildings," *Journal of Wind Engineering and Industrial Aerodynamics*, vol. 36, no. 1–3, pp. 559–569, 1990.
- [20] Y. Chen and G. Ahmadi, "Wind effects on base-isolated structures," *Journal of Engineering Mechanics*, vol. 118, no. 8, pp. 1708–1727, 1992.
- [21] A. Kareem, "Modelling of base-isolated buildings with passive dampers under winds," *Journal of Wind Engineering and Industrial Aerodynamics*, vol. 72, pp. 323–333, 1997.
- [22] B. Liang, X. Shishu, and T. Jiaxiang, "Wind effects on habitability of base-isolated buildings," *Journal of Wind Engineering and Industrial Aerodynamics*, vol. 90, no. 12–15, pp. 1951–1958, 2002.
- [23] C. Feng and X. Chen, "Evaluation and characterization of probabilistic alongwind and crosswind responses of base-isolated tall buildings," *Journal of Engineering Mechanics*, vol. 145, no. 12, Article ID 04019097, 2019.
- [24] R. Zhang and B. M. Phillips, "Numerical study on the benefits of base isolation for blast loading," in *Joint 6th International Conference on Advances in Experimental Structural Engineering (6AESE) and 11th International Workshop on Advanced Smart Materials and Smart Structures Technology (11ANCRiSST)*, Champaign, IL, USA, August 2015.
- [25] R. Zhang and B. M. Phillips, "Performance and protection of base-isolated structures under blast loading," *Journal of Engineering Mechanics*, vol. 142, no. 1, Article ID 04015063, 2016.
- [26] M. Z. Kangda and S. Bakre, "Positive-phase blast effects on base-isolated structures," *Arabian Journal for Science and Engineering*, vol. 44, no. 5, pp. 4971–4992, 2018.
- [27] P. D. Mondal, A. D. Ghosh, and S. Chakraborty, "Performance of N-Z base isolation system for structures subject to underground blast," in *Proceedings Of the International Symposium On Engineering under Uncertainty: Safety Assessment And Management (ISEUSAM-2012)*, Springer, Berlin, Germany, pp. 1007–1020, 2012.
- [28] P. D. Mondal, A. D. Ghosh, and S. Chakraborty, "Performance of N-Z systems in the mitigation of underground blast induced vibration of structures," *Journal of Vibration and Control*, vol. 20, no. 13, pp. 2019–2031, 2013.
- [29] P. D. Mondal, A. D. Ghosh, and S. Chakraborty, "Control of underground blast-induced building vibration by shape-memory-alloy rubber bearing (SMARB)," *Structural Control and Health Monitoring*, vol. 24, no. 10, p. e1983, 2017.
- [30] P. D. Mondal, A. D. Ghosh, and S. Chakraborty, "Performances of various base isolation systems in mitigation of structural vibration due to underground blast induced ground motion," *International Journal of Structural Stability and Dynamics*, vol. 17, no. 4, p. 1750043, 2017.
- [31] J. P. Talbot and H. E. M. Hunt, "Isolation of buildings from rail-tunnel vibration: a review," *Building Acoustics*, vol. 10, no. 3, pp. 177–192, 2003.
- [32] L. S. Wei and F. L. Zhou, "Vibration and seismic isolation design for buildings on subway platform," in *Proceedings of the Fourteenth World Conference on Earthquake Engineering*, Beijing, China, October 2008.
- [33] D. Makovicka and D. Makovicka, "Structure isolation in order to reduce vibration transfer from the subsoil," *International Journal of Computational Methods and Experimental Measurements*, vol. 2, no. 1, pp. 1–13, 2014.
- [34] Y. K. Wen, "Method for random vibrations of hysteretic systems," *Journal of the Engineering Mechanics Division*, vol. 102, no. 2, pp. 249–263, 1976.
- [35] Y. K. Wen, "Methods of random vibration for inelastic structures," *Applied Mechanics Reviews*, vol. 42, no. 2, pp. 39–52, 1989.
- [36] Y. J. Park, Y. K. Wen, and A. H.-S. Ang, "Random vibration of hysteretic systems under Bi-directional ground motions," *Earthquake Engineering & Structural Dynamics*, vol. 14, no. 4, pp. 543–557, 1986.
- [37] V. A. Matsagar and R. S. Jangid, "Viscoelastic damper connected to adjacent structures involving seismic isolation," *Journal of Civil Engineering and Management*, vol. 11, no. 4, pp. 309–322, 2005.
- [38] R. S. Jangid, "Computational numerical models for seismic response of structures isolated by sliding systems," *Structural Control and Health Monitoring*, vol. 12, no. 1, pp. 117–137, 2005.
- [39] R. S. Jangid, "Optimum lead-rubber isolation bearings for near-fault motions," *Engineering Structures*, vol. 29, no. 10, pp. 2503–2513, 2007.
- [40] E. M. L. Carvalho and R. C. Battista, "Blast-induced vibrations in urban residential buildings," in *Proceedings of the Institution of Civil Engineers-Structures and Buildings*, vol. 156, no. 3, pp. 243–253, 2003.
- [41] C. Wu and H. Hao, "Numerical study of characteristics of underground blast induced surface ground motion and their effect on above-ground structures. Part I. Ground motion characteristics," *Soil Dynamics and Earthquake Engineering*, vol. 25, no. 1, pp. 39–53, 2005.

Research Article

Development of Rocking Isolation for Response Mitigation of Elevated Water Tanks under Seismic and Wind Hazards

Hassan Alemzadeh,¹ Hamzeh Shakib ,¹ and Mohammad Khanmohammadi²

¹School of Civil and Environmental Engineering, Tarbiat Modares University, Tehran, P.O. Box 14115-111, Iran

²School of Civil Engineering, College of Engineering, University of Tehran, Tehran, P.O. Box 14155-6619, Iran

Correspondence should be addressed to Hamzeh Shakib; shakib@modares.ac.ir

Received 11 December 2019; Revised 15 August 2020; Accepted 3 September 2020; Published 5 October 2020

Academic Editor: Vasant Matsagar

Copyright © 2020 Hassan Alemzadeh et al. This is an open access article distributed under the Creative Commons Attribution License, which permits unrestricted use, distribution, and reproduction in any medium, provided the original work is properly cited.

Elevated water tanks are categorized as strategic components of water supply systems in modern urban management. Past earthquake events have revealed the high vulnerability of these structures. This paper investigates the development of rocking isolation (RI) to these structures as a response mitigation technique. Using an analytical approach, a dynamic model is developed for two isolation cases: (1) at the pedestal base and (2) under the tank. The model incorporates a simplified analogy for simulating the liquid-tank system which is modified for a tank under rocking motions. Based on the dynamics of rocking structures, the equations of motion, impact, and uplift transitions are derived. Then, free vibration and seismic response history analyses are carried out on a sample structure. Discussions are made on the effect of RI on the dynamic and seismic responses of the pedestal and components of the liquid-tank system. Effects of various RI cases, pedestal heights, and tank filling levels are studied for a group of structures excited by an ensemble of ground motions. Considering that the system may be vulnerable to other lateral loadings, the combined effects of seismic and wind hazards are also studied. The wind loads are assumed to act statically and simultaneously with the seismic excitations. Results show that the first case of RI decreases the acceleration demands of mid-rise and tall structures, thus lowering the structural demands to 50% of the fixed-base system. However, the second case of RI has almost no effect on the performance of the system, upgrading only the response of mid-rise structures. Both RI cases also aggravate the wave oscillations and increase the freeboard requirements. Finally, while the combined seismic and wind hazards have almost no effect on the operational performances, the force demands of the structures are increased by 10%.

1. Introduction

Rocking mechanism is a low-damage technology that not only reduces the spread of nonlinear damage to structural components but also mitigates the downtime and repair cost of structures after an earthquake event [1]. Moreover, when the excitation is over, the rocking structure will return to its original position and unlike fixed-base structures, no residual deformations are observed. This also provides resilient behavior against cascading hazards such as multiple aftershocks. These aspects of rocking mechanism, in addition to the ancient structures with unintentional rocking behavior or modern ones equipped with rocking isolation (RI), which performed well during past earthquakes [2, 3], have drawn

the attention of many researchers. The first analytical model for a rigid-like structure rocking on a rigid base was proposed by Housner [2] in an effort to investigate the behavior of tall slender structures such as elevated water tanks that survived during the 1960 Chilean earthquakes. It was shown that despite the appearance of instability for these structures, there is a scale effect making the larger structures more stable than smaller ones with similar geometry.

Hereafter, application of this technique to various structural systems like buildings and bridge piers has been the objective of many theoretical [3–11] and experimental studies [5, 8, 12, 13]. Many of these studies showed the remarkable dynamic stability and low-damage capability for both rigid [4–8] and deformable structures [9–13]. This also includes the

studies on assemblies of rocking bodies such as stacked blocks [14], rocking ancient frames and elements [15], and rocking assemblies coupled with SDOF systems such as rocking podium structures [16] or with TMDs [7, 17]. Moreover, there are some studies conducted on the intentional application or development of rocking mechanism for nonbuilding structures such as industrial equipment [18], bridge piers [19], and architectural or art objects [20].

Nevertheless, there are relatively fewer studies on the rocking behavior of liquid storage tanks and even scarce ones on the RI application to tanks. First, there is a handful of studies which investigated the effect of rotational/rocking component of the base excitation on the response of tanks and the fluid-structure interaction (FSI) system [21, 22]. This group of studies has a similar approach to the one that was firstly proposed by Housner [21], i.e., an equivalent analytical model is presented for seismic response analysis of tanks under the action of rocking base excitation. The advantage of this model is the rotational mass component added to the former equivalent mechanical model of the liquid-tank system, which can be used in similar models of rocking tanks. The other category of these studies mainly focuses on the “unintentional” uplift of the bottom plate of ground-supported tanks [23–25] under seismic or dynamic actions. Finally, most of the studies carried on the seismic performance upgrade of storage tanks are involved with the application of slide isolation technique by using elastomeric bearings [26–28] or application of baffled damping plates [29]. Hence, to the knowledge of the authors, there is no study devoted to the “intentional” application of RI mechanism to liquid storage tanks (elevated or else) as a seismic response upgrade strategy. It is noteworthy that the main difference between the unintentional rocking of the structures and the intentional application of RI is that the structure is required to return to its original undeformed position and no sliding or stepping out is allowed, i.e., a necessity for a system with resilient behavior.

Although a detailed investigation of the experimental studies carried on rocking structures is beyond the scope of this paper, some of the recent campaigns [8, 12, 13] showed the difficulties and limitations of these studies. Thus, development of analytical or numerical models for analysis of rocking structures was considered by many researchers. In this regard, multiple FEM-based models are proposed for “rigid” and “deformable” [30–32] rocking structures most of which validate their corresponding analytical models. Accordingly, the authors applied a FEM-based approach [33] using OpenSees framework for seismic analysis of ground-supported tanks with RI which was limited to ground steel tanks. However, this model was not validated by the previous analytical or experimental approaches [23] due to the limitations of the impact modeling techniques. Thus, development of an analytical model for liquid storage tanks with rocking motion is proved to be essential.

To the best of our knowledge, the study by Taniguchi [24] is the only research to partly investigate the rocking behavior of ground-supported tanks using an analytical model. Taniguchi applied a Housner-like [2] approach to the rigid flat-bottom tanks under the action of the horizontal base

excitation and derived the equations of the rocking motion. Although he simplified the equivalent analytical model by omitting the sloshing or convective component from the liquid-tank system and assuming the tank wall flexibility component only, the total liquid mass is assumed for studying the global stability of the structure. Moreover, the effect of impacts at the rocking interfaces on the response of the structure is not discussed in his model.

Initially, this paper focuses on addressing the shortcomings of Taniguchi’s model and further developing this model for planar (2D) seismic analysis of intentionally rock-isolated elevated tanks under horizontal and vertical base excitations. For this purpose, firstly the equations and systematic approach used in the aforementioned studies are reviewed. Then, the general assumptions made for the developed model of rocking elevated tanks are presented. Moreover, the effects of impacts at rocking interfaces on the global responses are revisited. A numerical algorithm is also presented for solving the equations of motions which appears to be less time-consuming in some specific prototypes with mathematically “stiff” equations.

Hereafter, another objective of the paper is to obtain basic information on the applicability and effectiveness of RI as a seismic response upgrade technique. Thus, following a similar approach applied in previous studies on slide-isolated elevated tanks or similar structures [26–28, 34], two cases of RI are investigated: (1) isolation at the base and (2) isolation under the tank. In both cases, the elevated tanks are assumed to be located on stiff soil sites and soil-foundation interaction is neglected. Considering that the proposed system may be vulnerable to other lateral loadings, the combined effects of seismic and wind loads are also studied. The wind loads are assumed to act statically and simultaneously with the seismic excitations. Accordingly, parametric studies are carried out on a group of prototypes with various pedestal/shaft heights and tank filling levels which are analyzed under the combined action of seismic and wind hazards.

2. Analytical Model of the Rocking Elevated Tank

2.1. Review of Similar Analytical Models. Firstly, by applying the same assumptions applied in Housner’s analytical model [2], the equation of rocking motion for a 2D homogenous rigid block with an aspect ratio of α and a diagonal of length $2R$ under the horizontal and vertical base excitation is as follows:

$$\begin{aligned} I_O \ddot{\theta} = & -m(g + \ddot{u}_g^Y)R \sin[\text{asgn}\theta(t) - \theta(t)] \\ & -m\ddot{u}_g^X(t)R \cos[\text{asgn}\theta(t) - \theta(t)], \end{aligned} \quad (1)$$

where θ is the rotational response of the block, m is the total mass of the block, and I_O is the rotational mass inertia of the block about one of its pivot points (O or O’). Also, \ddot{u}_g^X and \ddot{u}_g^Y are, respectively, the horizontal and vertical components of base acceleration.

Taniguchi [23] applied the same approach to a ground-supported steel tank under horizontal base excitation (Figure 1). Considering only the first vibration mode of the liquid-tank system, the equations of planar rocking motion are derived as follows:

$$I_O \ddot{\theta} = -M_O g R_O \sin[\alpha_O - \theta(t)] + \text{sgn}\theta(t) H_I (C_I \dot{x}_I + K_I x_I), \quad (2)$$

$$\begin{aligned} M_I \ddot{x}_I - \text{sgn}\theta(t) M_I g \sin \theta + \text{sgn}\theta(t) M_I R_I \dot{\theta}^2 \sin \alpha_I \\ + \text{sgn}\theta(t) M_I R_I \ddot{\theta} \cos \alpha_I + M_I \ddot{u}_g^X \cos \theta + C_I \dot{x}_I + K_I x_I \\ = 0, \end{aligned} \quad (3)$$

where M_I , K_I , and C_I are, respectively, the mass, stiffness, and damping coefficients corresponding to the first vibration mode of the liquid-tank system and x_I is the first mode displacement response. Also, θ is the rocking response of the tank. Finally, M_O and I_O are, respectively, the mass and rotational mass inertia of all tank liquid about one of its pivot points (O or O').

Regarding its assumptions and approach, Taniguchi's model has the following shortcomings:

- (i) Including the total values of liquid mass M_O and its rotational inertia I_O in equation (2) unrealistically stabilizes the tank during rocking motion and thus produces smaller and nonconservative values for rotational and translational responses. Accordingly, researchers have shown that proportions, and not the total values, of these parameters especially for I_O should be used in the analysis of rocking tanks [21, 22] disregarding the rigidity of the bottom plate.
- (ii) The effect of the convective component of the liquid-tank system is not included in this model, which, as discussed later, shows notable effects on the global dynamic stability and rocking and displacement responses of rocking elevated tanks.
- (iii) The details of the analytical model for including the effect of the impacts at rocking interfaces on the postimpact responses of the tank are not discussed in this model and only an imperfect restitution coefficient (e), the value and calculation method of which is not clarified, is used for determination of postimpact rotational response.
- (iv) Change in the pressure responses acting on the tank wall due to the rocking motion of various components of the system is not studied.

Observing the aforementioned remarks, one of the main goals of this paper is to focus on resolving these shortcomings and develop the model for seismic analysis of rocking elevated tanks.

2.2. General Assumptions of the Developed Model. As mentioned before, a rocking elevated tank with shaft staging is studied in this paper. Two cases of RI at different levels are presumed for this structure: (C1) at the base or under the

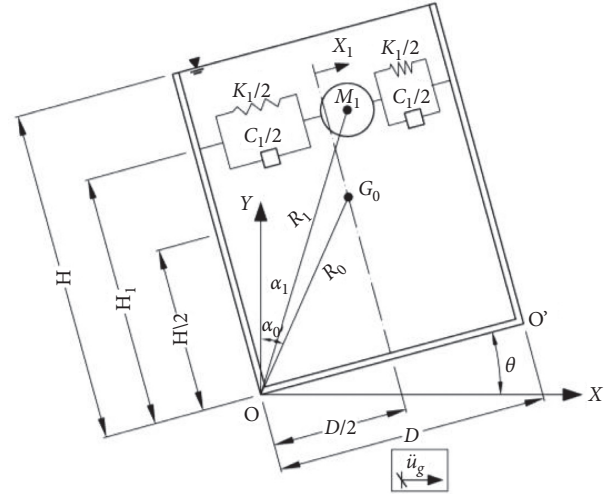


FIGURE 1: Analytical model for the rocking behavior of ground-supported tanks presented by Taniguchi [23].

pedestal/shaft (Figure 2) and (C2) under the tank or top of the pedestal (Figure 3). As shown Figures 2 and 3, the liquid-tank system is modeled by an equivalent mechanical analogy including lumped masses, springs, and dashpots. Properties of this simplified model which is a combination of analytical approaches presented by Housner [35], Haroun [36], and Haroun and Ellaithy [21] are shown in Figure 4. The main advantage of this analogy is its ability to study the combined effect of translational and rocking motions on the response of the liquid-tank system. This is mainly accomplished by considering a modified rotational inertia (I_r) for the liquid-tank impulsive/rigid component which is of great importance in analyzing systems experiencing rocking motions. In Figures 2–4, the subscripts of “C,” “1,” and “0” describe the “full-contact” geometrical properties (aspect ratio, α , and radial distance to the pivot points, R) of the masses corresponding to the convective, wall flexibility, and impulsive components of the simplified liquid-tank system, respectively. Similarly, the subscripts of “r,” “f,” and “S” correspond to the tank roof, tank floor, and supporting shaft centers of gravity (C.G.). H_I is also the filling level of the “liquid.” Moreover, the following assumptions are made while analyzing both RI cases:

- (i) The tank structure storing liquid and its components including roof slab, floor slab, and its framing beams and also the foundation of the structure are assumed to be rigid. However, in all cases, the supporting/shaft structure is assumed to be laterally deformable. The tank wall flexibility is also considered via the aforementioned simplified liquid-tank system (Figure 4).
- (ii) The liquid-tank system is assumed to be fully constrained with the tank structure in the perpendicular direction of the floor, and its components move rigidly with the tank wall in that direction.
- (iii) For the system to be resilient, the rocking body (shaft in C1 or tank in C2) is constrained not to slide or roll out of its initial position. This constraint is

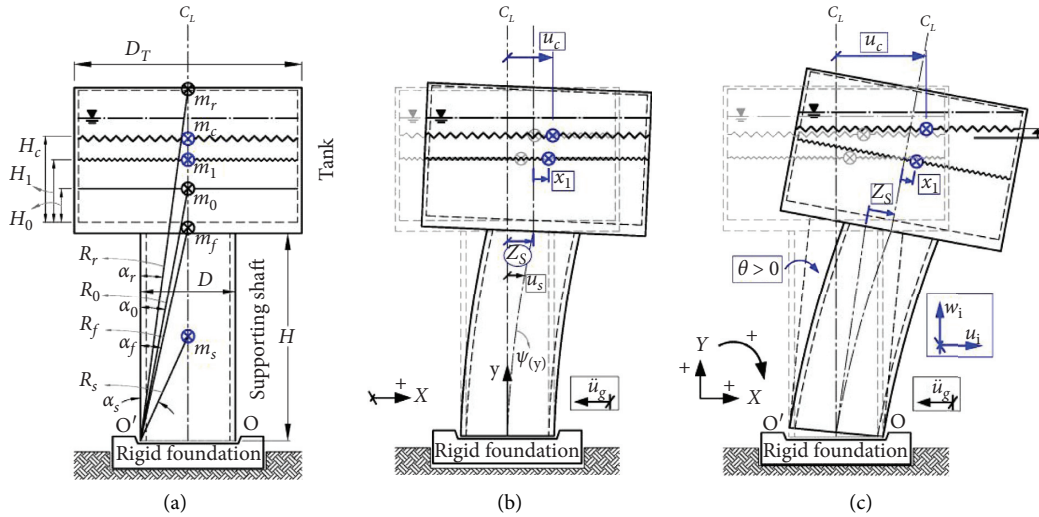


FIGURE 2: Configuration of rocking elevated tank model with isolation at the base (C1): (a) initial position; (b) preuplift phase of motion; (c) under rocking motion.

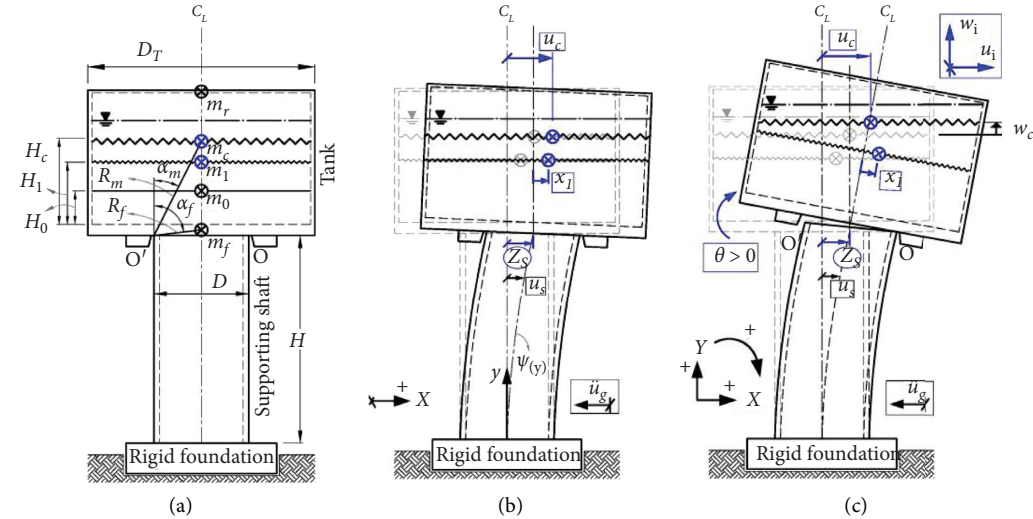


FIGURE 3: Configuration of rocking elevated tank model with isolation under the tank (C2): (a) initial position; (b) preuplift phase of motion; (c) under rocking motion.

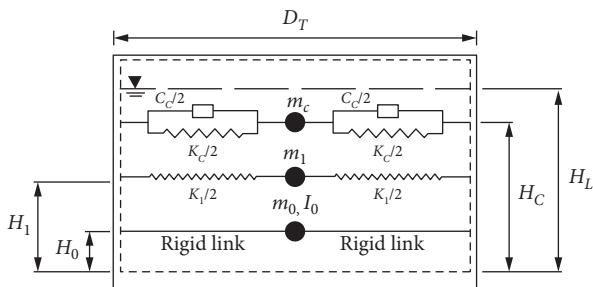


FIGURE 4: Mechanical analogy of the simplified liquid-tank system for a tank under combined translational and rocking motion.

assumed to be a shear key provided at the interfaces. In the first case (C1), the shear key is provided in the foundation and under the bottom of the shaft

(Figure 2). For the second case (C2), a similar shear key is assumed in the bottom face of the tank floor and over the top of the shaft. These shear keys are assumed to ensure the direct transformation of shear forces and deformations between the shaft and the foundation or tank.

- (iv) The structures are assumed to be located on stiff soil sites (class B or C according to ASCE 7-16 [37]), and soil-foundation interaction is negligible. Specifically, it is assumed that in the first case of RI, the structure rocks on a rigid foundation which is fully constrained to the bottom soil.
- (v) The rocking or contact surfaces in both isolation cases are assumed to remain intact and without crushing during the rocking motion. Moreover, sliding is constrained on these surfaces.

- (vi) The impact effects on postimpact response condition of the structure and energy dissipations are mainly based on assumptions of Housner's analytical approach [2] and other following researchers such as Chopra and Yim [4] and Vassiliou et al. [10]. More detailed assumptions are presented and discussed for each RI case.

2.3. Preuplift Phase of Motion and Uplift Transition. The first class of equations needed for analyzing the rocking structure includes (1) equations of motion in the preuplift/

full-contact phase and (2) uplift initiation equation which is usually defined as a conditional equation for the minimum horizontal acceleration needed to initiate rocking of the structure. As shown in Figures 2(b) and 3(b), in the preuplift phase, the system acts like a fixed-base structure and has three degrees of freedom that are u_C (total displacement of the convective mass), x_1 (relative displacement of the wall flexibility mass), and z_S (flexural deformation of shaft top end). Therefore, the motion of the system is described by the following system of differential equations:

$$\begin{bmatrix} m_C & 0 & 0 \\ 0 & m_1 & m_1 \\ 0 & 0 & \tilde{m}_S + m_{\text{imp}} \end{bmatrix} \begin{bmatrix} \ddot{u}_C \\ \ddot{x}_1 \\ \ddot{z}_S \end{bmatrix} + \begin{bmatrix} C_C & 0 & -C_C \\ 0 & C_1 & 0 \\ -C_C & -C_1 & \tilde{C}_S + C_C \end{bmatrix} \begin{bmatrix} \dot{u}_C \\ \dot{x}_1 \\ \dot{z}_S \end{bmatrix} + \begin{bmatrix} K_C & 0 & -K_C \\ 0 & K_1 & 0 \\ -K_C & -K_1 & \tilde{K}_S + K_C \end{bmatrix} \begin{bmatrix} u_C \\ x_1 \\ z_S \end{bmatrix} = -\ddot{u}_g^X \begin{bmatrix} m_C \\ m_1 \\ \tilde{L}_S + m_{\text{imp}} \end{bmatrix}, \quad (4)$$

where m_C , C_C , and K_C are the mass, damping, and stiffness coefficients corresponding to the convective component of response in the liquid-tank system, respectively. Similarly, m_1 , C_1 , and K_1 are the mass, damping, and stiffness coefficients of the wall flexibility component. The mass of impulsive components, i.e., roof m_r , floor m_f , and m_0 , is also summarized in m_{imp} . Also, \tilde{m}_S , \tilde{C}_S , \tilde{K}_S , and \tilde{L}_S are the generalized mass, damping coefficient, stiffness coefficient, and excitation coefficient of the shaft, respectively, which are defined by assuming the shaft as a generalized SDOF system. Thus, lateral deformation of the shaft top end ($z_S(t)$) is assumed as the

generalized coordinate of the shaft with uniform mass and flexural stiffness.

Following the previous studies, the uplift criterion for the planar rocking of a rigid block is derived by equating the static overturning and restoring moments about one of the pivot points. However, for the rocking elevated tank, the presence of the liquid-tank system in addition to the system geometrical and mechanical properties modifies this equation. According to Figure 2, the overturning (M_{OT}) and restoring moment (M_{RT}) of the forces acting on the whole structure with C1 during the preuplift phase and immediately before uplift are as follows:

$$M_{\text{OT}} = -(\ddot{u}_g^X + \ddot{z}_S) \left(\sum_{i=0,r,f} m_i R_i \cos \alpha_i \right) - \int_0^H [\ddot{z}_S \psi(y) + \ddot{u}_g^X] y dm - \sum_{j=1,C} m_j R_j \cos \alpha_j (\ddot{u}_g^X + \ddot{u}_j), \quad (5)$$

$$M_{\text{RT}} = (g + \ddot{u}_g^Y) \left[\sum_{i=0,r,f} m_i \left(\frac{D}{2} \mp z_S \right) + m_s \left(\frac{D}{2} \mp 0.363 z_S \right) + \sum_{j=1,C} m_j \left(\frac{D}{2} \mp u_j \right) \right], \quad (6)$$

where D , $m_{(ij)}$, $\alpha_{(ij)}$, and $R_{(ij)}$ are the parameters used for the definition of mass and different geometrical properties of various components of the structure ($i = r, f, S$) and the liquid-tank system ($i = 0, j = 1, C$) (Figure 2). Also,

considering the relative displacement of the flexibility mass, x_1 , one can obtain in the preuplift phase: $u_1 = x_1 + z_S$. By equating these, the rocking criterion is determined as follows:

$$\begin{aligned} |M_{\text{OT}}| > M_{\text{RT}} &\implies \left| -(\ddot{u}_g^X + \ddot{z}_S) \left(\sum_{i=0,r,f} m_i R_i \cos \alpha_i \right) - m_s H \left(0.269 \ddot{z}_S + \frac{1}{2} \ddot{u}_g^X \right) - \sum_{j=1,C} m_j R_j \cos \alpha_j (\ddot{u}_g^X + \ddot{u}_j) \right| \\ &> (g + \ddot{u}_g^Y) \left[\sum_{i=0,r,f} m_i \left(\frac{D}{2} \mp z_S \right) + m_s \left(\frac{D}{2} \mp 0.363 z_S \right) + \sum_{j=1,C} m_j \left(\frac{D}{2} \mp u_j \right) \right], \end{aligned} \quad (7)$$

where m_S is the total mass of the shaft. The upper signs in equations (5)–(7) correspond to uplift about the right pivot point ($\ddot{u}_g^X < 0$) and vice versa. Accordingly, for C2, external

forces acting on the shaft are omitted and the effect of its deformability is considered as follows (Figure 3(b)):

$$\begin{aligned} & \left| -(\ddot{u}_g^X + \ddot{z}_S) \left(\sum_{i=0,r,f} m_i R_i \cos \alpha_i \right) - m_C R_C \cos \alpha_C (\ddot{u}_g^X + \ddot{u}_C) - m_1 R_1 \cos \alpha_1 (\ddot{u}_g^X + \ddot{x}_1 + \ddot{z}_S) \right| \\ & > (g + \ddot{u}_g^Y) \left\{ \left(\frac{D}{2} \right) \left(\sum_{i=0,r,f} m_i \right) + m_C \left[\left(\frac{D}{2} \right) \mp (u_C - z_S) \right] + m_1 \left[\left(\frac{D}{2} \right) \mp (x_1) \right] \right\}. \end{aligned} \quad (8)$$

2.4. Equations of Rocking Motion. After the initiation of rocking, the motion of the system in both cases of RI is described by four degrees of freedom: θ (rocking response), u_C (horizontal displacement of the convective mass), x_1 (relative displacement of the flexibility mass), and z_S (relative displacement of the shaft top end). The equations of motion (EOM) are derived using Lagrangian formulation:

$$\frac{d}{dt} \left(\frac{\partial T}{\partial \dot{q}_i} \right) - \left(\frac{\partial (T - V)}{\partial q_i} \right) = Q_{q_i} = \left(\frac{\partial W}{\partial q_i} \right), \quad (9)$$

where T and V are the kinetic and potential energy of the system, respectively, and Q_{q_i} is the nonconservative force acting along the DOF q_i , which for the studied model is the damping forces of various component. The latter is determined by the variation of work (δW) done by the

nonconservative force during an admissible virtual displacement of δq_i :

$$Q_{q_i} = \left(\frac{\partial W}{\partial q_i} \right) \equiv \left(\frac{\delta W}{\delta q_i} \right). \quad (10)$$

Equation (9) is also known as Lagrange's EOMs which are a direct result of applying Hamilton's variational principle [38] to all systems (linear or nonlinear) with a specific condition: that the energy and work terms can be expressed by the selected DOFs (q_i), their time derivatives, and also their variations (\dot{q}_i and δq_i).

Placing origin of the axis at the centerline of the shaft on its base (Figure 2(c)), total displacement field of various components of the system with C1 is given by the following expressions:

$$\begin{aligned} u_i &= R_i (\sin [\operatorname{sgn}(\theta) \alpha_i] - \sin [\operatorname{sgn}(\theta) \alpha_i - \theta]) + z_S \cos \theta, \quad i = 0, r, f, m, \\ w_i &= R_i (\cos [\operatorname{sgn}(\theta) \alpha_i - \theta] - \cos [\operatorname{sgn}(\theta) \alpha_i]) - z_S \sin \theta, \quad i = 0, r, f, m. \end{aligned} \quad (11)$$

It is worth to note that the subscript m stands for the equal-displacement point m representing the tank wall at the level of the convective mass (Figure 5). Similarly, for C2, displacement field of the tank is obtained by following expressions:

$$u_i = z_S + R_i (\sin [\operatorname{sgn}(\theta) \alpha_i] - \sin [\operatorname{sgn}(\theta) \alpha_i - \theta]), \quad i = 0, r, f, m, \quad (12)$$

$$w_i = R_i (\cos [\operatorname{sgn}(\theta) \alpha_i - \theta] - \cos [\operatorname{sgn}(\theta) \alpha_i]), \quad i = 0, r, f, m. \quad (13)$$

The equal-displacement "point" m is a virtual point assumed to be located at the level of the convective mass with equal distance from the tank walls and moves rigidly with them (Figure 5(b)). The location of this point is of great importance in simplification and describing the terms of convective damping and potential energy of the liquid-tank system. Moreover, considering assumptions of the simplified model introduced in Figure 5 and observations made in some experimental programs [23], the convective mass link to the tank wall is presumed to remain horizontal during rocking motions.

Accordingly, for C1, the total displacement field of the tank wall flexibility component including the relative displacement (x_1) measured in its normal direction (Figure 2(c)) is as follows:

$$\begin{aligned} u_1 &= R_1 (\sin [\operatorname{sgn}(\theta) \alpha_1] - \sin [\operatorname{sgn}(\theta) \alpha_1 - \theta]) + (x_1 + z_S) \cos(\theta), \\ w_1 &= R_1 (\cos [\operatorname{sgn}(\theta) \alpha_1 - \theta] - \cos [\operatorname{sgn}(\theta) \alpha_1]) - (x_1 + z_S) \sin(\theta), \end{aligned} \quad (14)$$

where the term $x_1 + z_S$ is equal to the selected DOF for the flexibility component (z_1). Now, by applying equation (9) to the first DOF (u_C), first EOM for C1 is as follows:

$$\begin{aligned} & \ddot{u}_C - \left(\frac{1}{2} \right) \left\{ \dot{\theta}^2 [2u_C - \operatorname{sgn}(\theta) D] + 2\dot{\theta} \dot{z}_S \sin \theta \right\} \\ & + \omega_C^2 [u_C - R_m (\sin [\operatorname{sgn}(\theta) \alpha_m] - \sin [\operatorname{sgn}(\theta) \alpha_m - \theta]) \\ & - z_S \cos \theta] + 2\xi_C \omega_C (\dot{u}_C - R_m \dot{\theta} (\cos [\operatorname{sgn}(\theta) \alpha_m - \theta]) \\ & - \dot{z}_S \cos \theta + z_S \dot{\theta} \sin \theta) = -\ddot{u}_g^X, \end{aligned} \quad (15)$$

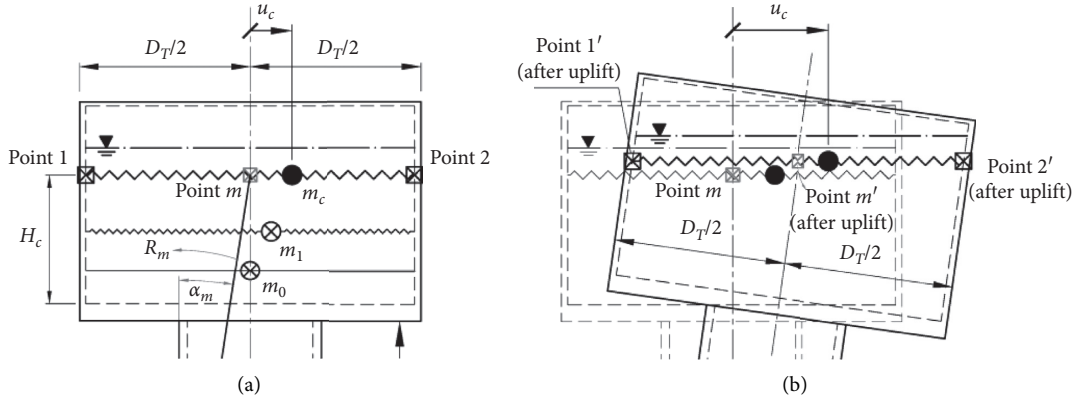


FIGURE 5: Geometrical properties used in analysis of the tank structure, specifically, the location of virtual point (m) (a) before and (b) after uplift.

where ω_C and ξ_C are the equivalent fundamental frequency and viscous damping ratio corresponding to the convective component of the liquid-tank system, respectively. The other EOM corresponding to the second DOF (x_1) is also obtained as follows for C1:

$$\begin{aligned} \ddot{x}_1 + \ddot{z}_S + 2\xi_1\omega_1\dot{x}_1 + \omega_1^2x_1 + R_1\ddot{\theta}\cos[\text{sgn}(\theta)\alpha_1] \\ - \dot{\theta}^2(z_S + x_1 - R_1\sin[\text{sgn}(\theta)\alpha_1]) + \ddot{u}_g^X\cos\theta \\ - (g + \ddot{u}_g^Y)\sin\theta = 0, \end{aligned} \quad (16)$$

where ω_1 is the fundamental frequency of the tank wall flexibility component.

Equations (14) and (15) are similarly developed for C2 considering the displacement field described by equations (12) and (13). For the sake of brevity, these EOMs in addition to the ones corresponding to the third and fourth DOFs, i.e., z_S and θ , are presented in [39]. It should be noted that for C1, by omitting the rotational responses ($\ddot{\theta}$, $\dot{\theta}$, and θ) from equations (15) and (16), the EOMs in preuplift phase (equation (4)) and rocking initiation equation (equation (7)) are reproduced. This gives the second class of equations needed for analyzing the rocking elevated tanks under horizontal and vertical base excitations.

2.5. The Impact Effects. Among important issues to be addressed about rocking structures are the impacts at the rocking surfaces and modification methodology of the postimpact responses of the structure. These specifically

include the postimpact velocities of the 4 DOFs of the structure. The continuation of the rocking motion after each impact “event” directly relates to the calculation of these responses as the “next” initial values of the motion. The postimpact motion of the structure is analyzed by the same EOMs, but by using the new initial values obtained from the “immediate” postimpact state. Although various analytical models for the impact transitions of rocking structures have been proposed by many researchers [2, 4, 8–10], the main assumptions of most of these models are almost as follows: (1) the impact transitions are inelastic, (2) the impact transitions and the change of rocking corners are instantaneous, and (3) the impact forces are concentrated at the new pivot point (impacting corner). Following an approach firstly mentioned by Meek [40] and extended by Vassiliou et al. [10], it is observed to be more conservative to presume the impacts to be “perfectly” inelastic with no bouncing. It means that at each impact event, the structure sticks to the rocking interface in a “full-contact” phase and the vertical component of the shaft velocity is damped out. Hence:

$$\theta_2 = \dot{\theta}_2 = 0, \quad (17)$$

where the index “2” corresponds to the postimpact state. Moreover, the conservation of linear momentum (COLM) of the whole system along the horizontal direction gives an equation for the postimpact velocity of the shaft, $\dot{z}_{S,2}$. For C1, it is given by (Figures 6(a) and 6(b))

$$(\dot{z}_{S,2} - \dot{z}_{S,1})\left(\tilde{I}_S + \sum_{i=0,r,f} m_i\right) + (-\dot{\theta}_1)\left[\frac{m_s H}{2}\right] + \sum_{i=0,r,f} m_i R_i \cos\alpha_i + \sum_{j=1,C} m_j (\dot{u}_{j,2} - \dot{u}_{j,1}) = 0, \quad (18)$$

where m_s is the total mass of shaft. All other parameters have been defined and shown in Figures 2(a), 6(a), and 6(b).

Removing effect of the rocking shaft also gives the following equation for C2:

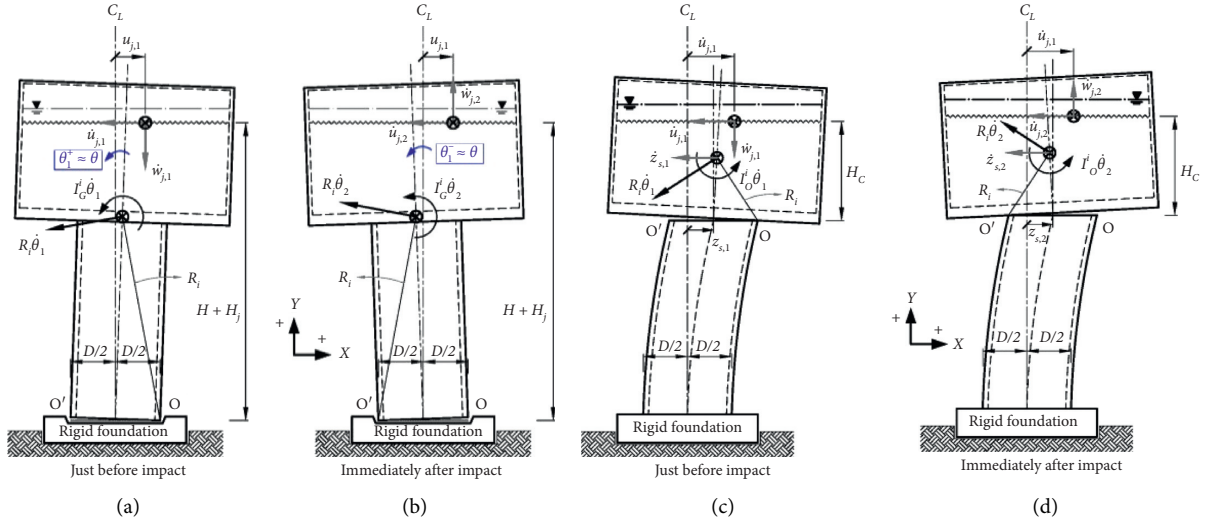


FIGURE 6: Configuration of the rocking elevated tanks with (right) C1 and (left) C2: (a, c) just before and (b, d) immediately after the impact at the left corner (O').

$$\begin{aligned} & (\dot{z}_{s,2} - \dot{z}_{s,1}) \left(\bar{I}_S + \sum_{i=0,r,f} m_i \right) + (-\dot{\theta}_1) \left(\sum_{i=0,r,f} m_i R_i \cos \alpha_i \right) \\ & + \sum_{j=1,C} m_j (\dot{u}_{j,2} - \dot{u}_{j,1}) = 0. \end{aligned} \quad (19)$$

It should be noted that the velocity field of the above components is derived from different displacement fields of the corresponding RI cases. Regarding the 4 DOFs of the system, two more equations are needed to find the post-impact responses. The other two impact conditions are based on this assumption that the relative velocities between the convective and flexibility components and the tank structure do not change before and after an impact. Thus:

$$(\dot{u}_C - \dot{u}_m)_1 = (\dot{u}_C - \dot{u}_m)_2, \quad (20)$$

$$(\dot{x}_1)_1 = (\dot{x}_1)_2. \quad (21)$$

By solving the equations (17)–(21) simultaneously, one can obtain the postimpact responses of the rocking elevated tank. Accordingly, the transition of the motion to other phases is chosen by substituting these responses in equation (7) or (8), which can be the continuation of rocking motion (Section 2.4) or restart of the prelift phase of motion (Section 2.3). It is worth to note that by adopting $m_C = m_1 = 0$ in C2, a set of equations similar to those presented in [6] for a rocking block standing free on a seismically isolated base is derived.

2.6. Validation of the Analytical Model. The analytical approach used in this study basically originates from the approach which was first introduced by Housner [2] and later was developed in other studies, such as Meek [40], Chopra and Yim [4], and Spanos et al. [14]. Although rigorous FEM

models for rocking structures are much more developed in recent years, these models still needed an acceptable benchmark to be compared and validated with. Due to the difficulties and limitations of experimental campaigns [8, 12, 13, 23, 31], this benchmark was usually chosen from well-established analytical problems to test the numerical model in the limit case [10, 16, 17, 31].

Accordingly, although the present work is not completely new, the approach itself was the first step in a validation process. The authors used this approach and also experimental campaigns [33, 39] to validate and improve a previously introduced FEM model [33].

Nevertheless, some verifications were also conducted [39] based on the result of similar analytical problems. For the first case of RI (C1), by removing the convective and flexibility components ($m_C = m_1 = 0$), the results were verified by those presented for a deformable cantilever structure rocking on a rigid surface [10]. Similarly, the analytical model developed for C2 was compared well with that of a rocking block standing free on a seismically isolated base [6].

3. Procedure of the Numerical Solution

Despite some differences between the RI system and its governing equations studied in this paper, the algorithm of the analysis (Figure 7) is basically similar to that of other rocking structures [4, 8, 10]. Nevertheless, there are some modifications. Firstly, the EOMs are integrated numerically using “ode45” solver package of MATLAB [41]. This package is based on an explicit Runge–Kutta (4, 5) formula, namely, the Dormand–Prince pair [42], which is a one-step differential equation solver needing only the solution at the immediately preceding time point. During each phase of the motion, the EOMs are integrated using the initial state value (IVs) of each component, including initial displacement and velocity fields.

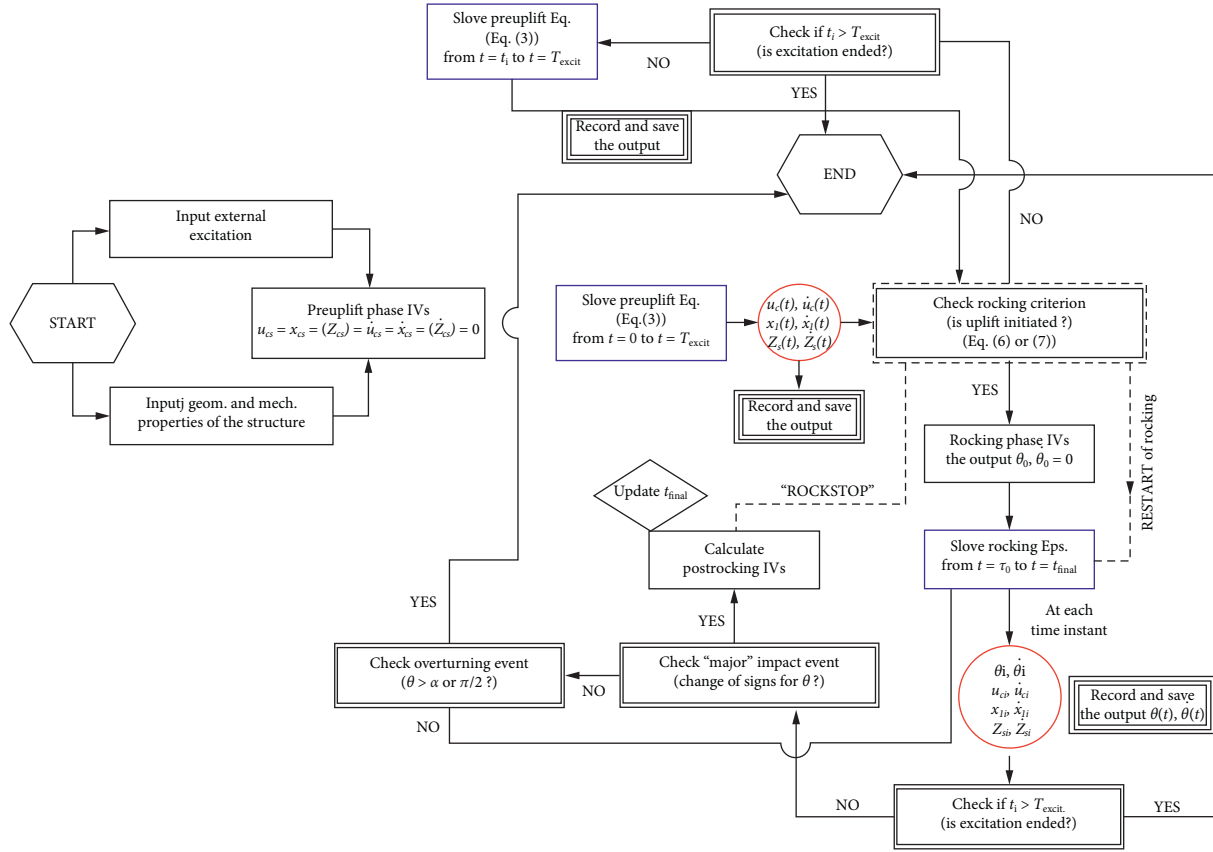


FIGURE 7: Flowchart of the analysis procedure implemented in MATLAB.

To produce solutions with enough accuracy, a local error (ϵ) is estimated at each time step by the solver which must be less than or equal to an acceptable error (ϵ_a) as follows:

$$\epsilon \leq \epsilon_a = \max[\text{RelTol} \times \text{abs}(y(i)), \text{AbsTol}(i)]. \quad (22)$$

In this equation, RelTol is a scale of the error relative to the size of each solution component and roughly controls the number of correct digits in all solution components. Also, AbsTol is a limit quantity below which the value of each component is “unimportant.” This tolerance specifically determines the accuracy when a solution component approaches zero [41], as in the impact events of rocking structures where θ and $\dot{\theta}$ reaches zero.

Accordingly, the aforementioned acceptable error is used to control the time-step size (dt) used in the integration process. This, again, should be carefully controlled during the impact events. On the other hand, since the EOMs in the rocking phase of motion are nonlinear and mathematically “stiff,” the maximum time-step size should be limited so that the solver does not increase the time step too much and step over the impact events or other critical events.

In addition to the above arguments, relative tolerances, absolute tolerances, and the maximum step size used in this study were determined based on a sensitivity analysis of the results. Thus, the relative and absolute tolerances were selected as small as 10⁻¹¹ and 10⁻¹², respectively, which the former corresponds to a same rate of accuracy. Finally, considering the smallest vibration

period of the system components, the maximum time-step was set to 10⁻³.

In addition to the numerical stiffness of the EOMs, the solver configurations described above resulted in time-consuming calculations. Thus, another modification was also adopted. It was observed that over 90% of the time needed for running the analysis procedure of a sample structure is consumed in the rocking phase of motion and for detecting the “major” impact events. The term “major” is described as follows: it is observed that a major impact is followed by a combination of multi serial microimpacts located at very small time intervals and also negligible postimpact response amplitudes (see Section 5.1). Generally, solution of the rocking EOMs is done over the time intervals of t_{uplift} (uplift time instant) to t_{final} , which is the time instant for a major impact. From this instant onward, there is not a significant rocking motion for some time. Thus, if t_{final} is determined, neglecting the effect of other microimpacts, whose calculation is futile and time-consuming, the rocking phase can be stopped sooner and the time needed for running the script reduces significantly. For this purpose, if the time intervals between the microimpact events and their corresponding postimpact responses simultaneously become too small (<10⁻⁸), it is concluded that the rocking phase was terminated by a “major” impact. While these conditions are not verified for most of the analyses on C1, the solution process of which is not very time-consuming, this strategy is more useful for C2. The aforementioned

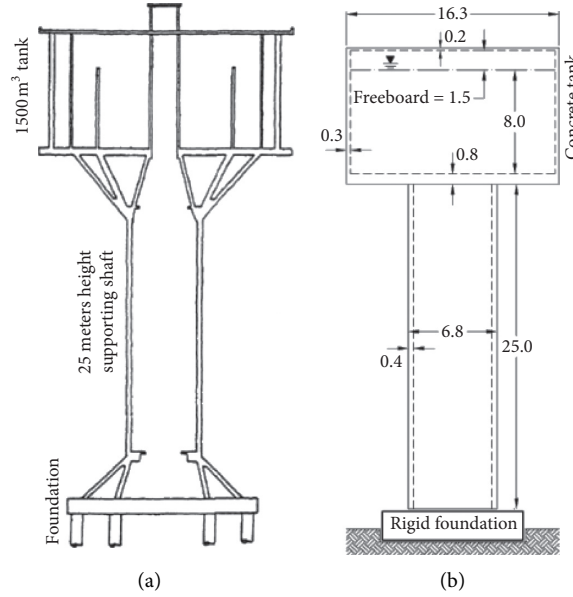


FIGURE 8: (a) Schematic section of water tower No. 1 located in Rasht, north of Iran, which collapsed during Manjil, 1990, earthquake, and (b) dimensions of the simplified concrete model

numerical procedure is implemented in an original MATLAB script, the flowchart of which is illustrated in Figure 7.

4. Description of the Study Group

A study group including 18 structures with various geometrical and structural properties as the “prototypes” is selected in this paper so that the extensibility of the analyses can be verified. The base geometry of the prototypes was selected in accordance with a real structure, namely, water tower No. 1 which was located in Rasht, north of Iran, and collapsed during 1990 Manjil earthquake [43]. A schematic section of this structure is shown in Figure 8(a). Dimensions of the simplified model studied here with a concrete tank is shown in Figure 8(b).

Assuming the basic 25-meter-high shaft as a mid-rise structure, two other heights, 15 (m) for low-rise and 35 (m) for high-rise structures, were also chosen to include the effect of shaft height in the study. Moreover, 3 different tank filling levels (full, half, and empty) are also selected to study the effect of liquid heights on the flexibility and convective components of the response. Both the shaft and the tank of all prototypes are presumed to be symmetric cylindrical shell structures. Finally, assuming (H_L/R) equals 1 and the wall thickness to radius ratio (t/R) equals 0.04 for the concrete tank, characteristics of the equivalent models are calculated per the analytical analogy of Figure 4 and Section 2.2 and given in Table 1.

5. Results Description for a Sample Structure

5.1. Free Vibration Analysis. One of the introduced prototypes with a 25-meters high shaft and a concrete tank in full case (25-1-CONC) is chosen as the sample structure. The normalized free vibration response of this sample structure to a given initial tilt angle of $\theta_0 = 0.0065$ (rad) is

shown for the first and second cases of RI in Figure 9. These results are also compared to those of a “similar” fixed-base structure (with subscript “mFB”) which is analyzed with an initial displacement of $\theta_0 H_S$ assigned at the end of its shaft. Portions of the flexibility response in Figure 9 (blue boxes) which experience high-frequency vibrations are shown separately in zoomed-in views of Figure 10.

It is worth to note that in these analyses, the fixed-base damping ratio of the shaft and the tank wall is taken to be 0.015 while the damping ratio of the convective component is equal to 0.005. These values are proposed mainly for a structure/tank which is assumed to remain elastic during a seismic excitation [10, 44]. Accordingly, the following remarks are drawn:

- (a) Convective response: between every two consecutive impacts, the system components except convective enter a state of motion, i.e., “uplifted state,” which experiences higher frequency elastic vibrations and damping ratio. This is a similar state reported by other researchers for structures with foundation uplift [4] or deformable rocking structures [10]. However, the response of the convective component does not follow this state and frequency decreases in both RI cases. For instance, linearizing equation (15) and omitting the term of base excitation gives

$$\ddot{u}_C + \left(\omega_C^2 - \dot{\theta}^2 \right) (u_C - z_S) + 2\xi_C \omega_C [\dot{u}_C - (\dot{z}_S + H_m \dot{\theta})] = 0. \quad (23)$$

Hence, from equation (23), the uplifted frequency, $\omega_{C,up}$, and uplifted damping ratio, $\xi_{C,up}$, of the convective component are approximately as follows:

TABLE 1: The characteristics of the equivalent simplified liquid-tank system calculated for the sample structures with various filling levels.

System parameters		Analytical values		
		Full case	Half-full case	Empty case
Convective component	m_C (ton)	667.0	513.2	—
	H_{Cb} (m)*	6.2	6.1	—
	K_C (kN/m)	1463.1	866.3	—
Flexibility component	C_C (kN.s/m)	9.9	6.7	—
	m_1 (ton)	1060.0	524.6	—
	H_{1b} (m)*	5.8	5.4	—
Impulsive component	K_1 (kN/m)	5.9×10^7	1.1×10^8	—
	m_0 (ton)	181.3	76.8	358.1+
	I_G^0 (ton.m2)	7.8×10^3	7.9×10^3	1.4×10^4
	H_{0b} (m)*	3.8	3.8	4.75++

*The subscript “b” indicates that the equivalent heights are calculated with the inclusion of the effect of the pressure variation on the tank floor. +Mass of the tank wall. ++C.G. height of the tank wall.

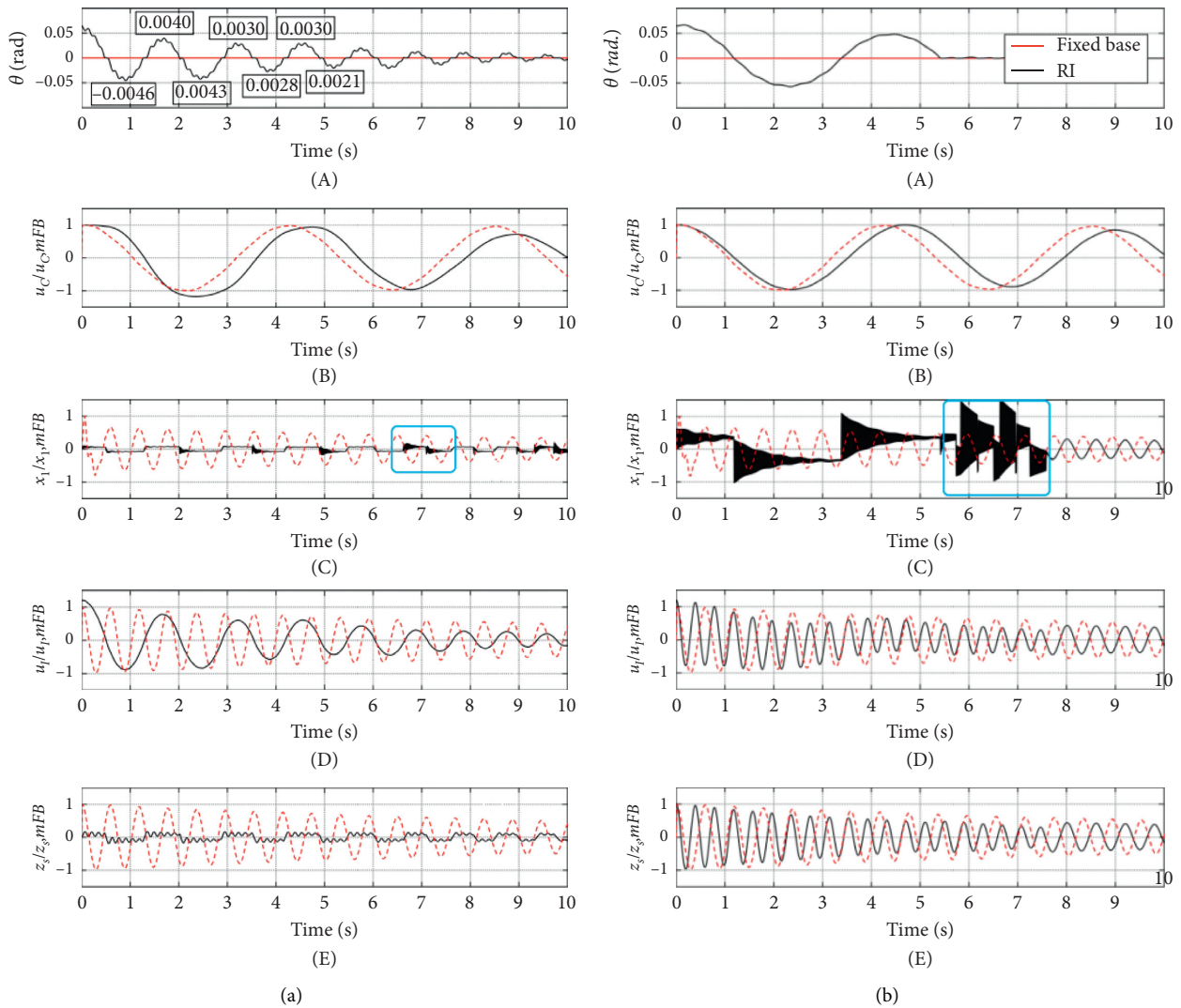


FIGURE 9: Normalized time histories of free (A) rocking, (B) convective, (C) wall flexibility, (D) impulsive, and (E) shaft top end responses for a sample structure with “first case of RI-C1” (a) and “second case of RI-C2” (b) to an initial tilt angle.

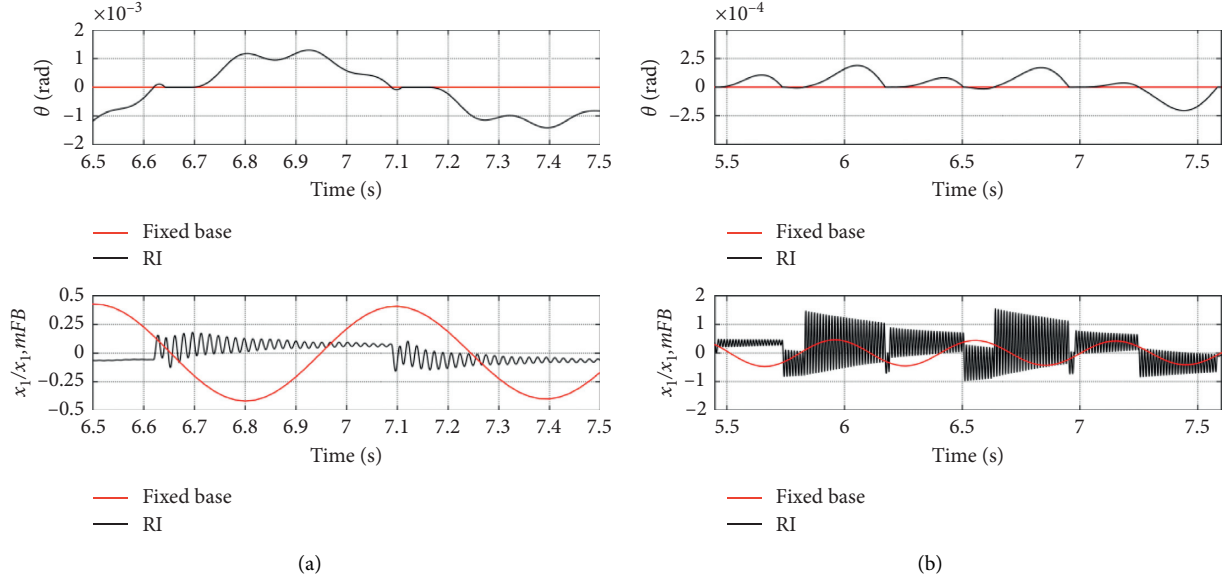


FIGURE 10: Zoomed-in views of the high-frequency vibrations of flexibility components in Figure 9 for the system with C1 (a) and C2 (b).

$$\omega_{C,\text{up}} = \sqrt{\omega_C^2 - \dot{\theta}^2}, \quad (24)$$

$$\xi_{C,\text{up}} \approx \xi_C \left(\frac{\omega_C}{\sqrt{\omega_C^2 - \dot{\theta}^2}} \right), \quad (25)$$

where by increasing $\dot{\theta}$, the uplifted frequency decreases but the damping ratio increases.

- (b) Wall flexibility response: it has been reported experimentally [12] that stiffer structures experience stronger vibrations after each impact. This explains the high-frequency vibrations of the wall flexibility components illustrated in Figure 10. But, from another point of view, wall flexibility component is so stiff ($\omega_{\text{fund}} > 200$) that its motion is constrained with the shaft motion, i.e., moving “in phase” with the shaft and oscillating with a close amplitude ratio of the shaft:

$$\left(\frac{x_1}{x_{1,mFB}} \right) \approx \left(\frac{z_S}{z_{S,mFB}} \right). \quad (26)$$

Hence, even after uplift, oscillation amplitude of the wall flexibility component in the first case of RI (C1) is reduced with almost the same ratio of the shaft. But similar high-frequency vibrations (Figure 10(a)) persist because of its even larger stiffness ($\omega_{1,\text{up}} > \omega_{1,\text{fund}}$). This is not, however, the case for the second case (C2). Applying the RI only to the tank does not reduce the shaft response as that of C1. Thus, the wall flexibility component in C2 is affected more by the impacts and experiences stronger frequency vibrations (Figure 10(b)). This results in even larger deformations than the fixed-base structure.

- (c) Impulsive and shaft responses: the impulsive response in C1, which is also studied as the tank C.G., is dominated by the rocking response of the whole structure and increases up to 12% of that of the fixed-base system. But, in C2, it is a superposition of the shaft and rocking responses with more domination from the shaft. Thus, it does not change notably compared to the fixed-base system.
- (d) Interaction of convective and rocking response: in structures with C1, the interaction of convective response affects the history of rocking response (θ), number of impacts, and the ratio of dissipated energy. For instance, after the second impact at 1.4 (s), while the third peak θ tends to decrease, the convective response acts in the opposite direction, and hence the peak decreases more. In this case, the convective and rocking responses acted “out of phase.” But, the opposite happens after the third impact at 2.1 (s). While it is expected that θ decreases because of the new impact and its energy dissipation mechanism, being the convective component, “in phase” of θ results in a larger absolute peak (0.0043 (rad)) in comparison to the previous peak value (0.0040 (rad)). Although this continues for the rest of the motion, the rocking response keeps decreasing in an irregular pattern (Figure 11(a)) that differs from other structures with RI. Comparison of these results with those of a similar RI system with equivalent mass and geometry but without the “interacting” effect of the convective component is shown in Figure 11(a). As illustrated for the sample structure, existence of the convective component increases the number of impacts and also the amount of dissipated energy over the same time duration (Figure 11(b)). This also shows that the convective component can be proposed as an “additional” energy dissipation

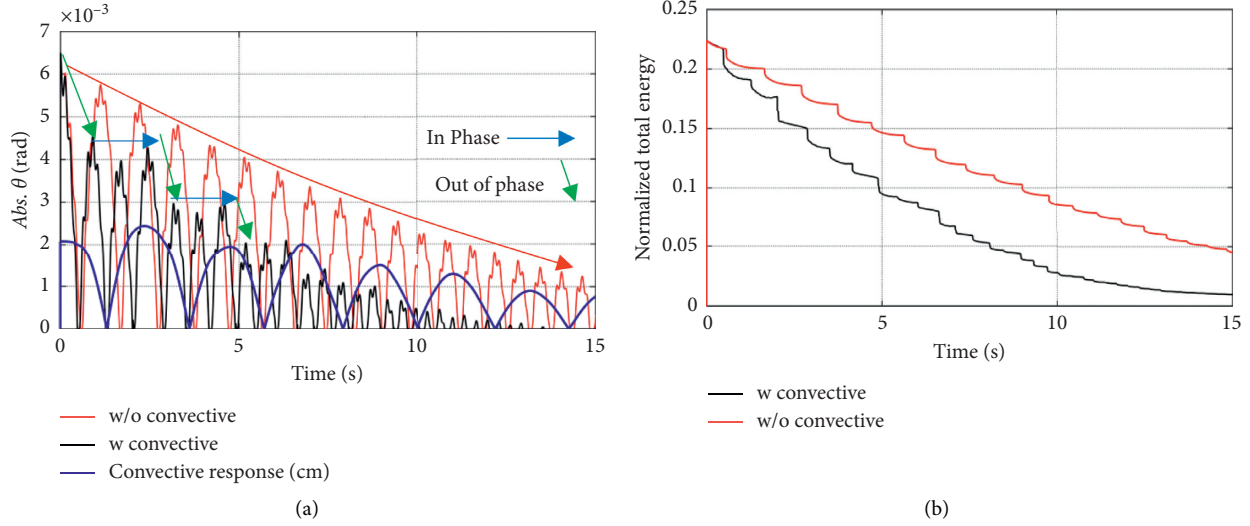


FIGURE 11: Time history of absolute rocking response (b) and normalized total energy (a) of the system with C1: “with” and “without” the convective component.

and damping mechanism in structures with free rocking motion, which are generally considered as systems with very low radiation damping [45, 46], i.e., from the radiated energy on each impact. Thus, the convective component plays a notable role in the dynamic analysis of liquid tanks with RI.

- (e) Energy dissipation in C2: as discussed in [45, 46], squat rocking structures ($H/B \leq 1$) show larger radiation damping. Hence, after the third impact in C2, the rocking response damps out greatly, approximately becoming zero. However, it is then followed by a series of microimpact-uplift transitions as shown in Figure 10 (right top) which is originally a numerical instability issue emerging from the procedure described in Section 3. Nevertheless, this phenomenon has resulted in resonance and high-frequency vibrations of the flexibility component as described in (c).

5.2. Seismic Response History Analysis (SRHA)

5.2.1. Deformation and Rotation-Based Responses. The results of seismic response history analyses of the same sample structure under the action of 1990 Manjil earthquake recorded at Tonekabon station (R#4-PEER RSN 1640 [47]) (Figure 12) are presented in this section. As shown later (Section 6.1), this was a far-field event with a weak vertical component and higher spectral powers in the frequency ranges of 1.2–1.5 (Hz). Namely, the lateral displacement and hydrodynamic pressure demands of the convective (u_C and P_C), flexibility (x_1 and P_1), and impulsive (u_I and P_I) components of the liquid-tank system in addition to the deformation response of the shaft (z_S) are obtained and normalized to the maximum responses of the similar fixed-base structure (mFB). Deformation responses of the sample structure with “first case of RI” (C1-isolation at

the base) and “second case of RI” (C2-isolation under the tank) are, respectively, shown in Figure 13.

As discussed in free vibration analysis (FVA), under the action of 1990 Manjil earthquake, same “uplifted states” are observed. This is specifically the case for the shaft flexural response in C1. Moreover, while the oscillation amplitude of the tank wall decreases up to 40% of the fixed-base system with C1, it increases up to 20% for C2. Similarly, other remarks explained in FVA section hold for the response of other components. It is noteworthy that the seismic rocking motion of C2 is a serial pulse-like motion with rocking responses as low as 0.0004 (rad.) (Figure 13(a)). Firstly, it seems that these finite uplifts make no difference in the seismic response, comparing to a fixed-base tank. But the succession of these finite uplifts simulates an uplifted state which results in lower deformation responses of the tank and shaft (Figures 13(b) (D) and (E)). But, the convective response of the system is not affected by this phenomenon due to small values of $\dot{\theta}$ (equation (24)). Nevertheless, response of the shaft in C2 acts more like the slide-isolated systems [26, 28] with no considerable change in oscillation frequency or phase.

5.2.2. Acceleration-Based Responses. For response assessment of rocking structures, the effect of RI is often studied on the rotational [2–8] or displacement demands [9–11, 16, 48] of the system. However, in liquid storage tanks, acceleration is also a crucial response component for determining force and pressure demands. The lateral hydrodynamic pressure demand P_n induced by each component of the liquid-tank system is calculated by

$$P_n = \ddot{u}_n^{\text{total}} m_n, \quad (27)$$

where m_n is the mass of the corresponding component ($n = C, x, I$) and $\ddot{u}_n^{\text{total}}$ is the “total” acceleration response which is described by

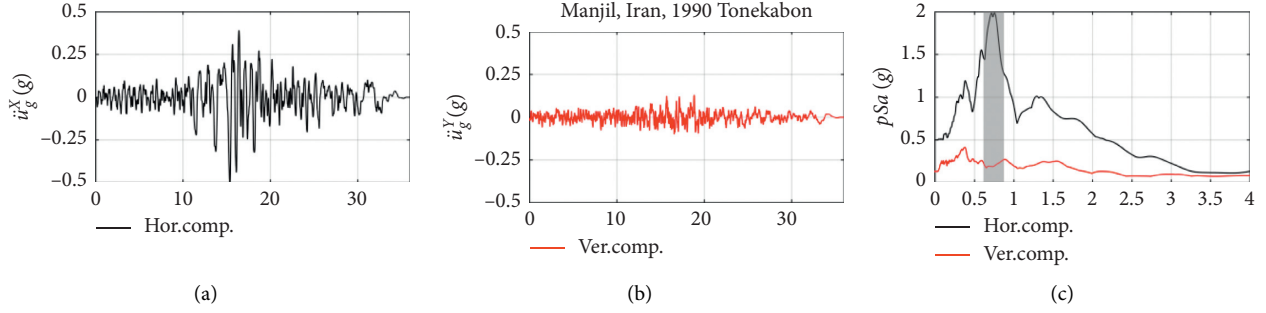


FIGURE 12: 1990 Manjil earthquake recorded at Tonekabon station: (a) horizontal component, (b) vertical component, and (c) the pseudoacceleration spectra where ranges of period with higher horizontal spectral power are shown in grey.

$$\ddot{u}_n^{\text{total}} = R_n \ddot{\theta} \cos \alpha_n + R_n \dot{\theta}^2 \sin \alpha_n + \ddot{z}_n, \quad (28)$$

for various components. Sum of these hydrodynamic forces gives the total shear at the base of the tank wall.

Accordingly, time histories of the normalized hydrodynamic forces acting on the tank wall of this prototype are plotted in Figure 14. As defined by equation (27), it can be shown that the same discussions for deformation responses, such as uplifted states, govern acceleration responses of the system too. Hence, the same changes are observed in acceleration responses and hydrodynamic force histories of the liquid-tank system. However, $\ddot{u}_n^{\text{total}}$ for flexibility and impulsive components is also affected by the sudden changes in the signs and values of angular/translational velocity components ($\dot{\theta}, \dot{z}_n$) due to impact transitions (equations (19)–(21)). The effect of close/serial impacts is the other parameter acting on the acceleration responses; specifically look at response of the structure with C2 (Figure 13(a)) or the beginning part of the response of the one with C1 (Figure 13(a)). The larger are the time intervals between the two consecutive impacts; the structure has more time to damp out the vibrations and to reduce the acceleration responses. Thus, it can be concluded that the first case of RI (C1) generally decreases the acceleration responses of the structure, while C2 holds the opposite. Nevertheless, in neither of the RI cases, the acceleration response of the convective component (\ddot{u}_C^t) is not affected by the impact transitions, as discussed in the next section.

Superposition of all hydrodynamic forces of the liquid-tank system gives the “tank-base” shear force history (V_{Tank}). Impulsive force demands of tank roof and floor are also added to this force. Then, by adding this shear force to the shear force induced by shaft vibrations, total base shear (V_{Total}) (shaft-base) is calculated (Figure 15). As shown, (V_{Tank}) and (V_{Total}) of the structure with RI are reduced more in C1 (10%) than C2 (50%). Moreover, studying (V_{Total}), while the rocking shaft in C1 decreases (V_{Tank}) by almost 4% more, the fixed-base shaft in C2 increases (V_{Tank}) by almost the same amount. It should be noted that although hydrodynamic forces of flexibility and impulsive components in both RI cases are separately larger than those of the fixed-base structure in some timespans (Figure 14), but the components act in the opposite direction of each other during these timespans.

Hence, the summation, i.e., (V_{Tank}), is lower than the fixed-base structure.

5.2.3. Sloshing and Wave Oscillations. Finally, the fluid inside storage tank sloshes during an earthquake event, and thus a freeboard allowance is needed. For this purpose, maximum wave oscillation Δ_{wave} caused by earthquake acceleration and the required freeboard allowance is defined and calculated as the vertical displacement of the fluid surface by

$$\Delta_{\text{wave}} = \left(\frac{D}{2}\right) (A_{\text{tot}}/g), \quad (29)$$

where D is inside diameter of the tank, A_{tot} is the total acceleration of the convective component ($\ddot{u}_C^t = \ddot{u}_C + \ddot{u}_g^x$) of the liquid-tank system, and g is the gravitational acceleration.

Time histories of wave oscillation of the sample structure are normalized to the 1.5 m freeboard provided for the similar fixed-base structure (Figure 8) and shown in Figure 16. As discussed previously (equation (24)), seismic oscillation frequency of the convective component decreases in the system with both RI cases.

Additionally, interacting effect between rocking and convective motions in C1, as discussed in the FVA section, leads to slightly larger convective acceleration response. Thus, larger wave vibrations are obtained. However, the sample structure with C2 does not experience any notable change in acceleration response under the action of 1990 Manjil earthquake (R#4). It is shown in the next section that freeboard requirements of rocking elevated tanks are needed to be revisited.

6. Parametric Analysis of the Response under Multiple Hazards

In previous sections, the analytical abilities of the developed model are exemplified. Hereafter, the objective of the study is to obtain basic information on the applicability of the RI as a seismic response upgrade technique for elevated tanks. Various parameters were included in the analysis based on the various properties of the study group introduced in Section 4.

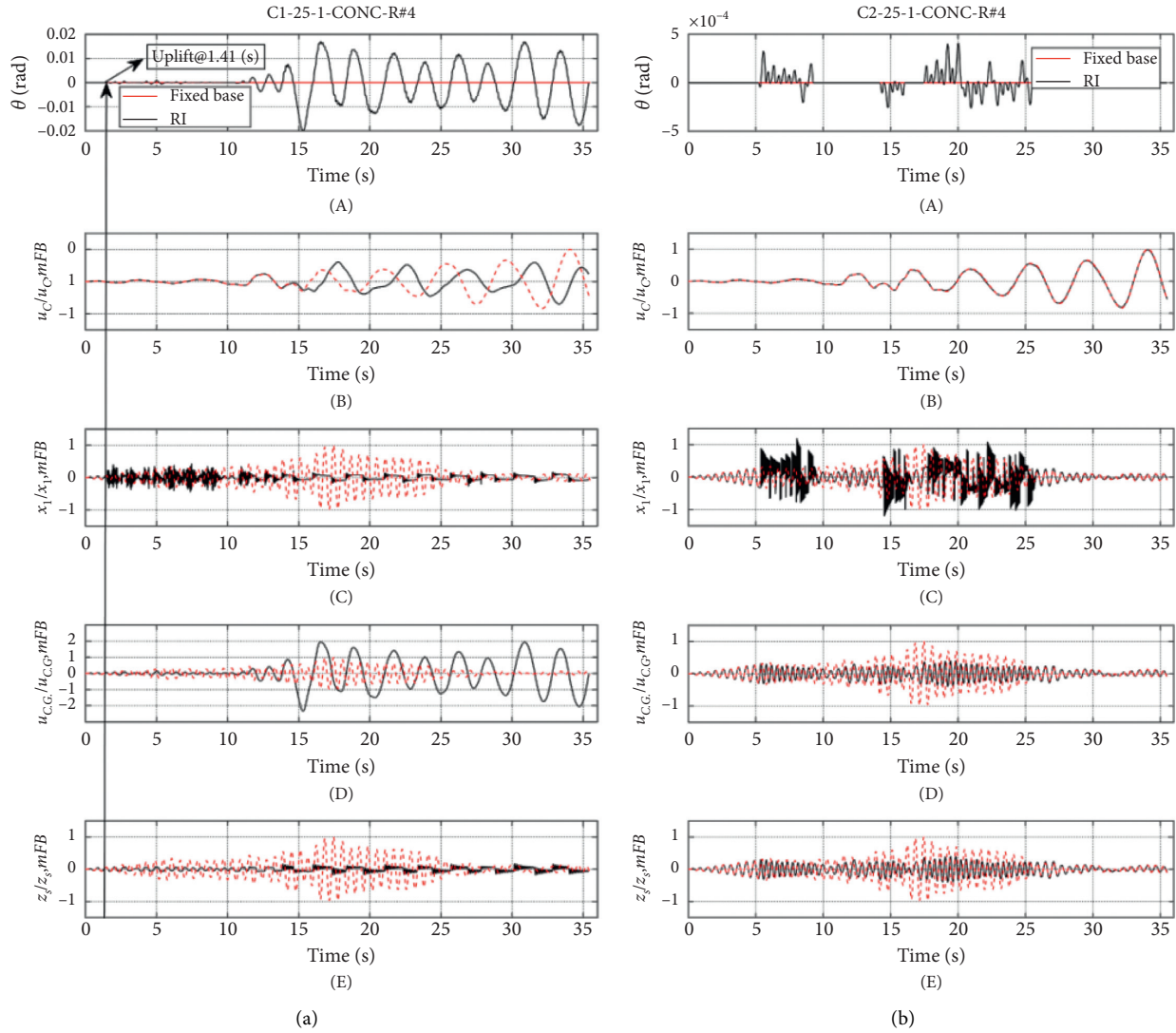


FIGURE 13: Normalized time histories of (A) rocking, (B) convective, (C) flexibility, (D) impulsive, and (E) shaft top end deformation responses for the structure with C1 (a) and with C2 (b).

Additionally, considering that the system with RI may also be vulnerable to other lateral loadings, the effects of wind loads are also studied in this section. The wind loads were assumed to act statically in two combinations: (1) independently before or after the seismic excitation and (2) simultaneously with the seismic excitation. In the latter case, it is assumed that the wind duration was long enough [49] to happen concurrently with the maximum ground accelerations. It is worth to note that in some seismic prone zones, such as the city of Manjil, north of Iran, average wind speed is always so high [50]. Thus, the second combination could be the worst scenario of lateral loads acting on an essential structure such as an elevated water tank.

6.1. Seismic Excitations. The introduced study group (Section 4) was excited by an ensemble of 3 pairs of recorded far-field ground motions with properties shown in Table 2. Each pair includes the horizontal and vertical components of the event (Figure 17). The accelerograms are recorded mostly on firm site

(site class C) and are chosen from the PEER NGA-West 2 database [47]. The records were scaled to the MCER response spectrum of ASCE 7-16 [37] for the high-seismicity zones, i.e., $SD1 = 0.66$ (g) and $SDS = 1.26$ (g).

In free rocking structures such as the system studied here, the oscillation frequencies change with the rocking amplitudes and there are no unique fundamental frequencies. However, as discussed in Section 5.1, the system can be studied over a range of frequencies close to the frequencies of the similar fixed-base system. Thus, the period range for scaling has an upper bound corresponding to the “first convective mode” and a lower bound that corresponds to the first vibration mode of an empty structure, i.e., almost 0.15 (s). The records were scaled such that the average spectrum of all horizontal components does not fall below 90% of the target spectrum for any period within the mentioned range (Figure 17(c)). Accordingly, the spectral properties of the ensemble were chosen so that each pair excites various

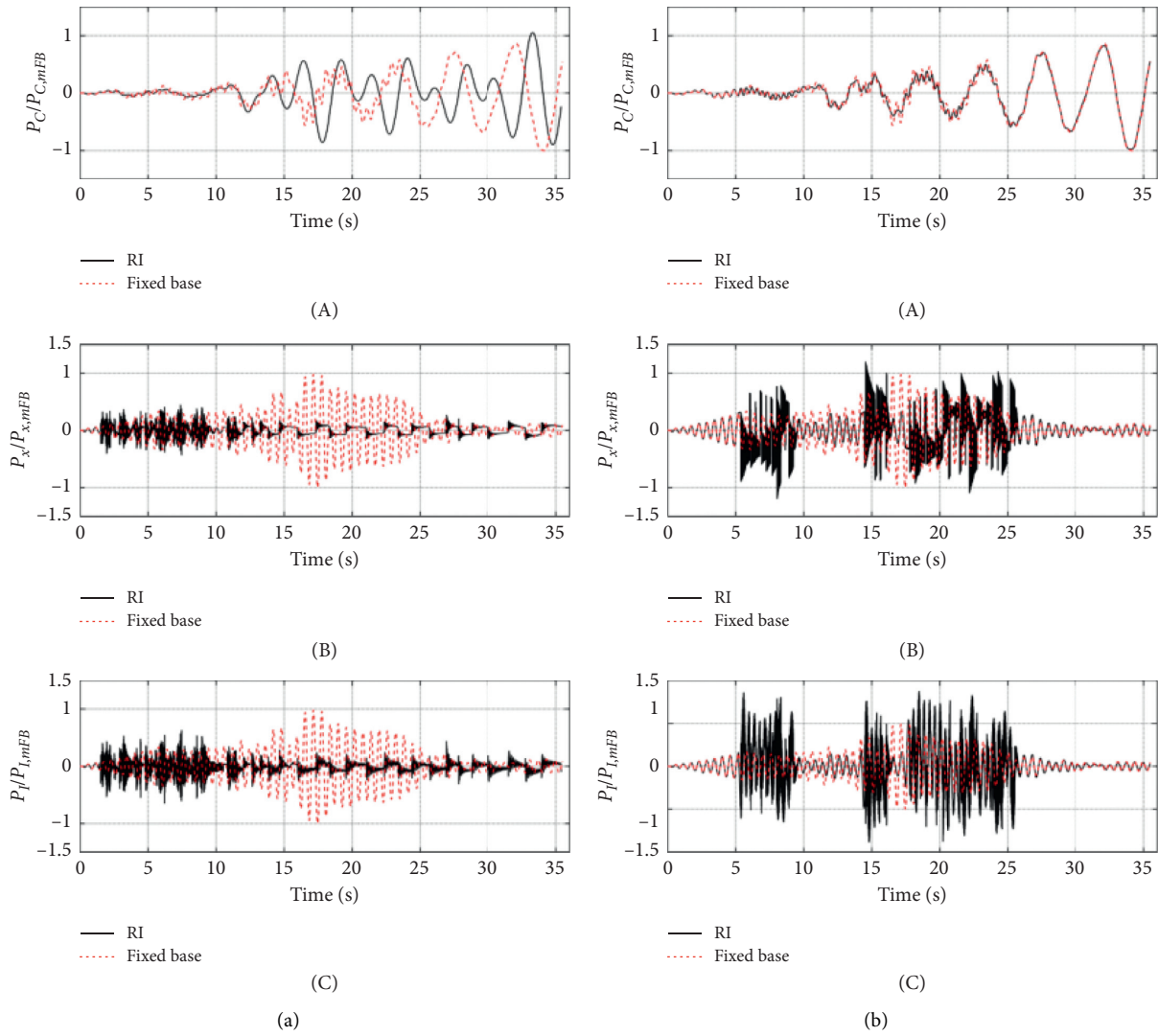


FIGURE 14: Normalized time histories of the distributed hydrodynamic forces induced by (A) convective, (B) flexibility, and (C) impulsive components for the structure with C1 (a) and C2 (b).

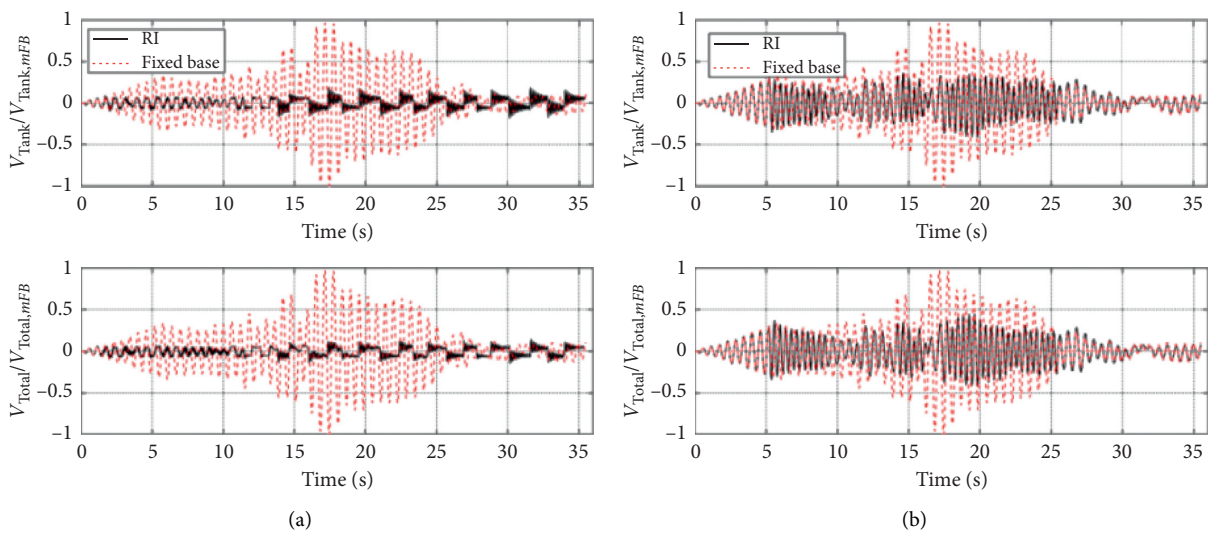


FIGURE 15: Normalized tank-base (V_{Tank}) (top) and shaft-base (V_{Total}) (bottom) shear forces for the sample structure with C1 (a)(left) and C2 (b).

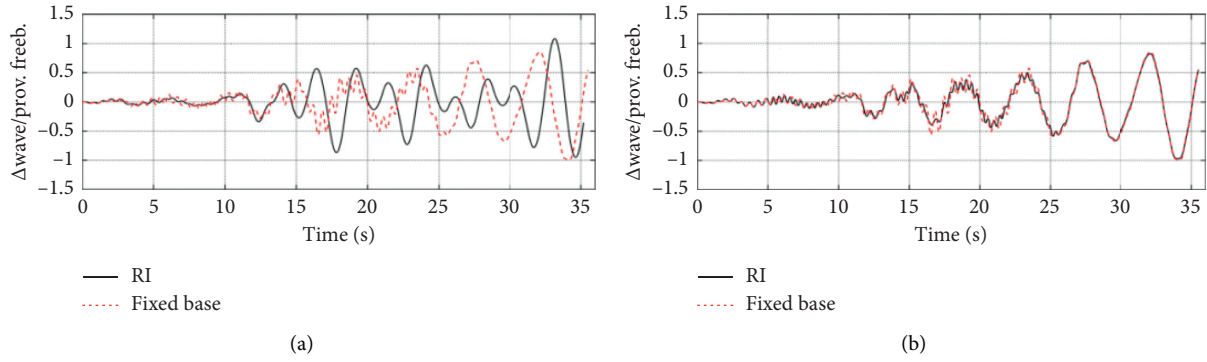


FIGURE 16: Normalized tank-base (top) and shaft-base (bottom) shear forces for the sample structure with C1 (a) and C2 (b).

TABLE 2: Properties of the recorded ground motions used for the seismic response analysis.

No.	Event	Year	Station	PEER RSN	M_W	RDF* (Hz)	VCS**	PGA _{scaled} (g) ***
1	Manjil	1990	Tonekabon	1640	7.4	1.2–1.5	Low	0.53
2	Manjil	1990	Abhar	1634	7.4	0.27–0.32 1.5–4.0	Low	0.43
3	Landers	1992	Yermo Fire Station	900	7.3	0.6–5.0	High	0.61

*Record dominant frequencies: the range of frequencies with higher spectral power. **Vertical component significance: “high” for records with strong vertical component and vice versa. ***PGA of the scaled horizontal component (g).

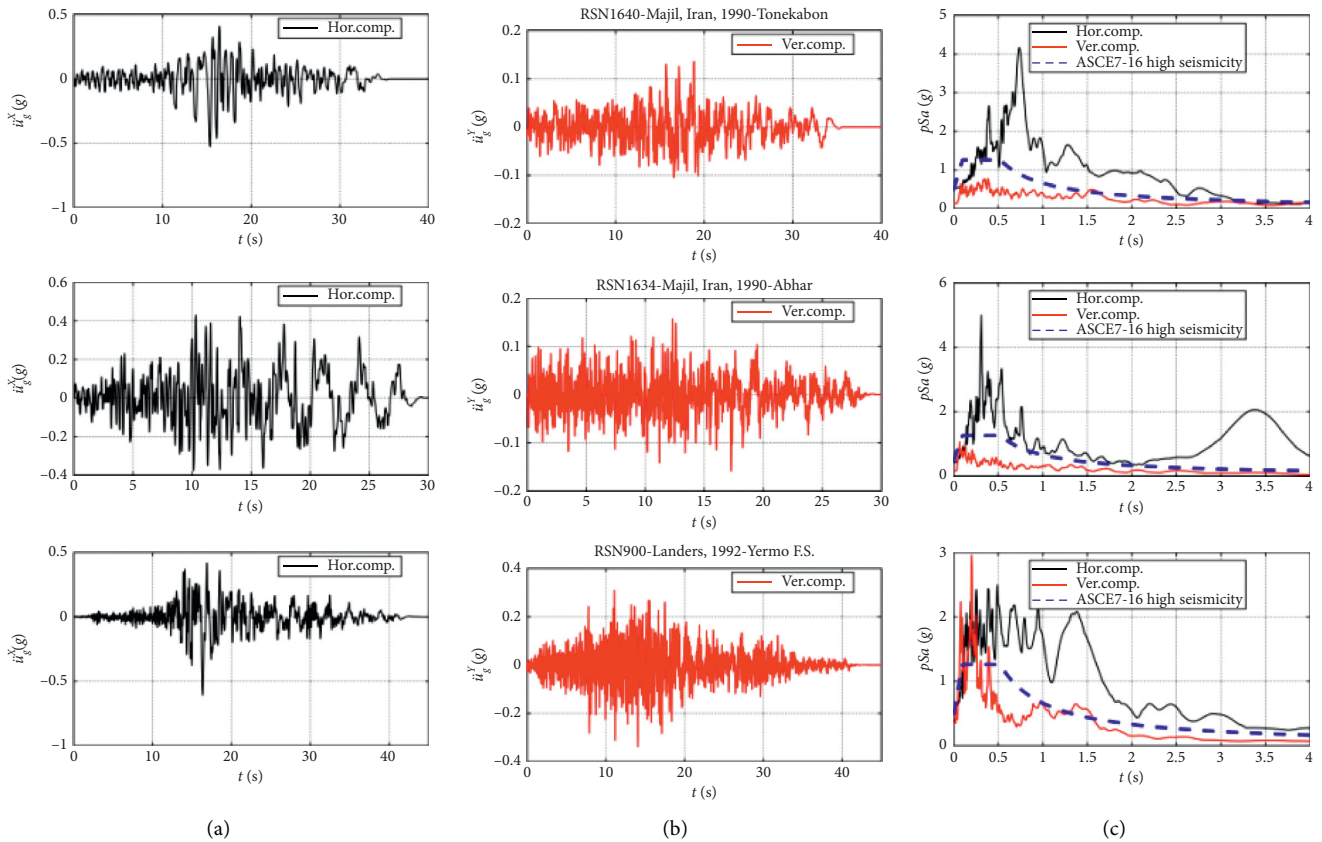


FIGURE 17: Ensemble of the scaled seismic records used as the base excitations: (a) (left) horizontal components, (b) (middle) vertical components and (c) (right) comparison of pseudo-acceleration spectra with the target spectrum.

TABLE 3: Design wind load parameters of the circular shaft and tank.

Risk Category	V (m/s)	Exposure Category	Enclosure Classification	K_d	K_{zt}	K_e	G	K_z ($\alpha = 0.9, z_g = 274$)	C_f
IV	45.0	C	Partially open	1.0	1.0	1.0	0.85 (rigid structure)	$2.01 (4.6/z_g)^{\frac{2}{3}}, z \leq 4.6(m)$ $2.01 (z/z_g)^{\frac{2}{3}}, 4.6 < z < z_g$	0.7

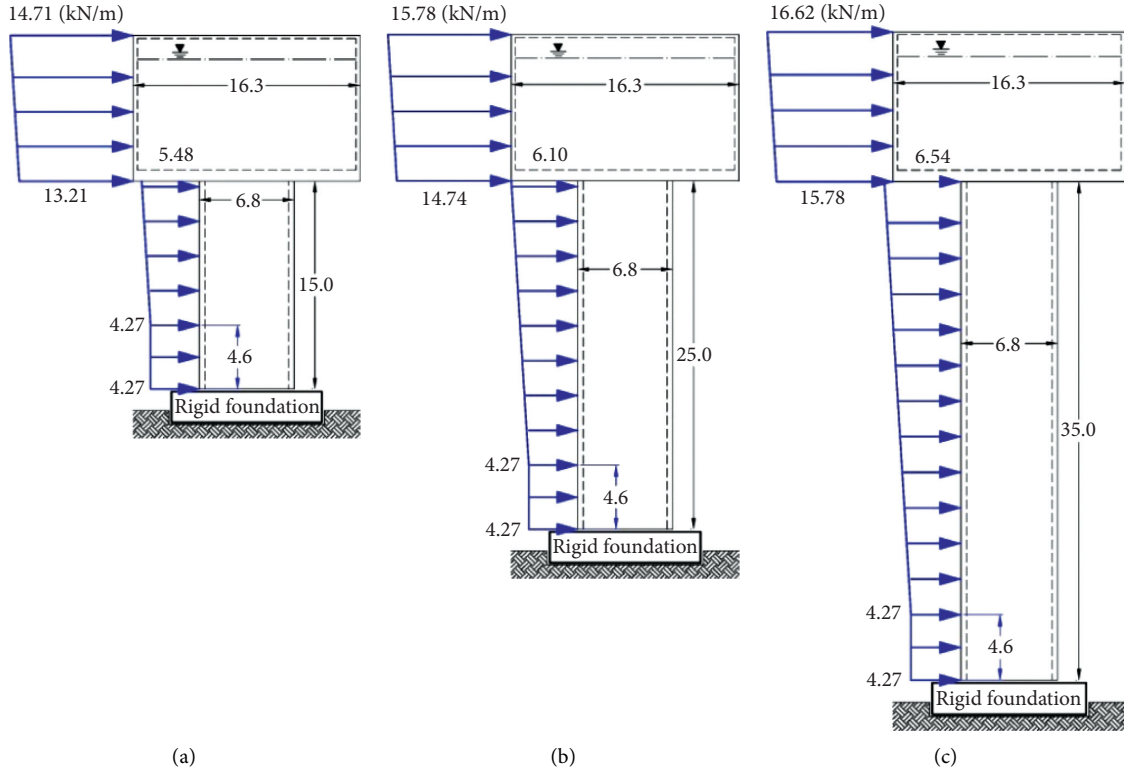


FIGURE 18: Distributions of design wind load in the height of the prototypes (dimensions are in meters). (a) 15-meter-high shaft. (b) 25-meter-high shaft. (c) 35-meter-high shaft.

ranges of frequency. The third pair (RSN900) was specifically chosen to study the effect of vertical component.

6.2. Details of the Wind Load. The wind loads are evaluated based on the requirements of ASCE 7 for Risk Category IV structures [37]. The basic wind speed for determination of the design loads was selected to be 45 (m/s) which corresponds to wind hazard zones with highest gust speed in Iran [51], such as Manjil. Wind load parameters are summarized in Table 3. Distributions of design wind loads in the height of the prototypes are also shown in Figure 18.

6.3. Dimensionless Parameters. Numerous properties of the selected prototype structures and also a high number of dominant parameters make dimensionless response assessment difficult. However, the responses can be normalized to those of a fixed-base structure with similar geometrical and engineering properties. Thus, interpretation of the results and lateral performance upgrade of the

prototypes become more practical. For this purpose, 5 dimensionless parameters (λ_s s for deformation and Π_s s for force/moment responses), each as a ratio of the maximum responses, were defined as follows:

$$\lambda_{\Delta} = \left(\frac{\Delta_{\text{wave,RI}}^{\max}}{\text{Prov.Freeb.for FB}} \right),$$

$$\lambda_{C.G.} = \left(\frac{u_{0,RI}^{\max}}{u_{0,FB}^{\max}} \right),$$

$$\lambda_S = \left(\frac{z_{S,RI}^{\max}}{z_{S,FB}^{\max}} \right), \quad (30)$$

$$\Pi_V = \left(\frac{V_{\text{base,RI}}^{\max}}{V_{\text{base,FB}}^{\max}} \right),$$

$$\Pi_M = \left(\frac{M_{\text{base,RI}}^{\max}}{M_{\text{base,FB}}^{\max}} \right),$$

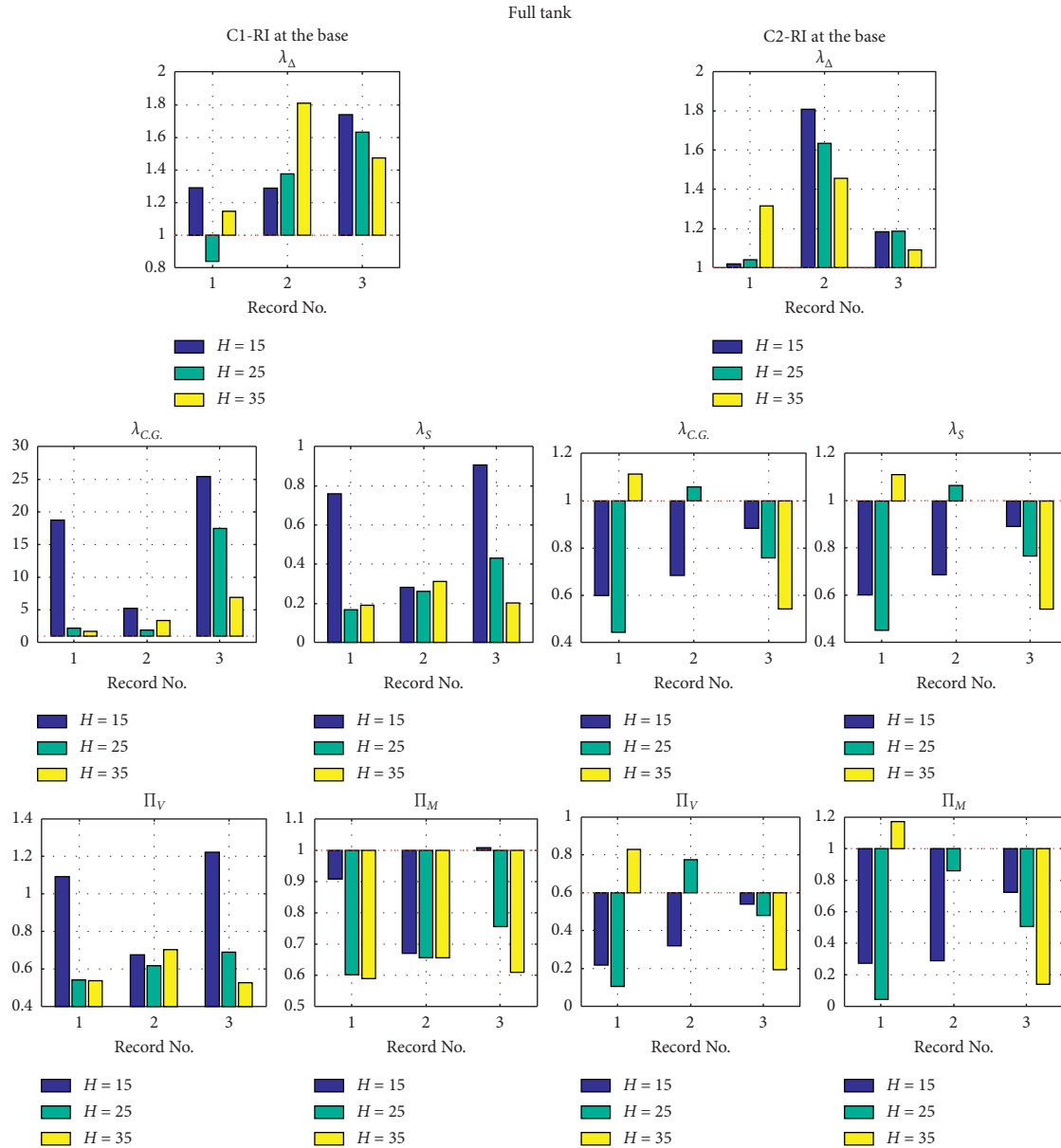


FIGURE 19: Performance of the prototype structures with “full tank” and various “shaft heights” (15, 25, and 35 (m)).

where the parameters with subscript “FB” corresponds to the similar “fixed-base” structure with its provided freeboard assumed to be 1.5 (m). Moreover, u_0 is the horizontal displacement of the impulsive mass (m_0 in Figure 4) which approximately estimates the displacement at the C.G. of the liquid-tank system. It is worth to note that the practical ratios of importance factor to the response modification factor (I/R_u) for the fixed-base elevated storage tanks are almost equal or smaller than 1 [37, 44]. Thus, the aforementioned parameters provided comparable information about design applicability and effectiveness of RI for response mitigation of elevated liquid storage tanks. Using these parameters, “three” main performance categories of the systems were evaluated: (1) operational ($\lambda_{\Delta}, \lambda_{C.G.}$), (2) structural (λ_S), and (3) force performances (Π_V, Π_M).

In the following illustrations (Figures 19–22), the dimensionless parameters were obtained and compared for various RI cases, seismic excitations, shaft heights, and tank filling levels. Accordingly, two load combinations including (1) independent seismic hazard and (2) concurrent seismic and wind hazards ($S + W$), were distinguished in these illustrations. Moreover, the red dashed baseline in some graphs showed the cases that their responses went beyond those of a similar fixed-base structure. Specifically for force/moment responses, this demonstrates the downgrade of the performance.

7. Discussion of the Results and Performances

In this section, the effect of various parameters on the (1) operational, (2) structural, and (3) force performances of the proposed RI systems is discussed.

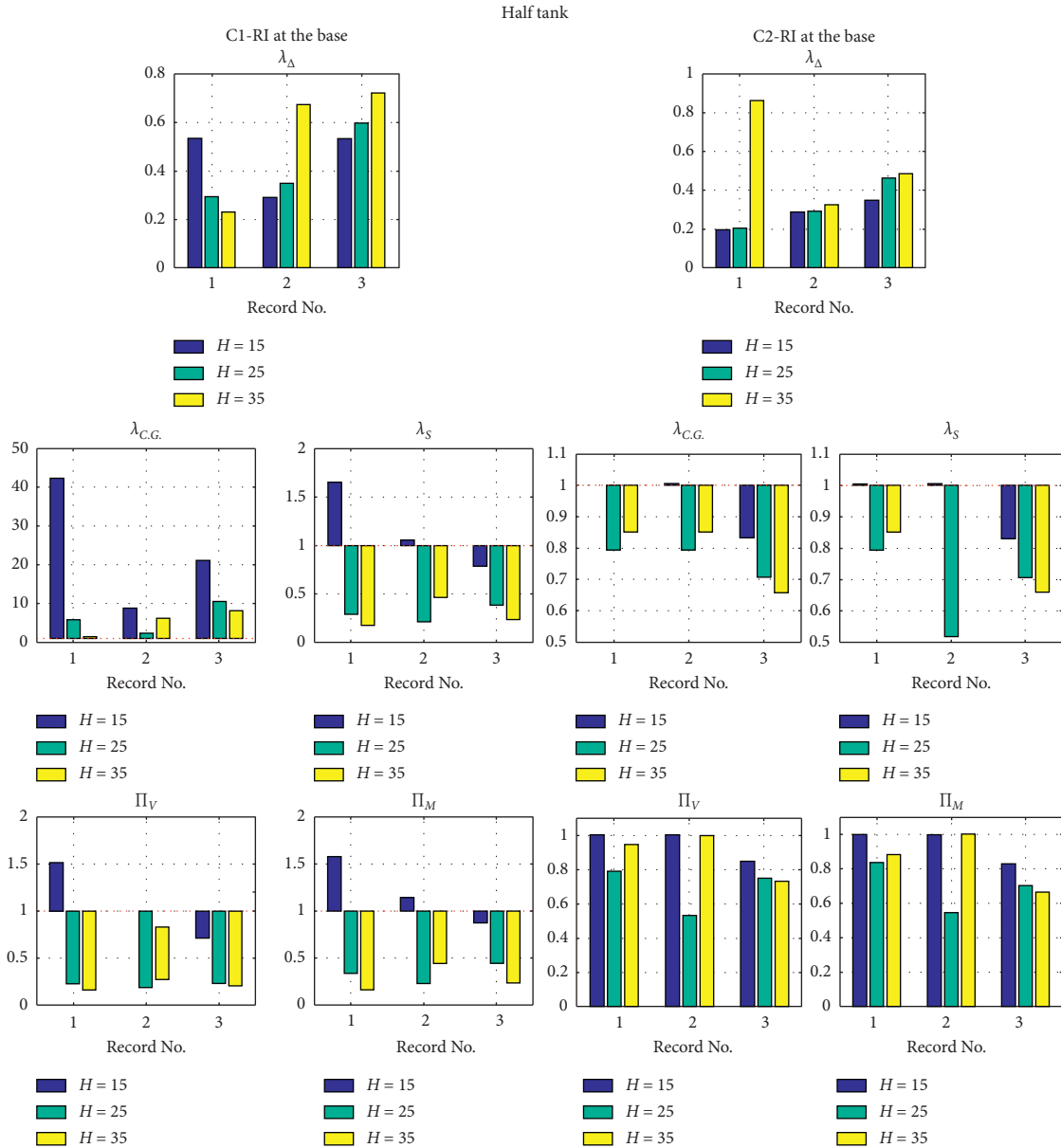


FIGURE 20: Performance of the prototype structures with “half tank” and various “shaft heights” (15, 25, and 35 (m)).

7.1. The Effect of RI Cases

- (1) The convective response and wave oscillations, as main “operational” components, are directly affected by RI. The wave oscillations are increased by both large rocking responses (θ) and also amplified convective accelerations (\ddot{u}_C) at the level of the tank. The other operational component is the tank C.G. displacement (u_0) which is mainly affected by rocking response of the whole system.

As discussed in Section 5, the first RI case (C1: RI at the base) developed larger rocking responses (?) than C2. Thus, the prototypes with C1 experienced larger C.G. displacements than those with C2 (Figure 19, 20, 22 (middle), and 21 (top)). Under the action of

the considered ensemble of the seismic motion, the prototypes with C2 showed almost no advantage over the fixed-base structures. Nevertheless, the prototypes with C1 underwent responses 10 to 50 times larger than those of the fixed-base structures. This corresponded to rocking responses about 0.1 (rad), which was also in a safe margin of overturning, i.e., $\theta_{cr} \approx 0.2$ (Figure 22).

Unlike the C.G. displacements, the convective performances and freeboard allowances were downgraded in both RI cases. Although highly affected by the properties of the seismic excitation, the prototypes with C2 which were more stiff than C1 oscillated with higher frequencies (Figure 8(b)) and thus developed larger accelerations. This

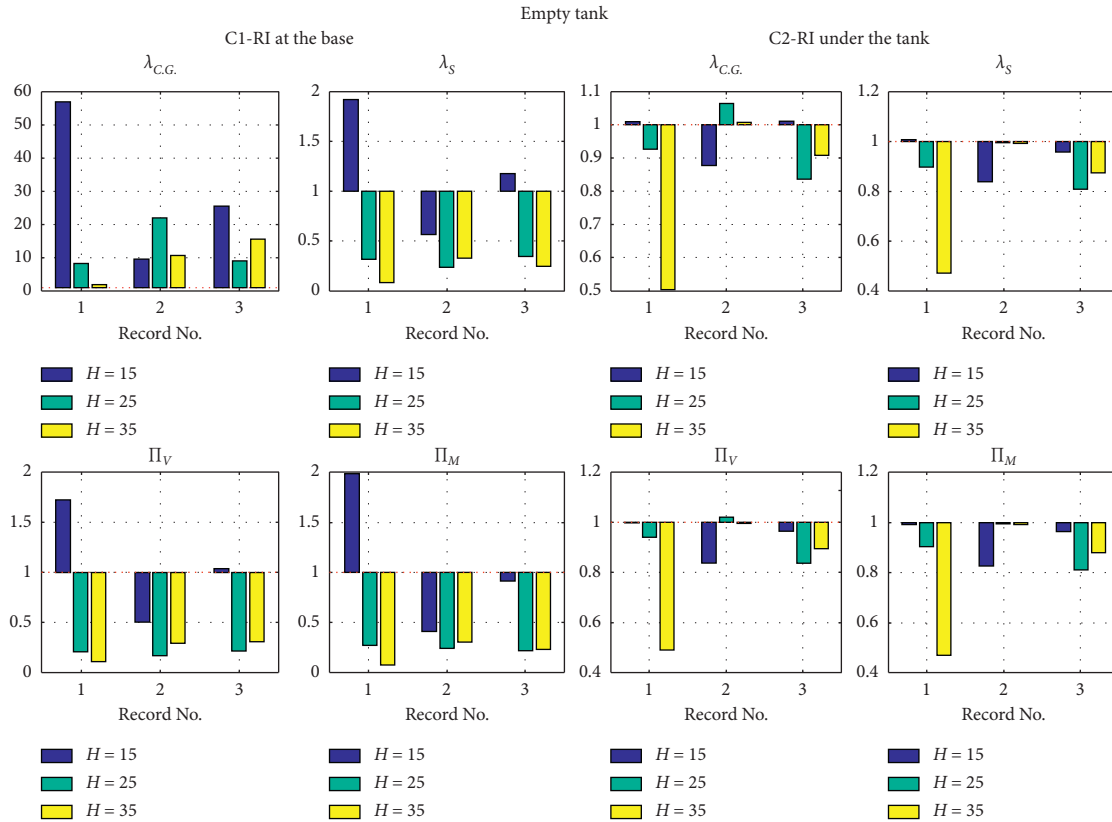


FIGURE 21: Performance of the prototype structures with “empty tank” and various “shaft heights” (15, 25, and 35 (m)).

resulted in larger wave oscillations (equation (29)). However, in the case of prototypes with C1, wave oscillations were mainly caused by larger rocking responses, rather than amplified accelerations. This phenomenon was also observed in similar rocking structures [10].

- (2) “Structural” performances which were described by the shaft response followed the similar pattern of the C.G. displacements. Under the action of the considered ensemble of the seismic motion, the structural performance of C2 prototypes showed almost no advantage over the fixed-base structures ($0.8 < \lambda_S < 1.1$). Similarly, short C1 prototypes (C1-15) experienced such strong impacts and high-frequency oscillations that the displacements became larger than those of the corresponding fixed-base structure ($\lambda_S \approx 1.8$). However, the structural performance of the mid-rise and tall C1 prototypes (C1-25 and C1-35) were upgraded to at least 50%, i.e., decreasing the deformation demands of the shaft to half of the corresponding fixed-base structure ($\lambda_S \leq 0.5$). Thus, the best structural performances were expected from slender prototypes equipped with C1.
- (3) As shown in the bottom row of Figures 19–22, the “force” performances followed the similar patterns of the C.G. and shaft displacements. Thus, the force performance ratios were almost equal to those of the structural performances.

7.2. The Effect of Seismic Base Excitations. The effect of earthquake records on the performance of prototype structures was implicitly discussed in previous section. It was shown that the records with predominant ranges of frequencies (or periods) close to the components of the liquid-tank system or the shaft imposed higher demands on these components.

- (1) As shown in Figure 17, record no. 2 had higher spectral power around the frequency of the convective component. Thus, it developed larger accelerations and convective responses for stiff prototypes. However, for flexible prototypes, such as those with C1, large convective responses were also developed under the action of record no. 3. This record pair covered a wider range of frequencies and also a stronger vertical component (higher VCS). Thus, it produced larger rocking responses. Same patterns were also observed for C.G. displacements and performances. It was concluded that the operational performances could be more downgraded under the action of the records with wider ranges of dominant frequencies.
- (2) The structural performances of the mid-rise and tall C1 prototypes (C1-25 and C1-35), with the highest upgrade ratios, were not affected by the properties of the seismic records. However, the performances of other prototypes were affected by the records predominant ranges of frequencies. For instance, the response of the short C1 prototypes (C1-15) was more affected by record no. 1.

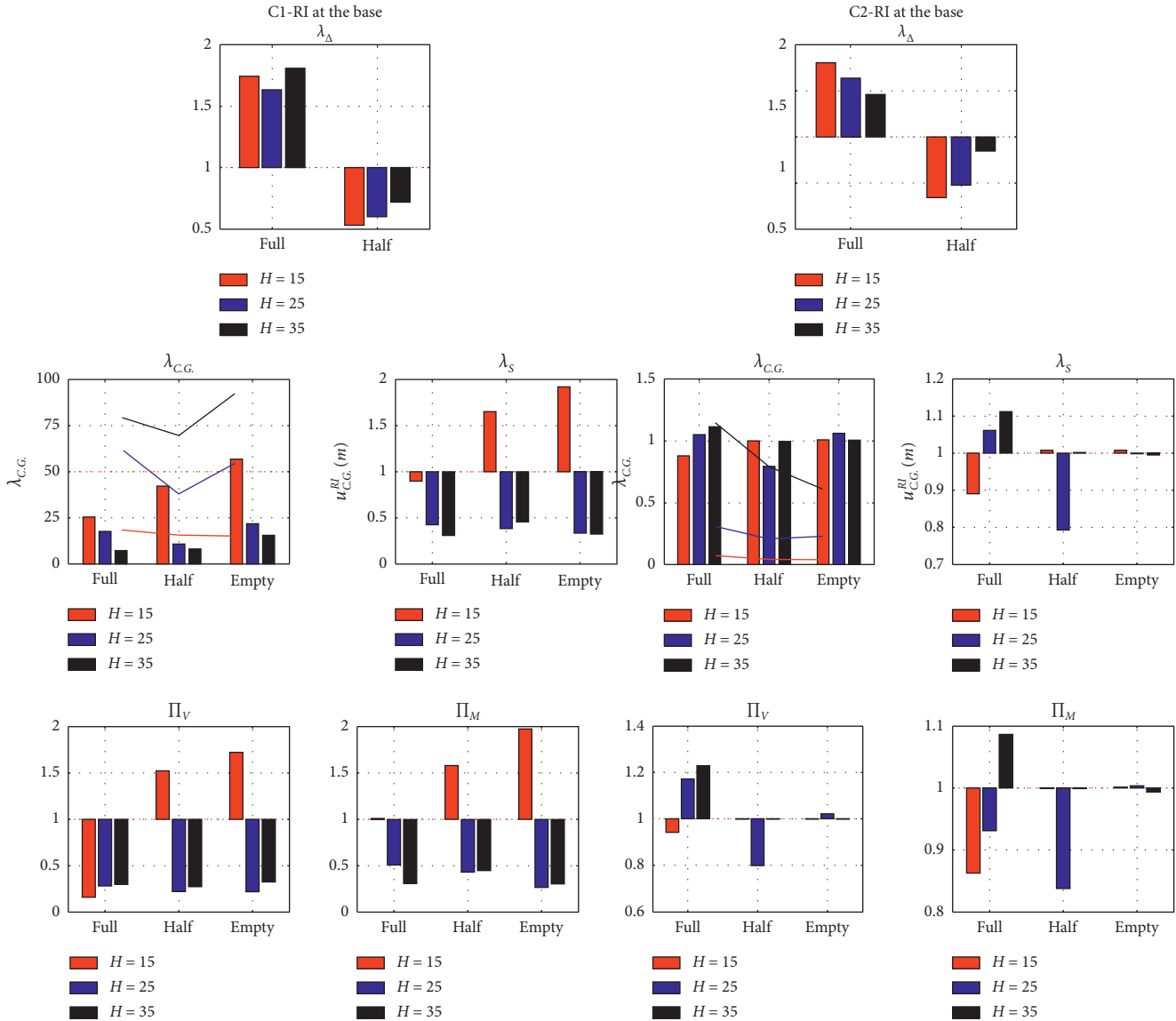


FIGURE 22: Maximum performance parameters of the prototypes with various “tank filling levels” (full, half, and empty) and “shaft heights” (15, 25, and 35 (m)).

- (3) As shown in the bottom row of Figures 19–21, the “force” performances followed the similar patterns of the structural performances and C.G. displacements.

7.3. The Effect of Shaft Heights

- (1) As shown in Figures 19–22, various shaft heights had almost no effect on the operational performances. However, the short prototypes with C1 experienced larger C.G. displacements than the corresponding fixed-base structures. This, as described before, was a result of high-frequency oscillations and stronger impacts which is experienced by stiff rocking structures.
- (2) The shaft height had almost no effect on the operational performances of the C2 prototypes. However, as discussed before, due to higher stiffness, short C1 prototypes (C1-15) underwent larger shaft

displacements than the mid-rise or tall prototypes. The latter demonstrated almost similar performances.

- (3) As shown in the bottom row of Figures 19–22, the “force” performances followed the similar patterns of the structural performances and C.G. displacements.

7.4. The Effect of Tank Filling Levels

- (1) Various tank fillings levels, as shown in Figure 22, had almost no effect on the operational performances of full tanks. Nevertheless, the prototypes with half tanks experienced lower wave oscillations than those of the corresponding fixed-base structures ($\lambda_{\Delta} < 1.0$). However, the freeboard allowances must be evaluated based on the results of the full-tank prototypes, which are 1.5–2 times of the required freeboard of the fixed-

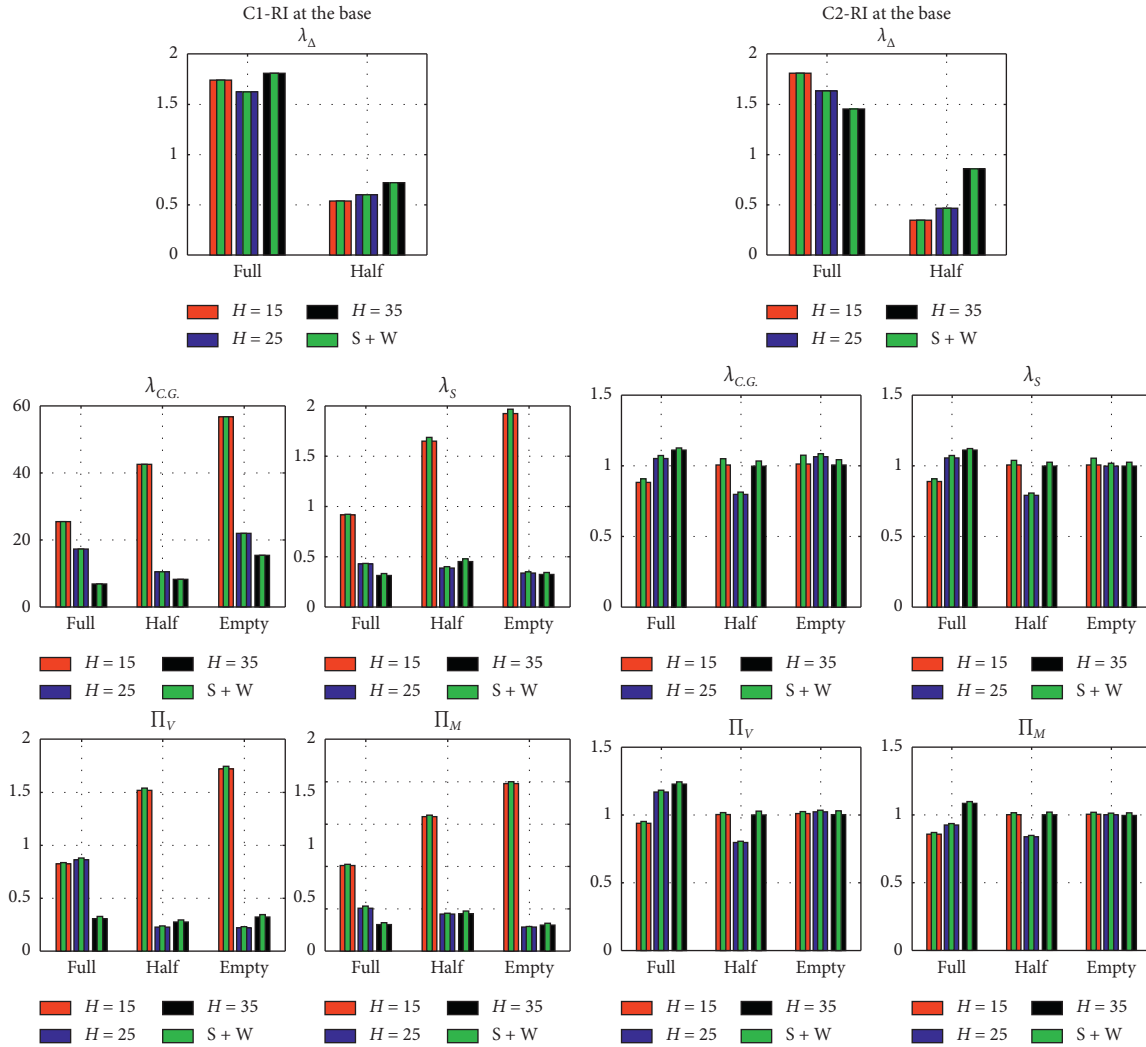


FIGURE 23: Maximum performance parameters of the prototypes under various lateral load combinations (green bars: seismic + wind).

base structures. It is noteworthy that, as shown in Figure 22 (middle), the full and empty tanks developed almost similar C.G. displacements. Thus, unlike the fixed-base structures, the empty structures should also be considered as a critical design case.

- (2) Similarly, various tank fillings had almost no effect on the structural performances of C1 prototypes. However, half and empty short structures (C1-15) experienced larger shaft displacements. The C2 prototypes with half and empty tanks were also not affected by RI.

7.5. The Effect of Combined Seismic and Wind Hazards.

The concurrent effect of seismic and wind hazards on the maximum responses of the prototypes is summarized in Figure 23. Moreover, Figure 24 shows the maximum difference ratios of various parameters which were produced under combined loadings. Since the wind loading, as described in Section 6.2, was assumed to act statically, no changes were applied to dynamic responses of system, such as the acceleration. Only the static deformation and displacement of the tank and shaft were superposed with the

responses of the seismic loading. Moreover, due to higher stiffness of the tank structure in comparison to the supporting shaft, the tank deformations under wind were also smaller than those of the shaft.

- (1) Accordingly, the convective responses and maximum wave oscillations under concurrent seismic and wind loadings (S+W) were not modified in comparison to the seismic-only responses. As shown in Figure 24, the maximum ratio of the convective responses was less than 1%, which was produced due to the increased rotation of the liquid-tank system under wind loading.

Similar pattern was observed for the C.G. displacements of the prototypes with C1. Since the tank in C1 is constrained to the shaft, wind loading did not increase C.G. displacement any more. However, considering that the tank is free to rotate in C2, larger rotations than those of the C1 were observed. Thus, the C.G. displacements of C2 prototypes were increased up to 7% under combined loadings.

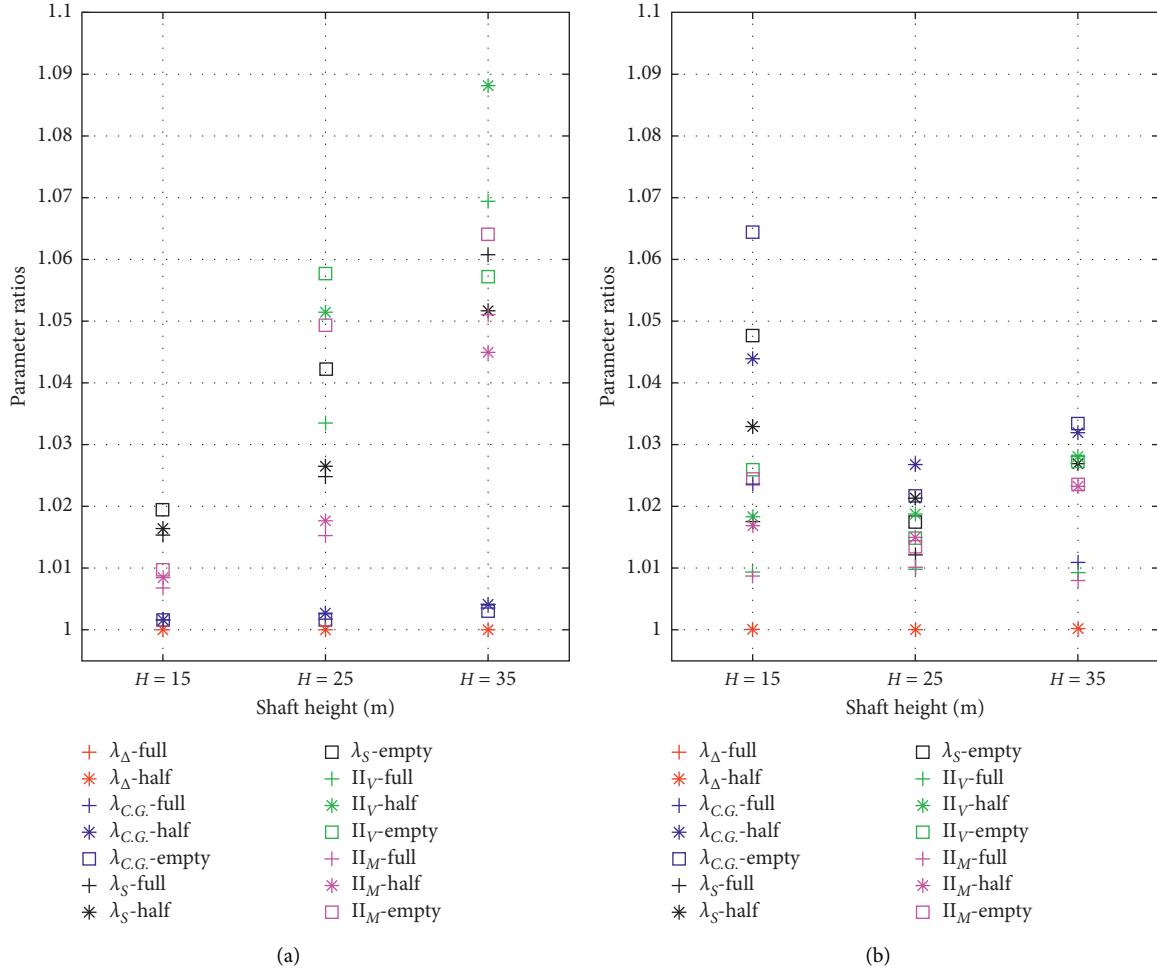


FIGURE 24: Maximum ratios of various response parameters under the assumed lateral load combinations (seismic + wind/seismic). (a) C1 RI at the base. (b) C2 RI under the tank.

- Following a similar pattern, the shaft displacements and structural performance of the C1 prototypes were increased up to 7% under combined loadings. This ratio was about 5% for C2 prototypes.
- Considering that the main part of the wind load is acting on the shaft, force performances of C2 prototypes were modified less than 3% under combined loadings. However, for tall structures with C1, the base shear ratio was about 10%, the largest ratio under combined loadings.

8. Conclusions

This paper addressed response mitigation of elevated liquid storage tanks equipped with RI using a developed analytical model. Two different positions of isolation were assumed. The study was carried out for a study group geometrically similar to a real structure, but with various shaft heights, tank materials, and filling levels. Additionally, considering that the system with RI may also be vulnerable to other lateral loadings, the combined effects of seismic and wind loads were also studied in this paper. An unprecedented interacting effect of the convective component and rocking

motion was noted for this system which also provided an additional source of energy dissipation. Unlike the other components, frequency decrease was observed for the convective component. This showed that the convective component plays a critical role in seismic analysis of these structures. The effect of RI was then studied on the acceleration response of the system, directly affecting the hydrodynamic pressure, base shear, and base moment demands. Parametric studies showed that the first case of RI (C1) decreases the acceleration demands of slender structures, while C2 had almost no effect on the response. As a result, one could obtain more economic designs for the shaft and foundation of the slender system with C1. Moreover, various shaft heights and tank filling levels had almost no effect on the operational and structural performances. Finally, while the combined seismic and wind hazards had almost no effect on the operational performances, the force performances of the C1 prototypes were increased up to 10%.

It was also shown that earthquake records with strong vertical components aggravate performance of the structures with C1. Additionally, the performance of various components is more intensified by the records with wider ranges of

predominant frequencies. Nevertheless, probabilistic analyses with a higher number of seismic excitations might be needed for a better understanding of the effect of various properties of the earthquake excitations. Finally, some of the short prototypes with half or empty tanks and C1 isolation case undergo such large rocking responses that application of additional restoring systems, such as vertical restrainers, might become a necessity. However, this is the goal of future studies.

Data Availability

The data used to support the findings of this study including the MATLAB script developed for the dynamic analysis are available from the corresponding author upon request.

Conflicts of Interest

The authors declare that there are no conflicts of interest regarding the publication of this paper.

References

- [1] Canterbury Earthquakes Royal Commission, "Low-damage building technologies," vol. 3, Canterbury Earthquakes Royal Commission, Christchurch, New Zealand, 2012, Final report.
- [2] G. W. Housner, "The behavior of inverted pendulum structures during earthquakes," *Bulletin of the Seismological Society of America*, vol. 53, no. 2, pp. 403–417, 1963.
- [3] N. Makris, "A half-century of rocking isolation," *Earthquakes and Structures*, vol. 7, no. 6, pp. 1187–1221, 2014.
- [4] A. K. Chopra and S. C. S. Yim, "Simplified earthquake analysis of structures with foundation uplift," *Journal of Structural Engineering*, vol. 111, no. 4, pp. 906–930, 1985.
- [5] Q. T. M. Ma, *The Mechanics of Rocking Structures Subjected to Ground Motion*, Ph.D. Dissertation, Department of Civil and Environmental Engineering, University of Auckland, Auckland, New Zealand, 2010.
- [6] M. F. Vassiliou and N. Makris, "Analysis of the rocking response of rigid blocks standing free on a seismically isolated base," *Earthquake Engineering & Structural Dynamics*, vol. 41, no. 2, pp. 177–196, 2012.
- [7] L. Collini, R. Garziera, K. Riabova, M. Munitsyna, and A. Tasora, "Oscillations control of rocking-block-type buildings by the addition of a tuned pendulum," *Shock and Vibration*, vol. 2016, Article ID 8570538, 11 pages, 2016.
- [8] J. A. Bachmann, M. Strand, M. F. Vassiliou, M. Broccardo, and B. Stojadinović, "Is rocking motion predictable?" *Earthquake Engineering & Structural Dynamics*, vol. 47, no. 2, pp. 535–552, 2018.
- [9] S. Acikgoz and M. J. DeJong, "The interaction of elasticity and rocking in flexible structures allowed to uplift," *Earthquake Engineering and Structural Dynamics*, vol. 41, no. 15, pp. 2177–2194, 2012.
- [10] M. F. Vassiliou, R. Truniger, and B. Stojadinović, "An analytical model of a deformable cantilever structure rocking on a rigid surface: development and verification," *Earthquake Engineering & Structural Dynamics*, vol. 44, no. 15, pp. 2775–2794, 2015.
- [11] A. Agalianos, A. Psychari, M. F. Vassiliou, B. Stojadinovic, and I. Anastasopoulos, "Comparative assessment of two rocking isolation techniques for a motorway overpass bridge," *Frontiers in Built Environment*, vol. 3, p. 47, 2017.
- [12] R. Truniger, M. F. Vassiliou, and B. Stojadinović, "An analytical model of a deformable cantilever structure rocking on a rigid surface: experimental validation," *Earthquake Engineering & Structural Dynamics*, vol. 44, no. 15, pp. 2795–2815, 2015.
- [13] S. Acikgoz, Q. Ma, A. Palermo, and M. J. DeJong, "Experimental identification of the dynamic characteristics of a flexible rocking structure," *Journal of Earthquake Engineering*, vol. 20, no. 8, pp. 1199–1221, 2016.
- [14] P. D. Spanos, P. C. Roussis, and N. P. A. Politis, "Dynamic analysis of stacked rigid blocks," *Soil Dynamics and Earthquake Engineering*, vol. 21, no. 7, pp. 559–578, 2001.
- [15] V. Drosos and I. Anastasopoulos, "Shaking table testing of multidrum columns and portals," *Earthquake Engineering & Structural Dynamics*, vol. 43, no. 11, pp. 1703–1723, 2014.
- [16] J. A. Bachmann, M. F. Vassiliou, and B. Stojadinović, "Dynamics of rocking podium structures," *Earthquake Engineering & Structural Dynamics*, vol. 46, no. 14, pp. 2499–2517, 2017.
- [17] G. Simoneschi, A. M. de Leo, and A. Di Egidio, "Effectiveness of oscillating mass damper system in the protection of rigid blocks under impulsive excitation," *Engineering Structures*, vol. 137, pp. 285–295, 2017.
- [18] R. D. Sharpe and R. I. Skinner, "The seismic design of an industrial chimney with rocking base," *Bulletin of the New Zealand National Society for Earthquake Engineering*, vol. 16, no. 2, pp. 98–106, 1983.
- [19] J. L. Beck and R. I. Skinner, "The seismic response of a reinforced concrete bridge pier designed to step," *Earthquake Engineering & Structural Dynamics*, vol. 2, no. 4, pp. 343–358, 1973.
- [20] A. Di Egidio, D. Zulli, and A. Contento, "Comparison between the seismic response of 2D and 3D models of rigid blocks," *Earthquake Engineering and Engineering Vibration*, vol. 13, no. 1, pp. 151–162, 2014.
- [21] M. A. Haroun and H. M. Ellaithy, "Model for flexible tanks undergoing rocking," *Journal of Engineering Mechanics*, vol. 111, no. 2, pp. 143–157, 1985.
- [22] A. S. Veletsos and Y. Tang, "Rocking response of liquid storage tanks," *Journal of Engineering Mechanics*, vol. 113, no. 11, pp. 1774–1792, 1987.
- [23] T. Taniguchi, "Rocking behavior of unanchored flat-bottom cylindrical shell tanks under action of horizontal base excitation," *Engineering Structures*, vol. 26, no. 4, pp. 415–426, 2004.
- [24] M. N. Ahari, S. Eshghi, and M. G. Ashtiany, "The tapered beam model for bottom plate uplift analysis of unanchored cylindrical steel storage tanks," *Engineering Structures*, vol. 31, no. 3, pp. 623–632, 2009.
- [25] A. Zingoni, "Liquid-containment shells of revolution: a review of recent studies on strength, stability and dynamics," *Thin-Walled Structures*, vol. 87, pp. 102–114, 2015.
- [26] M. K. Shriali and R. S. Jangid, "Earthquake response of isolated elevated liquid storage steel tanks," *Journal of Construction Steel Research*, vol. 59, no. 10, pp. 1267–1288, 2003.
- [27] M. R. Shekari, N. Khaji, and M. T. Ahmadi, "A coupled BE-FE study for evaluation of seismically isolated cylindrical liquid storage tanks considering fluid-structure interaction," *Journal of Fluids and Structures*, vol. 25, no. 3, pp. 567–585, 2009.
- [28] M. Moslemi and M. R. Kianoush, "Application of seismic isolation technique to partially filled conical elevated tanks," *Engineering Structures*, vol. 127, pp. 663–675, 2016.

- [29] A. Maleki and M. Ziyaeifar, "Sloshing damping in cylindrical liquid storage tanks with baffles," *Journal of Sound and Vibration*, vol. 311, no. 1-2, pp. 372–385, 2008.
- [30] H. N. Phan, F. Paolacci, and S. Alessandri, "Fragility analysis methods for steel storage tanks in seismic prone areas," in *Proceedings of the ASME 2016 Pressure Vessels and Piping Conference*, Article ID V008T08A023, American Society of Mechanical Engineers (ASME), Vancouver, Canada, July, 2016.
- [31] M. F. Vassiliou, K. R. Mackie, and B. Stojadinović, "A finite element model for seismic response analysis of deformable rocking frames," *Earthquake Engineering & Structural Dynamics*, vol. 46, no. 3, pp. 447–466, 2017.
- [32] S. Diamantopoulos and M. Fragiadakis, "Seismic response assessment of rocking systems using single degree-of-freedom oscillators," *Earthquake Engineering & Structural Dynamics*, vol. 48, no. 7, pp. 689–708, 2019.
- [33] H. Alemzadeh and H. Shakib, "Numerical study on the response of steel ground tanks with free rocking motion under horizontal earthquake excitation," *Journal of Structure and Steel*, vol. 1395, no. 20, pp. 71–79, 2017.
- [34] M. W. Hur and T. W. Park, "Performance evaluation of seismic isolation system by installation location in lighthouse structures," *Shock and Vibration*, vol. 2018, Article ID 5751623, 13 pages, 2018.
- [35] G. W. Housner, "The dynamic behavior of water tanks," *Bulletin of the Seismological Society of America*, vol. 53, no. 2, pp. 381–387, 1963.
- [36] M. A. Haroun, "Vibration studies and tests of liquid storage tanks," *Earthquake Engineering & Structural Dynamics*, vol. 11, no. 2, pp. 179–206, 1983.
- [37] ASCE 7, *Minimum Design Loads for Buildings and Other Structures*, vol. 7, American Society of Civil Engineers, Reston, VA, USA, 2016.
- [38] R. W. Clough and J. Penzien, *Dynamics of Structures*, Computers and Structures, Inc., Berkeley, CA, USA, 1995.
- [39] H. Alemzadeh, *Development of Controlled Rocking and Self-Centering Mechanisms for Improving Seismic Performance of Elevated Water Tanks*, Ph.D. Dissertation, Department of Civil and Environmental Engineering, Tarbiat Modares University, Tehran, Iran, 2019.
- [40] J. W. Meek, "Effects of foundation tipping on dynamic response," *Journal of the Structural Division*, vol. 101, no. 7, pp. 1297–1311, 1975.
- [41] L. F. Shampine, I. Gladwell, and S. Thompson, *Solving ODEs with Matlab*, Cambridge University Press, New York, NY, USA, 2003.
- [42] J. R. Dormand and P. J. Prince, "A family of embedded Runge-Kutta formulae," *Journal of Computational and Applied Mathematics*, vol. 6, no. 1, pp. 19–26, 1980.
- [43] A. M. Memari, M. M. Ahmadi, and B. Rezaee, "Behaviour of RC water towers during Manjil-Roudbar earthquake of June 1990," in *Proceedings of the 10th World Conf. on Earthquake Engineering*, Madrid, Spain, July 1992.
- [44] ACI 350.3-06, *Seismic design of liquid containing concrete structures and commentary*, American Concrete Institute, Farmington Hills, MI, USA, 2006.
- [45] J. B. Mander and C. T. Cheng, "Seismic Resistance of Bridge Piers Based on Damage Avoidance Design," *Technical Report NCEER-97-0014*, Department of Civil, Structural and Environmental Engineering, State University of New York at Buffalo, New York, NY, USA, 1997.
- [46] N. H. Hamid and J. B. Mander, "Damage avoidance design for buildings," *KSCE Journal of Civil Engineering*, vol. 18, no. 2, pp. 541–548, 2014.
- [47] T. D. Ancheta, R. B. Darragh, J. P. Stewart et al., *Peer NGA-West2 Database*, Pacific Earthquake Engineering Research Center (PEER), University of California, Berkeley, CA, USA, 2013, <https://ngawest2.berkeley.edu/>.
- [48] N. Reggiani Manzo and M. F. Vassiliou, "Displacement-based analysis and design of rocking structures," *Earthquake Engineering & Structural Dynamics*, vol. 48, no. 14, pp. 1613–1629, 2019.
- [49] A. G. Davenport, "How can we simplify and generalize wind loads?" *Journal of Wind Engineering and Industrial Aerodynamics*, vol. 54-55, pp. 657–669, 1995.
- [50] E. Assareh, M. A. Behrang, M. Ghalambaz, A. R. Noghrehabadi, and A. Ghanbarzadeh, "An analysis of wind speed prediction using artificial neural networks: a case study in Manjil, Iran," *Energy Sources, Part A: Recovery, Utilization, and Environmental Effects*, vol. 34, no. 7, pp. 636–644, 2012.
- [51] National Building Regulations, *Part 6 Design Loads for Buildings Part 6-92*, Bureau for compiling and promoting national regulations for buildings, Ministry of Housing and Urbanism, Tehran, Iran, 2013.

Research Article

Development of a Frequency-Adjustable Tuned Mass Damper (FATMD) for Structural Vibration Control

Huaguo Gao,¹ Congbao Wang,¹ Chen Huang,² Wenlong Shi,³ and Linsheng Huo ²

¹School of Civil Engineering, University of Science and Technology Liaoning, Anshan, Liaoning 114051, China

²State Key Laboratory of Coastal and Offshore Engineering, Dalian University of Technology, Dalian, Liaoning 116024, China

³Department of Civil Engineering, Shanghai University, Shanghai 200444, China

Correspondence should be addressed to Linsheng Huo; lishuo@dlut.edu.cn

Received 2 February 2020; Revised 5 September 2020; Accepted 11 September 2020; Published 21 September 2020

Academic Editor: Vasant Matsagar

Copyright © 2020 Huaguo Gao et al. This is an open access article distributed under the Creative Commons Attribution License, which permits unrestricted use, distribution, and reproduction in any medium, provided the original work is properly cited.

The tuned mass damper (TMD) can be applied to suppress earthquake, wind, and pedestrian- and machine-induced vibration in factory buildings or large span structures. However, the traditional TMD with a fixed frequency will not be able to perform effectively against the frequency variations in multiple hazards. This paper proposed a frequency-adjustable tuned mass damper (FATMD) to solve this limitation of current TMD. The FATMD presented in this paper is composed of a simple assembly consisting of a supported beam with a mass, in which the frequency of the FATMD is changed by adjusting the span of the beam. The kinematic equation of a single degree of freedom (SDOF) structure installed with an FATMD is established to analyze the effect of the damping ratio, mass ratio, and stiffness on the vibration damping. The fundamental frequency of the FATMD at different spans is verified by simulation and experiments. Forced vibration experiments with different excitation frequencies are also conducted to verify the performance of the FATMD. The results show that the proposed FATMD can effectively suppress the vertical vibration of structures at different excitation frequencies, including frequencies at a range higher than what a traditional TMD may not be able to suppress. Additionally, the proposed FATMD is applied to a long-span pedestrian bridge which vibrates frequently due to the walking of pedestrians, the running of escalators, and earthquakes. The numerical results indicate that the FATMD can effectively reduce the vertical vibration of the pedestrian bridge under the excitations of pedestrians, escalators, and earthquakes.

1. Introduction

The rapid development of mechanical automation has given rise to the increasing presence of large equipment in factories and the construction of large span structures. Factory buildings and large span structures often house high-power equipment, which can generate strong vibrations that can affect the integrity of the surrounding structures. If the structural vibration exceeds a certain level, it will negatively affect the function and performance of other devices in the building [1, 2]. The vibration can also lead to a reduced level of comfort for the working personnel [3, 4]. In extreme cases, the vibration can even cause structural damage [5]. There are numerous ways to reduce the vibration of a structure within comfortable levels. One way is to increase the stiffness of the structure, thereby increasing the natural

frequency of the structure and shifting it from the range in which it can be easily reached [6, 7]. Wang et al. [8] strengthened the floor slab and secondary beams to increase the natural frequency of the floor, thereby reducing floor vibrations caused by wheat bran finishers and flour purifiers. However, increasing stiffness may waste the performance of the material and can become expensive. Another method is to utilize vibration-control technologies. Since the concept of vibration control was first proposed by Yao [9] in 1972, numerous vibration-control techniques have been developed and applied to enhance the functionality and safety of structures. Lee et al. [10] utilized multiple viscoelastic dampers to suppress microvibrations in the floor induced by automated guided vehicles in thin-film transistor liquid crystal display factories. The dampers effectively suppressed the dynamic responses to a desired vibration criterion level.

Zordan et al. [11] proposed an active micromachined vibration isolator to isolate high-frequency mechanical vibrations in low-pressure environments, which is suitable for use in or as packaging for sensitive electronic and microelectromechanical systems (MEMS). Setareh et al. [12] proposed a pendulum tuned mass damper to control the excessive vibrations of building floors.

As one of the most popular and flexible vibration control devices, the tuned mass damper (TMD) boasts the advantages of a simple set up, effective vibration suppression, and not needing an energy source (i.e., passive control). TMDs are widely applied in the engineering community, such as in the Condo tower in San Francisco and the Citicorp Building in New York City. Sun et al. [13] analyzed the vibration control effect of TMDs installed on the Chongqing Bridge under Typhoon Chan-hom and demonstrated the effectiveness of the TMDs and their ability to suppress vibrations under a wide range of wind conditions. Caetano et al. [14, 15] evaluated the efficiency of the lateral and vertical TMDs on the Pedro e Inês footbridge in Portugal. Carpineto et al. [16] simulated the dynamic response of suspension footbridges with and without multiple TMDs (MTMDs) under pedestrian-induced excitations. The simulation indicated that MTMDs can effectively reduce vibrations of suspension footbridges. Considering uncertainties present in the structural parameters and the MTMD design, Vellar et al. [17] proposed a new methodology for simultaneous optimization of parameters and positions of MTMDs in buildings that may be subjected to earthquakes. They applied the proposed methodology in a 10-story building to confirm its effectiveness. Elias et al. [18] applied different TMD schemes to reduce structural dynamics under wind and earthquake excitations and found that, for the purposes of multihazard response control, distributed TMDs with equal stiffnesses are preferable compared to those with equal masses. Gerges and Vickery [19] demonstrated the superiority a wire rope spring TMD over a normal TMD and verified the vibration control performance of the new TMD through shaking table tests. He et al. [20] set up TMDs in a cabin to restrain large vibration displacements caused by loads from offshore floating wind turbines, which often face harsh marine conditions. The researchers also simulated the dynamic responses of the wind turbine with and without TMDs under different combined wind and wave loads. Their analyses showed that TMDs can effectively reduce vibration responses for offshore floating wind turbines. Wu et al. [21] proposed a magnetic TMD which is reliable and robust in controlling the vibrations of structures. Bakre and Jangid [22] derived optimum parameters for a TMD system attached to a viscous damped main system. The TMD was able to be tuned for various combinations of excitation and response parameters. Kang and Peng [23] determined the optimal parameters for large mass ratio TMDs subjected to harmonic loads and random, stationary white noise loads and studied the control effect of large mass ratio TMDs. Lu et al. [24] proposed a particle TMD and evaluated its damping performance through aeroelastic wind tunnel tests on a benchmark high-rise building. The results showed that the particle TMD can effectively suppress the wind-induced

vibration of the structure. Lu et al. [25] evaluated the effectiveness of the eddy-current TMD (EC-TMD) in suppressing the vibration of the structure through shaking table tests, and the results showed that the EC-TMD can effectively reduce the displacement response, acceleration response, interstory drift ratio, and maximum strain of the columns under different earthquake excitations. Zhang et al. [26] proposed a pounding TMD (PTMD) and numerically simulated the PTMD on a 55 m tower model to verify the effectiveness of the pounding TMD. The results demonstrated that the PTMD is able to suppress vibrations faster and more strongly than the normal TMD. Xue et al. [27] examined the application of the PTMD in reducing the vibration of offshore jacket-type platforms and showed that the PTMD performed better than the traditional TMD in the desired frequency bandwidth. He et al. [28] proposed a TMD with poles and torsional pendulums (TMDPP). The TMDPP can simultaneously control the translational responses and the torsional angle of asymmetric structures. Santos et al. [29] tested a TMD control system to reduce the excessive vibrations of a gym floor in a commercial building in Brasilia, Brazil. Nguyen [30] optimized the parameters of a symmetric TMD using an analytical method that considers specific vibration duration and stability criteria. Tarng et al. [31] mounted a piezoelectric inertia actuator on the cutting tool, which can suppress the vibration and improve cutting stability in turning operations. Yang et al. [32] designed and optimized MTMDs to increase the chatter resistance of machine tool structures.

However, a major drawback of the conventional TMD is that if the TMD is detuned from the natural frequency, a significant loss of vibration control performance can occur. Therefore, the conventional TMD with a fixed frequency cannot perform effectively against the frequency variations in multiple hazards. To overcome this issue, many semiactive or active methods have been proposed. Chang et al. [33] reported the use of an adjustable, vertically moving TMD (VTMD) to suppress machine-induced vertical vibration of structures. Abdel-Rohman et al. [34] studied the influence of the time delay on the performance of a semiactive TMD and proposed two methods to compensate for the time delay and ensure the vibration suppression effect. Jiang and Hanagan [35] proposed a semiactive variable damping TMD (SAVDTMD) with piezoelectric friction dampers as an alternative to existing methods to control floor vibrations, especially vibrations induced by pedestrian traffic. Esteki et al. [36] described the use of a magnetorheological fluid-based semiactive TMD to suppress the seismic response of a 40-story steel-frame building in Vancouver. The new semiactive suppressed structural vibrations more effectively than the classic passive TMD. Nagarajaiah et al. [37, 38] developed a semiactive or smart TMD (STMD) using a semiactive variable stiffness system, which is robust against changes in the natural frequency of the host structure since the STMD always stays tuned. Ryan et al. [39] proposed an adaptive passive vibration absorber and experimentally validated the effectiveness through experiments. The results demonstrated that the adaptive absorber is able to achieve 25 dB of attenuation in the vibration of a model building. Contreras

et al. [40, 41] proposed an adaptive length pendulum smart TMD (ALP-STMD) in which natural frequencies are time invariant. They experimentally validated the ability of an ALP-STMD to adequately control a structural system. Similar devices were applied towards bridge vibration control [42]. Shi et al. [43] proposed a self-adjustable variable mass TMD (SAVM-TMD) and experimentally validated the effectiveness under different pedestrian excitations. The results demonstrated that the SAVM-TMD is able to suppress pedestrian vibrations better than the normal TMD. Venanzi et al. [44] proposed an active TMD to mitigate wind-induced vibrations of tall buildings and optimized the number and positions of active TMDs. Rahman et al. [45] investigated the seismic performance of a 10-story building and demonstrated the efficiency of using multiple adaptive TMD to dampen seismic-induced structural vibrations.

The traditional TMD is a type of frequency sensitive control device. Thus, the potential for unintended detuning of the TMD's natural frequency is a major drawback of the traditional TMD. When the frequency of the TMD is not matched with the frequency of the host structure, the TMD can suffer a significant loss of vibration control performance. The vibration frequencies of structures are often varied due to the degradation of structural parameters in multiple hazard scenarios, which requires that the frequency of TMD should be easily tuned to better respond to this variation. The natural frequency of the TMD is determined partially by its stiffness, which, in current TMDs, is usually provided by springs. The stiffness of the spring is difficult to be set precisely due to unavoidable errors in the manufacturing process, and thus, it is difficult to guarantee the exact frequency of the vibration control system. Therefore, the TMD is usually adjusted by changing the mass of the system after the spring is fabricated. However, doing so means that there is a very narrow tuning range for setting the frequency of the TMD. Furthermore, the traditional TMD is only suitable for mitigating low-frequency vibrations and has trouble of controlling high frequency vibrations often generated by mechanical equipment. To overcome these issues, a frequency-adjustable tuned mass damper (FATMD) is proposed in this study. The FATMD utilizes a beam instead of a spring to provide the stiffness to the control device and can effectively suppress high-frequency vibrations. The frequency of the FATMD can be adjusted by adjusting the span of the beam. In this paper, the kinematic equations of the structure with a FATMD are established to analyze the effect of damping ratio, mass ratio, and stiffness on its ability to dampen vibrations. Subsequently, the fundamental frequencies of the FATMD with different adjusted spans are verified by simulation and experiments. To verify the vibration suppression performance of the FATMD, the FATMD is subjected to forced vibrations at different excitation frequencies.

2. The FATMD

The schematic of the FATMD is shown in Figure 1. The FATMD consists of an easy-to-implement assembly of a bottom plate, vertical columns, a weighted steel plate, and a

beam. As shown in Figure 1(b), the pedestals of columns (3) are bolted between the bottom plate (1) and the pressure plate (2). Before the columns are fixed, the span of the beam (6) can be adjusted by moving the pedestals of the columns (3) along the length of the bottom plate (1) and, thereby, allow the continuous adjustment of the natural frequency of the FATMD. The beam (6) is installed on the rectangular platform of formed by the columns (3) and is fixed via the bolted column fastener (7). The weighted box (4) is fixed to the beam (6) through a set of fasteners. The beam (6) is clamped between the weighted box (4) and the fastener, and a gasket placed between the beam and the weighted box prevents the weighted box from sliding along the beam's axis. The bolt holes are set to straight notches, which are perpendicular to the axial direction. The weighted box (4) can be finely adjusted along the length of the beam to avoid any eccentricity of the FATMD caused by the weight box. The counterweight steel plate (5) hangs from the weighted box and, thus, reduces the footprint of the FATMD. The frequency of the FATMD can be finely adjusted by changing the mass of the plates.

3. Control Equations of an SDOF Structure with the FATMD

The TMD is one of the earliest passive control devices used in structural vibration control. When the main structure vibrates under external excitation, the TMD control system is driven to vibrate together with the structure. Then, inertial forces generated by the relative motion of the TMD acts against the motions of the structure and, thus, can reduce the dynamic response of the structure. To illustrate the working principle, a single degree of freedom (SODF) primary structure installed with the FATMD is illustrated in Figure 2, where m_1 , c_1 , and k_1 are, respectively, the mass, damping, and stiffness of the SDOF structure. m_2 , c_2 , and k_2 are the mass, damping, and stiffness of the FATMD, respectively.

According to D'Alembert's principle, the kinematic equations of the SDOF structure with the FATMD are as follows:

$$\begin{aligned} m_1 \ddot{x}_1 + (c_1 + c_2) \dot{x}_1 - c_2 \dot{x}_2 + (k_1 + k_2) x_1 - k_2 x_2 &= f(t), \\ m_2 \ddot{x}_2 + c_2 (\dot{x}_2 - \dot{x}_1) + k_2 (x_2 - x_1) &= 0, \end{aligned} \quad (1)$$

where x_1 , \dot{x}_1 , and \ddot{x}_1 are the displacement, velocity, and acceleration of the structure relative to the ground, respectively. x_2 , \dot{x}_2 , and \ddot{x}_2 are the displacement, velocity, and acceleration of the FATMD relative to the ground, respectively.

The equations can be solved by expressing them in the form of a transfer function. Thus, after applying the Laplace transform,

$$\begin{aligned} [m_1 s^2 + (c_1 + c_2) s + (k_1 + k_2)] X_1 - (c_2 s + k_2) X_2 &= f(s), \\ (m_2 s^2 + c_2 s + k_2) X_2 - (c_2 s + k_2) X_1 &= 0, \end{aligned} \quad (2)$$

where s represents the independent variable after the Laplace transform of the original function.

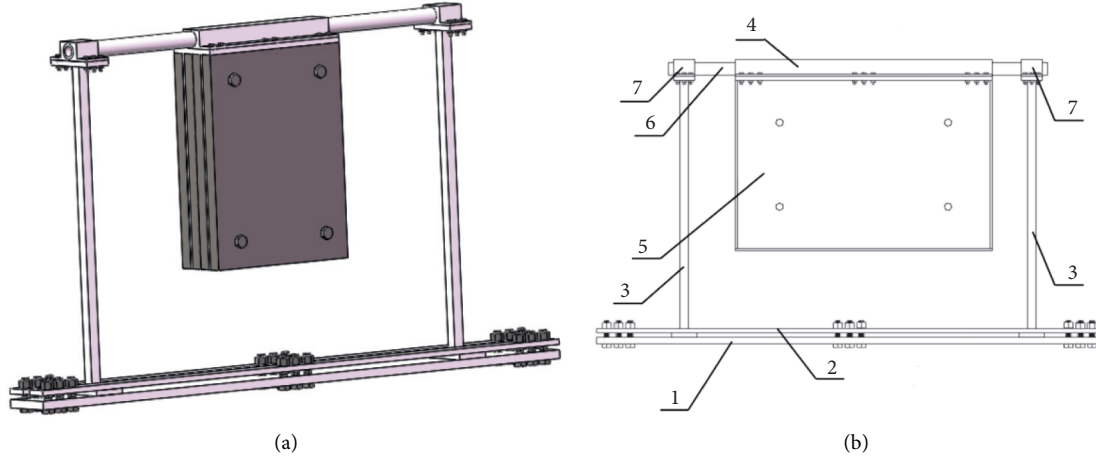


FIGURE 1: Schematic of the FATMD. (a) Three-dimensional schematic, (b) elevation drawing. 1—bottom plate; 2—pressure plate; 3—column; 4—weighted box; 5—counterweight steel plate; 6—Beam; and 7—column fastener.

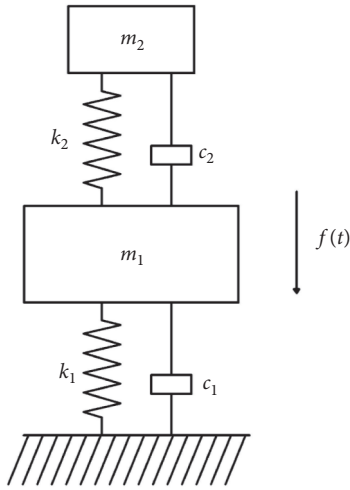


FIGURE 2: Diagram of an SDOF structure with an installed FATMD.

Equation (5) can be organized as follows:

$$(s^2 + 2\omega_1\xi_1s + \omega_1^2)X_1 + \mu s^2X_2 = \frac{f(s)\lambda^2\mu\omega_1^2}{k_2}, \quad (3)$$

where ω_1 and ξ_1 are, respectively, the frequency and the damping ratio of the structure. μ is the ratio of the mass of the TMD to the total mass of the structure.

$$\begin{aligned} \omega_1 &= \sqrt{\frac{k_1}{m_1}}, \\ \xi_1 &= \frac{c_1}{2m_1\omega_1}, \\ \mu &= \frac{m_2}{m_1}. \end{aligned} \quad (4)$$

Thus, the overall transfer function for the primary structure is as follows:

$$H(s) = \frac{1}{m_1s^2 + (c_1 + c_2)s + (k_1 + k_2) - \left(\frac{(c_2s + k_2)^2}{(m_2s^2 + c_2s + k_2)} \right)} \quad (5)$$

4. Parametric Analysis of the FATMD

The previous section considered the SDOF structure coupled with an FATMD (Figure 2) as an analytical model and established the control equations for the whole system. In this section, a parametric analysis for the system under the sinusoidal excitation is provided to verify the influences of parameters of the FATMD on its effectiveness, which can provide useful information for designing the FATMD. The parameters of the FATMD are as follows based on practicality:

- (1) λ : the ratio of the frequency of the FATMD to the fundamental frequency of the structure
- (2) μ : the ratio of the mass of the FATMD to the total mass of the structure
- (3) ξ : the damping ratio of the FATMD

As shown in Figure 3, the logarithmic amplitude-frequency characteristic curves of the structure with and without the FATMD are plotted for different values of λ when $\mu = 0.01$. The curves can illustrate the trend of changes on the amplitude of the structural response at different frequencies. By comparing the amplitudes of the uncontrolled and controlled structural vibrations, it is noted that the vibration of the structure can be effectively reduced by the FATMD. When the frequency of the external excitation is 15.7 Hz, the vibration of the structure without control peaks is due to resonance. The vibration suppression effect of the FATMD is stable between $\lambda = 0.9-1.1$, with $\lambda = 1.0$ being a relatively optimal value according to the curves. Additionally, the vibration suppression effect of the FATMD is pronounced when the frequency of the FATMD matches the excitation frequency.

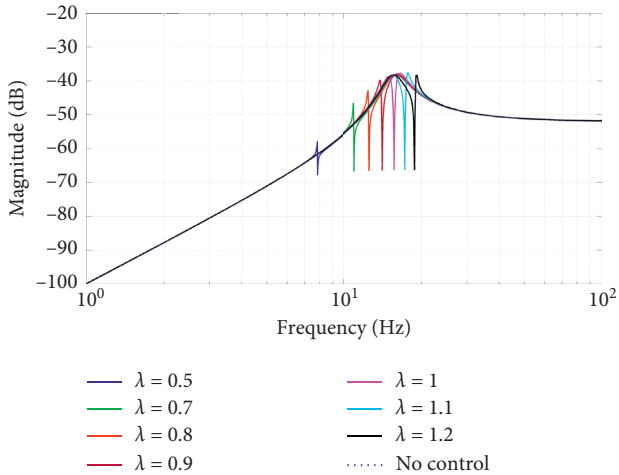


FIGURE 3: Logarithmic amplitude-frequency characteristic curves of the structure with and without the FATMD (varying λ).

In Figure 4, the logarithmic amplitude-frequency characteristic curves of the system are plotted for different values of μ when $\lambda = 1.0$. A comparison of the seven curves with and without control reveals the obvious vibration mitigation effect of the FATMD. By increasing the mass of the FATMD, the effective bandwidth of the FATMD widens and the vibration suppression effect on the structural vibrations also increases. Furthermore, in Figure 5, the logarithmic amplitude-frequency characteristic curves of the system are plotted for different values of ξ when $\lambda = 1.0$ and $\mu = 0.01$. The figure shows that the greater the damping ratio, the weaker the vibration reduction effect of the FATMD becomes. Thus, the damping ratio of the FATMD should be minimized in the cases that the frequencies of excitation deviate far from the one of the structure.

5. Vibration Control Experiments of the FATMD

5.1. Experimental Setup. To verify the vibration suppression performance of the FATMD, the FATMD and the structure are subjected to forced vibrations at different excitation frequencies. The primary structure is a model steel floor elevated on four steel legs. The size of the steel floor is $100 \times 20 \times 1.5$ cm. The height of the structure is 40 cm, and the total weight of the structure is 32.52 kg. The natural frequency of the structure is 25.8 Hz. As shown in Figure 6, the FATMD mainly consists of a bottom plate, vertical columns, a steel weight, and a beam, similar to the schematic shown in Figure 1. The beam is a steel pipe with a length of 1 m and 1 mm thick steel walls. Two kinds of steel pipes with different diameters are tested for the verification experiment. One pipe has a line inner radius of 5 mm, and the other has a line inner radius of 6 mm. The rubber gaskets are installed between the column and the beam to prevent the beam from sliding in the axial direction between the platform and fastener of the column. A mass of 0.5 kg is fixed in the middle of the beam and the frequency of FATMD can be fine-tuned by changing the mass.

As shown in Figure 7, the shaker is installed at the bottom of the primary structure and is used to excite the vertical vibration of the primary structure during the test. The shaker (model: JZK-20) can be controlled by a signal generator and can continuously output a sinusoidal signal with a frequency between 1–10000 Hz. Without any loads, the maximum displacement is 10 mm, and the maximum output force is 200 N. Two accelerometers (model: Lance LC0101) are mounted to measure the absolute acceleration. One is fixed onto the primary structure, and the other is fixed onto the FATMD. Data are collected by using an acquisition device (Model: NI 6366) connected to a laptop installed with LabVIEW.

To demonstrate that the frequency of the FATMD is adjustable, the first-order frequency of the FATMD under different spans is measured by the knocking method [46]. Then, the FATMD is tested with forced vibrations at different excitation frequencies and configurations. The direction of the applied excitation is vertical. The vibrations of the structure and the FATMD are also vertical.

5.2. Experimental Results. The first-order frequency of the FATMD at different adjusted spans is plotted in Figures 8 and 9, and the values of the frequency are listed in Table 1. L is length of the beam span in the FATMD. The figures show that the frequency of the FATMD decreases when the beam span increases. As shown in Table 1, when the beam has a radius (r) of 5 mm and a span of 0.5 m, the first-order frequency of FATMD is 38 Hz. When the span of the beam increases to 1 m, the first-order frequency of FATMD is 17.3 Hz. As shown in Table 1, when the beam has a radius of 6 mm and a span of 0.5 m, the first-order frequency of FATMD is 42.7 Hz. When the span of the beam increases to 1 m, the first-order frequency of FATMD is 20.1 Hz. The data, therefore, demonstrates that by changing of the beam span, the frequency of the FATMD can be adjusted.

To evaluate the vibration control performance of the FATMD, the vibration reduction ratio (J) is defined as described in equation (8).

$$J = \frac{a_0 - a_1}{a_0} \times 100\%, \quad (6)$$

where a_1 and a_0 are the maximum vertical acceleration of the structure with and without the FATMD, respectively.

As shown in Figure 10, the vertical accelerations of the primary structure with and without the FATMD are plotted against time for the tested excitation frequencies. Table 2 lists the vibration reduction ratios of the FATMD under different excitation frequencies. In the experiment, the span was adjusted to make the frequency of the FATMD match the excitation frequency. When frequencies of the excitation and FATMD are both 26.5 Hz, the vibration reduction ratio of the FATMD is 96.1%, thus effectively suppressing the forced vibration of the structure. As shown in Figures 10(g)–10(n), the FATMD can still effectively suppress the structural vibration at other high frequency excitations. For example, when the excitation frequency increases to 38.0 Hz, the vibration reduction ratio is 64.7%. In case where the

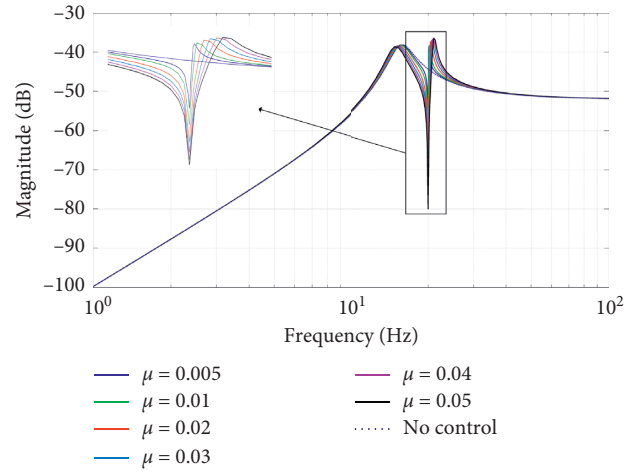


FIGURE 4: Logarithmic amplitude-frequency characteristic curves of the structure with and without the FATMD (varying μ).

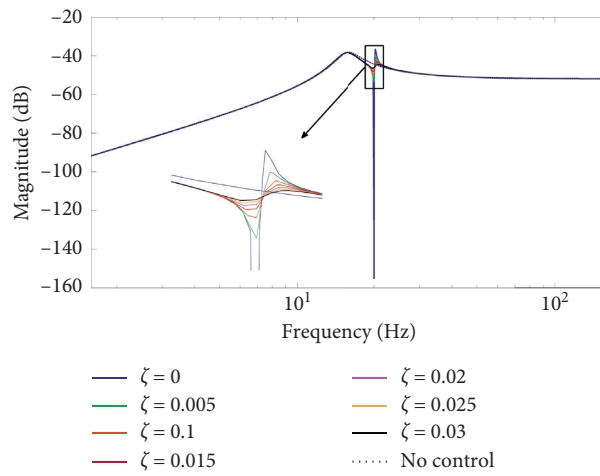


FIGURE 5: Logarithmic amplitude-frequency characteristic curves of the structure with and without the FATMD (varying ξ).

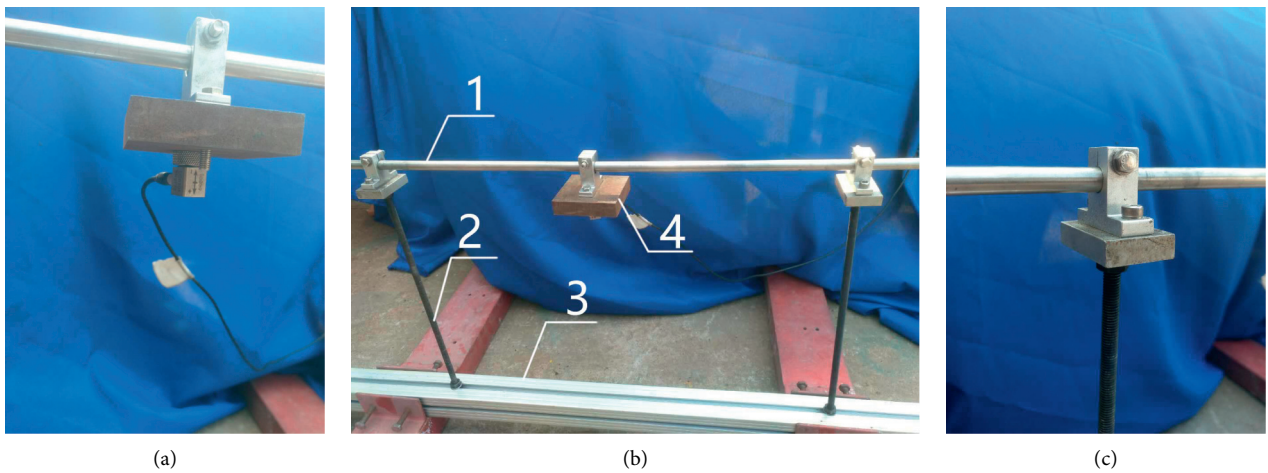


FIGURE 6: Photos of the FATMD (1—beam; 2—column; 3—bottom plate; and 4—counterweight).

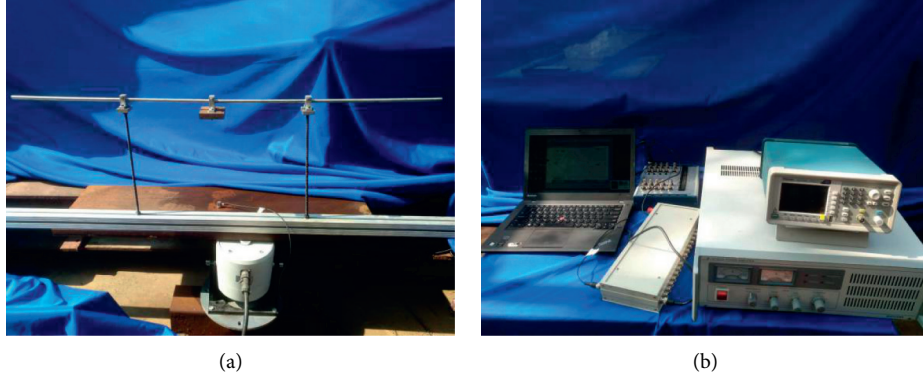


FIGURE 7: The experimental setup and data acquisition system.

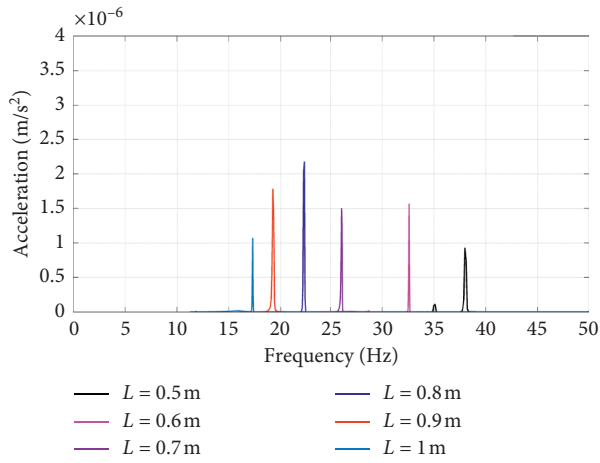
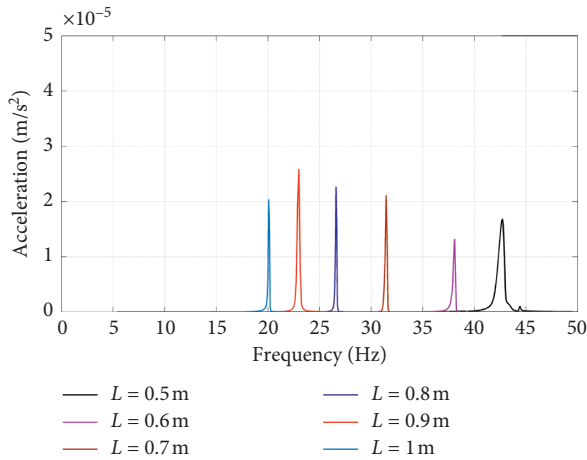
FIGURE 8: The first-order frequency of the FATMD with different spans ($r = 5$ mm).FIGURE 9: The first-order frequency of the FATMD with different spans ($r = 6$ mm).

TABLE 1: First-order frequency of the FATMD at different spans.

Span (m)	0.5	0.6	0.7	0.8	0.9	1.0
Frequency (Hz) $r = 5$ mm	38.0	32.6	26.1	22.3	19.2	17.3
Frequency (Hz) $r = 6$ mm	42.7	38.0	31.5	26.5	23.0	20.1

frequency of the external excitation or structure changes, the beam span can be changed to adjust the frequency of the FATMD accordingly to preserve highly effective vibration suppression.

6. Vibration Control of a Long-Span Pedestrian Bridge with the FATMD

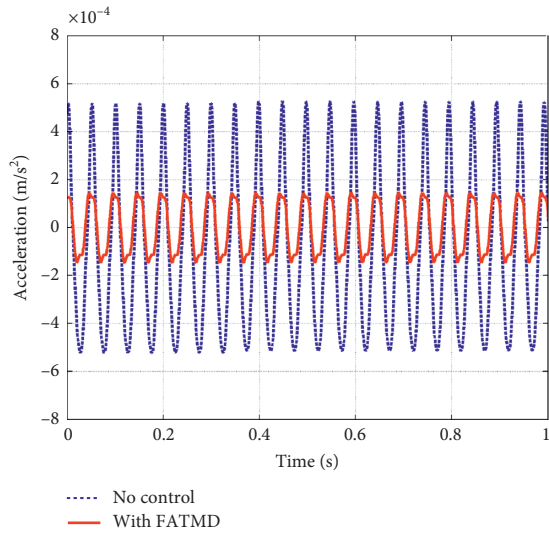
There is a pedestrian bridge in Shenyang, China, with the span of 49 m. The main structure of the bridge is a single-span steel box girder with the simple support at both ends. The deck width of the bridge is 3 m, and the linear density of the bridge is 1.179136 kg/m. The moment of inertia of the girder section is 0.0694 m⁴, and the elastic modulus is 200 GPa. The first frequency of the structure on the vertical direction is 2.2 Hz, which is close to the one of pedestrian walking. As a result, the large vibration can be felt when people walk through the bridge. In addition, the running of escalators connected to the bridge can also excite the vibration of the bridge. The vibration of bridge due to the walking of pedestrians and running of escalators can cause the uncomfortableness of people on the bridge and even result the fatigue damage of the structure. An FATMD is installed on the midspan of the pedestrian bridge to reduce the vertical vibrations under the excitations of pedestrians, escalators, and earthquakes. As shown in Figure 11, the FATMD can be installed under the guardrails of the pedestrian bridge, which will not affect the normal use of the bridge. The ratio of the total mass of the FATMD to the one of the bridge is 2%. Considering that the counterweight steel plates of the FATMD are relatively large, the stiffness and the span of the beam on the FATMD should be designed reasonably.

Figure 12 shows the simplified analysis model of the pedestrian bridge installed with an FATMD. The kinematic equations of the bridge with the FATMD are as follows:

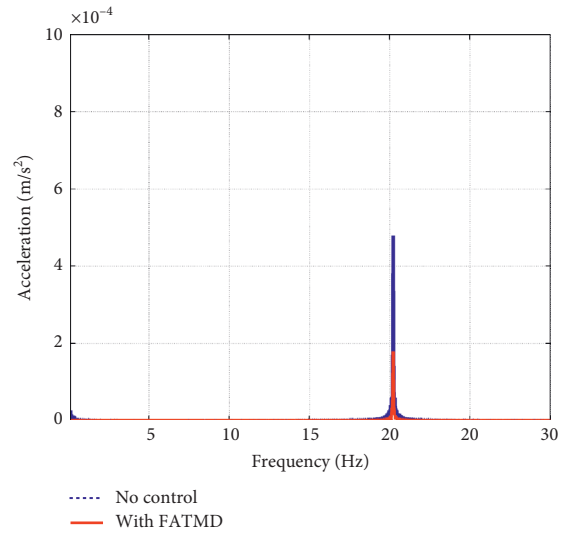
$$EI \frac{\partial^4 y}{\partial x^4} + \overline{M} \frac{\partial^2 y}{\partial t^2} + C \frac{\partial y}{\partial t} = F + f, \quad (7)$$

$$m \ddot{y}_1 + c(\dot{y}_1 - \dot{y}_0) + k(y_1 - y_0) = 0,$$

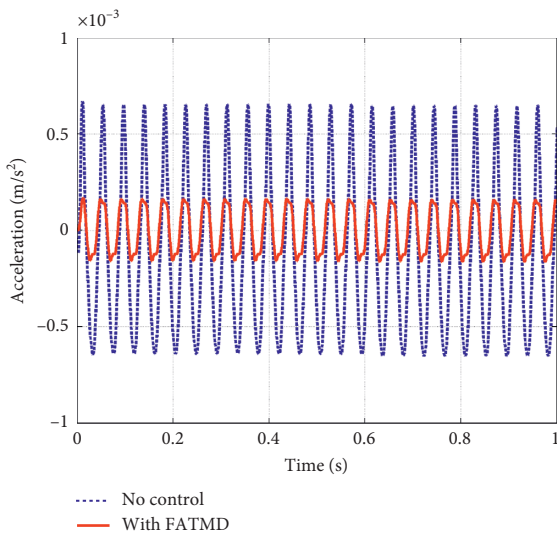
where EI is the flexural stiffness of the bridge. $M(\text{---})$ is the linear density of the bridge. m , c , and k are the mass,



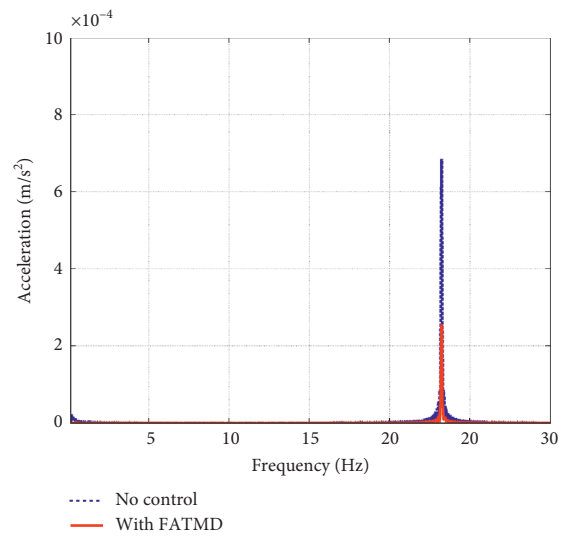
(a)



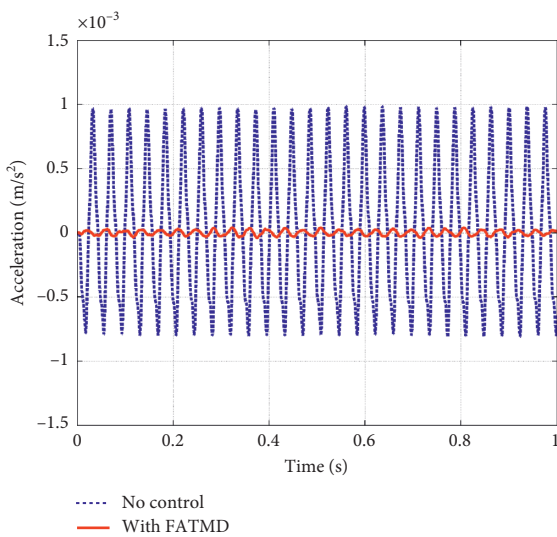
(b)



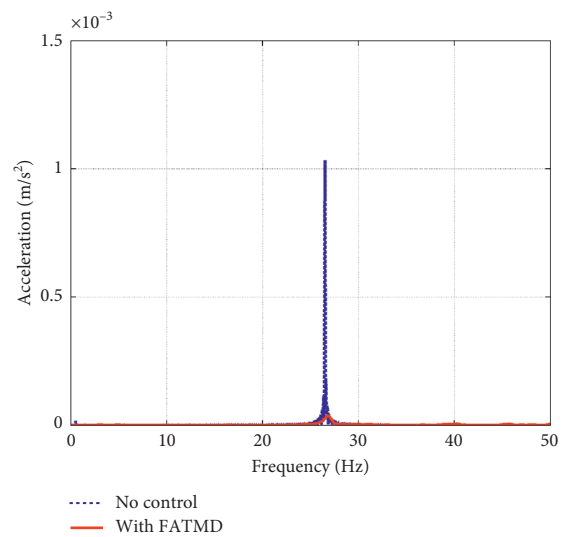
(c)



(d)

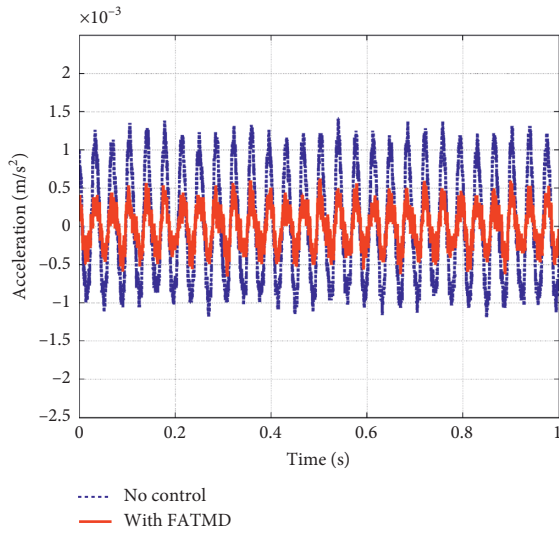


(e)

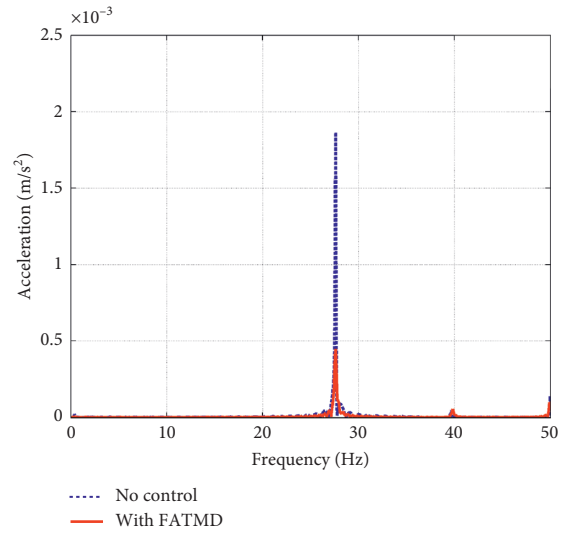


(f)

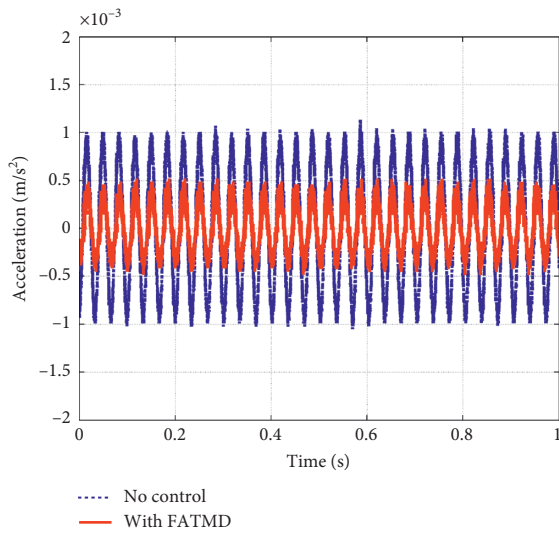
FIGURE 10: Continued.



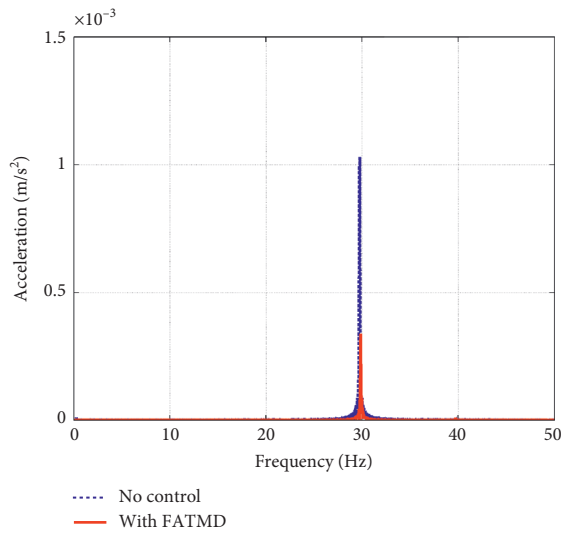
(g)



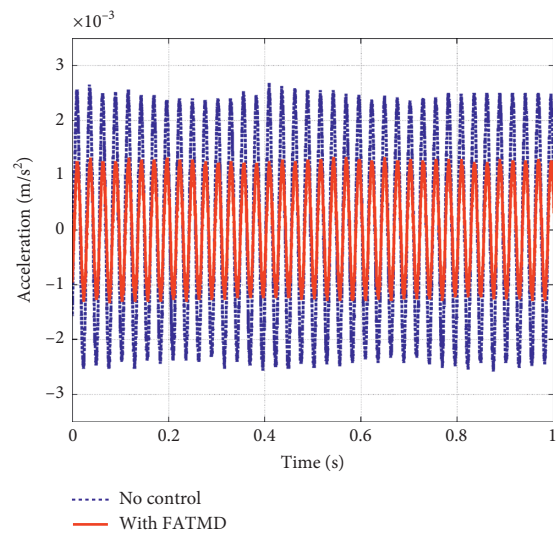
(h)



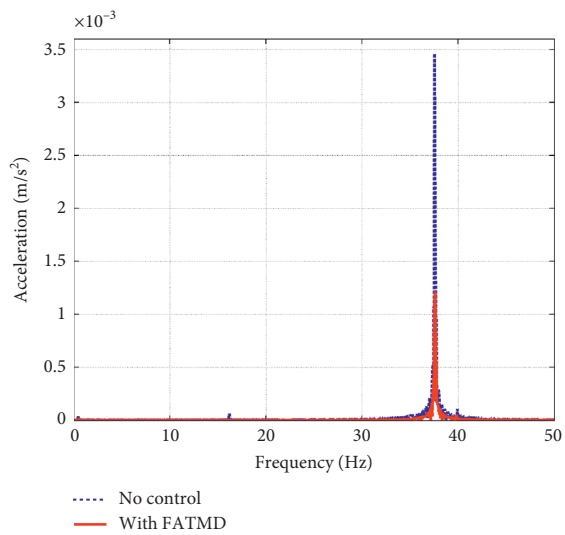
(i)



(j)



(k)



(l)

FIGURE 10: Continued.

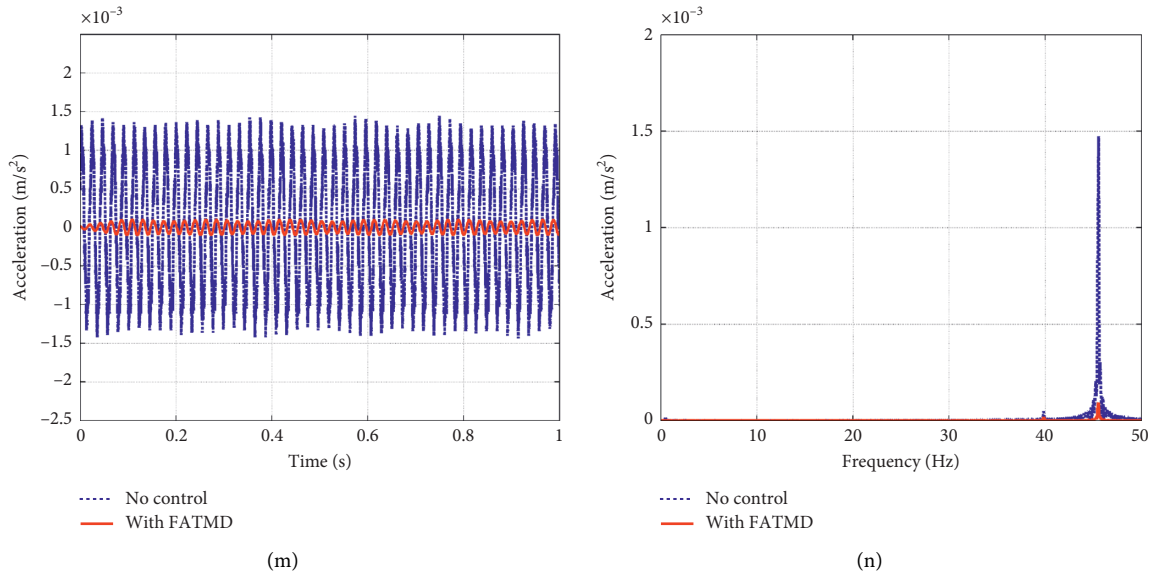


FIGURE 10: Acceleration of the structure with and without an FATMD for different excitation frequencies. (a) Acceleration of the structure vs. time ($f=20.1$ Hz, $L=1.0$ m), (b) acceleration of the structure vs. frequency ($f=20.1$ Hz, $L=1.0$ m), (c) acceleration of the structure vs. time ($f=23.0$ Hz, $L=0.9$ m), (d) acceleration of the structure vs. frequency ($f=23.0$ Hz, $L=0.9$ m), (e) acceleration of the structure vs. time ($f=26.5$ Hz, $L=0.8$ m), (f) acceleration of the structure vs. frequency ($f=26.5$ Hz, $L=0.8$ m), (g) acceleration of the structure vs. time ($f=28.5$ Hz, $L=0.76$ m), (h) acceleration of the structure vs. frequency ($f=28.5$ Hz, $L=0.76$ m), (i) acceleration of the structure vs. time ($f=30.0$ Hz, $L=0.72$ m), (j) acceleration of the structure vs. frequency ($f=30.0$ Hz, $L=0.72$ m), (k) acceleration of the structure vs. time ($f=38.0$ Hz, $L=0.6$ m), (l) acceleration of the structure vs. frequency ($f=38.0$ Hz, $L=0.6$ m), (m) acceleration of the structure vs. time ($f=45.5$ Hz, $L=0.43$ m), and (n) acceleration of the structure vs. frequency ($f=45.5$ Hz, $L=0.43$ m).

TABLE 2: Vibration reduction ratios of the FATMD.

Excitation frequency (Hz)	Acceleration (mm/s ²)		Vibration reduction ratio (%)
	Uncontrolled	With FATMD	
20.1	0.497	0.179	64.0
23.0	0.685	0.256	62.6
26.5	1.033	0.040	96.1
28.5	1.864	0.447	76.0
30.0	1.030	0.338	67.2
31.5	1.108	0.386	65.2
38.0	3.463	1.217	64.9
42.7	1.633	0.407	75.1
45.5	1.473	0.094	93.6

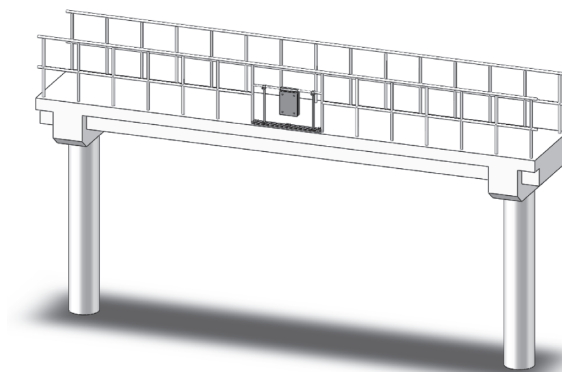


FIGURE 11: Schematic of a pedestrian bridge installed with an FATMD.

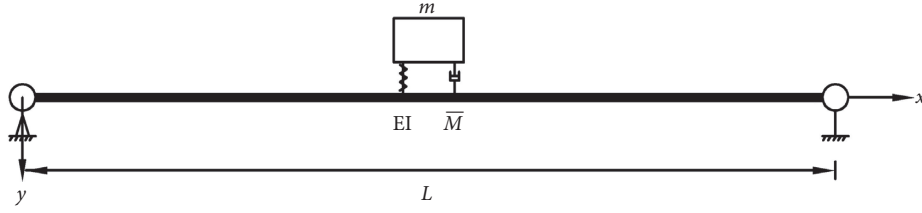


FIGURE 12: The simplified model of a pedestrian bridge with an FATMD.

damping, and stiffness of the FATMD, respectively. y is the displacement of the bridge in the vertical direction. y_0 is the vertical displacement of the midspan of the bridge. y_1 is the displacement of the FATMD in the vertical direction. F is the external excitation. f is the control force exerted on the structure by the FATMD.

$$f = c(\dot{y}_1 - \dot{y}_0) + k(y_1 - y_0). \quad (8)$$

According to the mode analysis method, the vertical responses of the bridge can be expressed as follows:

$$y(x, t) = \sum_n Y_n(t) \phi_n(x), \quad (9)$$

where $Y_n(t)$ is the generalized coordinate; $\phi_n(x)$ is the mode function.

$$\phi_n(x) = \sin \frac{n\pi x}{L}. \quad (10)$$

Thus, the kinematic equations of the bridge with the FATMD can be simplified as follows:

$$\ddot{Y}_n + 2\xi_n \omega_n \dot{Y}_n + \omega_n^2 Y_n = \frac{1}{M_n} (F_1 + f_1) \quad (11)$$

$$m\ddot{y}_1 + c[\dot{y}_1 - \dot{Y}_n \phi_n(x)] + k[y_1 - Y_n \phi_n(x)] = 0,$$

where

$$M_n = \int_0^L \phi_n^2(x) \bar{m} dx,$$

$$\omega_n = n^2 \pi^2 \sqrt{\frac{EI}{\bar{m}L^4}},$$

$$\xi_n = \frac{C_n}{2M_n \omega_n}, \quad (12)$$

$$F_1 = \int_0^L \phi_n(x) F dx,$$

$$f_1 = \int_0^L \phi_n(x) f dx = \phi_n(x) \left\{ c[\dot{y}_1 - \dot{Y}_n \phi_n(x)] + k[y_1 - Y_n \phi_n(x)] \right\}.$$

According to research by Poovarodom et al. [47], the effect of the crowd dynamic load on the pedestrian bridge can be converted into a concentration force at the midspan of the bridge as follows:

$$p(t) = 0.4W \sqrt{n_p} \sin(2\pi f_p t), \quad (13)$$

where W is the average weight of pedestrians on the bridge and taken as 700 N in this paper; n_p is the number of people walking on the bridge at the same time, and the maximum value can be about 265 based on the area of the bridge deck; and f_p is the frequency of pedestrian loads.

The vertical responses of the bridge with and without the FATMD are computed under different frequencies of the pedestrian load. The frequency of the FATMD is set to match the excitation frequency. Figure 13 shows the acceleration time history in the midspan of the bridge under the frequency of the pedestrian load is 2.2 Hz. The first 10 s is the forced vibration of the bridge under the pedestrian load, and the last 5 s is the free vibration of the bridge. It can be seen that the FATMD can effectively reduce the forced and the free vibration of the bridge. Figure 14 shows the acceleration envelope diagram of the bridge. A comparison of the two curves reveals the obvious vibration mitigation effect of the FATMD on the peak acceleration of the whole bridge. Table 3 lists the dynamic responses of the bridge with and without the FATMD under different frequencies of the pedestrian load. The results show that the FATMD can effectively suppress the maximum responses of the bridge under various frequencies of the pedestrian load, especially at the excitation frequency of 2.2 Hz, in which the vibration reduction rate is over 75%.

According to the code for design of antimicrovibration of a multistory factory floor (GB 50190-93) [48], the disturbing force of the escalators can be computed as follows:

$$p_0(t) = m_0 e_0 \omega_0^2 \sin \omega_0 t, \quad (14)$$

where m_0 is the total mass of the escalators; e_0 is the eccentricity; and ω_0 is the working circular frequency of the escalators.

In this section, the frequency of external excitation generated by the escalator is 21 Hz and the amplitude of the excitation is 3216.3 N. The frequency of the FATMD is set to match the excitation frequency. Figure 15 shows the time history of the vertical acceleration in the midspan of the bridge under the action of escalators. Figure 16 shows the acceleration envelope diagram of the bridge. The results show that the FATMD can effectively reduce the vertical vibration of the bridge. The vibration reduction rate of the peak acceleration is 70.4%.

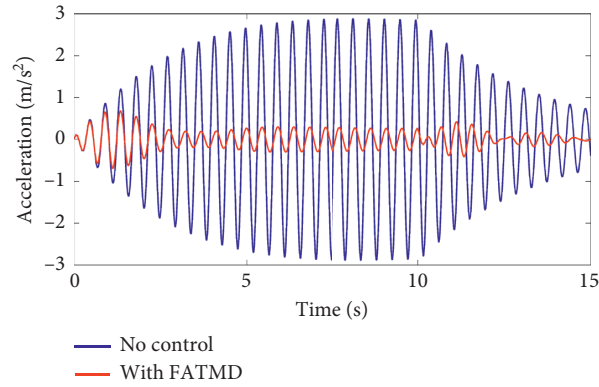


FIGURE 13: The acceleration time history in the midspan of the bridge ($f_p = 2.2$ Hz).

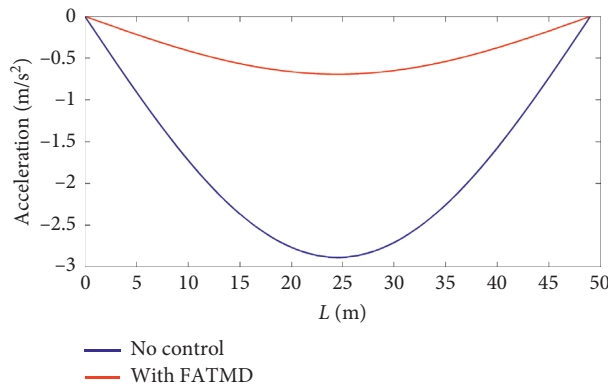


FIGURE 14: The acceleration envelope diagram of the bridge ($f_p = 2.2$ Hz).

TABLE 3: Dynamic responses in the midspan of the bridge with and without the FATMD.

f_p (Hz)	Peak displacement (mm)		Vibration reduction ratio (%)	Peak acceleration (m/s^2)		Vibration reduction ratio (%)
	Uncontrolled	With FATMD		Uncontrolled	With FATMD	
1.8	0.35	0.24	31.43	0.54	0.36	32.58
2.0	0.57	0.30	47.37	0.97	0.50	48.45
2.2	1.50	0.36	76.00	2.89	0.69	76.12
2.5	0.53	0.24	54.72	1.20	0.53	55.83

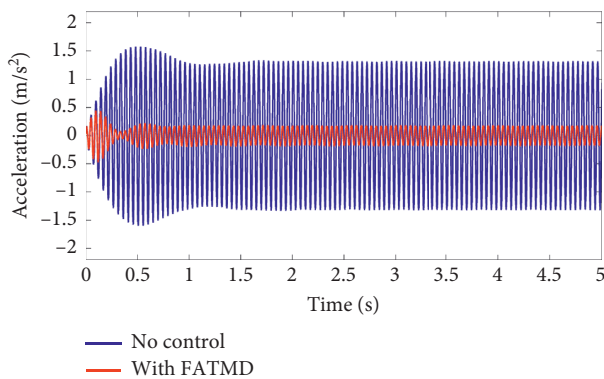


FIGURE 15: The acceleration time history in the midspan of the bridge.

Furthermore, the vertical responses of the bridge with and without the FATMD are computed under three different seismic records (Table 4), including the Imperial Valley earthquake, the Kobe earthquake, and the Borrego earthquake. The frequency of the FATMD is set to match the natural frequency of the bridge. The peak ground accelerations (PGA) of each seismic record are, respectively, adjusted to be 0.2g. Figure 17 shows the time history of the vertical acceleration in the midspan of the bridge under the three earthquakes. Table 5 lists the dynamic responses of the bridge with and without the FATMD under different earthquakes. It is concluded that the FATMD can effectively suppress the vertical accelerations and displacements in the midspan of the bridge under the three earthquakes.

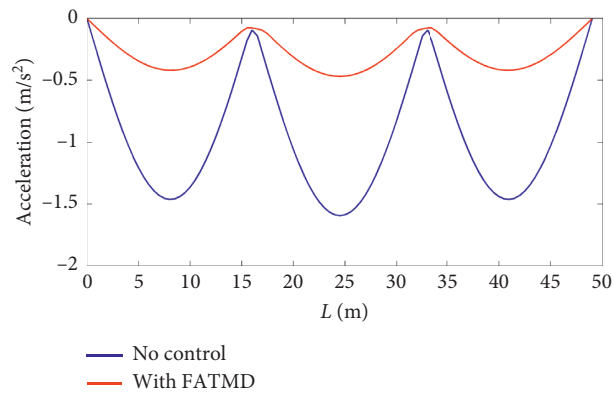


FIGURE 16: The acceleration envelope diagram of the bridge.

TABLE 4: Seismic records.

Earthquake	Event date	Recording station	Acceleration component	Peak ground acceleration (m/s ²)
Imperial Valley	5/19/1940	El Centro	East-west	0.659
Kobe	1/16/1995	Taka tori	North-south	8.178
Borrego	10/21/1942	El Centro	East-west	1.961

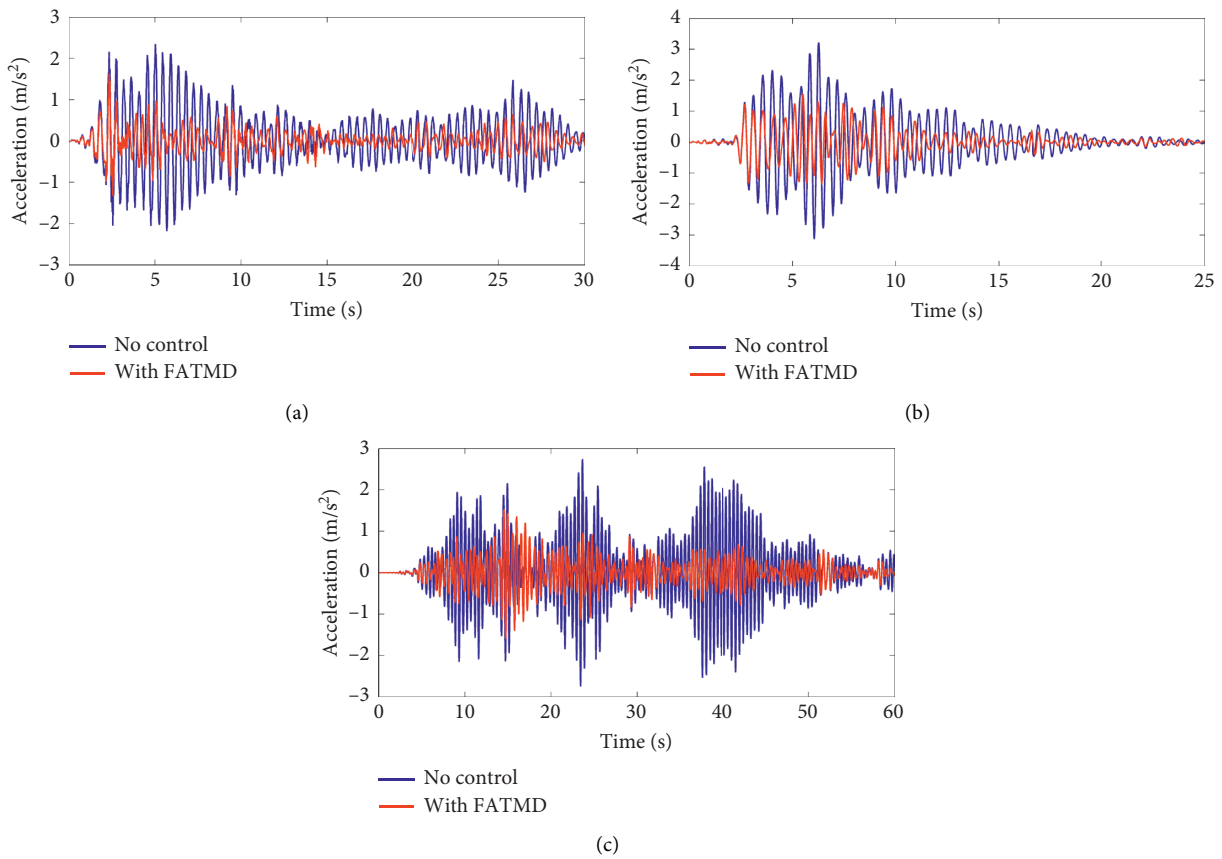


FIGURE 17: The acceleration time history in the midspan of the bridge. (a) Imperial Valley earthquake, (b) Kobe earthquake, and (c) Borrego earthquake.

TABLE 5: Dynamic responses in the midspan of the bridge with and without the FATMD.

Earthquake	Imperial Valley	Kobe	Borrego
Peak displacement (mm)			
Uncontrolled	1.29	1.65	1.80
With FATMD	0.69	0.85	0.98
Vibration reduction ratio (%)	46.51	48.48	45.56
Peak acceleration (m/s^2)			
Uncontrolled	2.34	3.21	2.74
With FATMD	1.62	1.55	1.59
Vibration reduction ratio (%)	30.77	51.71	41.97

7. Conclusions

In this paper, an FATMD composed of a simple supported beam with a mass is proposed to suppress high-frequency vibrations that can be generated by heavy machinery. Forced vibration experiments are conducted to verify the vibration suppression capabilities of the FATMD. Numerical and experimental analysis verified that the natural frequency of the FATMD can be adjusted and that the FATMD frequency decreases with the increased beam span. The FATMD can effectively reduce the structural vibrations at different tested high frequencies. The vibration suppression effect of the FATMD is stable between $\lambda = 0.9$ – 1.1 , with $\lambda = 1.0$ being a relatively optimal value according to the curves. The vibration control effect of the FATMD increases with increased mass ratio and decreased damping ratio. Furthermore, the FATMD is an easily assembled structure that can be quickly adjusted for various natural frequencies, thus enabling the FATMD to be simpler to use than the normal TMD. The numerical results of the pedestrian bridge with an FATMD indicate that the FATMD has a significant effect on reducing the vibration of the pedestrian bridge under the excitations of pedestrians, escalators, and earthquakes.

However, the beam needs to remain in its elastic range for the FATMD to be effective, which limits the allowable range of stiffness that the FATMD can be tuned. Therefore, the FATMD may be detuned under high-intensity excitations, and its effectiveness may be significantly degraded. In the future work, the proposed FATMD will be optimally designed to improve its vibration control performance. The multiple FATMDs will be numerical and experimentally studied for the vibration control of structures with the consideration of multiple hazards, including the machine-, pedestrian-, earthquake-, and wind-induced vibrations.

Data Availability

The data used to support the findings of this study are available from the corresponding author upon request.

Conflicts of Interest

The authors declare that they have no conflicts of interest regarding the publication of this paper.

Acknowledgments

This work was partially supported by the General Project of the Natural Science Foundation of China (Grant No. 51578114).

References

- [1] T.-C. Pan, A. Mita, and J. Li, "Vehicle-induced floor vibrations in a multistory factory building," *Journal of Performance of Constructed Facilities*, vol. 15, no. 2, pp. 54–61, 2001.
- [2] J. M. W. Brownjohn, T. C. Pan, C. Middleton, S. C. Tan, and G. Yang, "Floor vibration serviceability in a multistory factory building," *Journal of Performance of Constructed Facilities*, vol. 30, no. 1, Article ID 04014203, 2016.
- [3] N. W. M. Bishop, M. Willford, and R. Pumphrey, "Human induced loading of flexible staircases," *Engineering Structures*, vol. 23, no. 1, pp. 37–45, 2001.
- [4] C. J. Middleton and J. M. W. Brownjohn, "Response of high frequency floors: a literature review," *Engineering Structures*, vol. 32, no. 2, pp. 337–352, 2010.
- [5] G. E. Thermou, S. J. Pantazopoulou, and A. S. Elnashai, "Design methodology for seismic upgrading of substandard reinforced concrete structures," *Journal of Earthquake Engineering*, vol. 11, no. 4, pp. 582–606, 2007.
- [6] C. Jaafari and J. Mohammadi, "Floor vibration control as a serviceability requirement in design standards and practices: review," *Practice Periodical on Structural Design and Construction*, vol. 23, no. 2, Article ID 04018003, 2018.
- [7] A. Ebrahimpour and R. L. Sack, "A review of vibration serviceability criteria for floor structures," *Computers & Structures*, vol. 83, no. 28–30, pp. 2488–2494, 2005.
- [8] Z. Wang, F. Liu, Z. Wu, and C. Zhang, "Vibration control of floor for a flour mill building," *Building Structure*, vol. 45, no. 19, pp. 32–36, 2015.
- [9] J. T. P. Yao, "Concept of structural control," *Journal of the Structural Division*, vol. 98, no. ST7, pp. 1567–1574, 1972.
- [10] C.-L. Lee, Y.-P. Wang, and R. K. L. Su, "Assessment of vibrations induced in factories by automated guided vehicles," *Proceedings of the Institution of Civil Engineers—Structures and Buildings*, vol. 166, no. 4, pp. 182–196, 2013.
- [11] T. Zordan, T. Liu, B. Briseghella, and Q. Zhang, "Improved equivalent viscous damping model for base-isolated structures with lead rubber bearings," *Engineering Structures*, vol. 75, pp. 340–352, 2014.
- [12] M. Setareh, J. K. Ritchey, and T. M. Murray, "A study of the application of the pendulum tuned mass dampers in building floor vibration controls," in *Proceedings of the Second International Conference on High Performance Structures and Materials*, pp. 287–296, Ancona, Italy, 2004.
- [13] Z. Sun, Z. L. Zou, X. Y. Ying, and X. Q. Li, "Tuned mass dampers for wind-induced vibration control of chongqi bridge," *Journal of Bridge Engineering*, vol. 25, no. 1, Article ID 05019013, 2020.
- [14] E. Caetano, Á. Cunha, F. Magalhães, and C. Moutinho, "Studies for controlling human-induced vibration of the Pedro e Inês footbridge, Portugal. Part 1: assessment of dynamic behaviour," *Engineering Structures*, vol. 32, no. 4, pp. 1069–1081, 2010.
- [15] E. Caetano, Á. Cunha, C. Moutinho, and F. Magalhães, "Studies for controlling human-induced vibration of the Pedro e Inês footbridge, Portugal. Part 2: implementation of tuned mass dampers," *Engineering Structures*, vol. 32, no. 4, pp. 1082–1091, 2010.

- [16] N. Carpineto, W. Lacarbonara, and F. Vestroni, "Mitigation of pedestrian-induced vibrations in suspension footbridges via multiple tuned mass dampers," *Journal of Vibration and Control*, vol. 16, no. 5, pp. 749–776, 2010.
- [17] L. S. Vellar, S. P. Ontiveros-Perez, L. F. F. Miguel, and L. F. F. Miguel, "Robust optimum design of multiple tuned mass dampers for vibration control in buildings subjected to seismic excitation," *Shock and Vibration*, vol. 2019, Article ID 9273714, 9 pages, 2019.
- [18] S. Elias, R. Rupakhty, and S. Olafsson, "Analysis of a benchmark building installed with tuned mass dampers under wind and earthquake loads," *Shock and Vibration*, vol. 2019, Article ID 7091819, 13 pages, 2019.
- [19] R. R. Gerges and B. J. Vickery, "Parametric experimental study of wire rope spring tuned mass dampers," *Journal of Wind Engineering and Industrial Aerodynamics*, vol. 91, no. 12–15, pp. 1363–1385, 2003.
- [20] E.-M. He, Y.-Q. Hu, and Y. Zhang, "Optimization design of tuned mass damper for vibration suppression of a barge-type offshore floating wind turbine," *Proceedings of the Institution of Mechanical Engineers, Part M: Journal of Engineering for the Maritime Environment*, vol. 231, no. 1, pp. 302–315, 2017.
- [21] Q. Wu, W. Zhao, W. G. Zhu, R. C. Zheng, and X. L. Zhao, "A tuned mass damper with nonlinear magnetic force for vibration suppression with wide frequency range of offshore platform under earthquake loads," *Shock and Vibration*, vol. 2018, Article ID 1505061, 18 pages, 2018.
- [22] S. V. Bakre and R. S. Jangid, "Optimum parameters of tuned mass damper for damped main system," *Structural Control and Health Monitoring*, vol. 14, no. 3, pp. 448–470, 2007.
- [23] Y.-J. Kang and L.-Y. Peng, "Optimisation design and damping effect analysis of large mass ratio tuned mass dampers," *Shock and Vibration*, vol. 2019, Article ID 8376781, 16 pages, 2019.
- [24] Z. Lu, D. Wang, and Y. Zhou, "Experimental parametric study on wind-induced vibration control of particle tuned mass damper on a benchmark high-rise building," *The Structural Design of Tall and Special Buildings*, vol. 26, no. 8, p. e1359, 2017.
- [25] Z. Lu, B. Huang, Q. Zhang, and X. Lu, "Experimental and analytical study on vibration control effects of eddy-current tuned mass dampers under seismic excitations," *Journal of Sound and Vibration*, vol. 421, pp. 153–165, 2018.
- [26] P. Zhang, G. Song, H.-N. Li, and Y.-X. Lin, "Seismic control of power transmission tower using pounding TMD," *Journal of Engineering Mechanics*, vol. 139, no. 10, pp. 1395–1406, 2013.
- [27] Q. C. Xue, J. C. Zhang, J. He, and C. W. Zhang, "Control performance and robustness of pounding tuned mass damper for vibration reduction in SDOF structure," *Shock and Vibration*, vol. 2016, Article ID 8021690, 15 pages, 2016.
- [28] H. He, W. Wang, and H. Xu, "Multidimensional seismic control by tuned mass damper with Poles and torsional pendulums," *Shock and Vibration*, vol. 2017, Article ID 5834760, 14 pages, 2017.
- [29] M. D. S. D. Santos, D. V. F. Lima, J. E. C. Carmona, S. M. Avila, and G. N. D. D. Carvalho, "Vibration control of a gym floor using tuned mass dampers: a numerical analysis," *Modern Mechanical Engineering*, vol. 3, no. 3, pp. 9–16, 2013.
- [30] D.-C. Nguyen, "Determination of optimal parameters of the tuned mass damper to reduce the torsional vibration of the shaft by using the principle of minimum kinetic energy," *Proceedings of the Institution of Mechanical Engineers, Part K: Journal of Multi-Body Dynamics*, vol. 233, no. 2, pp. 327–335, 2019.
- [31] Y. S. Tarn, J. Y. Kao, and E. C. Lee, "Chatter suppression in turning operations with a tuned vibration absorber," *Journal of Materials Processing Technology*, vol. 105, no. 1–2, pp. 55–60, 2000.
- [32] Y. Yang, J. Munoa, and Y. Altintas, "Optimization of multiple tuned mass dampers to suppress machine tool chatter," *International Journal of Machine Tools and Manufacture*, vol. 50, no. 9, pp. 834–842.
- [33] M.-L. Chang, C.-C. Lin, J.-M. Ueng, K.-H. Hsieh, and J.-F. Wang, "Experimental study on adjustable tuned mass damper to reduce floor vibration due to machinery," *Structural Control and Health Monitoring*, vol. 17, no. 5, pp. 532–548, 2010.
- [34] M. Abdel-Rohman, M. J. John, and M. F. Hassan, "Compensation of time delay effect in semi-active controlled suspension bridges," *Journal of Vibration and Control*, vol. 16, no. 10, pp. 1527–1558, 2010.
- [35] G. Jiang and L. M. Hanagan, "Semi-active TMD with piezoelectric friction dampers in floor vibration control," in *Proceedings of the Smart Structures and Materials 2006: Damping and Isolation*, San Diego, CA, USA, 2006.
- [36] K. Esteki, A. Bagchi, and R. Sedaghati, "Semi-active control of seismic response of a building using MR fluid-based tuned mass damper," *Smart Structures and Systems*, vol. 16, no. 5, pp. 807–833, 2015.
- [37] N. Varadarajan and S. Nagarajaiah, "Wind response control of building with variable stiffness tuned mass damper using empirical mode decomposition/hilbert transform," *Journal of Engineering Mechanics*, vol. 130, no. 4, pp. 451–458, 2004.
- [38] S. Nagarajaiah, "Adaptive passive, semiactive, smart tuned mass dampers: identification and control using empirical mode decomposition, hilbert transform, and short-term fourier transform," *Structural Control and Health Monitoring*, vol. 16, no. 7–8, pp. 800–841, 2010.
- [39] M. W. Ryan, M. A. Franchek, and R. Bernhad, "Adaptive-passive vibration control of single frequency excitations applied to noise control," in *Proceedings of the 1994 National Conference on Noise Control Engineering*, pp. 461–466, Fort Lauderdale, FL, USA, 1994.
- [40] M. T. Contreras, D. T. R. Pasala, and S. Nagarajaiah, "Adaptive length SMA pendulum smart tuned mass damper performance in the presence of real time primary system stiffness change," *Smart Structures and Systems*, vol. 13, no. 13, pp. 219–233, 2014.
- [41] S. Nagarajaiah and D. T. R. Pasala, "NEESR-adapt-struct: semi-active control of ASD device—adaptive length pendulum dampers," in *Proceedings of the Analysis and Computation Specialty Conference*, pp. 325–334, Orlando, FL, USA, 2010.
- [42] O. B. Mekki, F. Bourquin, F. Maceri, and C. N. Van Phu, "An adaptive pendulum for evolving structures," *Structural Control and Health Monitoring*, vol. 19, no. 1, pp. 43–54, 2012.
- [43] W. Shi, L. Wang, and Z. Lu, "Study on self-adjustable tuned mass damper with variable mass," *Structural Control and Health Monitoring*, vol. 25, no. 3, p. e2114, 2018.
- [44] I. Venanzi, F. Ubertini, and A. L. Materazzi, "Optimal design of an array of active tuned mass dampers for wind-exposed high-rise buildings," *Structural Control and Health Monitoring*, vol. 20, no. 6, pp. 903–917, 2013.
- [45] M. S. Rahman, M. K. Hassan, S. Chang, and D. Kim, "Adaptive multiple tuned mass dampers based on modal parameters for earthquake response reduction in multi-story buildings," *Advances in Structural Engineering*, vol. 20, no. 9, pp. 1375–1389, 2017.

- [46] H. Sun, W. Wang, H. Ding, J. Li, and C. Zhang, "Natural frequency measurement of pipe vibration for vortex flowmeter," in *Proceedings of the 2019 IEEE International Instrumentation and Measurement Technology Conference*, Auckland, New Zealand, 2019.
- [47] N. Poovarodom, S. Kanchanosot, and P. Warnitchai, "Application of non-linear multiple tuned mass dampers to suppress man-induced vibrations of a pedestrian bridge," *Earthquake Engineering & Structural Dynamics*, vol. 32, no. 7, pp. 1117–1131, 2003.
- [48] GB50190-93, *Code for Design of Anti-microvibration of Multistory Factory Floor*, China Planning Press, Beijing, China, 1994.

Research Article

Effectiveness of Friction Dampers in Seismic and Wind Response Control of Connected Adjacent Steel Buildings

Anshul Malhotra, Tathagata Roy , and Vasant Matsagar 

Multi-Hazard Protective Structures (MHPS) Laboratory, Department of Civil Engineering, Indian Institute of Technology (IIT) Delhi, Hauz Khas, New Delhi 110 016, India

Correspondence should be addressed to Vasant Matsagar; matsagar@civil.iitd.ac.in

Received 20 December 2019; Revised 25 July 2020; Accepted 6 August 2020; Published 15 September 2020

Academic Editor: Evgeny Petrov

Copyright © 2020 Anshul Malhotra et al. This is an open access article distributed under the Creative Commons Attribution License, which permits unrestricted use, distribution, and reproduction in any medium, provided the original work is properly cited.

Effectiveness of friction dampers (FDs) is investigated for connected dynamically similar and dissimilar steel buildings under uncorrelated seismic ground motion and wind excitations. The steel buildings involving moment-resisting frame (MRF) and braced frame (BF) are varied from five storeys to twenty storeys, which are connected by different configurations of the FDs. The steel buildings without and with bracing systems are modeled as plane frame structures with inertial masses lumped at each joint node. The FDs are modeled an element having yield force equal to slip load, with force-deformation behavior as elastic-perfectly plastic material. The dynamic responses of the unconnected and connected steel buildings are obtained in terms of top floor displacement and acceleration under the considered ground motion and wind excitations. It is concluded that the FDs help minimizing the gap between two adjacent buildings having utilized the space to connect the buildings. Moreover, the effectiveness of the FDs in terms of response reduction in dynamically dissimilar buildings is more than that in the similar buildings under the considered excitation scenarios. However, the effectiveness of the installed devices varies significantly under the multiple loading scenarios. Finally, the separation gap may be reduced by ~30%, which would eventually minimize structural pounding as well as utilize the space for effective construction. Hence, important essential guidelines are outlined for structures installed with such passive control devices against such multiple scenario loadings.

1. Introduction

Structures constructed in moderate-to-high seismicity and windy regions have experienced damages due to extreme vibrational effects under severe ground shaking and gusty wind loading imparted [1–6]. To minimize these damaging effects and improve the behavior of the structures under such dynamic excitations, friction damper (FD) has been one of the potential passive response control devices developed in minimizing the large response of a structure under the extreme earthquake and wind excitations [7, 8]. In a typical FD, the generated frictional force helps to dissipate the external energy and stabilize the structure under the dynamic excitation scenarios [9]. The FDs are also not prone to thermal effects and possess a stable hysteretic behavior for a considerable number of cycles under such dynamic

excitations [10]. Moreover, the FDs have a reliable performance under the dynamic excitations as compared to the other conventional methods and their installation and maintenance are relatively simple. Therefore, these advantages make the FDs a suitable choice for design of new structures as well as rehabilitation and strengthening of existing structures to achieve safety of the structures under the multiple catastrophic seismic and wind hazards [11, 12].

With the recent increase in urbanization and globalization, the structural engineers and designers are enforced to construct buildings at a close vicinity resulting in insufficient separation gap between the buildings. Such insufficient gap leads to structural pounding under the effects of seismic ground motions and gusty winds, which may lead to catastrophic collapse of the buildings, as observed during 1985 Mexico City earthquake. The primary reason of impact

between the adjacent buildings under the effects of earthquake (or wind excitations) is the difference in their dynamic properties. These differences in structural properties lead to out-of-phase vibrations causing structural pounding, which warrants technical knowhow for constructions in high-urbanized regions across the world [13]. Hence, in order to have effective utilization of the space between two structures, coupling of the adjacent structures with suitable control mechanisms becomes an effective solution to reduce the overall responses of the building systems under the effects of earthquake and wind excitations [14].

The friction damper (FD) was initially used in steel buildings for improving the seismic performance [15, 16]. The proposed device was helpful to upgrade the seismic resistance of the existing building frames. Thereafter, the FDs were adopted for braced frames, buildings with shear walls, and low-rise buildings to mitigate the large deformations caused by earthquake ground motions and winds [17–19]. The application of this novel structural system was further focused on construction of an 18-storey steel apartment building in India [20]. It was observed that significant seismic response reduction was achieved on application of the Pall FDs in the steel building. Research further progressed in assessing and designing the parameters of the FDs for different structural systems under ground motion excitations [10, 21]. Lately, the FDs were used in mid-rise to high-rise buildings along with diagonal bracing, which reduced the seismic responses considerably [22, 23]. Moreover, Montuori et al. [24] presented an innovative approach to design a seismic resistant system for the combination of moment-resisting frame (MRF) and a bracing system installed with the FDs. Thereafter, multi-objective optimization procedure was applied to find the optimal placements of the FDs in building frame [25–27]. Research is also conducted to optimize the slip load and investigate the hysteretic behavior of structures using rotational FD [28, 29]. The FD has also found its application in the infrastructure system, such as transmission tower to control the large seismic deformations [30].

Coupling of adjacent buildings has been an emerging technique to mitigate the large structural responses due to wind and seismic excitations [31, 32]. The concept allows two dynamically similar and/or dissimilar structures to exert the forces upon one another for overall response reduction of the system. The available studies showed improved performance of the structural systems by connecting different passive control devices to limit the pounding actions under earthquake ground motions [14, 33–39]. Overall, the FDs have offered its potential in minimizing the extreme vibrations installed in a structure; however, research strategies have not been implemented to assess the response and quantify the effectiveness of the FDs for coupled adjacent buildings under both seismic and wind excitations. Therefore, it becomes important to investigate the connected structures installed with the FDs to mitigate the responses of adjoining building and avoiding poundings against the multihazard scenario of earthquake and wind loadings during design life of structures.

Herein, effectiveness of the FDs is investigated for connected dynamically similar and dissimilar adjacent steel moment-resisting frame (MRF) and braced frame (BF) buildings with varying storeys under the multihazard uncorrelated scenarios of seismic and wind hazards. Site-specific earthquake ground motions and wind excitations are assumed to describe the multihazard scenario for assessment of the unconnected and connected steel structures. In view of the abovementioned gaps, the main objectives of the current study are as follows: (i) to study the effectiveness of the FDs for the connected dynamically similar and dissimilar multistorey buildings under multihazard earthquake and wind excitations and (ii) to investigate the effects of varying number of storeys of the connected dynamically similar and dissimilar multistorey buildings under earthquake and wind excitations evaluating the response of the FDs in multihazard conditions.

2. Mathematical Modeling

Mathematical models for N -storey dynamically similar and dissimilar moment-resisting frames (MRFs) and braced frames (BFs) connected by the FDs are developed for different configurations, as shown in Figures 1 and 2, under the dynamic earthquake and wind loadings. Three configuration systems for the connected buildings, viz., configuration A, B, and C are considered to assess the effectiveness of the FDs. Configuration A has two friction dampers at each storey in X crossing pattern, with cross-bracing at all floor levels, as shown in Figures 1(c) and 2(c). Configuration B has one friction damper at each storey in a zigzag pattern as shown in Figures 1(d) and 2(d). Configuration C has two friction dampers at each storey in X crossing pattern up to $0.4N$ of upper storey of the building from the top, as shown in Figures 1(e) and 2(e), where N is the number of storey. The assumptions made for developing the mathematical models are as follows: (i) the building members except the FDs are assumed to remain in the elastic limit, a design decision in structural control, (ii) one degree of freedom (DOF) at each floor level in the direction of earthquake ground motion and wind is considered, (iii) the inertial mass is lumped at each floor level, (d) the floors are assumed to be rigid in their own plane, and (e) strength degradation of friction dampers is presently ignored in the analysis.

2.1. Moment-Resisting Frame (MRF). The governing differential equation of motion for the MRF, in general, is written as

$$[M]\{\ddot{u}(t)\} + [C]\{\dot{u}(t)\} + [K]\{u(t)\} = F(t), \quad (1)$$

where $[M]$, $[C]$, and $[K]$ are the mass, damping, and stiffness matrices of the primary structure, respectively. Moreover, $\{\ddot{u}(t)\}$, $\{\dot{u}(t)\}$, and $\{u(t)\}$ are the acceleration, velocity, and displacement response of the primary structure, respectively. Furthermore, $F(t)$ is the external force exerted on the structure, either during the earthquake or wind event. Here, $F(t) = -[M]\{r\}\{\ddot{u}_g(t)\}$ is the inertial force vector induced because of the earthquake ground motion applied to the

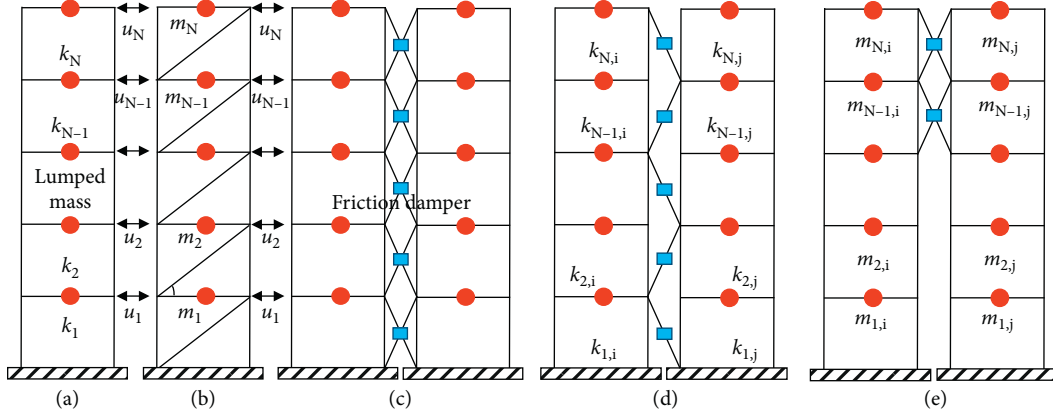


FIGURE 1: Mathematical models of N -storey: (a) unconnected (U) moment-resisting frame (MRF), (b) unconnected (U) braced frame (BF), (c) connected frames (configuration A), (d) connected frames (configuration B), and (e) connected frames (configuration C) for equal storey height.

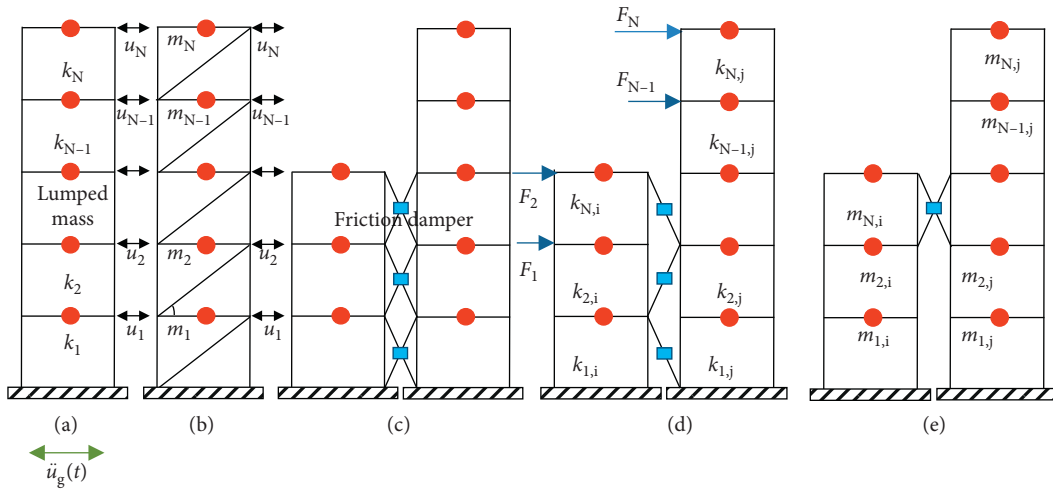


FIGURE 2: Mathematical models of N -storey: (a) unconnected (U) moment-resisting frame (MRF), (b) unconnected (U) braced frame (BF), (c) connected frames (configuration A), (d) connected frames (configuration B), and (e) connected frames (configuration C) for unequal storey heights.

structure (base-excited structure), or $F(t) = \{F_1, F_2, F_3, \dots, F_n\}^T$ is the applied wind force vector at the floor mass on each storey (mass-excited structure). Here, the earthquake ground acceleration is denoted by $\ddot{u}_g(t)$ and $\{r\}$ is the influence coefficient vector. The wind force, $F_n(t) = 0.5\rho C_d A(V + \Delta v)^2$, depends on the environment and building conditions, such as, density of air, ρ ; coefficient of drag, C_d ; depending on shape of the building; area of wind load exposure for n^{th} floor, A_n ; mean wind speed, V ; and fluctuating wind component, Δv . For the MRF, the structure is defined by its mass matrix, damping matrix, and stiffness matrix as $[M]$, $[C]$, and $[K]$, respectively. Here, $[M]$ is a diagonal matrix with the diagonal element $m_{jj} = m_j$, the mass lumped at the j^{th} floor. Flexural rigidity of the columns provides lateral force resistance in the MRF; therefore, only column stiffness contributes towards the formation of $[K]$ matrix. The mass and stiffness matrix of the N -storey MRF can be given as

$$[M] = \begin{bmatrix} m_1 & 0 & 0 & \dots & 0 & 0 \\ 0 & m_2 & 0 & \dots & 0 & 0 \\ 0 & 0 & m_3 & \dots & 0 & 0 \\ \vdots & \vdots & \vdots & \ddots & \vdots & \vdots \\ 0 & 0 & 0 & \dots & m_{N-1} & 0 \\ 0 & 0 & 0 & \dots & 0 & m_N \end{bmatrix}, \quad (2)$$

$$[K] = \begin{bmatrix} k_1 + k_2 & -k_2 & 0 & \dots & 0 & 0 \\ -k_2 & k_2 + k_3 & -k_3 & \dots & 0 & 0 \\ 0 & -k_3 & k_3 + k_4 & \dots & 0 & 0 \\ \vdots & \vdots & \vdots & \ddots & \vdots & \vdots \\ 0 & 0 & 0 & \dots & k_{N-1} + k_N & -k_N \\ 0 & 0 & 0 & \dots & -k_N & k_N \end{bmatrix}. \quad (3)$$

2.2. *Braced Frame (BF)*. The governing differential equation of motion for the BF is written as

$$[M]\{\ddot{u}(t)\} + [C]\{\dot{u}(t)\} + ([K] + [K_b]\cos^2\theta)\{u(t)\} = F(t), \quad (4)$$

where $[M]$ and $[C]$ matrices are constructed similar as that in case of the MRF. In the BF, stiffness of the structure is the combined effect of the stiffness imparted by the columns, i.e., $[K]$, and the braces, i.e., $[K_b]$. Here, θ_N is the angle of the brace with horizontal at the N^{th} storey level and $k_{bi} = k_{b1}, k_{b2}, k_{b3} \dots k_{bN}$ denote the axial stiffness of the braces:

$$[K_b] = \begin{bmatrix} k_{b1} + k_{b2} & -k_{b2} & 0 & \dots & 0 & 0 \\ -k_{b2} & k_{b2} + k_{b3} & -k_{b3} & \dots & 0 & 0 \\ 0 & -k_{b3} & k_{b3} + k_{b4} & \dots & 0 & 0 \\ \vdots & \vdots & \vdots & \ddots & \vdots & \vdots \\ 0 & 0 & 0 & \dots & k_{b(N-1)} + k_{bN} & -k_{bN} \\ 0 & 0 & 0 & \dots & -k_{bN} & k_{bN} \end{bmatrix}. \quad (5)$$

In the BF, the braces are assumed to carry only the axial force and the brace sections are so chosen to ensure that they do not buckle under compression and do not yield under tension.

2.3. *Connected Frame Using Friction Damper (FD)*.

Coulomb's dry friction is used to model the nonlinear behavior of the FDs. The nonlinearity is concentrated only in the friction dampers, assuming rest of the building members (the primary structural system) is in elastic range. This is done to ensure that the energy dissipation occurs in friction dampers only and not by yielding of any other structural members. Hence, the structures with the FDs can be treated as a dual system consisting of nonlinear energy-dissipating devices exhibiting elastoplastic behavior and a primary structural system exhibiting linear behavior. Based on this assumption, the governing equation of motion can be written as

$$[M_{eff}]\{\ddot{u}(t)\} + ([C_{eff}])\{\dot{u}(t)\} + [K_{eff}]\{u(t)\} + F_d = F(t), \quad (6)$$

where $C_{eff} = C + C_d$ and $K_{eff} = K + K_d$. C is the equivalent damping of the building systems, and C_d is the equivalent damping of the FD. Similarly, K is the equivalent stiffness of the building systems and K_d is the equivalent stiffness of the FD, which is assumed to be zero here. $F_d(t) = \mu m_N g \text{sgn}(\dot{u})$ is the frictional force exerted by the FD under the earthquake or wind load, and $m_N g$ or W is the slip load for the FD at each storey level, with g denoting the acceleration due to gravity. The matrices for equation (6) are discussed as follows:

$$[M_{eff}] = \begin{bmatrix} M_A & 0 \\ 0 & M_B \end{bmatrix}, \quad (7)$$

$$[M_A] = \begin{bmatrix} m_{1A} & 0 & 0 & \dots & 0 & 0 \\ 0 & m_{2A} & 0 & \dots & 0 & 0 \\ 0 & 0 & m_{3A} & \dots & 0 & 0 \\ \vdots & \vdots & \vdots & \ddots & \vdots & \vdots \\ 0 & 0 & 0 & \dots & m_{P-1,A} & 0 \\ 0 & 0 & 0 & \dots & 0 & m_{P,A} \end{bmatrix}, \quad (8)$$

$$[M_B] = \begin{bmatrix} m_{1B} & 0 & 0 & \dots & 0 & 0 \\ 0 & m_{2B} & 0 & \dots & 0 & 0 \\ 0 & 0 & m_{3B} & \dots & 0 & 0 \\ \vdots & \vdots & \vdots & \ddots & \vdots & \vdots \\ 0 & 0 & 0 & \dots & m_{Q-1,B} & 0 \\ 0 & 0 & 0 & \dots & 0 & m_{Q,B} \end{bmatrix}, \quad (9)$$

$$[K_{eff}] = \begin{bmatrix} K_A & 0 \\ 0 & K_B \end{bmatrix}, \quad (10)$$

$$K_A = \begin{bmatrix} k_{11,A} + k_{21,A} & -k_{21,A} & 0 & \cdots & 0 & 0 \\ -k_{21,A} & k_{21,A} + k_{31,A} & k_{21,A} + k_{31,A} & \cdots & 0 & 0 \\ 0 & -k_{31,A} & k_{31,A} + k_{41,A} & \cdots & 0 & 0 \\ \vdots & \vdots & \vdots & \ddots & \vdots & \vdots \\ 0 & 0 & 0 & \cdots & k_{P-11,A} + k_{P1,A} & -k_{P1,A} \\ 0 & 0 & 0 & \cdots & -k_{P1,A} & k_{P1,A} \end{bmatrix}, \quad (11)$$

$$K_B = \begin{bmatrix} k_{11,B} & -k_{21,B} & 0 & \cdots & 0 & 0 \\ -k_{21,B} & k_{21,B} + k_{31,B} & -k_{31,B} & \cdots & 0 & 0 \\ 0 & -k_{31,B} & k_{31,B} + k_{41,B} & \cdots & 0 & 0 \\ \vdots & \vdots & \vdots & \ddots & \vdots & \vdots \\ 0 & 0 & 0 & \cdots & k_{Q-11,B} + k_{Q1,B} & -k_{Q1,B} \\ 0 & 0 & 0 & \cdots & -k_{Q1,B} & k_{Q1,B} \end{bmatrix}, \quad (12)$$

$$[C_{eff}] = \begin{bmatrix} C_A & 0 \\ 0 & C_B \end{bmatrix}, \quad (13)$$

$$[C_A] = \begin{bmatrix} c_{11,A} + c_{21,A} & -c_{21,A} & 0 & \cdots & 0 & 0 \\ -c_{21,A} & c_{21,A} + c_{31,A} & -c_{31,A} & \cdots & 0 & 0 \\ 0 & -c_{31,A} & c_{31,A} + c_{41,A} & \cdots & 0 & 0 \\ \vdots & \vdots & \vdots & \ddots & \vdots & \vdots \\ 0 & 0 & 0 & \cdots & c_{P-11,A} + c_{P1,A} & -c_{P1,A} \\ 0 & 0 & 0 & \cdots & -c_{P1,A} & c_{P1,A} \end{bmatrix}, \quad (14)$$

$$[C_B] = \begin{bmatrix} c_{11,B} + c_{21,B} & -c_{21,B} & 0 & \cdots & 0 & 0 \\ -c_{21,B} & c_{21,B} + c_{31,B} & -c_{31,B} & \cdots & 0 & 0 \\ 0 & -c_{31,B} & c_{31,B} + c_{41,B} & \cdots & 0 & 0 \\ \vdots & \vdots & \vdots & \ddots & \vdots & \vdots \\ 0 & 0 & 0 & \cdots & c_{Q-11,B} + c_{Q1,B} & -c_{Q1,B} \\ 0 & 0 & 0 & \cdots & -c_{Q1,B} & c_{Q1,B} \end{bmatrix}, \quad (15)$$

$$[C_d] = \begin{bmatrix} [C_d] & 0 & [-C_d] \\ 0 & 0 & 0 \\ [-C_d] & 0 & [C_d] \end{bmatrix}, \quad (16)$$

$$[C_d] = \begin{bmatrix} c_{d1} & 0 & 0 & \cdots & 0 & 0 \\ 0 & c_{d2} & 0 & \cdots & 0 & 0 \\ 0 & 0 & c_{d1} & \cdots & 0 & 0 \\ \vdots & \vdots & \vdots & \ddots & \vdots & \vdots \\ 0 & 0 & 0 & \cdots & c_{d,N-1} & 0 \\ 0 & 0 & 0 & \cdots & 0 & c_{d,N} \end{bmatrix}. \quad (17)$$

Moreover, $F_d(t) = \mu m_{NG} \text{sgn}(\dot{u})$ is the frictional force exerted by the FD under the earthquake or wind load, and m_{NG} or W is the slip load for the FD at each storey level, with g denoting the acceleration due to gravity. Figure 3 shows the force-deformation behavior of the FD assumed for this study. Furthermore, the stiffness of the brace of the FD is neglected; however, considering realistically the force-

deformation behavior of the friction damper does include initial stiffness provided by the brace.

The numerical solution of the governing differential equations given above for the MRF and BF connected by the FD are obtained by using Newmark's method of nonlinear modal time history adopting linear variation of acceleration over an interval of Δt . The time interval for solving the

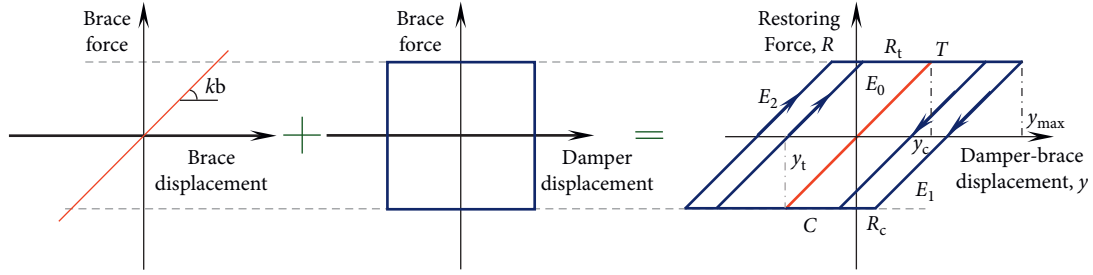


FIGURE 3: (a) Elastic behavior of brace, (b) hysteretic loop of friction damper, and (c) resultant elastoplastic behavior of the friction damper in brace.

TABLE 1: Modeling properties of the elastic-plastic friction damper (FD).

Properties of friction damper	Values
Effective stiffness	0
Stiffness	$5000k$, k is the stiffness of each storey
Yield strength	$0.3W$, W is the storey weight
Postyield stiffness ratio	1×10^{-6}
Yielding coefficient	20

equations of motion is taken as Δt , which also depends on the time step for the external load applied (earthquake ground motion or gusty wind loading).

3. Multihazard Scenario under Earthquake and Wind Excitations

The multihazard assessment strategy involves proper selection of hazard models to assess a structure under the effects of earthquake and wind loadings in a region [40]. The hazard models may be generated using empirical equations, spectra established on physical models, or adopting the already available data from the past earthquake or wind events recorded at the nearest station. For the present study, actual time history data of the earthquake from a recorded station and synthesized time history data of the wind loading from the same region are assumed to investigate the effectiveness of the FD when used to connect adjacent buildings. The time history data are chosen for two different regions, viz., California region of the United States of America (USA), and Kobe city in the southeast region of Japan. The locations are carefully chosen in such a way that the probability of occurrence of the multiple hazards is considerably higher than other regions of the world. Moreover, the considered earthquakes have caused extreme devastations to socioeconomic life as observed from the global statistics. The wind loads, with static and fluctuating components, are simulated from the NatHaz online wind simulator (NOWS): simulation of Gaussian multivariate wind fields [41]. The simulation technique involves obtaining discrete frequency function with Cholesky decomposition and fast Fourier transform (FFT) for wind speed, which is considered as the wind hazard parameter here. The time histories of the wind speeds are obtained thence by summing the static and the fluctuating

components obtained from the simulation based on Bernoulli's theorem.

4. Numerical Study

Herein, a numerical study is conducted to evaluate the effectiveness of the FDs for the connected steel MRF and BF buildings. Modal damping of $\xi = 2\%$ is considered for the two steel buildings. The normalized slip load for the FD at each storey level considered for the study is assumed 30% of the storey weight (W), which can suitably be optimized otherwise. The other relevant parameters adopted to model the FDs for the connected steel buildings are shown in Table 1. For further study, the variation of height is considered in 5, 10, 15, and 20 storey for dynamically similar and dissimilar building frames connected by the FDs. Free vibration analysis is conducted to obtain the modal responses for the unconnected MRFs and BFs, and the results are shown in Table 2. Four historical earthquake ground motions and synthesized wind excitations are selected for the numerical study, for which the details are given in Tables 3 and 4. The response spectrum of ground motion acceleration and displacement is plotted for the selected earthquakes to demonstrate the nature of the responses obtained for the steel buildings, as shown in Figure 4. The wind hazard incorporated in the study is simulated from the NatHaz online simulator with gust speed as 30 m/s, 37 m/s, 43 m/s, and 50 m/s located in urban and suburban areas with numerous closely spaced obstructions (category-B) having cutoff frequencies obtained from the free vibration analysis of the building frames. The gust wind speeds are noted from the regions of interest where multiple hazard scenarios exist. Time history of the wind excitation for different gust speeds along with the corresponding fast Fourier transform (FFT) for the steel buildings is plotted in Figure 5. The FFT spectrum refers to the frequency in the considered wind loads, essential in evaluating the nature of the structural

TABLE 2: Modal periods of the unconnected steel MRF and BF structures.

Building type	Modal periods		
	First	Second	Third
5-storey MRF	0.54	0.18	0.12
10-storey MRF	1.02	0.34	0.21
15-storey MRF	1.51	0.51	0.31
20-storey MRF	1.90	0.63	0.38
5-storey BF	0.32	0.11	0.07
10-storey BF	0.62	0.21	0.13
15-storey BF	0.91	0.31	0.18
20-storey BF	1.15	0.38	0.23

TABLE 3: Details of the earthquake ground motion.

Sl. No.	Earthquake	Year	Recording station	Component	PGA (g)
1	Imperial Valley	1940	El Centro	S00 E	0.34
2	Loma Prieta	1989	LGPC	N00 E	0.56
3	Northridge	1994	Rinaldi	N360S	0.83
4	Kobe	1995	JMA Record	EW	0.67

TABLE 4: Details of the wind time history.

Sl. No.	Wind speed (m/s)	Cutoff frequency (Hz)	Exposure category	Duration (s)
1	30			
2	37	0.5	B	3000
3	43			
4	50			

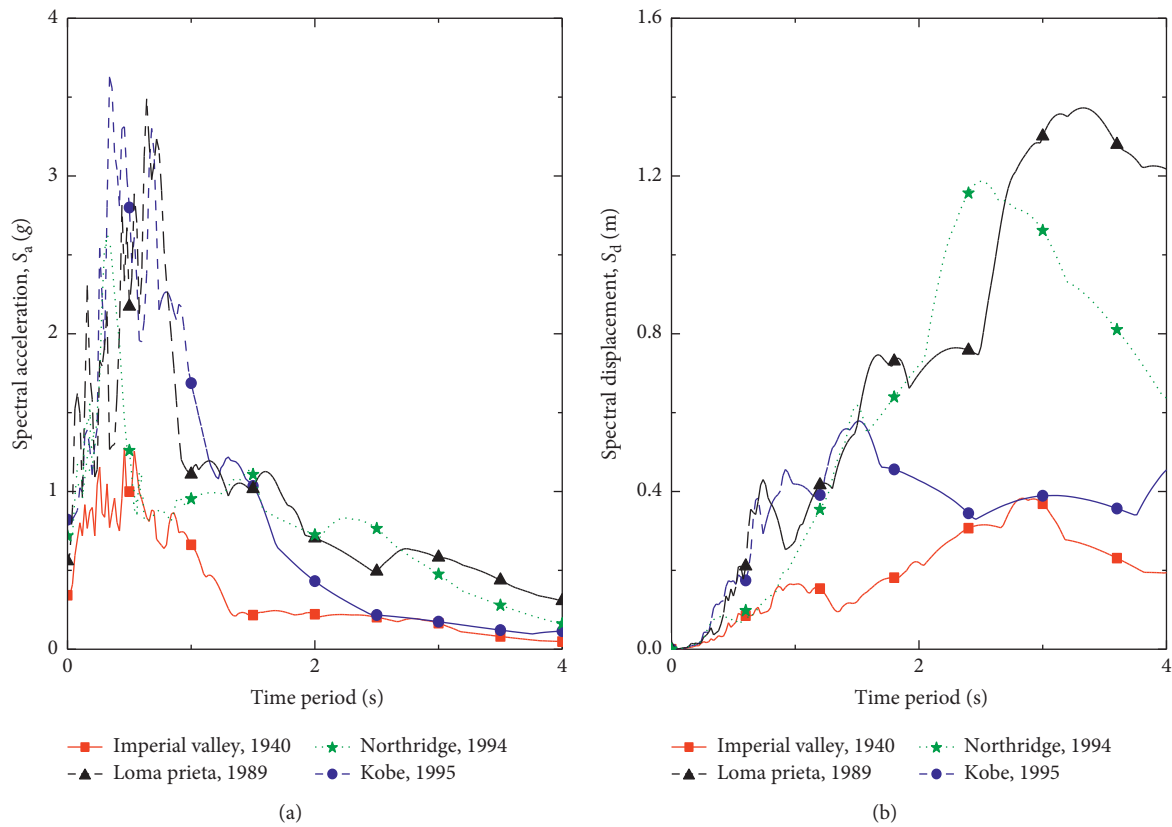


FIGURE 4: Acceleration and displacement response spectra of the considered historical earthquake ground motions.

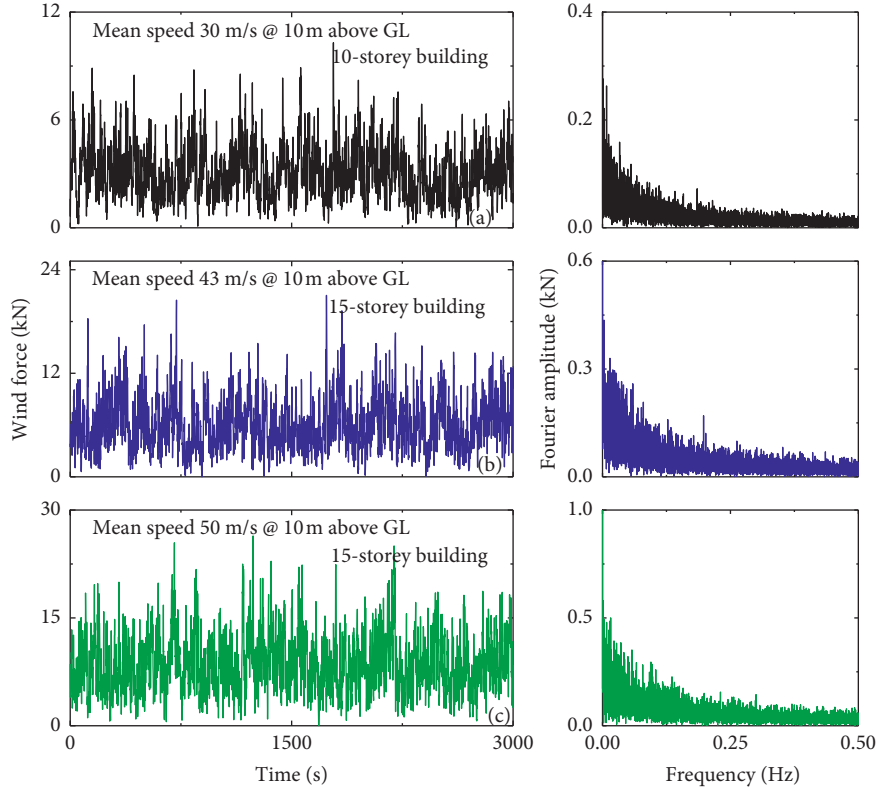


FIGURE 5: Wind speed at specific height for 10- and 15-storey buildings along with the frequency content (FFT spectra).

TABLE 5: Combinations of dynamically similar and dissimilar connected buildings considered for the study.

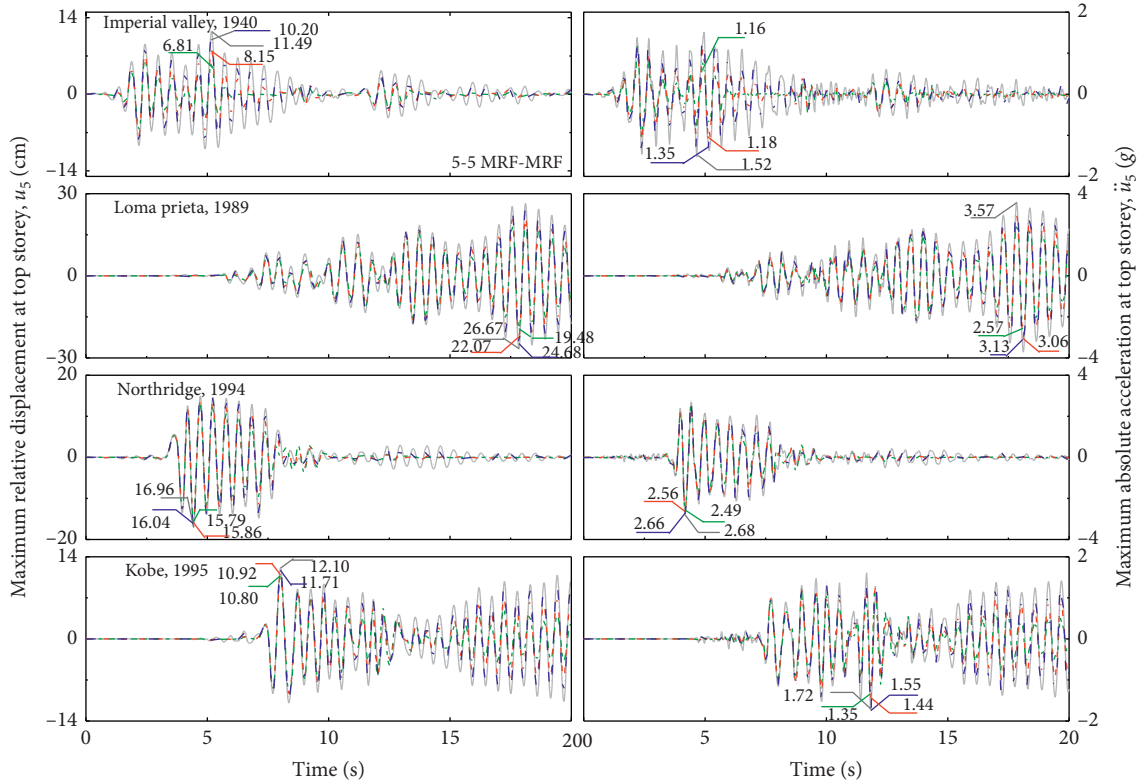
Similar buildings		Dissimilar buildings			
MRF*-MRF	BF*-BF	MRF*-BF	BF*-MRF	MRF*-MRF	BF*-BF
5-5	5-5	5-5	5-5	5-10	5-10
10-10	10-10	10-10	10-10	5-15	5-15
15-15	15-15	15-15	15-15	5-20	5-20
20-20	20-20	20-20	20-20	10-15	10-15
—	—	—	—	10-20	10-20
—	—	—	—	15-20	15-20

*Responses shown for that particular building.

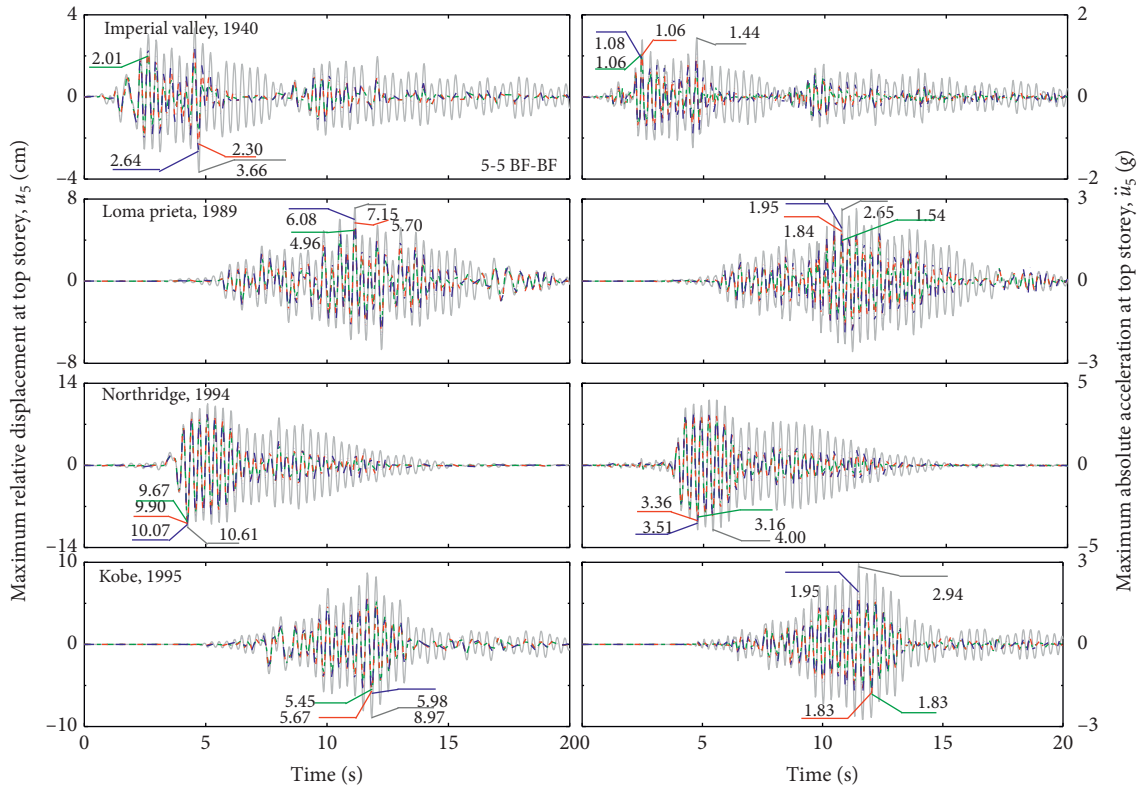
responses under the gusty wind loads. The top floor displacement (u_n , $n = 5, 10, 15$, or 20) and acceleration (\ddot{u}_n , $n = 5, 10, 15$, or 20) of dynamically similar and dissimilar unconnected buildings are compared with the connected buildings to evaluate the effectiveness and to obtain the best suitable configuration of the FDs. Note, hence on the peak top floor displacement is denoted by x_n ; whereas, the peak top floor acceleration is denoted by \ddot{x}_n . The connected structures considered in the study are as follows: (a) MRF-MRF, (b) BF-BF, (c) MRF-BF, (d) BF-MRF, (e) different storeys for MRF-MRF, and (f) different storeys for BF-BF, also summarized in Table 5, which constitutes of the most prominent configurations of the buildings. The direction of loading, earthquake or wind, is applied in the direction of left to right of the shear frames, i.e., along the degree of freedom (DOF) considered at the lumped masses. The wind load is applied from 10 m above ground level at the center of mass of the structure, as shown in Figure 2(d). The direction of

wind load has no contribution to the objective of the study, rather it is just a choice of analysis procedure. Finally, the buildings are connected by the FDs keeping 5 m separation gap distance, as recommended by most of the building bylaws across the world.

4.1. Effectiveness of FD for Dynamically Similar Connected Buildings. Herein, the effectiveness of the FDs is investigated by comparing the responses of the unconnected (U) and connected (C) steel MRFs and BFs for different configurations of the passive FD under earthquake ground motions and wind forces. The responses are illustrated in terms of time history plots under the considered loading scenarios to demonstrate the effectiveness of the FDs. Moreover, peak responses are plotted to understand the variation in the responses for the considered connected buildings obtained under the dynamic loading scenarios.



(a)



(b)

FIGURE 6: (a) Time history response of top floor displacement and acceleration of connected steel 5-5 MRF-MRF buildings under different earthquake ground motions. (b) Time history response of top floor displacement and acceleration of connected steel 5-5 BF-BF buildings under different earthquake ground motions.

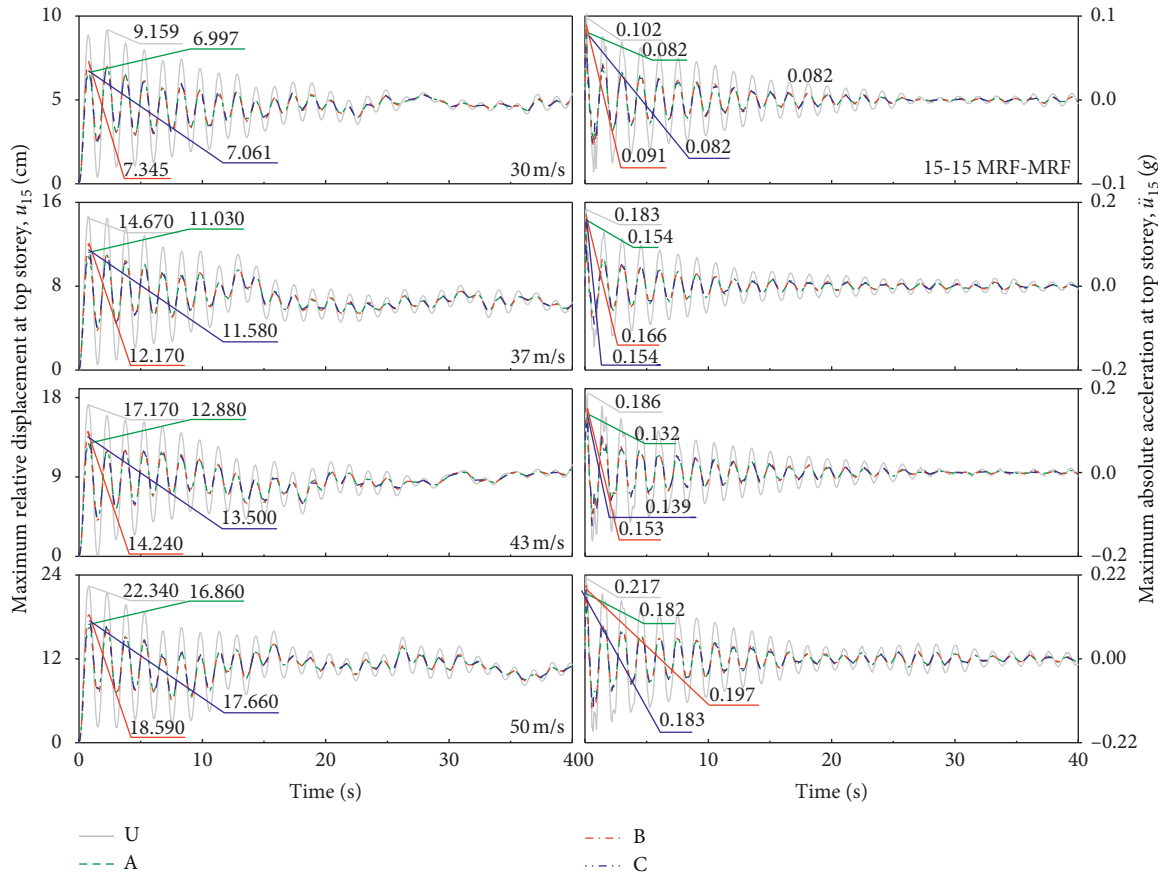


FIGURE 7: Time history response of top floor displacement and acceleration of connected steel 15-15 MRF-MRF buildings under different wind gust speeds.

Figures 6(a) and 6(b) show the displacement and acceleration responses in time history scale for the dynamically similar connected 5-storey MRF and BF under the considered earthquake ground excitations, whereas Figure 7 shows the dynamic responses of the connected 15-storey MRF under the considered wind forces.

Considering top floor displacement, the reduction in peak response for 5-5 MRF-MRF when connected using configuration A is obtained from ~7% to 41%, whereas the reduction is, respectively, obtained from 6% to 29% and ~3% to 11% for configurations B and C under the historical earthquakes. Furthermore, for the top floor acceleration, the response reductions for configurations A, B, and C are, respectively, obtained from ~7% to 28%, ~4% to 22%, and ~1% to 7%. Similar observations are also noted for the 5-5 BF-BF. Hence, the FDs used in configuration A are able to dissipate the highest amount of induced input energy as compared to the other configuration of FDs. For the considered wind loads, 15-storey connected MRF is studied, and it is observed that the reduction in the peak top floor displacement is also the highest for configuration A (~23% to 25%) as compared to configurations B (~17% to 20%) and C (~21% to 23%). However, the range of difference under the wind loads is quite small as compared to the range under the earthquakes. For the peak top floor acceleration, the highest response reduction is also obtained for configuration A (~16%

to 29%), whereas the least response reduction is observed under configuration B under both earthquake and wind loads.

Similarly, the displacement and acceleration responses for all the considered dynamically similar buildings with increased storey heights under earthquakes and winds are compared from Tables 6 and 7 as well as from Figures 8(a) and 8(b). Overall, under the earthquake excitations, the response reduction for top floor displacement and acceleration of the low-rise buildings is significantly higher as compared to high-rise buildings, which is observed to be contrary for the wind scenario that has increased response reduction for high-rise buildings. The characteristics of the obtained dynamic responses depend mainly on the modal properties of the structure and nature of the dynamic excitations. The displacement responses for the dynamically similar connected buildings under the earthquakes and winds increase with increase in building height. Moreover, the displacement responses obtained under the earthquakes increased significantly as compared to the responses obtained under the wind loadings. This implies that the energy content of the earthquake is comparably higher and has significant effect in determining the responses of the structure. On the other hand, the acceleration responses for the dynamically similar connected buildings under the earthquakes decrease with increase in building height. Conversely, the acceleration responses

TABLE 6: Peak top floor displacement and acceleration responses of similar connected buildings for equal storey height under historical earthquake ground motions.

Frame	Earthquake	Peak top floor displacement, x_n (cm)				Peak top floor acceleration, \ddot{x}_n (g)			
		U	A	B	C	U	A	B	C
5-5 MRF-MRF	Imperial Valley, 1940	11.49	6.81	8.15	10.20	1.52	1.16	1.18	1.35
	Loma Prieta, 1989	26.67	19.48	22.07	24.68	3.57	2.57	3.06	3.13
	Northridge, 1994	16.96	15.79	15.86	16.04	2.68	2.49	2.56	2.66
	Kobe, 1995	12.10	10.80	10.92	11.71	1.72	1.35	1.44	1.55
20-20 MRF-MRF	Imperial Valley, 1940	22.18	15.82	19.24	21.81	0.59	0.43	0.45	0.51
	Loma Prieta, 1989	81.23	59.32	68.11	73.82	2.10	1.74	1.81	1.86
	Northridge, 1994	81.67	72.70	76.64	78.10	1.63	1.53	1.54	1.58
	Kobe, 1995	37.41	30.32	35.72	36.78	1.31	1.12	1.24	1.29
5-5 BF-BF	Imperial Valley, 1940	3.66	2.01	2.30	2.64	1.44	1.06	1.06	1.08
	Loma Prieta, 1989	7.15	4.96	5.70	6.08	2.65	1.54	1.84	1.95
	Northridge, 1994	10.61	9.67	9.90	10.07	4.00	3.16	3.36	3.51
	Kobe, 1995	8.97	5.45	5.67	5.98	2.94	1.83	1.83	1.95
20-20 BF-BF	Imperial Valley, 1940	15.72	7.21	10.58	12.74	0.77	0.60	0.65	0.71
	Loma Prieta, 1989	46.08	35.28	42.91	44.81	1.86	1.60	1.75	1.80
	Northridge, 1994	40.27	29.97	34.87	36.71	2.25	1.94	2.15	2.15
	Kobe, 1995	33.50	27.11	27.53	28.55	2.08	1.74	1.89	1.94

TABLE 7: Peak top floor displacement and acceleration responses of similar connected buildings for equal storey height under simulated wind forces for different gust speeds.

Frame	Wind speed (m/s)	Peak top floor displacement, x_n (cm)				Peak top floor acceleration, \ddot{x}_n (g)			
		U	A	B	C	U	A	B	C
5-5 MRF-MRF	30	1.74	1.74	1.74	1.74	0.10	0.097	0.10	0.10
	37	2.16	2.16	2.16	2.16	0.24	0.24	0.24	0.25
	43	3.87	3.66	3.76	3.72	0.39	0.38	0.38	0.38
	50	3.90	3.69	3.69	3.69	0.30	0.29	0.29	0.29
20-20 MRF-MRF	30	25.74	16.74	18.74	17.74	0.23	0.15	0.17	0.16
	37	28.16	19.16	20.16	19.88	0.35	0.234	0.264	0.25
	43	32.87	21.66	23.76	22.82	0.42	0.27	0.31	0.29
	50	37.90	24.69	28.69	26.69	0.48	0.32	0.35	0.32
5-5 BF-BF	30	0.23	0.23	0.23	0.23	0.039	0.039	0.03	0.039
	37	0.29	0.29	0.29	0.29	0.093	0.093	0.09	0.093
	43	0.52	0.51	0.51	0.51	0.15	0.15	0.15	0.15
	50	0.50	0.50	0.50	0.50	0.094	0.093	0.094	0.093
20-20 BF-BF	30	4.09	3.31	3.60	3.42	0.064	0.059	0.061	0.060
	37	5.69	4.61	5.01	4.75	0.098	0.081	0.088	0.082
	43	6.75	5.47	5.94	5.64	0.12	0.098	0.11	0.10
	50	8.95	7.25	7.88	7.48	0.14	0.12	0.12	0.12

obtained under the wind loadings increases with increase in building height, thus demonstrating the influence of acceleration as a design parameter for high-rise structures. Therefore, installation of such passive device to minimize structural response under a particular hazard may not necessarily yield satisfactory performance under the other hazard, which becomes a possible example of a multi-hazard situation wherein careful selection of the design parameters for such structures is a necessity for modern constructions in the regions where such multihazard scenario prevails.

4.2. Effectiveness of FD for Dynamically Dissimilar Connected Buildings. The effectiveness of the FDs used to connect the adjacent steel buildings with dissimilar dynamic properties

is likewise assessed from the displacement and acceleration responses obtained under the earthquake ground motion and gusty wind excitations. The dissimilarity in their dynamic properties is judged based on the difference in modal properties as well as storey heights of the adjacent steel buildings, such as 5-5 MRF-BF and 5-10 MRF-MRF. Figures 9(a) and 9(b) and Tables 8 and 9 show the peak displacement and acceleration responses of the dynamically dissimilar connected buildings with equal storey height under earthquakes and winds. The peak displacement reduction for the dynamically dissimilar connected buildings with equal storey height is again observed to be the highest for configuration A; however, the range of the difference is significantly large as compared to the dynamically similar buildings of equal storey height.

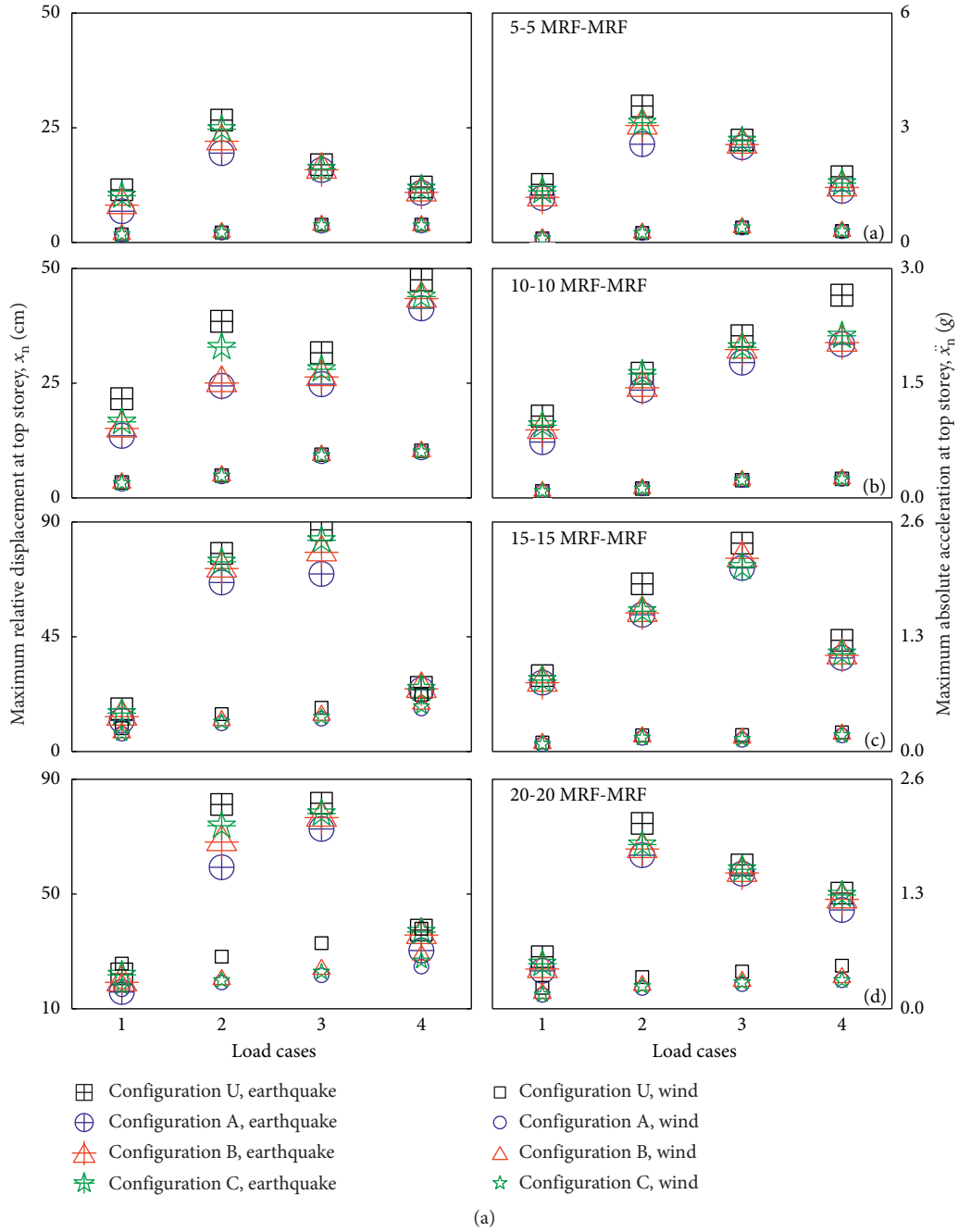


FIGURE 8: Continued.

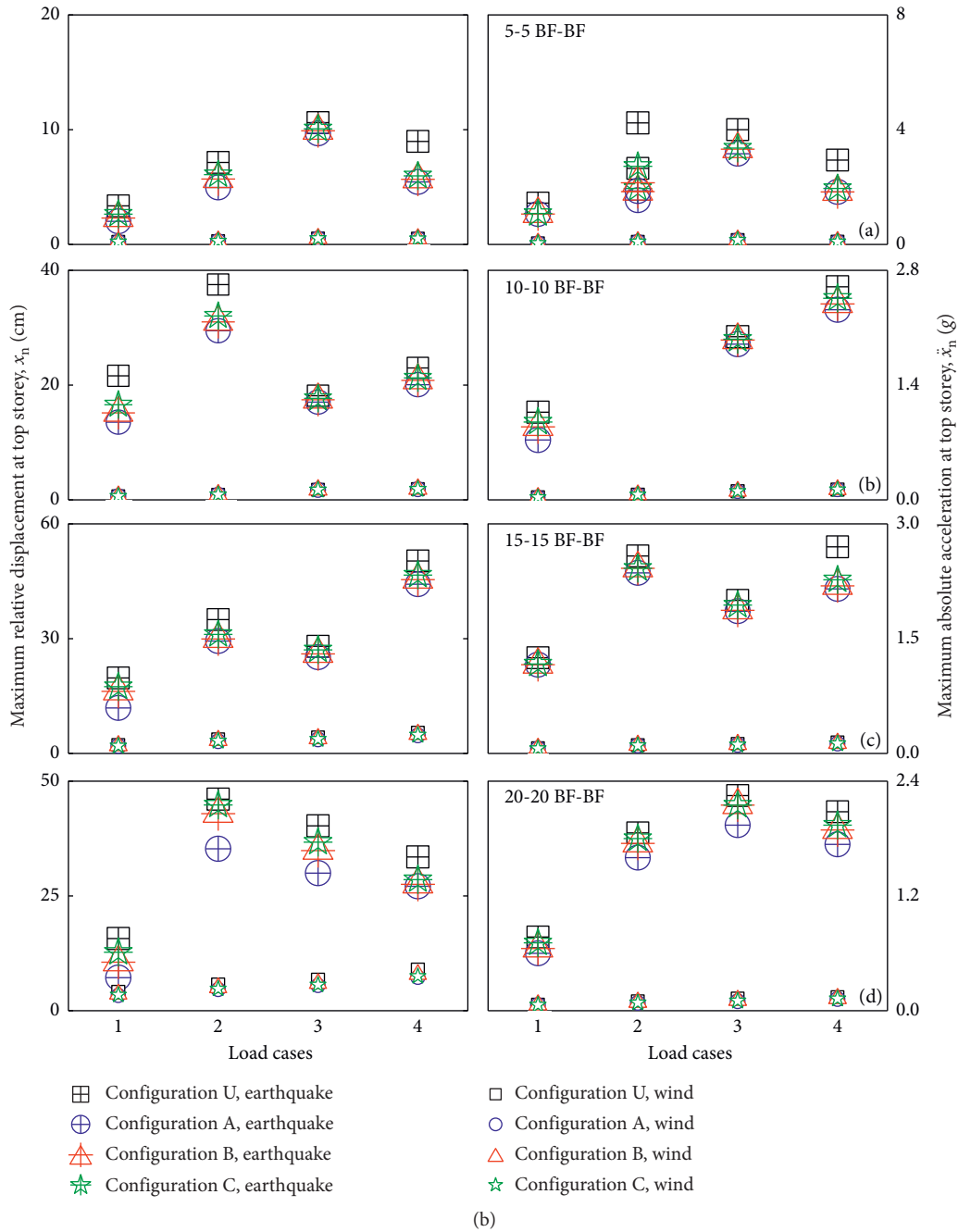


FIGURE 8: (a) Peak top floor displacement and acceleration responses of similar connected MRF-MRF buildings for equal storey height under historical earthquake ground motions and simulated wind forces. (b) Peak top floor displacement and acceleration responses of similar connected BF-BF buildings for equal storey height under historical earthquake ground motions and simulated wind forces.

Considering 5-5 MRF-BF and 5-5 BF-MRF, the displacement response reduction in the first building, i.e., MRF in first case and BF in second case, is observed in the range of ~19% to 80% and ~8% to 40%, respectively. Similarly, for the connected 20-20 MRF-BF and 20-20 BF-MRF, the range of displacement response reduction is also observed to be more for the first MRF building, although the difference in range is relatively lesser as compared to the 5-storey case. This indicates that the BF itself dissipates the earthquake-induced energy even before transferring to the FDs. Under the wind

loads, the reduction for the higher number of storey is similarly more as compared to the lower number of storey; however, the range of response reduction is rather negligible. This indicates that the wind force has negligible impact on low-rise building in case of the MRF, and for high-rise BF, the bracings resist the dynamic wind loads, thereby transferring lesser energy to the FDs. Similar observation is made for the peak top floor acceleration responses under both earthquake and wind loadings. Therefore, for the dynamically dissimilar connected buildings with equal storey height,

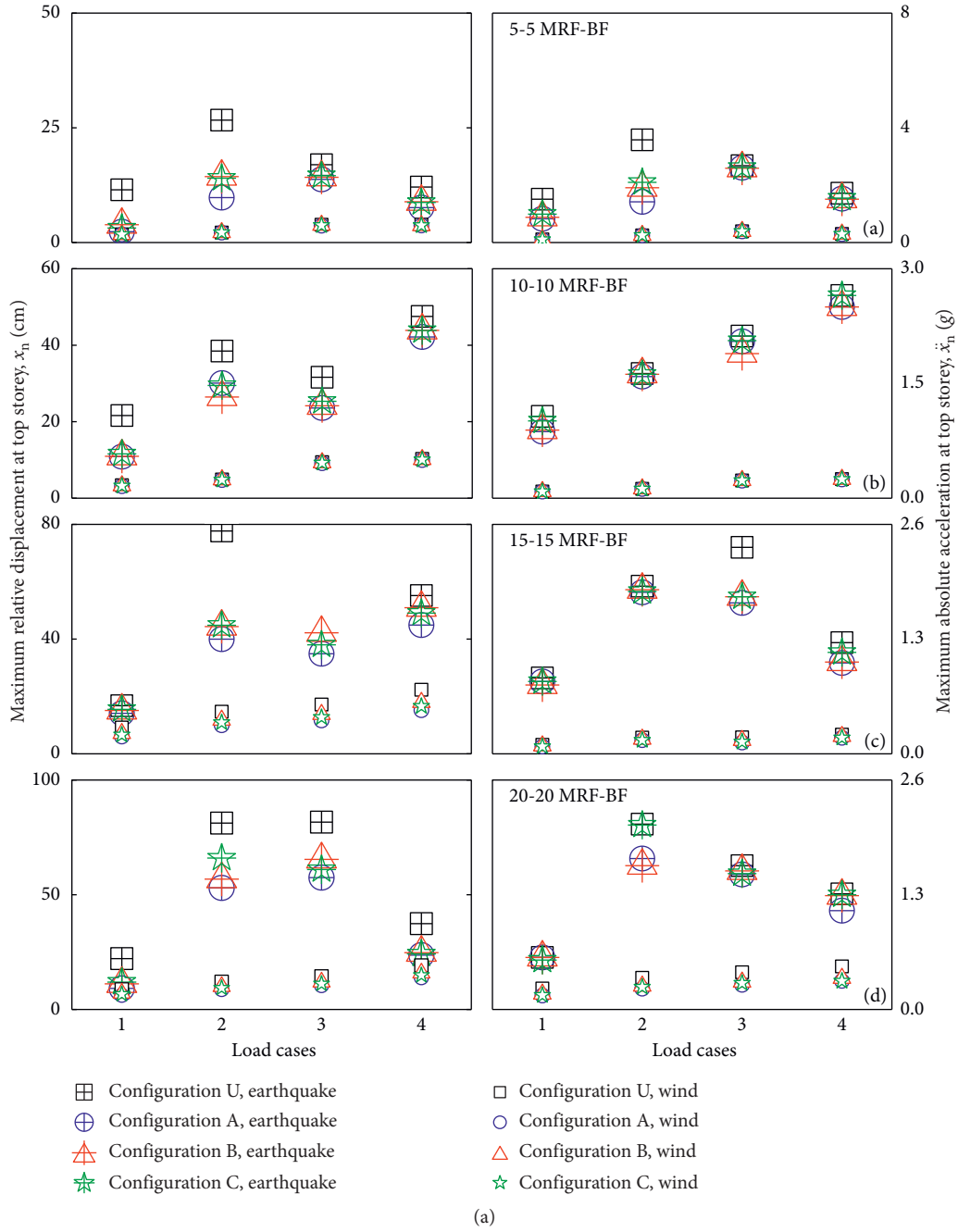


FIGURE 9: Continued.

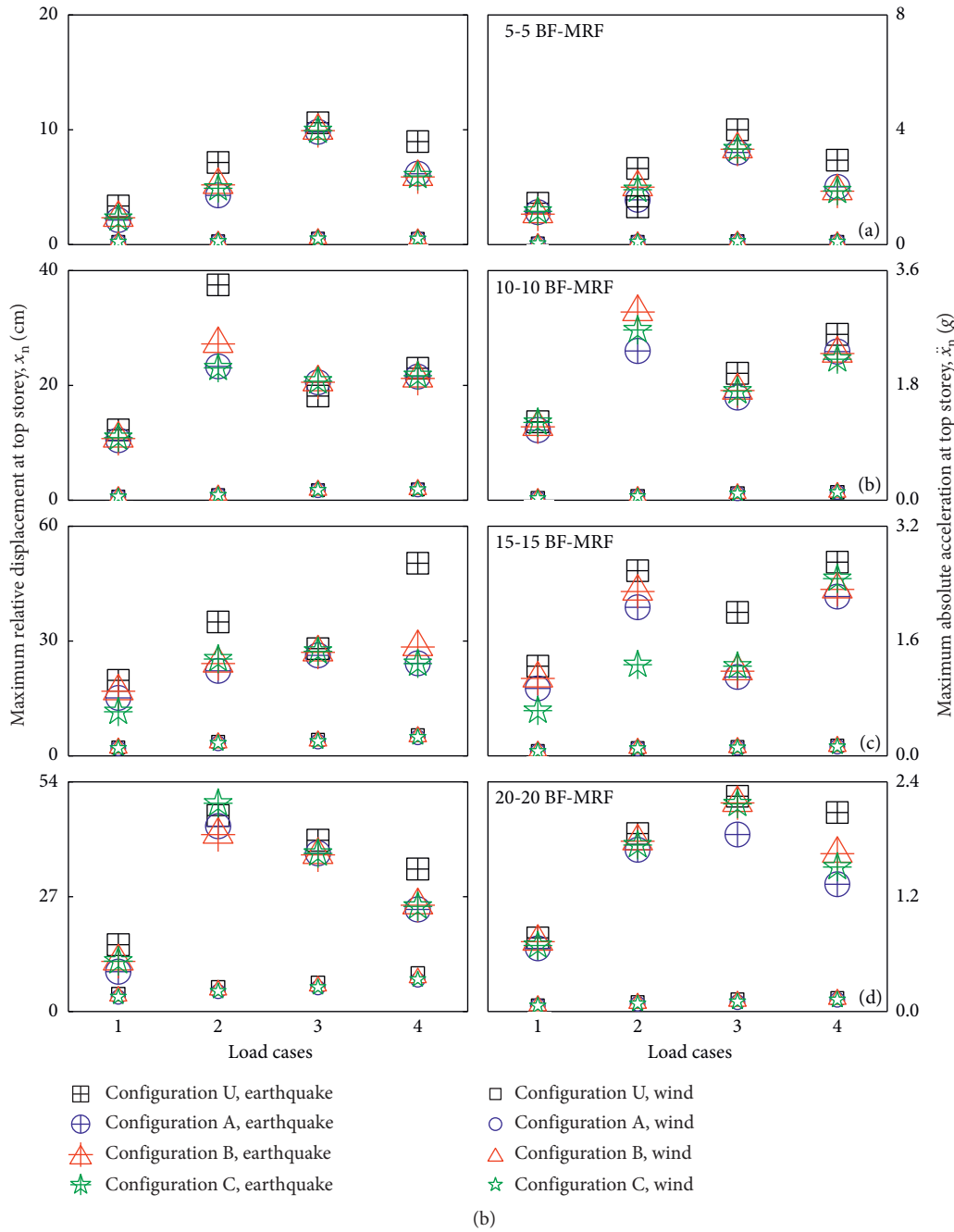


FIGURE 9: (a) Peak top floor displacement and acceleration responses of dissimilar connected MRF-BF buildings for equal storey height under historical earthquake ground motions and simulated wind forces. (b) Peak top floor displacement and acceleration responses of dissimilar connected BF-MRF buildings for equal storey height under historical earthquake ground motions and simulated wind forces.

configuration A serves as an excellent choice for the dynamic response reduction; on the other hand, configuration C is relatively inefficient to reduce the response significantly for dynamically dissimilar connected buildings.

Similarly, the responses for the adjacent steel buildings with dissimilar dynamic properties for unequal storey heights are also quantified under the considered ground motion and gusty wind excitations. Tables 10 and 11 show the peak responses of the first building for the dissimilar connected buildings under the earthquakes and winds,

respectively. Figures 10(a) and 10(b) also, respectively, illustrate the displacement and acceleration responses for the adjacent connected MRF and BF steel buildings with unequal storey height under earthquakes and winds. It is observed that the response reduction for the low-rise building (say, 5 storeys) by the FDs is significantly high under the earthquakes as compared to the winds. For the same configuration, the response reduction obtained for the high-rise building (say, 20 storeys) under the winds is substantially higher than the earthquakes as observed

TABLE 8: Peak top floor displacement and acceleration responses of dissimilar connected buildings for equal storey height under historical earthquake ground motions.

Frame	Earthquake	Peak top floor displacement, x_n (cm)				Peak top floor acceleration, \ddot{x}_n (g)			
		U	A	B	C	U	A	B	C
5-5 MRF-BF	Imperial Valley, 1940	11.49	2.37	3.88	3.17	1.51	0.83	0.88	0.99
	Loma Prieta, 1989	26.67	9.78	14.37	14.02	3.70	1.42	1.91	2.10
	Northridge, 1994	16.96	13.77	14.22	14.58	2.68	2.61	2.59	2.62
	Kobe, 1995	12.10	7.60	8.89	8.74	1.72	1.53	1.51	1.55
20-20 MRF-BF	Imperial Valley, 1940	22.18	9.19	11.17	11.93	0.79	0.79	0.76	0.79
	Loma Prieta, 1989	81.23	52.99	56.80	65.99	2.10	1.71	1.63	2.09
	Northridge, 1994	81.67	57.46	65.42	60.99	1.63	1.53	1.57	1.54
	Kobe, 1995	37.41	23.67	24.76	24.21	1.31	1.12	1.29	1.30
5-5 BF-MRF	Imperial Valley, 1940	3.36	2.13	2.33	2.27	1.44	1.13	1.06	1.16
	Loma Prieta, 1989	7.15	4.28	5.19	4.90	2.65	1.56	2.00	1.91
	Northridge, 1994	10.61	9.81	9.92	9.91	4.00	3.21	3.32	3.33
	Kobe, 1995	8.97	6.17	5.89	5.97	2.94	2.01	1.86	1.87
20-20 BF-MRF	Imperial Valley, 1940	15.72	9.36	11.79	11.84	0.77	0.66	0.73	0.69
	Loma Prieta, 1989	46.08	43.59	41.61	48.97	1.86	1.69	1.78	1.74
	Northridge, 1994	40.27	37.22	36.84	37.18	2.25	1.85	2.18	2.17
	Kobe, 1995	33.50	24.01	25.00	24.72	2.08	1.33	1.65	1.51

TABLE 9: Peak top floor displacement and acceleration responses of dissimilar connected buildings for equal storey height under simulated wind forces for different gust speeds.

Frame	Wind speed (m/s)	Peak top floor displacement, x_n (cm)				Peak top floor acceleration, \ddot{x}_n (g)			
		U	A	B	C	U	A	B	C
5-5 MRF-BF	30	1.74	1.74	1.74	1.74	0.11	0.097	0.10	0.10
	37	2.16	2.16	2.16	2.16	0.25	0.25	0.25	0.25
	43	3.87	3.65	3.75	3.72	0.39	0.39	0.39	0.39
	50	3.90	3.70	3.69	3.70	0.30	0.29	0.29	0.29
20-20 BF-MRF	30	4.09	3.37	3.62	3.45	0.064	0.059	0.061	0.060
	37	5.69	4.70	5.03	4.80	0.098	0.081	0.086	0.082
	43	6.75	5.58	5.97	5.70	0.13	0.097	0.11	0.10
	50	8.95	7.40	7.92	7.56	0.14	0.12	0.13	0.12

TABLE 10: Peak top floor displacement and acceleration responses of dissimilar connected buildings for unequal storey height under historical earthquake ground motions.

Frame	Earthquake	Peak top floor displacement, x_n (cm)				Peak top floor acceleration, \ddot{x}_n (g)			
		U	A	B	C	U	A	B	C
5-10 MRF-MRF	Imperial Valley, 1940	11.49	6.43	6.52	8.01	1.51	0.89	0.96	0.92
	Loma Prieta, 1989	26.67	12.86	9.09	11.32	3.58	1.65	1.36	1.85
	Northridge, 1994	16.96	10.43	11.73	12.35	2.68	2.06	2.59	2.08
	Kobe, 1995	12.10	10.47	10.01	11.20	1.72	1.69	1.65	1.58
15-20 MRF-MRF	Imperial Valley, 1940	16.77	10.79	14.82	15.20	0.86	0.65	0.61	0.50
	Loma Prieta, 1989	77.69	59.52	66.83	68.43	1.90	1.53	1.69	1.69
	Northridge, 1994	86.91	67.88	70.78	73.00	2.36	1.24	1.45	1.35
	Kobe, 1995	25.19	22.82	23.13	23.21	1.26	1.14	1.15	1.16
5-10 BF-BF	Imperial Valley, 1940	3.36	2.39	1.86	2.06	1.44	0.89	0.93	0.90
	Loma Prieta, 1989	7.15	3.87	4.10	4.37	2.65	1.08	1.14	1.34
	Northridge, 1994	10.61	7.39	8.46	8.14	4.00	2.44	2.72	2.67
	Kobe, 1995	8.97	3.84	4.64	4.43	2.94	1.43	1.67	1.56
15-20 BF-BF	Imperial Valley, 1940	19.74	6.19	9.11	10.67	1.25	0.85	0.67	1.02
	Loma Prieta, 1989	34.99	27.85	32.11	32.97	2.58	1.58	1.81	1.78
	Northridge, 1994	28.01	25.94	26.94	26.80	2.00	1.86	1.88	1.90
	Kobe, 1995	50.33	31.96	34.88	36.20	2.70	1.81	2.01	1.98

from the difference in the responses from the plots. From the response reductions obtained, configuration A again provides with the most effective option to mitigate the

dynamic responses under the earthquakes and winds, whereas the configuration C is apparently the least effective option.

TABLE 11: Peak top floor displacement and acceleration responses of dissimilar connected buildings for unequal storey height under simulated wind forces for different gust speeds.

Frame	Wind speed (m/s)	Peak top floor displacement, x_n (cm)				Peak top floor acceleration, \ddot{x}_n (g)			
		U	A	B	C	U	A	B	C
5-10 MRF-MRF	30	1.75	0.88	0.88	0.88	0.11	0.08	0.076	0.076
	37	2.17	2.16	2.17	2.17	0.25	0.25	0.25	0.25
	43	3.87	3.83	3.86	3.86	0.39	0.39	0.39	0.39
	50	3.91	3.70	3.72	3.69	0.30	0.29	0.29	0.29
15-20 BF-BF	30	2.20	2.23	2.30	2.26	0.068	0.068	0.071	0.068
	37	3.68	3.56	3.73	3.62	0.11	0.11	0.11	0.11
	43	4.21	4.07	4.25	4.14	0.12	0.11	0.12	0.11
	50	5.41	5.23	5.45	5.31	0.14	0.13	0.14	0.13

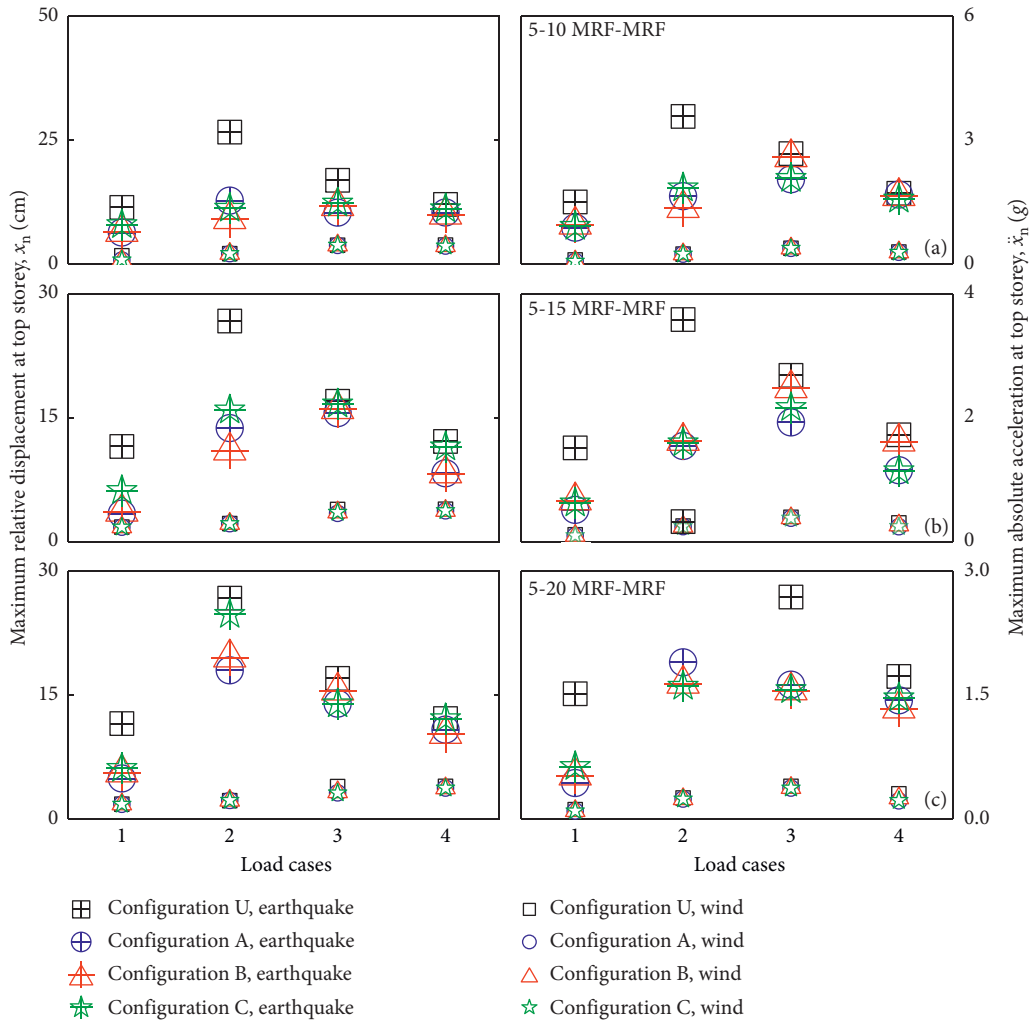


FIGURE 10: Continued.

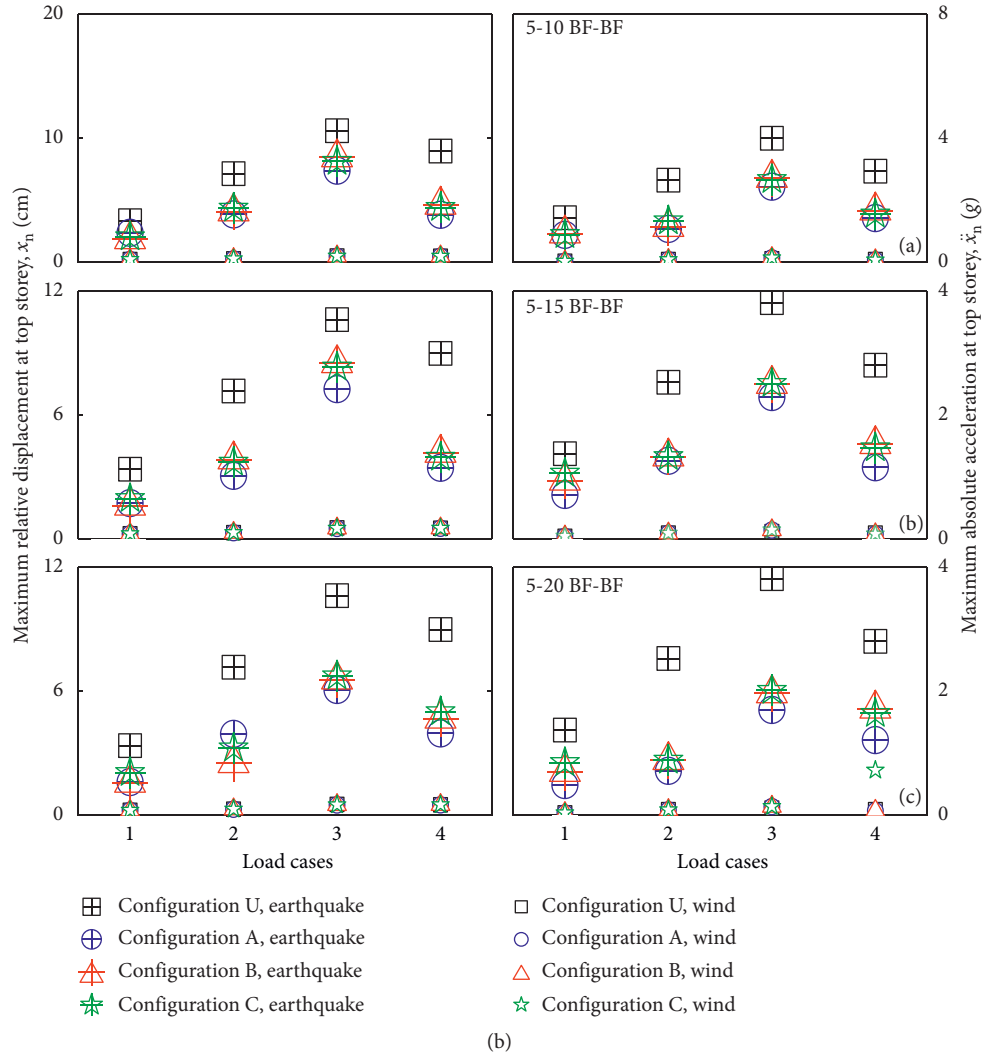


FIGURE 10: (a) Peak top floor displacement and acceleration responses of the adjacent dissimilar connected MRF-MRF buildings with unequal storey height under historical earthquake ground motions and simulated wind forces. (b) Peak top floor displacement and acceleration responses of the adjacent dissimilar connected BF-BF buildings with unequal storey height under historical earthquake ground motions and simulated wind forces.

Table 12 shows the effectiveness of the FDs in terms of average response reduction for the different configurations of the connected dynamically similar and dissimilar steel buildings. Based on the effectiveness achieved, it can be stated that configuration A is best suited to minimize the desired responses under the earthquakes and winds. On the other hand, the least effectiveness is achieved for configuration B for dynamically similar connected buildings and configuration C for dynamically dissimilar connected buildings. Moreover, for limited cases, with increasing the number of storeys, the effectiveness of the dampers increases for high-rise buildings under the wind loadings, becoming almost similar to response reductions under the earthquake loadings. Although the FDs are able to reduce the responses under the earthquakes for higher storeys, the effectiveness of the passive devices is restrained when used in higher stories, demonstrating a need for the multihazard analysis and design under earthquake and wind during design life of the

structures. To our belief, there are several structures influenced by the effects of earthquakes and winds, and such structures are required be assessed considering the multi-hazard effects during their design (service) life. Hence, it can be concluded that the passive FDs are more effective for low-rise buildings under the effect of seismic ground motions, whereas the same control devices show their effectiveness for high-rise buildings under the effect of gusty wind speeds.

As observed from the data, the maximum top floor displacement under the earthquakes for the unconnected MRFs of 5, 10, 15, and 20 storeys are, respectively, obtained as 11.49 cm to 26.67 cm, 21.61 cm to 47.53 cm, 16.77 cm to 86.91 cm, and 22.18 cm to 81.67 cm. Similarly, for the unconnected BFs, the peak displacements, respectively, range from 3.32 cm to 10.32 cm, 11.11 cm to 37.45 cm, 20.13 cm to 49.16 cm, and 15.69 cm to 45.67 cm for increasing height of the buildings. Considering 20-storey building, the minimum separation gap distance required to be kept is ~ 1.75 m for the

TABLE 12: Effectiveness of the FDs for different configurations of the connected dynamic similar and dissimilar steel buildings under earthquake ground motions and gust wind speeds.

Frame	Events	Peak top floor displacement, x_n (%)			Peak top floor acceleration, \ddot{x}_n (%)		
		A	B	C	A	B	C
5-5 MRF-MRF	Earthquake	21.33	15.63	6.83	20.07	14.35	8.53
	Wind	2.77	2.12	2.37	3.52	1.97	2.28
20-20 MRF-MRF	Earthquake	21.39	10.02	4.21	16.22	12.10	7.39
	Wind	33.97	26.90	30.15	33.90	26.59	31.28
5-5 BF-BF	Earthquake	29.72	23.82	18.70	31.75	27.92	25.27
	Wind	0.33	0.19	0.24	0.75	0.48	0.75
20-20 BF-BF	Earthquake	20.55	17.70	11.33	26.97	22.14	19.38
	Wind	19.01	11.99	16.45	15.36	9.94	13.20
5-5 MRF-BF	Earthquake	49.65	38.75	40.40	29.75	25.98	21.97
	Wind	2.75	2.08	2.33	3.52	1.86	2.45
20-20 MRF-BF	Earthquake	39.92	33.35	31.39	9.80	6.89	2.96
	Wind	28.28	17.68	22.78	33.90	26.59	31.28
5-5 BF-MRF	Earthquake	29.51	23.10	30.97	28.51	26.16	25.13
	Wind	1.37	0.42	1.37	0.34	0.14	0.24
20-20 BF-MRF	Earthquake	11.45	8.52	10.24	19.32	8.32	11.95
	Wind	17.43	11.52	15.65	15.56	10.28	13.74
5-10 MRF*-MRF	Earthquake	36.95	39.31	30.62	29.96	26.47	29.48
	Wind	14.03	13.64	13.87	8.53	8.07	8.30
15-20 MRF*-MRF	Earthquake	22.59	13.09	11.29	25.22	21.85	25.91
	Wind	20.61	12.36	16.70	12.44	9.56	12.44
5-10 MRF-MRF*	Earthquake	17.91	15.32	12.16	9.75	5.69	2.65
	Wind	14.93	14.63	14.78	2.63	2.14	2.42
15-20 MRF-MRF*	Earthquake	22.93	15.04	8.01	9.85	5.47	-2.94
	Wind	43.90	41.85	44.33	3.74	4.38	3.10

*Response reduction obtained for that building.

unconnected situation. Now, when this 20-storey building is connected by the passive response control devices, FDs, the separation gap distance reduces to minimum ~ 1.52 m considering the worst case out-of-phase movement at unconnected floors. Hence, there is an opportunity to reduce the separation gap distance by $\sim 30\%$, thereby constructing buildings at a close vicinity, which would eventually minimize, if not eliminate, structural pounding as well as utilizing the premium space for effective construction.

5. Conclusions

The performance of dynamically similar and dissimilar adjacent steel buildings connected with friction dampers (FDs) is assessed under a set of historical earthquake and simulated wind loadings. The displacement and acceleration responses are compared in order to establish effectiveness of the FDs under the multihazard uncorrelated scenarios of earthquakes and winds. The FDs are capable to reduce the displacement and acceleration responses substantially; however, different configurations are effective under the two

hazards for varying building types. This is a concern where the FDs designed for earthquake loading consideration may not necessarily perform better under wind loading. Hence, further investigations are deemed necessary on multihazard analysis and design of the passive response control devices. Nonetheless, from the study conducted herein, the major conclusions drawn are as follows:

- (1) The displacement response increases with increase in building height, whereas the acceleration response under the earthquakes decreases with increase in building height for the connected buildings under the seismic ground motions. On the other hand, the dynamic response obtained under the wind loadings generally increases with increase in height of the buildings.
- (2) The FDs are more effective in reducing the responses of connected dynamically dissimilar adjacent buildings as compared to the dynamically similar buildings, which is evident from the extent of dynamic response reduction achieved. Moreover, the effectiveness of the FDs has decreased under the earthquakes on increasing the number of stories, whereas their effectiveness substantially increased under the wind loading scenarios.
- (3) For the dynamically similar and dissimilar connected buildings, configuration A, with cross-bracing at all floor levels, is most effective in minimizing the responses under seismic and wind excitations, whereas configuration B and C are least effective, respectively, for the dynamically similar and dissimilar connected buildings.
- (4) The structures designed to resist the seismic forces in their design (service) life might become vulnerable against the wind loadings. Such structures are required to be assessed and designed carefully to mitigate the responses against the multihazard effects of earthquakes and winds.

Data Availability

All data used to support the findings of the study are included within the article.

Conflicts of Interest

The authors declare that they have no conflicts of interest.

References

- [1] S. Chapain and A. M. Aly, "Vibration attenuation in high-rise buildings to achieve system-level performance under multiple hazards," *Engineering Structures*, vol. 197, Article ID 109352, 2019.
- [2] S. Elias, "Seismic energy assessment of buildings with tuned vibration absorbers," *Shock and Vibration*, vol. 2018, Article ID 2051687, 2018.
- [3] S. Elias, R. Rupakhety, and S. Olafsson, "Analysis of a benchmark building installed with tuned mass dampers under

- wind and earthquake loads," *Shock and Vibration*, vol. 2019, Article ID 7091819, 2019.
- [4] K. S. Numayr, S. T. Mesmar, and M. A. Haddad, "Dynamic analysis of tapered thin-walled masts," *Journal of Engineering Science and Technology*, vol. 13, no. 7, pp. 2106–2124, 2018.
 - [5] T. Roy and V. Matsagar, "Effectiveness of passive response control devices in buildings under earthquake and wind during design life," *Structure and Infrastructure Engineering*, vol. 15, no. 2, pp. 252–268, 2019.
 - [6] T. Roy and V. Matsagar, "Probabilistic assessment of steel buildings installed with passive control devices under multi-hazard scenario of earthquake and wind," *Structural Safety*, vol. 85, Article ID 101955, 2020.
 - [7] S. Cherry and A. Filiatrault, "Seismic response control of buildings using friction dampers," *Earthquake Spectra*, vol. 9, no. 3, pp. 447–466, 1993.
 - [8] X. Zhou and L. Peng, "A new type of damper with friction-variable characteristics," *Earthquake Engineering and Engineering Vibration*, vol. 8, no. 4, pp. 507–520, 2010.
 - [9] B. He, H. Ouyang, S. He, and X. Ren, "Stick-slip vibration of a friction damper for energy dissipation," *Advances in Mechanical Engineering*, vol. 9, no. 7, pp. 1–13, 2017.
 - [10] L. M. Moreschi and M. P. Singh, "Design of yielding metallic and friction dampers for optimal seismic performance," *Earthquake Engineering & Structural Dynamics*, vol. 32, no. 8, pp. 1291–1311, 2003.
 - [11] S. Mathur and S. K. Deb, "Seismic response control of RC setback building with friction dampers," *Indian Concrete Journal*, vol. 77, no. 11, pp. 1469–1472, 2003.
 - [12] Y. L. Xu, W. L. Qu, and Z. H. Chen, "Control of wind-excited truss tower using semiactive friction damper," *Journal of Structural Engineering*, vol. 127, no. 8, pp. 861–868, 2001.
 - [13] S. Mahmoud, A. Abd-Elhamed, and R. Jankowski, "Earthquake-induced pounding between equal height multi-storey buildings considering soil-structure interaction," *Bulletin of Earthquake Engineering*, vol. 11, no. 4, pp. 1021–1048, 2013.
 - [14] C. C. Patel and R. S. Jangid, "Seismic response of dynamically similar adjacent structures connected with viscous dampers," *The IES Journal Part A: Civil & Structural Engineering*, vol. 3, no. 1, pp. 1–13, 2009.
 - [15] A. S. Pall and C. Marsh, "Seismic response of friction damped braced frames," *Journal of Structural Engineering (ASCE)*, vol. 109, no. 5, pp. 1313–1323, 1982.
 - [16] A. S. Pall, C. Marsh, and P. Fazio, "Friction joints for seismic control of large panel structures," *PCI Journal*, vol. 25, no. 6, pp. 38–61, 1980.
 - [17] H.-S. Chung, B.-W. Moon, S.-K. Lee, J.-H. Park, and K.-W. Min, "Seismic performance of friction dampers using flexure of RC shear wall system," *The Structural Design of Tall and Special Buildings*, vol. 18, no. 7, pp. 807–822, 2009.
 - [18] P. Colajanni and M. Papia, "Seismic response of braced frames with and without friction dampers," *Engineering Structures*, vol. 17, no. 2, pp. 129–140, 1995.
 - [19] A. S. Pall and C. Marsh, "Friction damped concrete shear walls," *American Concrete Institute*, vol. 78, no. 3, pp. 187–193, 1981.
 - [20] R. Chandra, M. Masand, S. K. Nandi, C. P. Tripathi, R. Pall, and A. Pall, "Friction-dampers for seismic control of the gardenia towers south city, Gurgaon, India," in *12th World Conference On Earthquake Engineering (12WCEE)*, Auckland, New Zealand, November 2000.
 - [21] I. H. Mualla and B. Belev, "Performance of steel frames with a new friction damper device under earthquake excitation," *Engineering Structures*, vol. 24, no. 3, pp. 365–371, 2002.
 - [22] S. Bagheri, M. Barghian, F. Saieri, and A. Farzinfar, "U-shaped metallic-yielding damper in building structures: seismic behavior and comparison with a friction damper," *Structures*, vol. 3, pp. 163–171, 2015.
 - [23] N. Kaur, V. A. Matsagar, and A. K. Nagpal, "Earthquake response of medium-rise to high-rise buildings with friction dampers," *International Journal of High-Rise Buildings*, vol. 1, no. 4, pp. 311–332, 2012.
 - [24] R. Montuori, E. Nistri, and V. Piluso, "Theory of plastic mechanism control for the seismic design of braced frames equipped with friction dampers," *Mechanics Research Communications*, vol. 58, pp. 112–123, 2014.
 - [25] N. Fallah and S. Honarparast, "NSGA-II based multi-objective optimization in design of Pall friction dampers," *Journal of Constructional Steel Research*, vol. 89, pp. 75–85, 2013.
 - [26] L. F. F. Miguel, L. F. F. Miguel, and R. H. Lopez, "Failure probability minimization of buildings through passive friction dampers," *The Structural Design of Tall and Special Buildings*, vol. 25, no. 17, pp. 869–885, 2016.
 - [27] J. Kim and S. An, "Optimal distribution of friction dampers for seismic retrofit of a reinforced concrete moment frame," *Advances in Structural Engineering*, vol. 20, no. 10, pp. 1523–1539, 2016.
 - [28] M. Anoushehei, F. Daneshjoo, S. Mahboubi, and S. Khazaeli, "Experimental investigation on hysteretic behavior of rotational friction dampers with new friction materials," *Steel and Composite Structures*, vol. 24, no. 2, pp. 239–248, 2017.
 - [29] A. Shirkhani, I. H. Mualla, N. Shabakhty, and S. R. Mousavi, "Behavior of steel frames with rotational friction dampers by endurance time method," *Journal of Constructional Steel Research*, vol. 107, pp. 211–222, 2015.
 - [30] B. Chen, S. Weng, L. Zhi, and D. Li, "Response control of a large transmission tower-line system under seismic excitations using friction dampers," *Advances in Structural Engineering*, vol. 20, no. 8, pp. 1155–1173, 2016.
 - [31] A. V. Bhaskararao and R. S. Jangid, "Seismic analysis of structures connected with friction dampers," *Engineering Structures*, vol. 28, no. 5, pp. 690–703, 2006.
 - [32] D. Wang, T. K. T. Tse, Y. Zhou, and Q. Li, "Structural performance and cost analysis of wind-induced vibration control schemes for a real super-tall building," *Structure and Infrastructure Engineering*, vol. 11, no. 8, pp. 990–1011, 2015.
 - [33] A. V. Bhaskararao and R. S. Jangid, "Seismic response of adjacent buildings connected with friction dampers," *Bulletin of Earthquake Engineering*, vol. 4, no. 1, pp. 43–64, 2006.
 - [34] F. Fathi and O. Bahar, "Hybrid coupled building control for similar adjacent buildings," *KSCCE Journal of Civil Engineering*, vol. 21, no. 1, pp. 265–273, 2017.
 - [35] Y. Fukumoto and I. Takewaki, "Critical earthquake input energy to connected building structures using impulse input," *Earthquakes and Structures*, vol. 9, no. 6, pp. 1133–1152, 2015.
 - [36] V. A. Matsagar and R. S. Jangid, "Viscoelastic damper connected to adjacent structures involving seismic isolation," *Journal of Civil Engineering and Management*, vol. 11, no. 4, pp. 309–322, 2005.
 - [37] V. A. Matsagar and R. S. Jangid, "Base-isolated building connected to adjacent building using viscous dampers," *Bulletin of the New Zealand Society for Earthquake Engineering*, vol. 39, no. 1, pp. 59–80, 2006.
 - [38] R. Rupakhety, S. Elias, and S. Olafsson, "Shared tuned mass dampers for mitigation of seismic pounding," *Applied Sciences*, vol. 10, no. 6, p. 1918, 2020.
 - [39] E. Tubaldi, "Dynamic behavior of adjacent buildings connected by linear viscous/viscoelastic dampers," *Structural*

Control and Health Monitoring, vol. 22, no. 8, pp. 1086–1102, 2015.

- [40] T. Roy and V. Matsagar, “Multi-hazard assessment of steel buildings retrofitted with passive control devices,” in *16th World Conference On Earthquake Engineering (16WCEE)*, Santiago, Chile, January 2017.
- [41] D. Kwon and A. Kareem, *NatHaz On-Line Wind Simulator (NOWS): Simulation of Gaussian Multivariate Wind Fields*, University of Notre Dame, Notre Dame, IN, USA, 2006.

Research Article

Unified Shear-Flexural Model for Vibration Control of Buildings Using Passive Dynamic Absorbers

Hugo Hernández-Barrios ^{1,2}, Iván F. Huergo,¹ Carlos Arce-León ³ and Carlos M. Patlán²

¹School of Engineering, Universidad Nacional Autónoma de México, Mexico City, Mexico

²School of Engineering, Universidad Michoacana de San Nicolás de Hidalgo, Morelia, Mexico

³Multidisciplinary Research Unit, FES Acatlán-UNAM, Naucalpan, Mexico

Correspondence should be addressed to Hugo Hernández-Barrios; hugohernandezbarrios@yahoo.com.mx

Received 4 May 2020; Revised 25 June 2020; Accepted 30 June 2020; Published 6 August 2020

Academic Editor: Said Elias

Copyright © 2020 Hugo Hernández-Barrios et al. This is an open access article distributed under the Creative Commons Attribution License, which permits unrestricted use, distribution, and reproduction in any medium, provided the original work is properly cited.

A unified design model is proposed for various kinds of passive dynamic absorbers (PDAs) attached to buildings with different lateral resisting systems. A total of five different PDAs are considered in this study: (1) tuned mass damper (TMD), (2) circular tuned sloshing damper (C-TSD), (3) rectangular tuned sloshing damper (R-TSD), (4) two-way liquid damper (TWLD), and (5) pendulum tuned mass damper (PTMD). The unified model consists of a coupled shear-flexural (CSF) discrete model with equivalent tuned mass dampers (TMDs), which allows the consideration of intermediate modes of lateral deformation. By modifying the nondimensional lateral stiffness ratio, the CSF model can consider lateral deformations varying from those of a flexural cantilever beam to those of a shear cantilever beam. The unified model was applied to a 144-meter-tall building located in the Valley of Mexico, which was subjected to both seismic and along-wind loads. The building has similar fundamental periods of vibration and different nondimensional lateral stiffness ratios for both translational directions, which shows the importance of considering both bending and shear stiffness in the design of PDAs. The results show a great effectiveness of PDAs in controlling along-wind RMS accelerations of the building; on the contrary, PDAs were ineffective in controlling peak lateral displacements. For a single PDA attached at the rooftop level, the maximum possible value of the PDA mass efficiency index increases as the nondimensional lateral stiffness ratio decreases; therefore, there is an increase in the vibration control effectiveness of PDAs for lateral flexural-type deformations.

1. Introduction

Increasing urbanization in recent decades has led to the construction of high-rise buildings, which are usually susceptible to wind loads worldwide. However, tall buildings located in seismic zones, e.g., cities along the Pacific coast of Mexico, are not only subjected to wind loads but also to seismic ones. While shear and flexural beams can provide adequate models for certain types of buildings, there are many types for which these two extreme modes of lateral deformation may not be appropriate. Generally speaking, low-rise buildings usually deform as pure shear beams, whereas in medium-rise and high-rise buildings, the flexural deformation is as significant as the shear deformation.

Complex structural systems as high-rise buildings can be reduced to equivalent continuous beam models using two different arrangements of bending and shear stiffness: (1) a continuous Timoshenko beam model that reflects a series coupling [1] and (2) a coupled shear-flexural (CSF) continuous model that couples both stiffness in parallel [2]. Dym and Williams [3] concluded that a series coupling of both stiffness does not display the correct dependence of frequency on building height, particularly in shear wall-frame buildings and tube-and-core constructions with the parallel nature of the two-beam model in which transverse displacements due to bending and to shear are identical. In conclusion, it appears that the CSF model seems to be the best model for estimating the frequencies of medium-rise to

high-rise buildings because it provides predictions that are consistent with the observed data [3].

Generally speaking, the common techniques used for vibration control can be classified into three categories: active, passive, and hybrid devices. Unlike active vibration control [4, 5], passive vibration control [6, 7] dissipates energy without incorporating mechanisms powered by an external energy source. On the other hand, hybrid vibration control [4, 8–14] combines features of active and passive control systems. Passive dynamic absorbers (PDAs) are devices tuned to a particular structural frequency so that when that frequency is excited, the device resonates out of phase with the structural motion. There are several types of PDAs such as tuned mass dampers (TMDs), tuned liquid dampers (TLDs), and pendulum tuned mass dampers (PTMDs), among others.

A tuned mass damper (TMD) is a device consisting of a mass, a spring, and a damper that is attached to a structure in order to reduce its dynamic response. Den Hartog [15] derived the formula for the optimum values of the TMD parameters for an undamped single degree of freedom (SDOF) structure subjected to harmonic excitation. Warburton and Ayorinde [16] derived closed-form expressions for obtaining TMD parameters for an undamped SDOF system for base harmonic and white noise random excitation. For seismic applications, Sadek et al. [17] suggested a method for estimating the design parameters of TMDs attached to a damped SDOF structure.

A tuned liquid damper (TLD) is a special type of TMD where the mass is replaced by a liquid (usually water). A TLD utilizes the sloshing of the liquid in the container, but only a fraction of the liquid participates in the sloshing motion tuned to the dominant vibration frequency of the primary structure. Tuned liquid column dampers (TLCDs) are a special type of TLDs that rely on the motion of a column of liquid in a U-tube like container to counteract the acting forces on the structures. In a similar way, tuned sloshing dampers (TSDs) are a special type of TLDs consisting of tanks partially filled with liquid that use the sloshing energy of water to reduce the dynamic response of the structure. There are two types of TSDs based on the geometry of the tank: circular tuned sloshing damper (C-TSD) and rectangular tuned sloshing damper (R-TSD). For bidirectional control of building structures, a two-way liquid damper (TWLD) is another special type of TLD that consists of a combination of a TLCD and a R-TSD to mitigate the dynamic response of the primary structure.

Kareem [18] studied the reduction of wind-induced motion in shear buildings using a TSD. Chang and Gu [19] studied the control effects of R-TSDs installed on a tall building that vibrates due to vortex excitation. For industrial practice, Wu et al. [20] proposed some useful guidelines for designing TLCDs for damped SDOF structures under a white noise type of wind excitation. Tait [21] developed equivalent linear damping ratio expressions for structure-TSD systems subjected to both sinusoidal and random excitation. Lee et al. [22] explored the effect of the coupled TLCD-TSD force on the dynamic properties of a TWLD. Subsequently, Min et al. [23] developed a design procedure

of TWLDs for attenuation of wind-induced responses of tall buildings, whereas Rozas et al. [24] proposed a new bidirectional tuned liquid column damper for controlling the seismic response of structures.

The natural frequencies of a structure are often difficult to predict accurately. For this reason, it is desirable that the natural frequency of the TMD be tunable on site, which can be easily accomplished by using TLDs or PTMDs. A pendulum tuned mass damper (PTMD) consists of a mass supported with cables, which allows the system to behave like a pendulum. Therefore, the device generates a horizontal force that opposes the floor motion. For high-rise buildings with large mass and low frequencies, a cable-supported pendulum system in which the natural frequency is tunable by changing the pendulum length is highly recommended [25]. For both seismic and wind loads, Gerges and Vickery [26] proposed optimum design parameters for PTMDs by using equivalent TMDs. Shu et al. [27] implemented the performance-based analysis and design methodology to assess the seismic vulnerability of a coal-fired power plant and to optimally design its equivalent pendulum-type tuned mass damper system such that the direct losses are minimized.

Assuming the primary structure as a generalized SDOF system, Chang et al. [28, 29] established unified design formulas for various kinds of PDAs (TMD, TLCD, and TSD) under both seismic and wind loads by using equivalent TMDs. Both studies [28, 29] demonstrated that PDAs can be modeled as equivalent TMDs; however, PDAs are usually studied using building models that cannot couple the bending and shear stiffness in parallel [30–35]. Balendra et al. [36] studied the effectiveness of TLCDs in reducing the along-wind response of tall buildings using a CSF continuous model subjected to a reduced external force; that is, they did not incorporate the TLCDs in the equations of motion of the CSF continuous model. Afterwards, Huergo and Hernández [37] proposed a CSF discrete model with TMDs, which adequately incorporates the TMDs in the equations of motion; therefore, the main novelty of this paper is the incorporation of different kinds of PDAs into the CSF discrete model by using equivalent TMDs. For practical design purposes, the consideration of different lateral resisting systems by using the CSF discrete model with TMDs [37] could lead structural engineers to optimize not only the design of TMDs but also the design of other kinds of PDAs such as TLDs.

In this paper, Section 2 shows the design procedure of five different kinds of PDAs (TMD, C-TSD, R-TSD, TWLD, and PTMD) by modeling the devices as equivalent TMDs. In Section 3, the five different kinds of PDAs are incorporated into the CSF discrete model [37] in order to reproduce the vibration control of buildings with different lateral resisting systems. In Section 4, the effect of the lateral resisting system on PDAs is shown for the maximum PDA/SDOF nondimensional mass ratio. Assuming a single PDA attached at the rooftop level, Section 5 shows the numerical assessment of a 144-meter-tall building subjected to both seismic and along-wind loads.

2. Design Procedure of Passive Dynamic Absorbers

The aim of Section 2 is to provide a unified analytical formulation for the CSF model with PDAs. The tuning of passive dynamic absorbers (PDAs) to a particular structural frequency achieves input energy dissipation due to the damper inertia force acting on the structure. For engineering purposes, PDAs can be modeled as equivalent tuned mass dampers (TMDs) [26, 28, 29]. Figure 1 shows the geometry of five different kinds of PDAs (TMD, C-TSD, R-TSD, TWLD, and PTMD), where m_{PDA} , k_{PDA} , and c_{PDA} are defined as the mass, spring stiffness, and damping coefficient of the PDA modeled as an equivalent TMD, respectively.

2.1. Tuned Mass Dampers. The mass of a TMD (see Figure 1(a)) is given by the following equation:

$$m_{PDA} = \mu m_{SDOF}, \quad (1)$$

where μ is the TMD/SDOF nondimensional mass ratio that may be chosen in the range of 1/50 to 1/15 for a first design approach [38] and m_{SDOF} is the structural mass of an equivalent single degree of freedom (SDOF) system, which is given by the following equation:

$$m_{SDOF} = \frac{\{\phi_i\}^T [M] \{\phi_i\}}{\phi_i^2(z_{PDA})}, \quad (2)$$

where $\{\phi_i\}$ is a vector containing the modal amplitudes of the i th lateral mode of vibration of the building that will be tuned to the frequency of the PDA, $[M]$ is the lumped mass matrix of the building, z_{PDA} is the height above ground level of the attachment point of the PDA, and $\phi_i(z_{PDA})$ is the modal amplitude of the i th lateral mode of vibration of the building at z_{PDA} . The angular frequency, spring, stiffness, and damping coefficient of the TMD are defined, respectively, as follows:

$$w_{PDA} = R_f w_i, \quad (3)$$

$$k_{PDA} = m_{PDA} (w_{PDA})^2, \quad (4)$$

$$c_{PDA} = 2\xi_{PDA} m_{PDA} w_{PDA}, \quad (5)$$

where w_i is the angular frequency of the i th lateral mode of vibration of the building that will be tuned to the frequency of the TMD, R_f is the TMD/SDOF nondimensional frequency ratio, and ξ_{PDA} is the optimum damping ratio of the TMD. Table 1 shows some optimum tuning conditions for damped TMDs attached to an undamped primary structure [39].

2.2. Circular Tuned Sloshing Dampers. Tuned sloshing dampers (TSDs) can be broadly classified into two categories: shallow-water and deep-water dampers. This classification is based on the ratio of the water surface elevation in the direction of motion to the water depth [18]. In the

shallow-water case, the TSD damping originates primarily from energy dissipation through the action of the internal fluid viscous forces and from wave breaking [18]. Wave motions in shallow-water TSDs are generally complex due to strong nonlinearities such as wave breaking; however, shallow-water TSDs provide high damping of liquid sloshing and an efficient moving mass [40]. On the other hand, deep-water TSDs provide low damping and an inefficient moving mass because a large portion of the liquid below the free surface does not participate in sloshing. However, the presence of baffles or screens may further increase the damping [18, 21].

It is important to consider the effect of the nonlinear water sloshing when a TSD is employed in a structure subjected to large amplitude excitations such as earthquakes. The presence of several sloshing modes, each with separate frequencies, reduces the inertial forces tuned to damped structural movement [41]. There has been research concerning the effectiveness of sloshing liquid damping systems for high amplitude excitations galore; however, it is important to realize that such systems act more like chaotic energy dissipators as opposed to indirect inertial damping systems [41–43].

On the other hand, when a TSD is subjected to small amplitude excitations, the nonlinearities in its response are largely absent. The amplitudes of motion resulting from wind loading are sufficiently small, so much so that the fundamental sloshing mode of a TSD is practically the only one that is excited. For this reason, and because of the highly periodic nature of wind excitation, TSDs are well suited to reduce structural motion due to wind [41]. Although researchers have extended the theoretical model to account for breaking wave motion in rectangular tuned sloshing dampers (R-TSDs) [44], it is difficult to develop a model for breaking wave motion in circular tuned sloshing dampers (C-TSDs) [43].

According to Chang and Qu [28], the mass, spring stiffness, and damping coefficient of a linear C-TSD (see Figure 1(b)) are given by the following equations:

$$\begin{aligned} m_{PDA} &= \frac{\rho\pi r^3}{4.39} \tanh\left(\frac{1.84h}{r}\right), \\ k_{PDA} &= 0.419\rho\pi g r^2 \tanh^2\left(\frac{1.84h}{r}\right), \end{aligned} \quad (6)$$

$$c_{PDA} = 2\xi_{PDA} m_{PDA} w_{PDA},$$

where ρ is the liquid density (usually water), r is the radius of the circular tank, h is the liquid depth, g is the gravitational acceleration, and ξ_{PDA} is the optimum damping ratio of the C-TSD.

Assuming a linear wave and small amplitudes, the fundamental angular frequency of the sloshing liquid is calculated as follows:

$$w_{PDA} = \sqrt{\frac{k_{PDA}}{m_{PDA}}} = \sqrt{\frac{1.84g}{r} \tanh\left(\frac{1.84h}{r}\right)}. \quad (7)$$

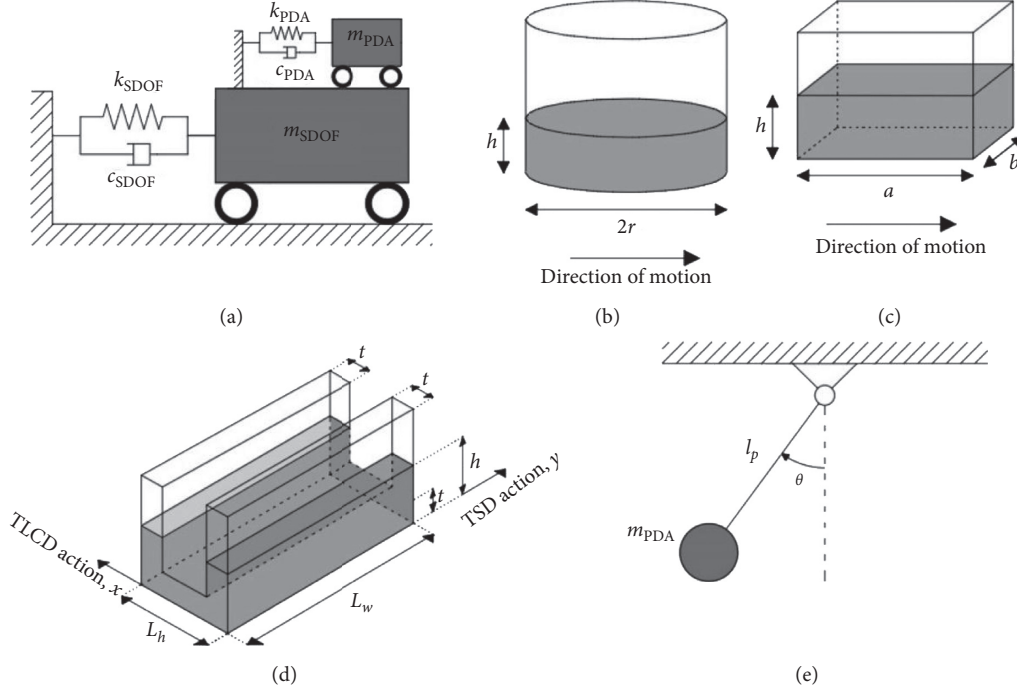


FIGURE 1: Geometry of the five PDAs. TMD: tuned mass damper; C-TSD: circular tuned sloshing damper; R-TSD: rectangular tuned sloshing damper; TWLD: two-way liquid damper; PTMD: pendulum tuned mass damper. (a) TMD-structure interaction system. (b) C-TSD. (c) R-TSD. (d) TWLD. (e) PTMD.

TABLE 1: Optimum tuning conditions for damped TMDs attached to an undamped primary structure.

Loading case	Optimization criteria	Optimum tuning conditions	
		R_f	ξ_{PDA}
Harmonic load applied to primary structure	Minimum relative displacement amplitude of primary structure	$1/(1 + \mu)$	$\sqrt{(3\mu)/(8(1 + \mu)^3)}$
	Minimum relative acceleration amplitude of primary structure	$1/\sqrt{1 + \mu}$	$\sqrt{(3\mu)/8(1 + 0.5\mu)}$
Harmonic base acceleration	Minimum relative displacement amplitude of primary structure	$(\sqrt{1 - 0.5\mu})/(1 + \mu)$	$\sqrt{(3\mu)/(8(1 + \mu)(1 - 0.5\mu))}$
	Minimum absolute acceleration amplitude of primary structure	$1/(1 + \mu)$	$\sqrt{(3\mu)/(8(1 + \mu))}$
Random load applied to primary structure	Minimum root mean square value of relative displacement of primary structure	$(\sqrt{1 - 0.5\mu})/(1 + \mu)$	$\sqrt{(\mu(1 + 0.75\mu))/(4(1 + \mu)(1 - 0.5\mu))}$
Random base acceleration	Minimum root mean square value of relative displacement of primary structure	$(\sqrt{1 - 0.5\mu})/(1 + \mu)$	$\sqrt{(\mu(1 - 0.25\mu))/(4(1 + \mu)(1 - 0.5\mu))}$

Substituting equation (3) into equation (7) leads to the following equation:

$$\begin{aligned}
 h &= 0.5435r \tanh^{-1} \left[\frac{0.5435r(R_f w_i)^2}{g} \right] \\
 &= 0.2718r \ln \left[\frac{g + 0.5435r(R_f w_i)^2}{g - 0.5435r(R_f w_i)^2} \right],
 \end{aligned} \tag{8}$$

where w_i is the angular frequency of the i th lateral mode of vibration of the building that will be tuned to the frequency of the PDA and R_f is the C-TSD/SDOF nondimensional

frequency ratio. In equation (8), only values of $r < g/[0.5435(R_f w_i)^2]$ guarantee real values of h .

According to Chang [28, 29], the C-TSD/SDOF non-dimensional mass ratio and the C-TSD mass efficiency index are defined, respectively, as follows:

$$\begin{aligned}
 \mu &= \frac{\rho \pi r^2 h}{m_{\text{SDOF}}}, \\
 \lambda &= \frac{m_{\text{PDA}}}{m_{\text{SDOF}}} = \frac{\rho \pi r^3}{4.39 m_{\text{SDOF}}} \tanh \left(\frac{1.84h}{r} \right),
 \end{aligned} \tag{9}$$

where m_{SDOF} is the structural mass of an equivalent SDOF system, which was defined in equation (2). Table 2 shows

TABLE 2: Optimum tuning conditions for TLDs attached to an undamped primary structure.

Optimization criteria	Loading case	Optimum tuning conditions	
		R_f	ξ_{PDA}
Minimum relative displacement amplitude of primary structure	Seismic load	$(\sqrt{1+\mu-1.5\lambda})/(1+\mu)$	$(1/2)\sqrt{(\lambda(1+\mu-1.25\lambda))/((1+\mu)(1+\mu-1.5\lambda))}$
	Along-wind load	$(\sqrt{1+\mu-0.5\lambda})/(1+\mu)$	$(1/2)\sqrt{(\lambda(1+\mu-0.25\lambda))/((1+\mu)(1+\mu-0.5\lambda))}$
	Across-wind load	$1/(\sqrt{1+\mu})$	$\sqrt{(\sqrt{1+\mu}-\sqrt{1+\mu-\lambda})/(2\sqrt{1+\mu})}$

some optimum tuning conditions for TLDs attached to an undamped primary structure [19, 29].

2.3. Rectangular Tuned Sloshing Dampers. For shallow-water dampers, the movement of the water within a tank is not as neat and easy to predict as the lateral oscillation of a mass-spring system. The presence of several different modes of sloshing coupled with nonlinear effects such as wave breaking and slamming impacts, can make an accurate prediction of sloshing behavior difficult [41]. To account for breaking waves inside rectangular containers, Sun and Fujino [44] proposed two coefficients into the equations of motion: a damping coefficient that represents the increase in liquid damping and the frequency shift coefficient that represents the phase velocity shift of liquid motion. The nonlinear damping force of a rectangular tuned sloshing damper (R-TSD) can be replaced by a linearized generalized damping term by minimizing the error between the actual damping force and the linearized generalized damping force [21, 45].

Neglecting the nonlinear behavior of liquid sloshing, the mass, spring stiffness, and damping coefficient of a R-TSD (see Figure 1(c)) are defined, respectively, as follows [28]:

$$\begin{aligned}
 m_{\text{PDA}} &= \frac{8\rho ba^2}{\pi^3} \tanh\left(\frac{\pi h}{a}\right), \\
 k_{\text{PDA}} &= \frac{8\rho bag}{\pi^2} \tanh^2\left(\frac{\pi h}{a}\right), \\
 c_{\text{PDA}} &= 2\xi_{\text{PDA}} m_{\text{PDA}} \omega_{\text{PDA}},
 \end{aligned} \tag{10}$$

where ρ is the liquid density (usually water), a is the length of the TLD along the liquid motion direction, b is the width of the tank, h is the liquid depth, g is the gravitational acceleration, and ξ_{PDA} is the optimum damping ratio of the R-TSD.

According to the shallow-water wave theory that is applied to the R-TSDs with the depth ratio h/a ranging from 0.04 to 0.5, the liquid level sloshes within a rectangular container with the following fundamental frequency [40]:

$$\omega_{\text{PDA}} = \sqrt{\frac{k_{\text{PDA}}}{m_{\text{PDA}}}} = \sqrt{\frac{\pi g}{a} \tanh\left(\frac{\pi h}{a}\right)}. \tag{11}$$

Substituting equation (3) into equation (11) leads to the following:

$$h = \frac{a}{\pi} \tanh^{-1} \left[\frac{a(R_f \omega_i)^2}{\pi g} \right] = \frac{a}{2\pi} \ln \left[\frac{\pi g + a(R_f \omega_i)^2}{\pi g - a(R_f \omega_i)^2} \right], \tag{12}$$

where ω_i is the angular frequency of the i th lateral mode of vibration of the building that will be tuned to the frequency of the PDA and R_f is the R-TSD/SDOF nondimensional frequency ratio. In equation (12), only values of $a < \pi g / (R_f \omega_i)^2$ guarantee real values of h .

According to Chang [28, 29], the R-TSD/SDOF nondimensional mass ratio and the R-TSD mass efficiency index are defined, respectively, as follows:

$$\begin{aligned}
 \mu &= \frac{\rho abh}{m_{\text{SDOF}}}, \\
 \lambda &= \frac{m_{\text{PDA}}}{m_{\text{SDOF}}} = \frac{8\rho ba^2}{\pi^3 m_{\text{SDOF}}} \tanh\left(\frac{\pi h}{a}\right),
 \end{aligned} \tag{13}$$

where m_{SDOF} is the structural mass of an equivalent SDOF system, which was defined in equation (2). According to Chang et al. [19, 29], the values of ξ_{PDA} and R_f can be obtained from Table 2.

2.4. Two-Way Liquid Dampers. Lee et al. [22] proposed a two-way-liquid damper (TWLD) which behaves as both tuned liquid column damper (TLCD) and tuned sloshing damper (TSD) in both orthogonal directions (see Figure 1(d)). For bidirectional control of building structures, the TLCD action (x -direction) is tuned to a particular structural frequency in xz plane and the TSD action (y -direction) is tuned to a particular structural frequency in yz plane. To ensure the U-shape, three constrained conditions are required: $2t < L_h$, $t < h$ and

$$L_e = 2h - t + L_h, \tag{14}$$

where L_e is the effective length of the TLCD, that is, the total liquid column length; h is the liquid depth; t is the thickness of the TLCD and L_h is the horizontal liquid column length.

For both orthogonal directions, the fundamental angular frequencies of both TLCD and TSD are defined, respectively, as follows [23]:

$$\omega_{\text{PDA},x} = \sqrt{\frac{2g}{L_e}}, \tag{15}$$

$$\omega_{\text{PDA},y} = \sqrt{\frac{\pi g}{L_w} \tanh\left(\frac{\pi h}{L_w}\right)},$$

where g is the gravitational acceleration and L_w is the width of TSD.

For TLCD action (x -direction), the TLCD/SDOF non-dimensional mass ratio and the TLCD mass efficiency index are defined, respectively, as follows [22, 23]:

$$\mu_x = \frac{\rho L_w t L_e}{m_{\text{SDOF},x}}, \quad (16)$$

$$\lambda_x = \mu_x \left(\frac{L_h}{L_e} \right)^2 = \frac{\rho L_w t L_h^2}{L_e m_{\text{SDOF},x}},$$

where ρ is the liquid density (usually water) and $m_{\text{SDOF},x}$ is the structural mass of an equivalent SDOF system in xz plane. For TSD action (y -direction), the TSD/SDOF non-dimensional mass ratio and the TSD mass efficiency index are defined, respectively, as follows [22, 23]:

$$\mu_y = \frac{2\rho L_w t h}{m_{\text{SDOF},y}}, \quad (17)$$

$$\lambda_y = \beta \mu_y = \frac{2\beta \rho L_w t h}{m_{\text{SDOF},y}},$$

where $m_{\text{SDOF},y}$ is the structural mass of an equivalent SDOF system in yz plane and β is the first modal mass participation factor of liquid sloshing, which is given by the following equation:

$$\beta = \frac{8L_w}{\pi^3 h} \tanh\left(\frac{\pi h}{L_w}\right). \quad (18)$$

According to Figure 1(d), L_e , L_w , L_h , h and t are computed by solving the following system of nonlinear equations:

$$\rho L_w t L_e - m_{\text{SDOF},x} \mu_x = 0, \quad (19a)$$

$$2\rho L_w t h - m_{\text{SDOF},y} \mu_y = 0, \quad (19b)$$

$$2h - t + L_h - L_e = 0, \quad (19c)$$

$$w_{xz,i} R_{f,x} - \sqrt{\frac{2g}{L_e}} = 0, \quad (19d)$$

$$w_{yz,i} R_{f,y} - \sqrt{\frac{\pi g}{L_w} \tanh\left(\frac{\pi h}{L_w}\right)} = 0, \quad (19e)$$

where $w_{xz,i}$ and $w_{yz,i}$ are the angular frequencies of the i th lateral mode of vibration of the building in xz plane and yz plane, respectively. According to Chang [19, 29], $R_{f,x}$ and $R_{f,y}$ can be obtained from Table 2 based on the values of μ_x , λ_x , μ_y , and λ_y .

For TLCD action (x -direction), the mass, spring stiffness, and damping coefficient are given by the following equations [22]:

$$m_{\text{PDA},x} = \rho L_w t L_e, \quad (20)$$

$$k_{\text{PDA},x} = m_{\text{PDA},x} (w_{\text{PDA},x})^2 = 2g\rho t L_w, \quad (21)$$

$$c_{\text{PDA},x} = 2\xi_{\text{PDA},x} m_{\text{PDA},x} w_{\text{PDA},x}, \quad (22)$$

where $\xi_{\text{PDA},x}$ can be obtained from Table 2 based on the values of μ_x and λ_x . For TSD action (y -direction), the mass, spring stiffness and damping coefficient are given by [22]

$$m_{\text{PDA},y} = \beta m_{\text{PDA},x} = \frac{8L_w^2 \rho t L_e}{\pi^3 h} \tanh\left(\frac{\pi h}{L_w}\right), \quad (23)$$

$$k_{\text{PDA},y} = m_{\text{PDA},y} (w_{\text{PDA},y})^2 = \pi g \beta \rho t L_e \tanh\left(\frac{\pi h}{L_w}\right) \\ = \frac{8L_w g \rho t L_e}{\pi^2 h} \tanh^2\left(\frac{\pi h}{L_w}\right), \quad (24)$$

$$c_{\text{PDA},y} = 2\xi_{\text{PDA},y} m_{\text{PDA},y} w_{\text{PDA},y}, \quad (25)$$

where $\xi_{\text{PDA},y}$ can be obtained from Table 2 based on the values of μ_y and λ_y .

2.5. Pendulum Tuned Mass Dampers. Neglecting both the rotational stiffness and rotational damping coefficient of the pendulum, the mass, spring stiffness, and damping coefficient of a PTMD (see Figure 1(e)) are defined, respectively, as follows [46]:

$$m_{\text{PDA}} = \mu m_{\text{SDOF}}, \\ k_{\text{PDA}} = \frac{m_{\text{PDA}} g}{l_p}, \quad (26)$$

$$c_{\text{PDA}} = 2\xi_{\text{PDA}} m_{\text{PDA}} w_{\text{PDA}},$$

where μ is the PTMD/SDOF nondimensional mass ratio that may be chosen in the range of 1/50 to 1/15 for a first design approach [38]; m_{SDOF} is the structural mass of an equivalent SDOF system, which was defined in equation (2); g is the gravitational acceleration; l_p is the pendulum length; ξ_{PDA} is the damping ratio of the PTMD; and w_{PDA} is the angular frequency of the pendulum, which is given by the following equation:

$$w_{\text{PDA}} = \sqrt{\frac{k_{\text{PDA}}}{m_{\text{PDA}}}} = \sqrt{\frac{g}{l_p}}. \quad (27)$$

Substituting equation (3) into equation (27) leads to the following equation:

$$l_p = \frac{g}{(R_f w_i)^2}, \quad (28)$$

where w_i is the angular frequency of the i th lateral mode of vibration of the building that will be tuned to the frequency of the PTMD and R_f is the PTMD/SDOF nondimensional frequency ratio. Table 3 shows some optimum tuning conditions for PTMDs attached to an undamped primary structure [26].

3. Coupled Shear-Flexural Discrete Model with PDAs

Huergo and Hernández [37] proposed a CSF discrete model with TMDs, which adequately reproduces the lateral deformation of buildings with different lateral resisting

TABLE 3: Optimum tuning conditions for PTMDs attached to an undamped primary structure.

Optimization criteria	Excitation	Optimum tuning conditions	
		R_f	ξ_{PDA}
Minimum root mean square value of relative displacement of primary structure	Force	$(\sqrt{1+0.5\mu})/(1+\mu)$	$\sqrt{(\mu+0.75\mu^2)/(4+6\mu+2\mu^2)}$
	Base acceleration	$(\sqrt{1-0.5\mu})/(1+\mu)$	$\sqrt{(\mu-0.25\mu^2)/(4+2\mu-2\mu^2)}$

systems. In this section, five different kinds of PDAs (TMD, C-TSD, R-TSD, TWLD, and PTMD) are unified by using equivalent TMDs. Therefore, a fixed-base N -story building with N_{PDA} PDAs can be schematically represented as shown in Figure 2.

According to Figure 2, the shear wall (flexural beam) and rigid frame (shear beam) are assumed to be connected by a finite number of axially rigid members that transmit horizontal forces; thus, both cantilever beams in the coupled system undergo the same lateral deformation, $u(z, t)$. For $j = 1, 2, 3, \dots, N$, the j th axially rigid member is represented by a spring whose stiffness tends to infinity, that is, $k_j^a \rightarrow \infty$, which guarantees a parallel coupling of the bending and shear stiffness of the building. The total length of each cantilever beam, H , is discretized into N linear finite elements, where the length of the j th finite element is denoted by $L_j (j = 1, 2, 3, \dots, N)$. The mass, spring stiffness, and damping coefficient of the j th PDA are represented by $m_{\text{PDA},j}$, $k_{\text{PDA},j}$ and $c_{\text{PDA},j}$, respectively, whereas the lateral displacement in the time domain of the j th PDA is represented as $u_{\text{PDA},j}(t)$.

If floor masses and lateral stiffness are assumed to remain constant along the height of the building, the degree of participation of overall flexural and overall shear deformations in the CSF model is controlled by a nondimensional lateral stiffness ratio given by the following equation:

$$\alpha = H \sqrt{\frac{GA^S}{EI}}, \quad (29)$$

where EI is the flexural rigidity of the building and GA^S is the effective shear rigidity of the building. A value of $\alpha \rightarrow 0$ represents a pure flexural model (Euler-Bernoulli beam), whereas a value of $\alpha \rightarrow \infty$ represents a pure shear model. According to Miranda and Reyes [47], the lateral deformation of shear wall buildings, shear wall-frame buildings, and moment-resisting frames can usually be approximated by using values of $0 \leq \alpha \leq 2$, $1.5 \leq \alpha \leq 6$, and $5 \leq \alpha \leq 20$, respectively. According to Miranda and Taghavi [2], EI and GA^S are given by the following equation:

$$EI = \frac{4\bar{m}\pi^2 H^4}{(T_1 \gamma_1)^2 (\gamma_1^2 + \alpha^2)}, \quad (30)$$

$$GA^S = \frac{4\bar{m}\pi^2 \alpha^2 H^2}{(T_1 \gamma_1)^2 (\gamma_1^2 + \alpha^2)}, \quad (31)$$

where \bar{m} is the mass per unit length of the building; H is the total height of the building; T_1 is the fundamental period of vibration of the fixed-base building, which can be computed by any of the existing empirical formulas [48–52]; and γ_1 is

an eigenvalue parameter related to the first mode shape of the CSF continuous model, that is, the first root of the following characteristic equation [2]:

$$2 + \left(2 + \frac{\alpha^4}{\gamma_i^2 (\alpha^2 + \gamma_i^2)} \right) \cos(\gamma_i) \cosh\left(\sqrt{\alpha^2 + \gamma_i^2}\right) + \left(\frac{\alpha^2}{\gamma_i \sqrt{\alpha^2 + \gamma_i^2}} \right) \sin(\gamma_i) \sinh\left(\sqrt{\alpha^2 + \gamma_i^2}\right) = 0, \quad (32)$$

where $i = 1, 2, 3, \dots, \infty$. In a pure shear model, $\alpha \rightarrow \infty$ and $\gamma_1 \rightarrow \pi/2$; however, Miranda and Reyes [47] indicated that $\alpha = 20$ represents a model very close to the pure shear model. Figure 3 shows the first root of equation (32) and its corresponding polynomial curve fitting.

For $0 \leq \alpha \leq 20$, the polynomial curve fitting shown in Figure 3 is given by the following equation:

$$\begin{aligned} \gamma_1 = & (8.0564 \times 10^{-10})\alpha^7 - (1.3677 \times 10^{-7})\alpha^6 \\ & + (8.4444 \times 10^{-6})\alpha^5 - (2.5511 \times 10^{-4})\alpha^4 \\ & + (4.0722 \times 10^{-3})\alpha^3 - (3.2706 \times 10^{-2})\alpha^2 \\ & + (9.0619 \times 10^{-2})\alpha + 1.8603. \end{aligned} \quad (33)$$

Neglecting axial deformation, each node of each cantilever beam (see Figure 2(b)) has two local degrees of freedom (transverse displacement and rotation). According to the Euler-Bernoulli beam theory, a 4×4 stiffness matrix is assumed for each finite element related to the flexural cantilever beam, considering the flexural rigidity, EI , shown in equation (30). On the other hand, according to the Timoshenko beam theory, a 4×4 stiffness matrix is assumed for each finite element related to the shear cantilever beam, considering an equivalent flexural rigidity, $(EI)^S \rightarrow \infty$, and the effective shear rigidity, GA^S , shown in equation (31). For the shear cantilever beam, pure shear deformation is guaranteed, regardless of the slenderness ratio, by assuming that $(EI)^S \rightarrow \infty$ [37]. Then, the $2N \times 2N$ stiffness matrices of both cantilever beams are assembled by the conventional numerical assembly technique for the finite element method. Subsequently, the condensed stiffness matrix of the decoupled flexural beam, $[K_\Delta^F]_{N \times N}$, and the condensed stiffness matrix of the decoupled shear beam, $[K_\Delta^S]_{N \times N}$, are computed by the well-known static condensation technique [53], considering that only translational degrees of freedom remain active. Reference [37] contains more explicit details on the formulation of the condensed stiffness matrices of both decoupled beams.

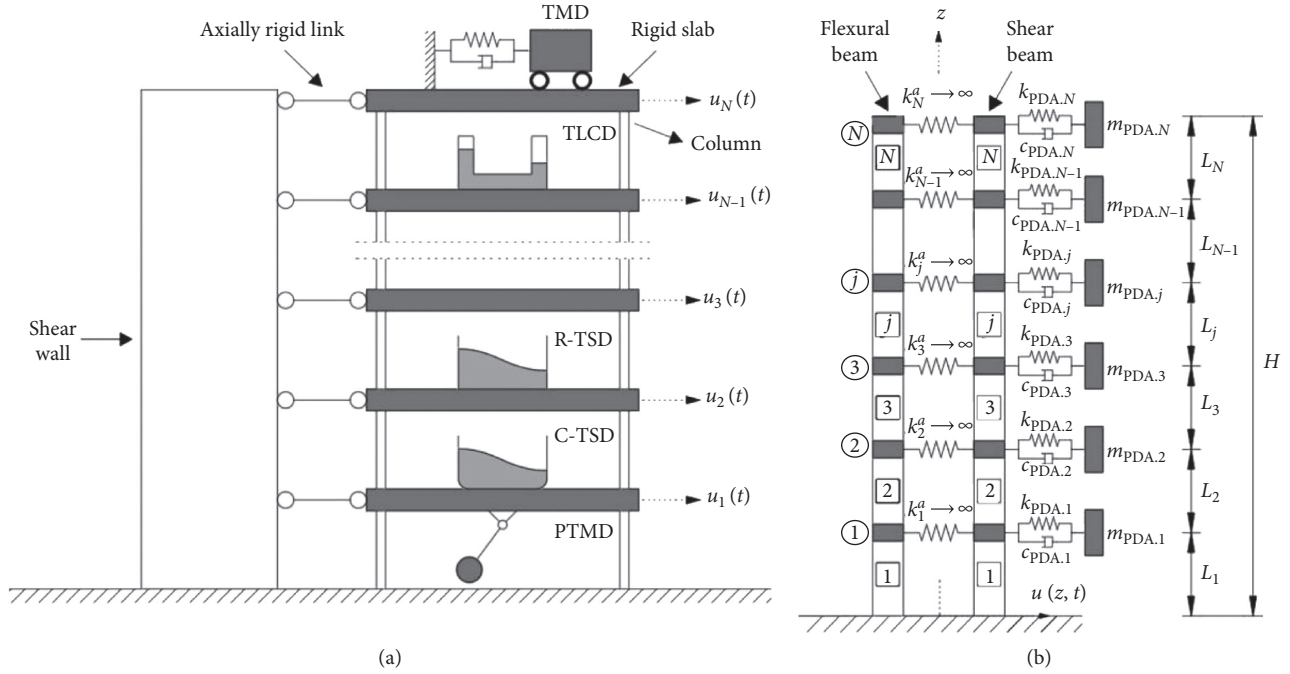


FIGURE 2: Coupled shear-flexural model for an N -story building with PDAs. (a) Sketch. (b) Equivalent discrete model [37].

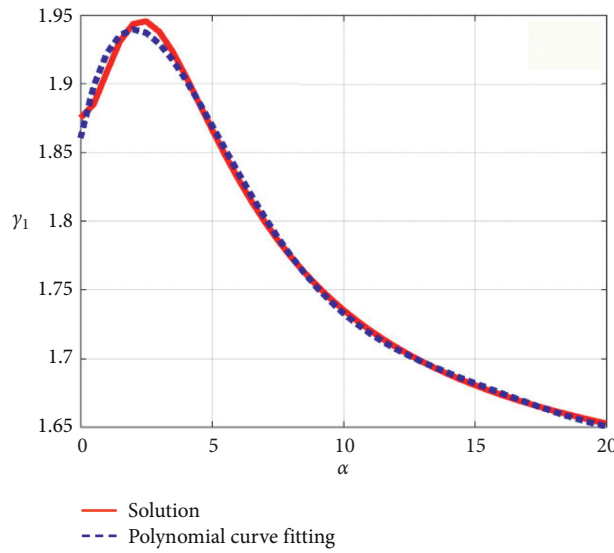


FIGURE 3: First root of the characteristic equation of the fixed-base CSF continuous model.

The lumped mass at the j th story of the building is represented by m_j ($j = 1, 2, 3, \dots, N$) in such a way that $m_N = 0.5\bar{m}(L_N)$ and $m_n = 0.5\bar{m}(L_n + L_{n+1})$, where $n = 1, 2, 3, \dots, (N-1)$ and \bar{m} is the mass per unit length of the building. Then, the total mass of the building is split in half; thereby, the lumped mass matrices of both decoupled beams are represented as $[M_{\Delta}^F]_{N \times N} = [M_{\Delta}^S]_{N \times N} = 0.5 \text{diag}[m_1 \dots m_N]$. According to Huergo and Hernández [37], the lateral damping matrix of the decoupled flexural beam, $[C_{\Delta}^F]_{N \times N}$, and the lateral damping matrix of the decoupled shear beam, $[C_{\Delta}^S]_{N \times N}$ are computed with the help of the

Rayleigh's approach [53] using the same damping ratio in all modes.

Assuming that $N_{\text{PDA}} = N$ (see Figure 2(b)), the equations of motion of the CSF model with PDAs can be grouped in the matrix system given by Huergo and Hernández [37]:

$$[M_{\text{CSF}}]\{\ddot{u}_{\text{CSF}}(t)\} + [C_{\text{CSF}}]\{\dot{u}_{\text{CSF}}(t)\} + [K_{\text{CSF}}]\{u_{\text{CSF}}(t)\} = \{F_{\text{CSF}}(t)\}, \quad (34)$$

where

$$[M_{\text{CSF}}] = \begin{bmatrix} [M_{\Delta}^F] & & & \\ & [M_{\text{PDA}}^F] & & \\ & & [M_{\Delta}^S] & \\ & & & [M_{\text{PDA}}^S] \end{bmatrix}, \quad (35)$$

$$[M_{\text{PDA}}^F] = [M_{\text{PDA}}^S] = \frac{1}{2} \begin{bmatrix} m_{\text{PDA},1} & & \\ & \ddots & \\ & & m_{\text{PDA},N} \end{bmatrix}, \quad (36)$$

$$[K_{\text{CSF}}] = \begin{bmatrix} [K_{\Delta}^F] + [K^A] + [K_{\text{PDA}}^F] & -[K_{\text{PDA}}^F] & -[K^A] & [0]_{N \times N} \\ -[K_{\text{PDA}}^F] & [K_{\text{PDA}}^F] & [0]_{N \times N} & [0]_{N \times N} \\ -[K^A] & [0]_{N \times N} & [K_{\Delta}^S] + [K^A] + [K_{\text{PDA}}^S] & -[K_{\text{PDA}}^S] \\ [0]_{N \times N} & [0]_{N \times N} & -[K_{\text{PDA}}^S] & [K_{\text{PDA}}^S] \end{bmatrix}, \quad (37)$$

$$[K^A] = \begin{bmatrix} k_1^a \rightarrow \infty & & \\ & \ddots & \\ & & k_N^a \rightarrow \infty \end{bmatrix}, \quad (38)$$

$$[K_{\text{PDA}}^F] = [K_{\text{PDA}}^S] = \frac{1}{2} \begin{bmatrix} k_{\text{PDA},1} & & \\ & \ddots & \\ & & k_{\text{PDA},N} \end{bmatrix}, \quad (39)$$

$$[C_{\text{CSF}}] = \begin{bmatrix} [C_{\Delta}^F] + [C_{\text{PDA}}^F] & -[C_{\text{PDA}}^F] & [0]_{N \times N} & [0]_{N \times N} \\ -[C_{\text{PDA}}^F] & [C_{\text{PDA}}^F] & [0]_{N \times N} & [0]_{N \times N} \\ [0]_{N \times N} & [0]_{N \times N} & [C_{\Delta}^S] + [C_{\text{PDA}}^S] & -[C_{\text{PDA}}^S] \\ [0]_{N \times N} & [0]_{N \times N} & -[C_{\text{PDA}}^S] & [C_{\text{PDA}}^S] \end{bmatrix}, \quad (40)$$

$$[C_{\text{PDA}}^F] = [C_{\text{PDA}}^S] = \frac{1}{2} \begin{bmatrix} c_{\text{PDA},1} & & \\ & \ddots & \\ & & c_{\text{PDA},N} \end{bmatrix}, \quad (41)$$

$$\{u_{\text{CSF}}(t)\} = \{ \{u_{\Psi}^F(t)\} \quad \{u_{\Psi}^S(t)\} \}^T, \quad (42)$$

$$\{u_{\Psi}^F(t)\} = \{u_{\Psi}^S(t)\} = \{u_1(t) \dots u_N(t) u_{\text{PDA},1}(t) \dots u_{\text{PDA},N}(t)\}. \quad (43)$$

For seismic loads, the external forces of the CSF model are given by

$$\{F_{\text{CSF}}(t)\} = -[M_{\text{CSF}}] \{1\}_{4N \times 1} \ddot{u}_g(t), \quad (44)$$

where $\ddot{u}_g(t)$ is the horizontal ground acceleration, whereas for wind loads, the external forces of the coupled system are given by the following equation:

$$\{F_{\text{CSF}}(t)\} = \frac{1}{2} \{F_1(t) \dots F_N(t) \{0\}_{1 \times N} F_1(t) \dots F_N(t) \{0\}_{1 \times N}\}^T, \quad (45)$$

where $F_j(t)$ is the wind force acting on the j th story.

The matrix equation (34) can be expressed as follows:

$$\{\dot{q}(t)\} = [A] \{q(t)\} + \{F_e(t)\}, \quad (46)$$

where for $N_{\text{PDA}} = N$,

$$\{q(t)\} = \begin{Bmatrix} \{u_{\text{CSF}}(t)\} \\ \{\dot{u}_{\text{CSF}}(t)\} \end{Bmatrix}_{8N \times 1},$$

$$\{\dot{q}(t)\} = \begin{Bmatrix} \{\dot{u}_{\text{CSF}}(t)\} \\ \{\ddot{u}_{\text{CSF}}(t)\} \end{Bmatrix}_{8N \times 1},$$

$$[A] = \begin{bmatrix} [0]_{4N \times 4N} & [I]_{4N \times 4N} \\ -[M_{\text{CSF}}]^{-1} [K_{\text{CSF}}] & -[M_{\text{CSF}}]^{-1} [C_{\text{CSF}}] \end{bmatrix}_{8N \times 8N},$$

$$\{F_e(t)\} = \begin{Bmatrix} \{0\}_{4N \times 1} \\ [M_{\text{CSF}}]^{-1} \{F_{\text{CSF}}(t)\} \end{Bmatrix}_{8N \times 1},$$

(47)

and $[I]_{4N \times 4N}$ is the identity matrix. The matrix equation for a numerical integration solution using the state space method [54] is as follows:

$$\{q(t_{v+1})\} = e^{[A]\Delta t} \{q(t_v)\} + e^{[A]\Delta t} \Delta t \{F_e(t_v)\}, \quad (48)$$

where Δt is the integration time step.

Once the relative displacements have been determined by equation (48), the element forces for structural design can be determined by static analysis of the structure at each time step. At any instant of time, the equivalent static forces are the external forces that will produce the relative displacements at the same instant of time in the stiffness component of the structure [53].

The i th effective modal mass of the fixed-base CSF model with PDAs is given by the following equation:

$$m_{\text{eff},i} = \frac{\left(\{\phi_{\text{CSF},i}\}^T [M_{\text{CSF}}] \{1\}_{4N \times 1} \right)^2}{\{\phi_{\text{CSF},i}\}^T [M_{\text{CSF}}] \{\phi_{\text{CSF},i}\}}, \quad (49)$$

where $\{\phi_{\text{CSF},i}\}$ is the i th mode shape vector of the coupled model. Therefore, the participating mass ratio of the i th mode of vibration is defined as $m_{\text{eff},i}/m_T$, where the total mass is given by $m_T = \sum_{j=1}^N m_j + m_{\text{PDA},j}$.

The consideration of $N_{\text{PDA}} < N$ is achieved by assuming that some PDAs have mass, spring stiffness, and damping coefficient equal to zero. In this case, the matrices $[M_{\text{CSF}}]$, $[K_{\text{CSF}}]$, and $[C_{\text{CSF}}]$ will have some rows and columns with all zero entries, which must be removed before performing a linear time-history analysis. In addition, the size of $\{u_{\text{CSF}}(t)\}$ and $\{F_{\text{CSF}}(t)\}$ must also be changed.

4. Effect of the Lateral Resisting System on PDAs

According to the uniform CSF continuous model [2], equation (2) can be expressed as follows:

$$m_{\text{SDOF}} = \frac{\bar{m}H \int_0^1 \phi_i^2(\bar{z}) d\bar{z}}{\phi_i^2(\bar{z}_{\text{PDA}})}, \quad (50)$$

where \bar{m} is the mass per unit length of the building; H is the total height of the building; $\bar{z} = z/H$; $\bar{z}_{\text{PDA}} = z_{\text{PDA}}/H$; and $\phi_i(\bar{z})$ is the i th mode shape of the CSF continuous model [2], which is given by the following equation:

$$\begin{aligned} \phi_i(\bar{z}) = & \sin(\gamma_i \bar{z}) - \frac{\gamma_i}{\sqrt{\alpha^2 + \gamma_i^2}} \sinh\left(\bar{z} \sqrt{\alpha^2 + \gamma_i^2}\right) \\ & - \eta_i \cos(\gamma_i \bar{z}) + \eta_i \cosh\left(\bar{z} \sqrt{\alpha^2 + \gamma_i^2}\right), \end{aligned} \quad (51)$$

where $i = 1, 2, 3, \dots, \infty$; γ_i is the i th root of equation (32) and

$$\eta_i = \frac{\gamma_i^2 \sin(\gamma_i) + \gamma_i \sqrt{\alpha^2 + \gamma_i^2} \sinh\left(\sqrt{\alpha^2 + \gamma_i^2}\right)}{\gamma_i^2 \cos(\gamma_i) + (\alpha^2 + \gamma_i^2) \cosh\left(\sqrt{\alpha^2 + \gamma_i^2}\right)}. \quad (52)$$

The effect of the lateral resisting system of the building on the value of m_{SDOF} is shown in Figure 4, considering different attachment point locations of the PDAs.

For a PDA tuned to the first mode of vibration, Figure 4 shows that for lower stories m_{SDOF} increases as α decreases; on the contrary, for upper stories, m_{SDOF} increases as α increases. Therefore, for lower stories, the PDA/SDOF nondimensional mass ratio, μ , increases as α increases; on the contrary, for upper stories, μ increases as α decreases. In conclusion, a PDA tuned to the first mode of vibration is more effective in controlling vibrations at lower stories when the primary structure deforms like a pure shear beam. On the contrary, its effectiveness in vibration control increases at upper stories for flexural-type deformations.

For both second and third modes of vibration, m_{SDOF} changes significantly for middle stories as α changes. For the second mode of vibration, μ increases as α increases when a single PDA is attached in the range $0.2H \leq z_{\text{PDA}} \leq 0.8H$, whereas for the third mode of vibration, μ increases as α decreases when a single PDA is attached in the range $0.4H \leq z_{\text{PDA}} \leq H$. Furthermore, for the first three modes of vibration, μ increases as α decreases when $z_{\text{PDA}} = H$; thus, a single PDA installed at the rooftop level could be more effective for multimode control than an equal-mass PDA installed at lower stories.

According to the shallow water wave theory [40], the depth ratios $h/2r$ and h/a of C-TSDs and R-TSDs, respectively, must be ranged from 0.04 to 0.05. Both depth ratios are generally in this range in order to obtain high damping of liquid sloshing and efficient moving mass [40]; that is, for the same value of μ , the values of ξ_{PDA} and m_{PDA} increase as the depth ratio decreases. Assuming shallow water waves with a mass density of 1000 kg/m^3 , Figure 5 shows the maximum efficient moving mass computed for both a circular tuned sloshing damper (C-TSD) and a rectangular tuned sloshing damper (R-TSD, $a = b$), considering a single TSD on the rooftop level tuned to the fundamental mode of vibration with a depth ratio equal to 0.46. The geometry and equivalent TMD mass related to Figure 5 are shown in Table 4.

Figure 5 shows that the maximum possible value of the mass efficiency index, γ , increases as the fundamental period of vibration of the building increases. Figure 5 also shows that γ increases as α decreases; thereby, larger TSDs can be installed at the rooftop level in buildings that deform as pure flexural beams in order to increase the effectiveness in vibration control. For the same depth ratios (see Figure 5 and Table 4), γ and m_{PDA} are greater for a square tuned sloshing damper even though the total liquid mass μm_{SDOF} is greater for a circular tuned sloshing damper. Therefore, a R-TSD could be a better option for vibration control than a C-TSD. Furthermore, a R-TSD is a more versatile device because it is able to be tuned to both translational directions by changing the dimensions of the tank.

For the special case of TWLDs, a parametric analysis for different values of α is impractical due to the system of nonlinear equations (19a)–(19e) and the three constrained conditions that ensure the U-shape on the device. However, greater values of μ and m_{PDA} can be expected for high-rise buildings that deform as pure flexural beams (see Table 5). In addition, equations (20) and (23) demonstrate that the equivalent TMD mass is always greater for the TLCD action.

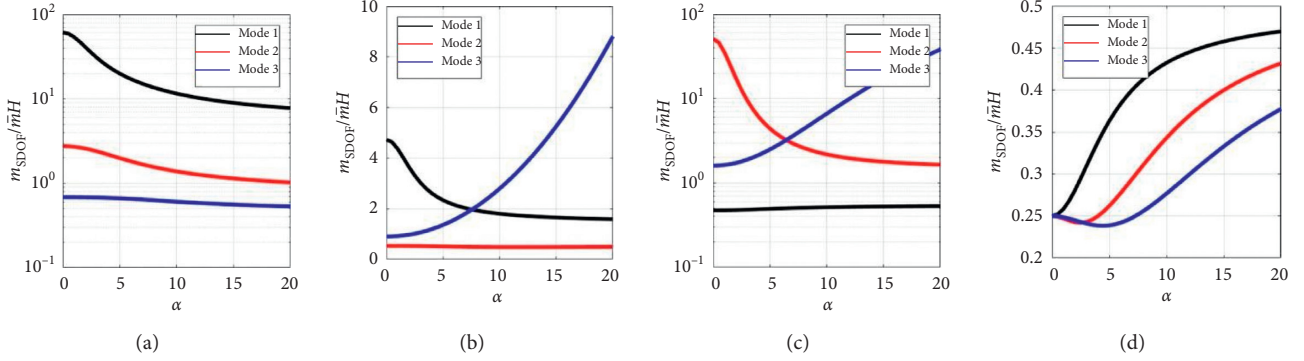


FIGURE 4: Structural mass of an equivalent SDOF system. (a) $Z_{\text{PDA}} = 0.2H$. (b) $Z_{\text{PDA}} = 0.4H$. (c) $Z_{\text{PDA}} = 0.8H$. (d) $Z_{\text{PDA}} = H$.

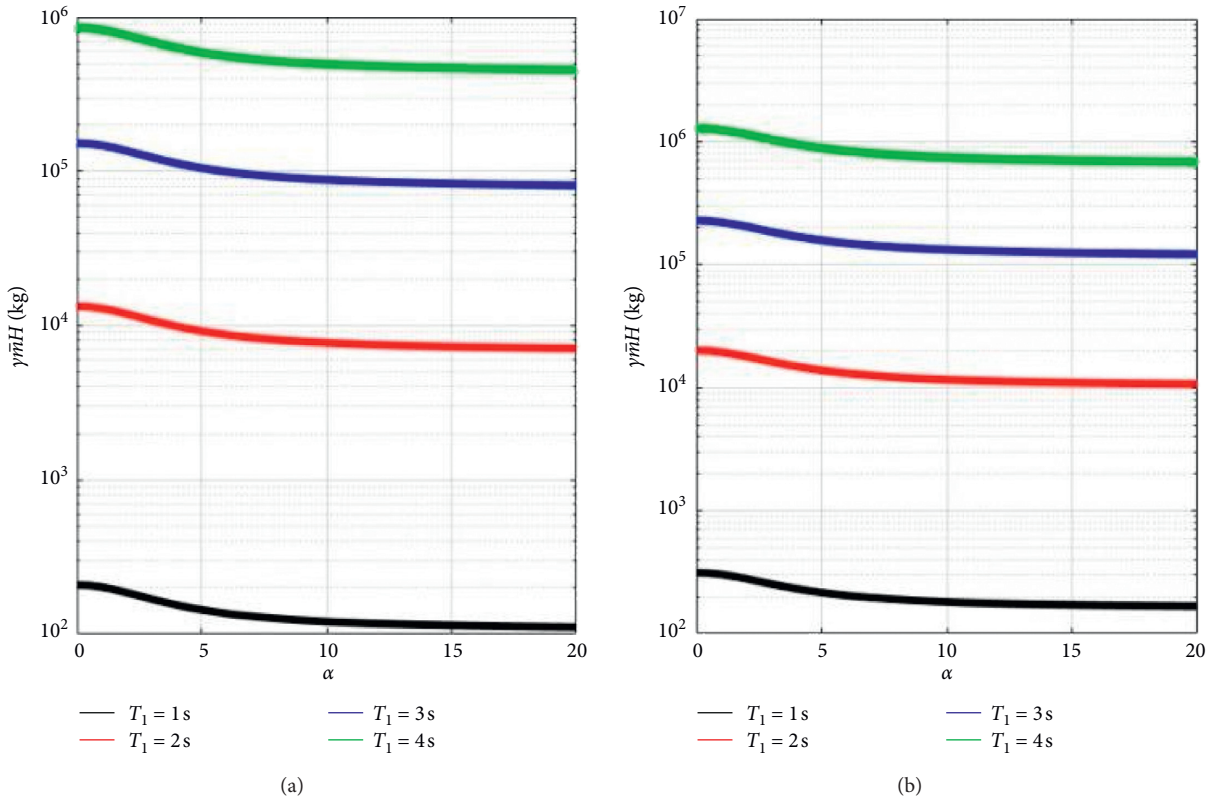


FIGURE 5: Maximum efficient moving mass of a single TSD attached at $z_{\text{PDA}} = H: h/2r = h/a = 0.46$ and $R_f = 1$. (a) C-TSD. (b) R-TSD ($a = b$).

TABLE 4: Geometry and equivalent TMD mass of a single TSD attached at $z_{\text{PDA}} = H: h/2r = h/a = 0.46$ and $R_f = 1$.

T_1 (s)	Type of TSD	$2r$ (cm)	$a = b$ (cm)	h (cm)	μm_{SDOF} (kg)	m_{PDA} (kg)
1	C-TSD	85.44	—	39.28	225.23	52.13
	R-TSD	—	69.82	32.07	156.32	78.52
2	C-TSD	341.76	—	157.13	14414	3336.6
	R-TSD	—	279.26	128.28	10004	5025.4
3	C-TSD	768.97	—	353.54	164190	38006
	R-TSD	—	628.59	289.1	114230	57333
4	C-TSD	1367.1	—	628.52	922530	213540
	R-TSD	—	1117	513.12	640270	321620

TABLE 5: Numerical example of the maximum mass parameters of a TWLD: $T_{1,x} = T_{1,y} = H/46$, $\bar{m} = 200000$ kg/m, and $R_f = 1$.

$T_{1,x}$ (s)	$T_{1,y}$ (s)	α	μ		γ		m_{PDA} (kg)	
			TLCD action	TSD action	TLCD action	TSD action	TLCD action	TSD action
4	4	0	0.015	0.01	0.0049	0.0064	138000	88297
		∞	—	—	—	—	—	—
6	6	0	0.04	0.035	0.0016	0.021	552000	326310
		∞	0.015	0.01	0.0022	0.0064	414000	265410
8	8	0	0.035	0.03	0.022	0.020	644000	431030
		∞	0.015	0.01	0.0018	0.0064	552000	353190

For the rooftop level, the same behavior occurs for the solid mass vibration absorbers (TMD and PTMD). That is, the maximum possible value of μ increases as T_1 increases and α decreases; however, the mass efficiency index, γ , for both devices is equal to one. Therefore, solid mass vibration absorbers generally are more effective in vibration control, even though both devices are more expensive than tuned liquid dampers. For PTMDs, the pendulum length increases as the fundamental period of vibration of the building increases.

According to Section 2, the PDA/SDOF nondimensional frequency ratio, R_f , and the PDA optimum damping ratio, ξ_{PDA} , represent the most important parameters for optimizing the vibration control of buildings. However, scientific literature [17, 19, 26, 29, 39] only features formulas for R_f and ξ_{PDA} that do not include the nondimensional lateral stiffness ratio, α . In future works, the optimum tuning conditions will be studied by using the CSF model with TMDs [37] subjected to several loading cases.

5. Numerical Example

In this section, the improved CSF model (see Figure 2(a)) is used to assess the vibration control of a 37-story building located in the Valley of Mexico (see Figure 6(a)). The length, depth, and height of the building are 44 m, 22 m, and 144.24 m, respectively. The building has composite steel deck floors with 4 cm concrete slabs (see Figure 6(b)). The lateral resisting system of the building in x -direction consists of moment-resisting frames. On the other hand, the lateral resisting system of the building in y -direction consists of a combination of 12 cm masonry shear walls and braced frames. The mechanical properties and dimensions of the structural elements of the building are described in detail by Huergo et al. [55]. For both translational directions, the first lateral modes of vibration of a fixed-base 3D finite element model (FEM) are shown in Figure 7.

The building was idealized as a fixed-base CSF discrete model, where each beam was discretized into 37 finite elements of equal length, that is, $L_j = 3.8984$ m for $j = 1, 2, 3, \dots, 37$. For this numerical example, it was assumed that $(EI)^S = 1 \times 10^{100}$ Nm², which guarantees a pure shear deformation for the shear cantilever beam. According to equation (38), it was assumed that $k_j^a = 1 \times 10^{15}$ N/m for $j = 1, 2, 3, \dots, 37$, which guarantees the parallel coupling between the flexural and shear cantilever beams. Table 6 shows the mechanical properties of the equivalent fixed-base CSF model. For the first mode shape in both translational

directions, Figure 8 shows a comparison between the fixed-base 3D FEM and the fixed-base CSF continuous model [2]. Furthermore, Table 7 and Figure 9 show the first three modes of vibration of the fixed-base building in both translational directions, which proves that the assumed values of α adequately represent the higher modes of vibration.

A single PDA (TMD, C-TSD, R-TSD, TWLD, and PTMD) attached at $z_{\text{PDA}} = H$ was tuned to $T_{xz,1} = 3.65$ s and $T_{yz,1} = 3.44$ s. Assuming the Cartesian coordinate system shown in Figure 6(b), the structural masses of the equivalent SDOF systems at $z_{\text{PDA}} = H$ are $m_{\text{SDOF},x} = 1.6996 \times 10^7$ kg and $m_{\text{SDOF},y} = 1.1009 \times 10^7$ kg for xz plane and yz plane, respectively. All the PDAs were optimized based on Tables 1–3. For the special case of a single TLD (C-TSD, R-TSD, and TWLD), the device was designed in such a way that its natural frequency is tunable by changing the liquid depth, assuming that the mass density of the water inside the container is equal to 1000 kg/m³.

According to the shallow-water wave theory [40], the maximum possible values of μ for C-TSDs were computed in such a way that both a real solution and a depth ratio of $h/2r < 0.5$ are guaranteed. The same values of μ were assumed for R-TSDs, which also guarantees shallow-water waves for rectangular containers. For R-TSDs, the depth ratio, h/a , is generally in the range of 0.04 to 0.5 in order to obtain high damping of liquid sloshing and efficient moving mass; that is, for the same value of μ , the values of ξ_{PDA} and m_{PDA} increase as the ratio h/a decreases. For both TMD and PTMD cases, the same values of μ computed for C-TSDs and R-TSDs were chosen in order to compare the effectiveness of the four different PDAs (TMD, PTMD, C-TSD, and R-TSD) in controlling the dynamic response of the building in both translational directions. For the TWLD case, the TLCDC action (x -direction) and the TSD action (y -direction) take place in xz plane and yz plane, respectively; however, the maximum possible values of μ are lower compared to those computed for the other four PDAs (TMD, PTMD, C-TSD, and R-TSD). The geometry and dynamic properties of the five different PDAs are shown in Tables 8–12.

For the numerical example, geometry and dynamic properties of the PDAs are shown in Tables 8–12, where T_{PDA} is the fundamental period of vibration of the PDA.

5.1. Earthquake-Induced Vibrations. For buildings without passive energy dissipation devices, the elastic CSF model is not useful when strong earthquakes generate an inelastic

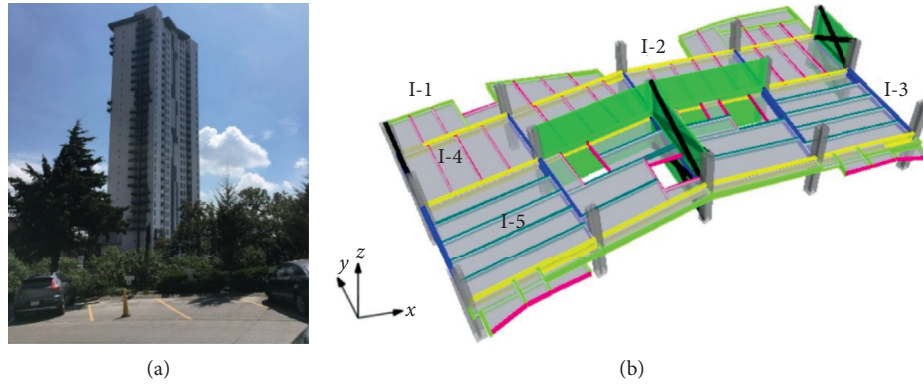


FIGURE 6: 144-meter-tall building located in the Valley of Mexico [55]. (a) General view. (b) Floor system.

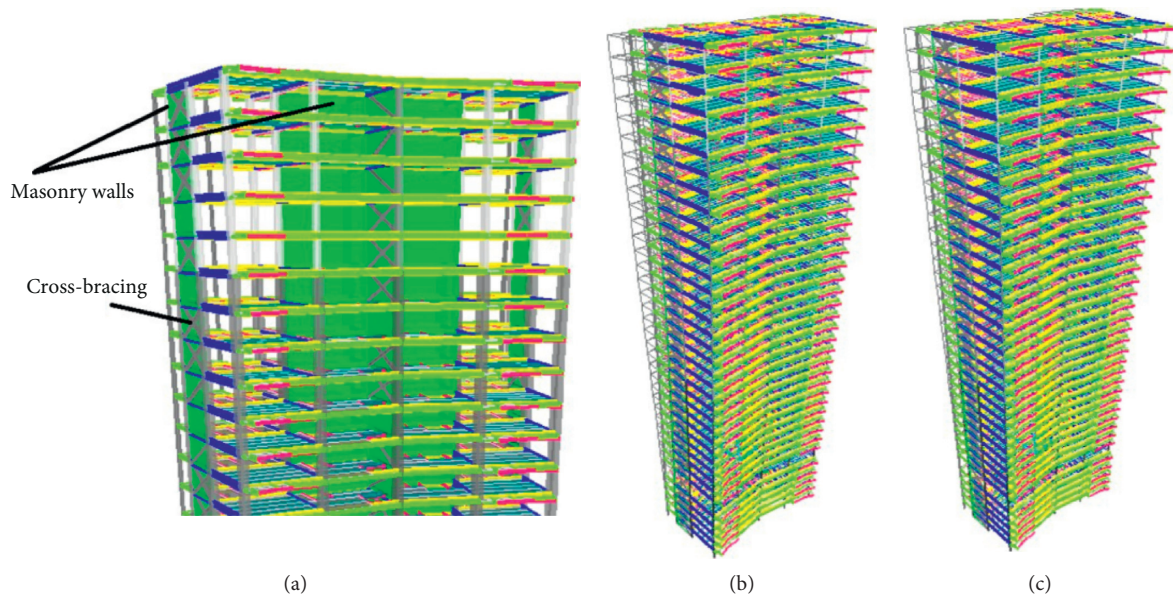


FIGURE 7: First lateral modes of vibration of a fixed-base 3D FEM [55]. (a) Lateral resisting system. (b) $T_{xz,1} = 3.65$ s. (c) $T_{yz,1} = 3.44$ s.

TABLE 6: Mechanical properties of the fixed-base CSF discrete model.

Mechanical property	xz plane	yz plane
\bar{m} (kg/m)	235664	235664
H (m)	144.24	144.24
T_1 (s)	3.65	3.44
γ_1	1.5708	1.9173
α	1×10^{100}	3.5
EI (N·m ²)	1.2251×10^{-186}	5.8129×10^{12}
GA^S (N)	5.8885×10^9	3.4225×10^9

dynamic response. For a time-domain inelastic analysis, maybe a possible solution could be to compute the elongation of the fundamental period (i.e., stiffness degradation) at each time step by using hysteresis loops. In this way, the stiffness matrix of the coupled system, $[K_{CSF}]$, could be assembled at each time step from the new values of EI and GA^S . However, further research related to the possibility of an extended CSF model capable of computing the inelastic response must be done. On the other hand, a linear elastic

behavior can be considered acceptable when the passive energy dissipation devices are effective in controlling earthquake-induced vibrations.

An earthquake ground motion record is composed by three orthogonal components: one vertical component and two horizontal components. For earthquakes acting in two directions, the two horizontal components of the ground acceleration must be applied to each translational direction of the CSF model by independent time-domain dynamic analyses. The Mexico City building code classifies the soil of the Valley of Mexico as firm (i.e., hard rock), lakebed (i.e., high water content clay underlain by resistant sands), and transition (i.e., between firm soil and lakebed zone). Three different stations are considered for the Mexico City earthquake of September 19, 1985: the N90E component recorded at station Central-de-Abastos-Frigorífico (CDAF), the N58E component recorded at station Sismex-Viveros (SXVI), and the S90W component recorded at station Ciudad-Universitaria-Mesa-Vibradora (CUMV). The earthquake ground motion records related to Table 13 are

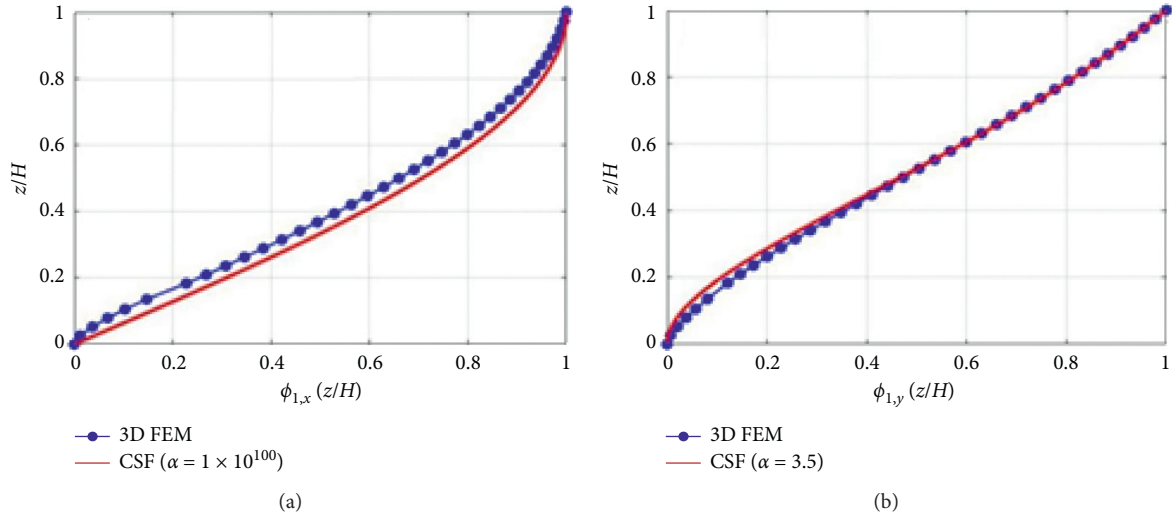


FIGURE 8: Mode shape of the first mode of vibration: 3D FEM vs. CSF model [55]. (a) xz plane. (b) yz plane.

TABLE 7: Periods and participating mass ratios of the fixed-base building: CSF model vs. 3D FEM [55].

Mode	Period (s)				Participating mass ratio (%)			
	xz plane		yz plane		xz plane		yz plane	
	CSF	3D FEM	CSF	3D FEM	CSF	3D FEM	CSF	3D FEM
1	3.65	3.65	3.44	3.44	81.03	77.26	67.94	66.01
2	1.22	1.25	0.89	0.98	8.98	8.86	13.17	10.62
3	0.73	0.75	0.38	0.48	3.22	2.76	5.71	3.57

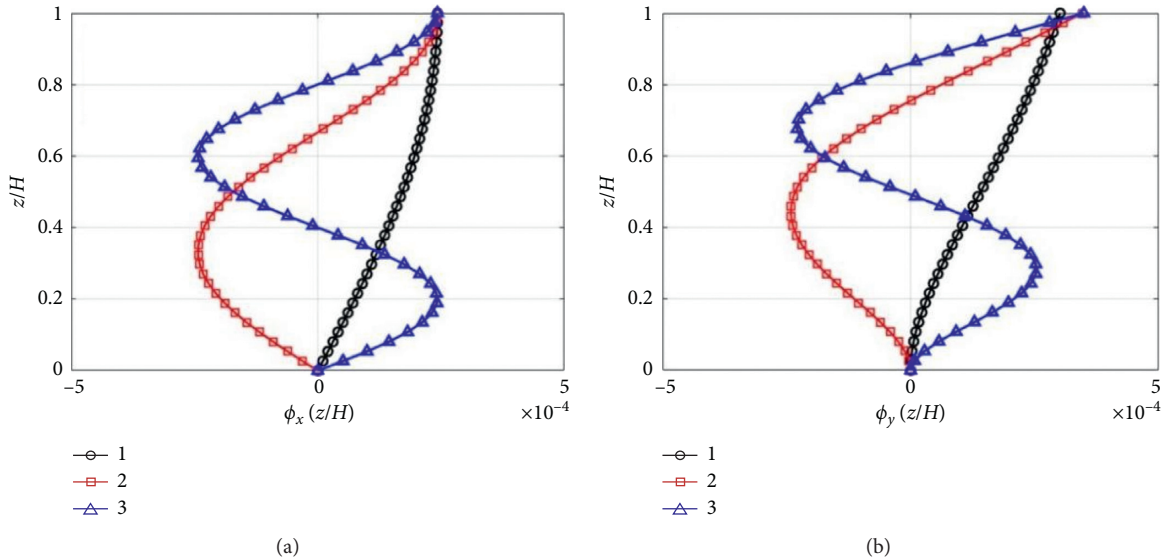


FIGURE 9: Mode shapes of the fixed-base building: CSF model without PDAs. (a) xz plane. (b) yz plane.

shown in Figure 10(a), whereas the elastic input energy spectra, related to a structural damping ratio of 5%, are shown in Figure 10(b). Both Table 13 and Figure 10 clearly show that the soil type significantly modifies the duration, peak ground acceleration, and energy content of the earthquake ground motion records, particularly for the

CDAF station, where the seismic waves were significantly amplified by the geologic conditions of the lakebed zone. For the three seismic records, Table 14 shows that peak values of input energy are related to periods lower than $T_{xz,1} = 3.65$ s and $T_{yz,1} = 3.44$ s. Therefore, PDAs could be less effective in controlling earthquake-induced vibrations because soil-

TABLE 8: Dynamic properties of a TMD attached at $z_{\text{PDA}} = H$.

Loading case and optimization criteria	Plane	μ	$T_{\text{PDA}}(\text{s})$	ξ_{PDA}	$m_{\text{PDA}}(\text{kg})$	$k_{\text{PDA}}(\text{N/m})$	$c_{\text{PDA}}(\text{N s/m})$
Harmonic base acceleration for minimum relative displacement amplitude of primary structure	xz	0.0140	3.71	0.0722	237944	680961	58132
	yz	0.0276	3.56	0.1011	303848	946709	108403
Harmonic load for minimum relative acceleration amplitude of primary structure	xz	0.0141	3.68	0.0725	239644	700260	59367
	yz	0.0281	3.49	0.1019	309353	1003833	113613

TABLE 9: Geometry and dynamic properties of a C-TSD attached at $z_{\text{PDA}} = H$.

Parameter	Seismic load		Along-wind load	
	xz plane	yz plane	xz plane	yz plane
μ	0.0140	0.0276	0.0141	0.0281
$T_{\text{PDA}}(\text{s})$	3.69	3.51	3.68	3.49
ξ_{PDA}	0.0323	0.0420	0.0324	0.0421
r (m)	5	5	5	5
h (m)	3.02	3.862	3.05	3.94
$m_{\text{PDA}}(\text{kg})$	71968	79600	72258	80125
$k_{\text{PDA}}(\text{N/m})$	208960	255630	210650	259010
$c_{\text{PDA}}(\text{N s/m})$	7930.3	11978	7993.8	12133

TABLE 10: Geometry and dynamic properties of a R-TSD attached at $z_{\text{PDA}} = H$.

Parameter	Seismic load		Along-wind load	
	xz plane	yz plane	xz plane	yz plane
μ	0.0140	0.0276	0.0141	0.0281
$T_{\text{PDA}}(\text{s})$	3.70	3.52	3.69	3.51
ξ_{PDA}	0.0448	0.0580	0.0448	0.0581
a (m)	8.69	8.68	8.69	8.68
b (m)	8.71	8.69	8.67	8.68
h (m)	3.14	4.03	3.18	4.10
$m_{\text{PDA}}(\text{kg})$	138030	151530	138170	152340
$k_{\text{PDA}}(\text{N/m})$	398040	482800	400610	488150
$c_{\text{PDA}}(\text{N s/m})$	20998	31356	21086	31691

TABLE 11: Geometry and dynamic properties of a TWLD attached at $z_{\text{PDA}} = H$.

Parameter	Seismic load		Along-wind load	
	xz plane	yz plane	xz plane	yz plane
μ	0.003	0.003	0.003	0.003
$T_{\text{PDA}}(\text{s})$	3.54	3.46	3.53	3.46
ξ_{PDA}	0.0273	0.0274	0.0160	0.0218
L_h (m)	3.60	—	3.62	—
L_w (m)	—	6.82	—	6.80
h (m)	2.02	2.02	2.01	2.01
t (m)	1.20	1.20	1.21	1.21
$m_{\text{PDA}}(\text{kg})$	50988	32469	50988	32503
$k_{\text{PDA}}(\text{N/m})$	160570	107240	161440	107480
$c_{\text{PDA}}(\text{N s/m})$	4949.2	3228	2896.6	2581.5

building resonance is avoided for both orthogonal directions. For the purposes of this numerical example, the soil-structure interaction effects are neglected; that is, the same modes of vibration of the fixed-based 144-meter-tall building are considered for the three seismic records shown in Figure 10(a).

According to the geometry and dynamic properties specified in Tables 8–12, 15 and 16 show the periods and modal participating mass ratios of the building with a single

PDA when the primary structure is subjected to the horizontal ground accelerations shown in Figure 10(a).

Tables 15 and 16 show that if a total of N_{PDA} PDAs are attached to the building, the first N_{PDA} modes of vibration will be under the influence of N_{PDA} PDAs, and the $(N_{\text{PDA}} + 1)^{\text{th}}$ mode of vibration will actually be the first mode of the building [37]. For example, if a single PDA is attached to the building, the first mode will be related to the PDA vibration, the second mode will be related to the first

TABLE 12: Geometry and dynamic properties of a PTMD attached at $z_{\text{PDA}} = H$.

Parameter	Base acceleration		Force	
	xz plane	yz plane	xz plane	yz plane
μ	0.0140	0.0276	0.0141	0.0281
$T_{\text{PDA}}(\text{s})$	3.71	3.56	3.69	3.51
ξ_{PDA}	0.0589	0.0822	0.0591	0.0829
l_p (m)	3.43	3.15	3.38	3.07
$m_{\text{PDA}}(\text{kg})$	237940	303850	239640	309350
$k_{\text{PDA}}(\text{N/m})$	680960	946710	695390	990120
$c_{\text{PDA}}(\text{N s/m})$	47381	88205	48220	91813

TABLE 13: General characteristics of the Mexico City earthquake of September 19, 1985.

Origin	Surface-wave magnitude	Depth (km)	Station	Soil type	Epicentral distance (km)	Peak ground acceleration (m/s^2)	Duration (s)
Subduction	8.1	15	CDAF	Lakebed	430	1.1749	143.19
			SXVI	Transition	422	0.4163	129.15
			CUMV	Firm	419	0.3828	62.58

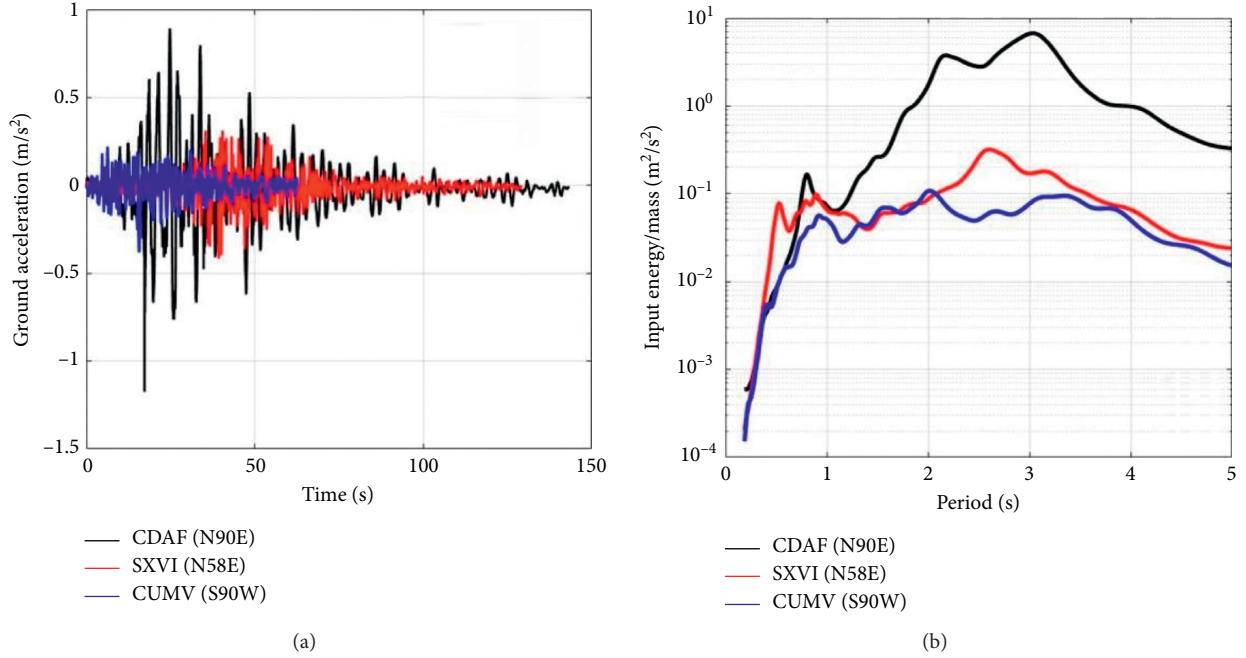


FIGURE 10: Mexico City earthquake of September 19, 1985. (a) Earthquake ground motion records. (b) Elastic input energy spectra.

TABLE 14: Elastic input energy of interest: Mexico City earthquake of September 19, 1985.

Station	CDAF			SXVI			CUMV		
Period (s)	3.03	3.44	3.65	2.60	3.44	3.65	2.02	3.44	3.65
Input energy/mass (m^2/s^2)	6.6986	2.0964	1.2506	0.3186	0.1150	0.0885	0.1083	0.0897	0.0682

mode without PDAs, and the third mode will be related to the second mode without PDAs, etc. For different lateral resisting systems, the structural mass of an equivalent SDOF system at $z_{\text{PDA}} = H$ increases as the value of α increases, that is, $m_{\text{SDOF},x} = 1.6996 \times 10^7$ kg and $m_{\text{SDOF},y} = 1.1009 \times 10^7$ kg. In a similar way, the participating mass ratio related to the first mode of vibration without PDAs also increases as the

value of α increases, that is, $m_{\text{eff},1}/m_T = 0.8103$ and $m_{\text{eff},1}/m_T = 0.6794$ for xz plane and yz plane, respectively.

For the five different PDAs shown in Tables 8–12, 36 time-history elastic analyses were carried out assuming that the building is subjected to the horizontal ground accelerations shown in Figure 10(a). Assuming a structural damping ratio of 5% and neglecting soil-structure

TABLE 15: Periods and participating mass ratios for xz plane of the building with a single PDA: seismic load.

Case	Period (s)				Participating mass ratio (%)			
	Mode 1	Mode 2	Mode 3	Mode 4	Mode 1	Mode 2	Mode 3	Mode 4
No PDAs	3.65	1.22	0.73	0.52	81.03	8.98	3.22	1.63
TMD	3.91	3.47	1.22	0.73	37.19	39.85	8.45	3.03
C-TSD	3.79	3.55	1.22	0.73	35.25	41.67	8.51	3.04
R-TSD	3.85	3.52	1.22	0.73	36.16	40.80	8.48	3.04
TWLD	3.71	3.48	1.22	0.73	58.96	17.95	8.51	3.05
PTMD	3.91	3.47	1.22	0.73	37.20	39.84	8.45	3.03

TABLE 16: Periods and participating mass ratios for yz plane of the building with a single PDA: seismic load.

Case	Period (s)				Participating mass ratio (%)			
	Mode 1	Mode 2	Mode 3	Mode 4	Mode 1	Mode 2	Mode 3	Mode 4
No PDAs	3.44	0.89	0.38	0.21	67.94	13.17	5.71	3.10
TMD	3.80	3.22	0.89	0.38	29.37	35.48	12.42	5.37
C-TSD	3.62	3.32	0.89	0.38	26.29	38.31	12.53	5.41
R-TSD	3.69	3.28	0.89	0.38	28.22	36.47	12.50	5.40
TWLD	3.54	3.35	0.89	0.38	29.08	35.47	12.56	5.42
PTMD	3.80	3.22	0.89	0.38	29.37	35.48	12.42	5.37

interaction effects, the peak displacements and peak inter-story drift ratios (IDR) are shown in Figures 11–14; whereas the peak values related to the critical storey are shown in Tables 17 and 18. Furthermore, Table 19 shows the peak values of both base shear force and base overturning moment, which were computed by the equivalent static load method [53].

According to Tables 17–19, all the PDAs are ineffective in vibration control for the CDAF and SXVI stations. According to Soto and Ruiz [56], the effectiveness of TMDs is higher for systems with small nonlinearity produced by small and moderate earthquakes, than for systems with high nonlinear behavior, generally associated with high-intensity motions. The ineffectiveness of vibration control of all PDAs in the CDAF and SXVI stations could be related to the high-intensity motion despite the assumed linear elastic behavior of the CSF model. The seismic response of a linear elastic building subjected to the narrow-band long duration can be significantly reduced if a TMD is included on its top; however, this reduction does not always represent a real advantage for buildings with a period near the dominant of the soil, because for intense motions the maximum-in-time base shear ratio still results too high [57], e.g., the case for 2 s period buildings located on soft soil in the Valley of Mexico.

For CUMV station, all the PDAs are slightly more effective for the vibration control of the primary structure. Approximately a 6% reduction is achieved for peak displacements and peak internal forces at the base. For low-to-moderate-intensity motion (e.g., CUMV station), the effectiveness of TMDs in vibration control of buildings with a period near the dominant of the soil (i.e., 2 s period building) can significantly increase as the value of μ increases (e.g., by using distributed multiple TMDs) [37]. However, larger values of μ are not possible when TLDs (C-TSD, R-TSD, TWLD) are attached to the 144-meter-tall building (see Tables 8–12). According to Tables 8–12, the same values of μ

for four different kinds of PDAs (TMD, C-TSD, R-TSD, and PTMD) lead to different values of m_{PDA} and ξ_{PDA} , that is, the PDA mass efficiency index, λ , of the liquid mass vibration absorbers leads to lower values of m_{PDA} and ξ_{PDA} . Therefore, the solid mass vibration absorbers (i.e., TMD and PTMD) are slightly more effective in controlling the seismic response in CUMV station (see Tables 17 to 19).

According to Table 18, the damage index is usually expressed in terms of the peak interstory drift ratio. For xz plane, the greatest damage is located at $z = 0.22H$, $z = 0.027H$ and $z = 0.027H$ for CDAF, SXVI and CUMV stations, respectively; however, for the solid mass vibration absorbers (TMD and PTMD), the greatest damage in the CUMV station is located at $z = 0.081H$. For yz plane, the greatest damage is located at $z = 0.51H$, $z = 0.68H$, and $z = 0.43H$ for CDAF, SXVI, and CUMV stations, respectively; however, for the solid mass vibration absorbers (TMD and PTMD), the greatest damage in the CUMV station is located at $z = 0.59H$. Therefore, the critical story depends not only on the value of α but also on the earthquake ground motion record and the equivalent parameters of the PDA.

The earthquake-induced vibrations shown in this section cannot be generalized because duration, peak ground acceleration, and energy content of earthquake ground motion records change depending on the epicentral distance, geologic conditions, and origin of the earthquake (e.g., local earthquakes, continental-plate earthquakes, normal-faulting earthquake, subduction earthquakes). In future works, the effectiveness of PDAs in controlling earthquake-induced vibrations will be studied using a flexible-base CSF model [58] subjected to several earthquake ground motion records.

5.2. Along-Wind Vibrations. The 144-meter-tall building is located in a suburban area with a roughness length of 0.3 m. Assuming an annual probability of 0.1, the mean wind

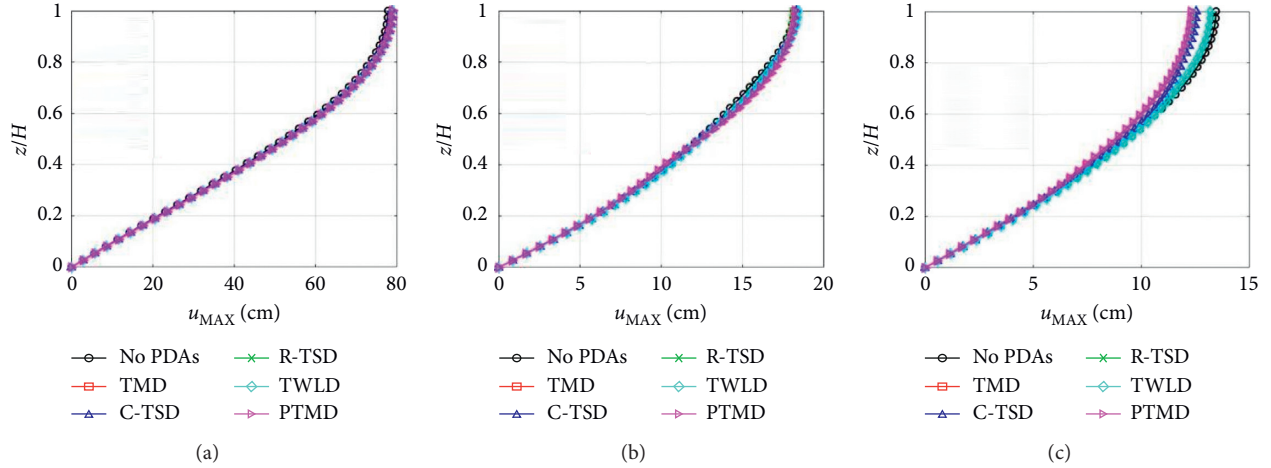


FIGURE 11: Seismic peak displacements of the building: xz plane. (a) CDAF. (b) SXVI. (c) CUMV.

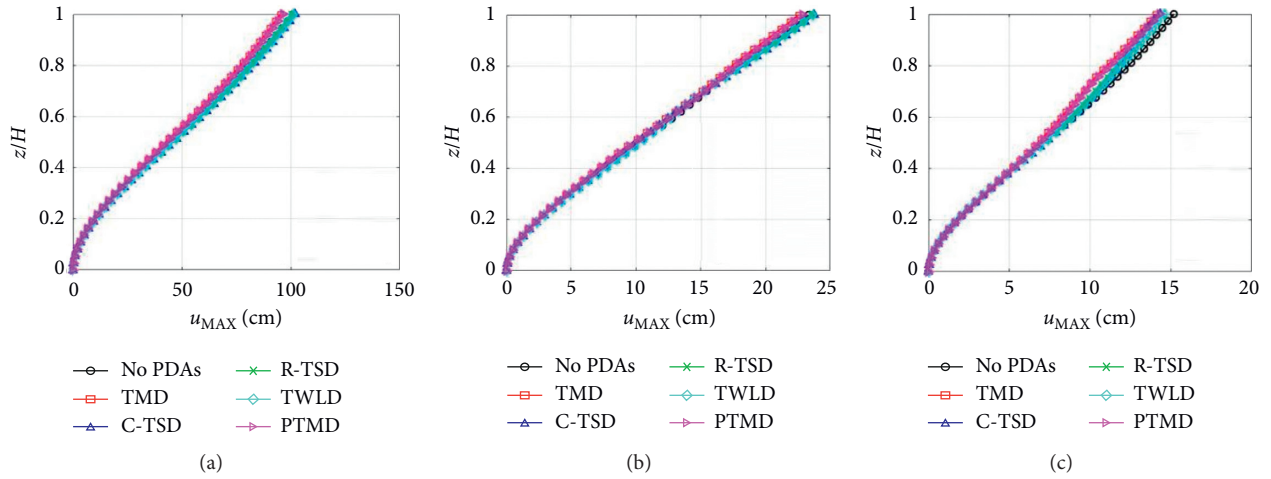


FIGURE 12: Seismic peak displacements of the building: yz plane. (a) CDAF. (b) SXVI. (c) CUMV.

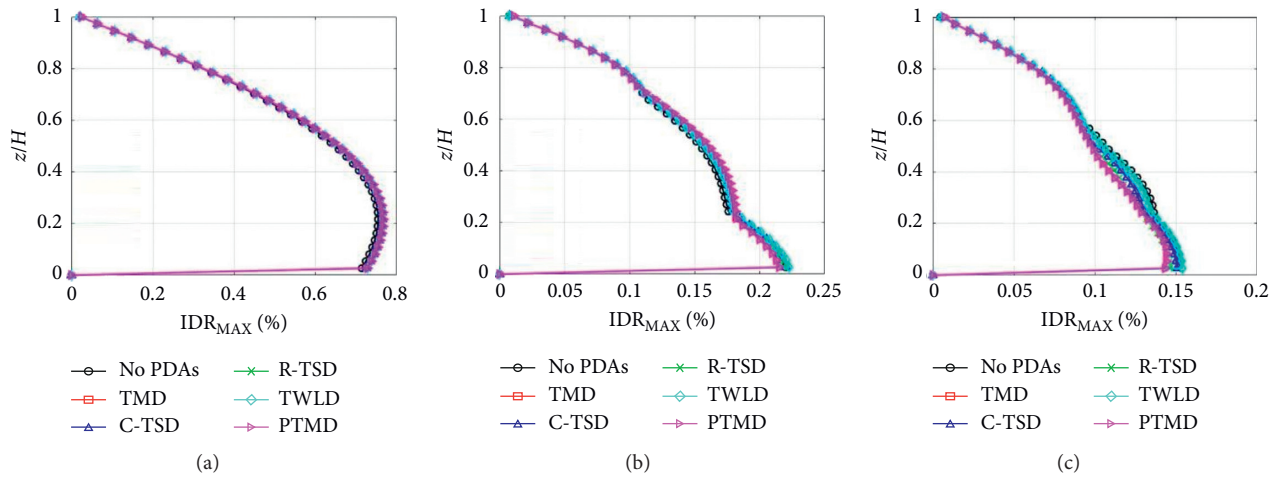
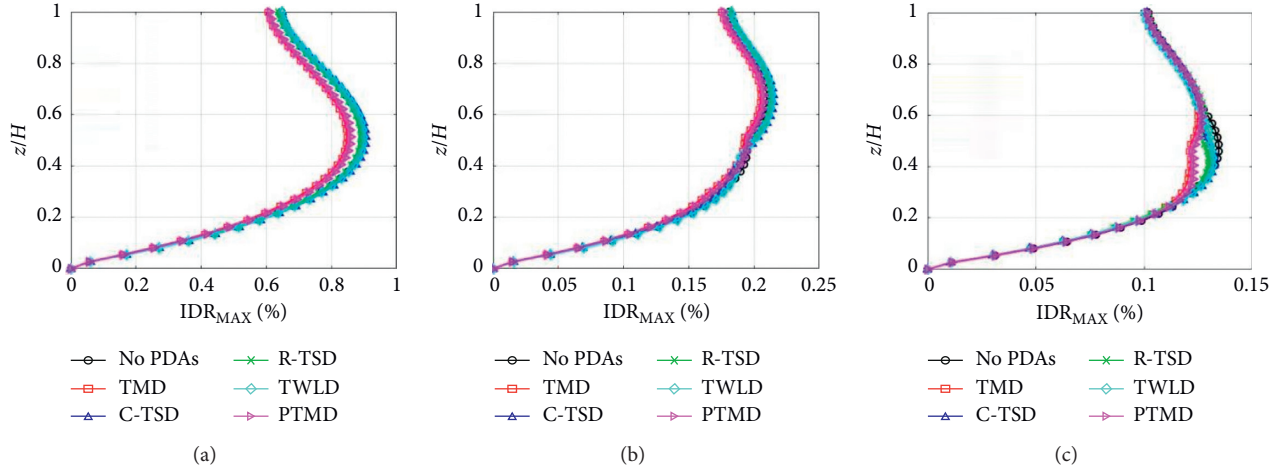


FIGURE 13: Seismic peak interstory drift ratios of the building: xz plane. (a) CDAF. (b) SXVI. (c) CUMV.

velocity at 10 m height is equal to 15.02 m/s [59]. In a wind field, the drag force at the j th story is given by the following equation:

$$F_j(t) = \frac{1}{2} \rho_a A_j C_D [\bar{U}(z_j) + u(z_j, t)]^2, \quad (53)$$

FIGURE 14: Seismic peak interstory drift ratios of the building: yz plane. (a) CDAF. (b) SXVI. (c) CUMV.TABLE 17: Peak seismic displacement [cm] at $z = H$.

Plane	Station	No PDAs	TMD	C-TSD	R-TSD	TWLD	PTMD
xz	CDAF	77.72	78.55	78.72	78.69	78.92	78.81
	SXVI	18.14	18.11	18.30	18.08	18.42	18.21
	CUMV	13.44	12.28	12.52	12.35	13.17	12.27
yz	CDAF	101.21	95.29	101.98	100.31	101.51	96.54
	SXVI	23.32	22.56	23.75	23.53	23.66	22.87
	CUMV	15.18	14.07	14.33	14.42	14.58	14.31

TABLE 18: Peak interstory drift ratio at the critical story.

Station	Case	xz plane		yz plane	
		z/H	Peak interstory drift ratio (%)	z/H	Peak interstory drift ratio (%)
CDAF	No PDAs	0.22	0.7542	0.51	0.8968
	TMD	0.22	0.7644	0.51	0.8468
	C-TSD	0.22	0.7644	0.51	0.9049
	R-TSD	0.22	0.7647	0.51	0.8907
	TWLD	0.22	0.7672	0.51	0.9002
	PTMD	0.22	0.7669	0.51	0.8584
SXVI	No PDAs	0.027	0.2198	0.68	0.2113
	TMD	0.027	0.2147	0.68	0.2050
	C-TSD	0.027	0.2204	0.68	0.2147
	R-TSD	0.027	0.2176	0.68	0.2129
	TWLD	0.027	0.2226	0.68	0.2140
	PTMD	0.027	0.2148	0.68	0.2075
CUMV	No PDAs	0.027	0.1536	0.46	0.1344
	TMD	0.081	0.1439	0.59	0.1247
	C-TSD	0.027	0.1503	0.43	0.1322
	R-TSD	0.027	0.1461	0.43	0.1297
	TWLD	0.027	0.1541	0.43	0.1319
	PTMD	0.081	0.1443	0.59	0.1267

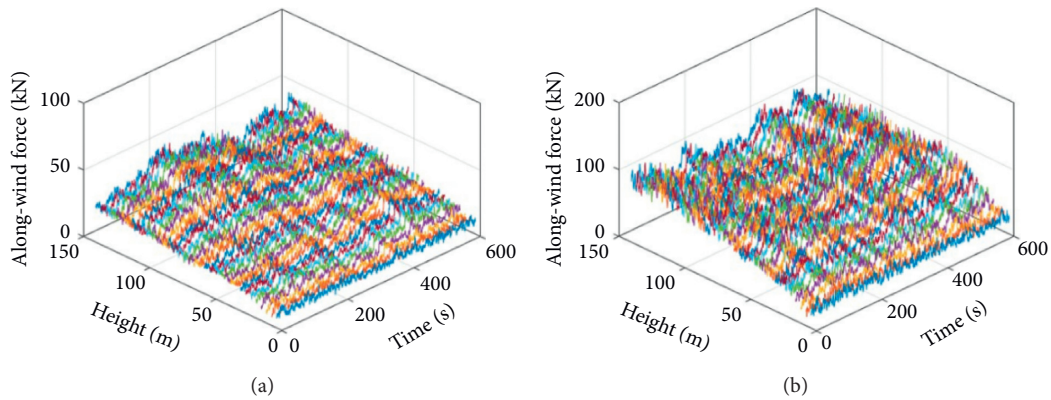
where ρ_a is the air density; A_j is the projected area of the j th story; C_D is the drag coefficient, which was assumed as equal to 1.1 and 1.45 for xz plane and yz plane, respectively [59]; $\bar{U}(z_j)$ is the mean wind velocity at z_j ; and $u(z_j, t)$ is the fluctuating part of the wind field, which can be treated mathematically as a stationary stochastic process with a zero mean value. Assuming the Solari spectrum [60], the fluctuating component was computed by using the spectral

representation technique [61]. According to equation (53), the simulated drag forces for the building are shown in Figure 15.

For wind engineering, the total damping ratio is composed of the structural part and the aerodynamic part, where the aerodynamic damping is caused by the interaction between the motion of a structure and motion of the air around it [62–64]. The aerodynamic damping increases the total

TABLE 19: Seismic peak values for the internal forces at the base.

Station	Case	Base shear force (MN)		Base overturning moment (GN m)	
		xz plane	yz plane	xz plane	yz plane
CDAF	No PDAs	42.051	47.731	4.5766	5.2590
	TMD	43.063	44.254	4.6588	4.9498
	C-TSD	43.060	47.654	4.6630	5.3189
	R-TSD	43.088	45.873	4.6473	5.2067
	TWLD	43.263	47.828	4.6798	5.2915
	PTMD	43.232	45.119	4.6726	5.0238
SXVI	No PDAs	13.099	14.283	1.065	1.1675
	TMD	12.818	13.572	1.0681	1.122
	C-TSD	13.148	14.081	1.0747	1.138
	R-TSD	12.988	13.748	1.0612	1.1362
	TWLD	13.266	14.299	1.0816	1.1482
	PTMD	12.827	13.776	1.0733	1.1425
CUMV	No PDAs	9.0401	10.64	0.7935	0.8227
	TMD	8.4385	10.338	0.7298	0.7466
	C-TSD	8.8659	10.06	0.7408	0.7997
	R-TSD	8.622	10.287	0.7308	0.7797
	TWLD	9.0824	10.43	0.7773	0.7994
	PTMD	8.4015	10.495	0.7289	0.7622

FIGURE 15: Along-wind forces for the building. (a) xz plane. (b) yz plane.

damping for along-wind vibration depending on the wind profile and the fundamental mode of vibration of the building [63], whereas the aerodynamic damping could be negative for across-wind vibrations [64]. In this paper, the aerodynamic contribution was neglected because the main aim is the unification of different PDAs by using a CSF model. The structural part of the damping ratio depends not only on the type of structural material but also on the intensity of the motion, which is why structural damping ratios are usually lower in wind engineering, particularly for the assessment of the serviceability limit state. According to Tamura and Kareem [62], the structural damping ratio of 100–200-meter-tall buildings under wind loads is approximately equal to 1%.

For the five different PDAs shown in Tables 8–12, 12 time-history elastic analyses were carried out, assuming that the building is subjected to the along-wind forces shown in Figure 15. Assuming a structural damping ratio of 1% and neglecting soil-structure interaction effects, the peak

displacements are shown in Figure 16, whereas Table 20 shows the peak values of the internal forces at the base, which were computed by the equivalent static load method [53].

Generally speaking, Figure 16 shows that the five different PDAs are ineffective in controlling the along-wind peak lateral displacements of the building in both translational directions. Figure 16(a) shows that the five different PDAs are slightly more effective in controlling the peak lateral displacements in xz plane. Consequently, Table 20 shows low effectiveness of PDAs in controlling both base shear force and base overturning moment.

The RMS accelerations are usually used to assess the serviceability limit state, which is why these are shown instead of the peak accelerations. The along-wind RMS accelerations are shown in Figure 17, where the rooftop RMS accelerations are shown in Table 21.

As was expected, Figure 17 shows a great effectiveness of the five different PDAs in controlling along-wind RMS

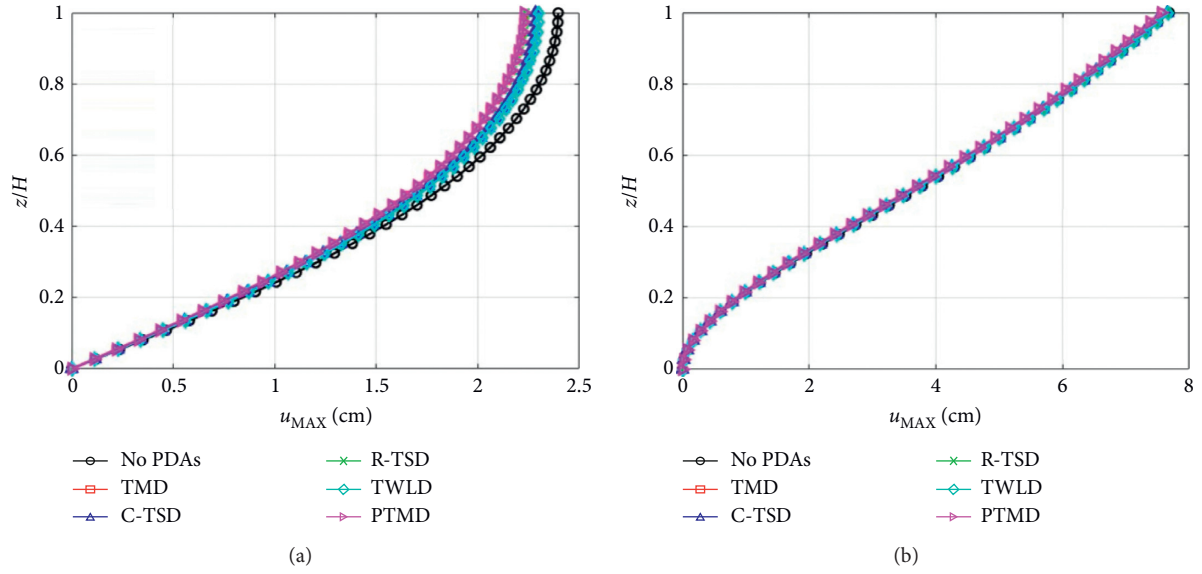


FIGURE 16: Along-wind peak displacements of the building. (a) xz plane. (b) yz plane.

TABLE 20: Along-wind peak values for the internal forces at the base.

Case	Base shear force (MN)		Base overturning moment (GN m)	
	xz plane	yz plane	xz plane	yz plane
No PDAs	1.7811	4.600	0.1411	0.4202
TMD	1.6624	4.5055	0.1312	0.4141
C-TSD	1.7091	4.5427	0.1345	0.4187
R-TSD	1.6661	4.5310	0.1311	0.4169
TWLD	1.7177	4.5490	0.1352	0.4195
PTMD	1.6625	4.5012	0.1311	0.4123

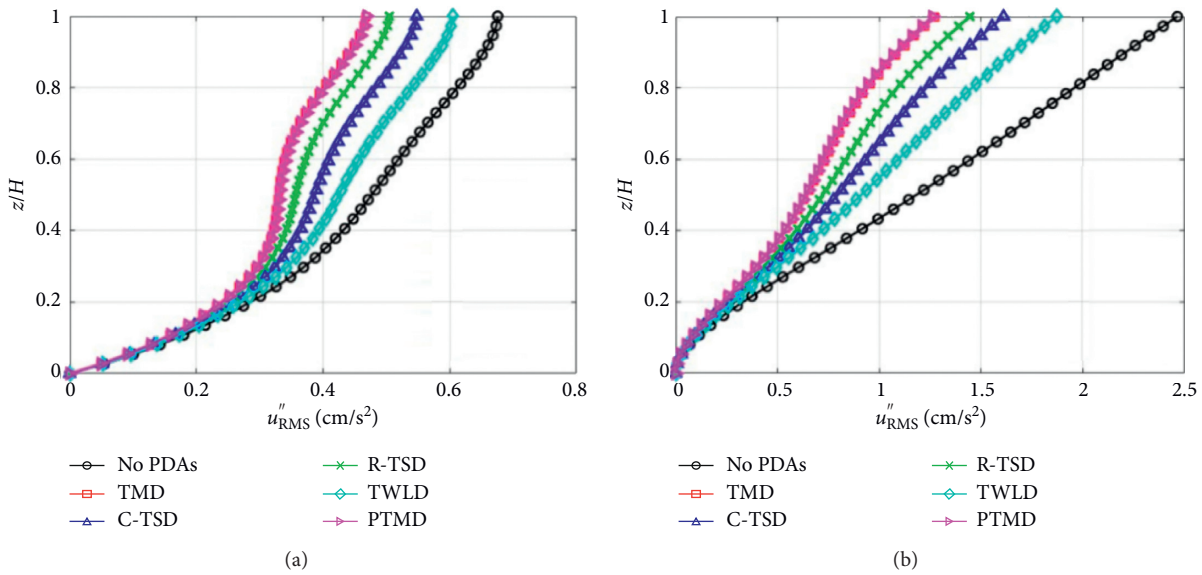


FIGURE 17: Along-wind RMS accelerations of the building. (a) xz plane. (b) yz plane.

accelerations of the building. According to Tables 8–12, values of μ are the same in each plane for TMD, R-TSD, C-TSD, and PTMD cases. Generally speaking, solid mass

vibration absorbers (TMD and PTMD) are more effective in vibration control of RMS accelerations than tuned sloshing dampers (C-TSD and R-TSD) because the mass efficiency

TABLE 21: Along-wind RMS accelerations at $z=H$.

RMS	Plane	No PDAs	TMD	C-TSD	R-TSD	TWLD	PTMD
Acceleration (milli-g)	xz	0.6889	0.4761	0.5586	0.5144	0.6165	0.4781
	yz	2.5124	1.2987	1.6417	1.4731	1.9075	1.2861
Reduction (%)	xz	—	30.88	18.92	25.33	10.51	30.59
	yz	—	48.31	34.65	41.37	24.08	48.81

index is equal to 100% for solid mass vibration absorbers. For the solid mass vibration absorbers, the RMS value of acceleration response at the rooftop is reduced by 31% and 49% in xz plane and yz plane, respectively.

As it was previously mentioned, when a TSD is subjected to small amplitude excitations such as wind vibrations, the fundamental sloshing mode of a TSD is practically the only one that is excited. For this reason, and because of the highly periodic nature of wind excitation, TSDs are well suited to reduce structural motion due to wind [41]. Both TSDs achieve a great effectiveness in vibration control even though the mass efficiency index is less than 100%; in fact, C-TSDs and R-TSDs achieve approximately 67% and 84% of the vibration control effectiveness of a TMD, respectively. Thereby, Figure 5 and Table 21 show that R-TSDs could be more effective in the vibration of RMS accelerations than C-TSDs; furthermore, a R-TSD is a more versatile device because it is able to be tuned to both translational directions by changing the dimensions of the tank. Unlike solid mass vibration absorbers (TMD and PTMD), tuned sloshing dampers offer the following benefits: low initial cost, easy and inexpensive installation, little to no maintenance, use in retrofit cases, and ease to design, among others.

According to Table 21, the TWLD was the least effective PDA in vibration control; however, the along-wind accelerations were significantly reduced even though the related values of μ are low in both translational directions (i.e., $\mu = 0.003$). For a TWLD, the participation of the liquid is always greater in the TLCD direction; therefore, the values of m_{PDA} and ξ_{PDA} are lower in the TSD direction. However, the RMS value of acceleration response at the rooftop is reduced by 10.51% and 24.08% in TLCD direction (xz plane) and TSD direction (yz plane), respectively; this demonstrates that the vibration control increases at upper stories for flexural-type deformations (see Figure 4). In fact, this particular behaviour is achieved with all kinds of PDAs attached at the rooftop level; that is, the effectiveness in vibration control of RMS accelerations increases as the value of α decreases (see Figure 4(d)).

In future works, the effectiveness of PDAs in controlling wind-induced vibrations will be studied using a flexible-base CSF model [58] subjected to both along-wind and across-wind forces.

6. Conclusions

A fixed-base coupled shear flexural (CSF) discrete model with TMDs is used to unify the design procedure of five different types of passive dynamic absorbers (PDAs): tuned mass damper (TMD), circular tuned sloshing damper (C-

TSD), rectangular tuned sloshing damper (R-TSD), two-way liquid damper (TWLD), and pendulum tuned mass damper (PTMD). By modifying the nondimensional lateral stiffness ratio, the CSF model can consider lateral deformations varying from those of a flexural cantilever beam to those of a shear cantilever beam. The unified model was applied to a 144-meter-tall building located in the Valley of Mexico, which was subjected to both seismic and along-wind loads. Accordingly, the following conclusions were obtained:

- For the first mode of vibration, the structural mass of an equivalent SDOF system at lower stories increases as the nondimensional lateral stiffness ratio decreases; on the contrary, for upper stories, it increases as the nondimensional lateral stiffness ratio increases. Therefore, if a single PDA attached at the rooftop level is tuned to the first mode of vibration, the maximum possible value of the mass efficiency index of the PDA increases as the nondimensional lateral stiffness ratio decreases. Furthermore, the mass efficiency index of the PDA also increases as the fundamental period of vibration of the building increases. Generally speaking, there is an increase in the vibration control effectiveness of PDAs for high-rise buildings that deform as pure flexural beams.
- For the second mode of vibration, the PDA/SDOF nondimensional mass ratio increases as the nondimensional lateral stiffness ratio increases when a single PDA is attached in the middle stories, whereas for the third mode of vibration, the PDA/SDOF nondimensional mass ratio increases as the nondimensional lateral stiffness ratio decreases when a single PDA is attached in the middle stories. For both the second and third mode of vibration, the PDA/SDOF nondimensional mass ratio increases as the nondimensional lateral stiffness ratio decreases, when a single PDA is attached at the rooftop level. Furthermore, for higher modes of vibration, the PDA/SDOF nondimensional mass ratio increases as the height of the attachment point of the PDA increases. Thus, a single PDA installed at the rooftop level could be more effective for multimode control than an equal-mass PDA installed at lower stories.
- For the same depth ratios, the mass efficiency index and the equivalent TMD mass of a TSD are greater for a rectangular container even though the total liquid mass is greater for a circular container. Therefore, a R-TSD could be a better option for vibration control than a C-TSD. Furthermore, a R-TSD is a more versatile device because it is able to

be tuned to both orthogonal directions by changing the dimensions of the tank. Wave motions in shallow-water TSDs are generally complex due to strong nonlinearities such as wave breaking; however, shallow-water TSDs provide high damping of liquid sloshing and an efficient moving mass.

- (d) For earthquake-induced vibrations, the location of the peak interstory drift ratio could depend not only on the value of the nondimensional lateral stiffness ratio but also on the features of the earthquake ground motion record and the equivalent parameters of the PDA. Particularly, the location of the peak interstory drift ratio changed at the CUMV station for the specific case of the solid mass vibration absorbers (TMD and PTMD). However, further research is needed in this regard.
- (e) For along-wind vibrations, the five different PDAs (TMD, C-TSD, R-TSD, TWLD, and PTMD) showed great effectiveness in controlling RMS accelerations. For the same values of the PDA/SDOF nondimensional mass ratios, solid mass vibration absorbers (TMD and PTMD) were more effective in vibration control of RMS accelerations than tuned sloshing dampers (C-TSD and R-TSD) because the mass efficiency index is equal to 100% for solid mass vibration absorbers. However, tuned sloshing dampers offer the following benefits: low initial cost, easy and inexpensive installation, little to no maintenance, use in retrofit cases, and ease to design, among others. The TWLD was the least effective PDA in vibration control. However, the along-wind accelerations were significantly reduced even though the maximum possible value of the PDA/SDOF nondimensional mass ratio was lower in both orthogonal directions.
- (f) The attachment of uniformly distributed PDAs could be related to great effectiveness in controlling the dynamic response compared to a single PDA attached at the rooftop. However, it is highly recommended to use uniformly distributed PDAs in taller buildings in order to guarantee both a real solution and a possible geometry for the devices, particularly when TLDs are used to dissipate input energy.
- (g) Literature features several formulas for optimum tuning conditions of PDAs; however, these formulas are not related to different lateral resisting systems. For this reason, these formulas are not the best option to optimize the passive vibration control in medium-rise to high-rise buildings, where the flexural deformation is as significant as the shear deformation.

Data Availability

The authors confirm that the data supporting the findings of this study are available within the article.

Conflicts of Interest

The authors declare that they have no conflicts of interest.

Acknowledgments

The authors would like to acknowledge CONACYT-Becas México for financially supporting the second author in conducting doctoral studies at Universidad Nacional Autónoma de México under the supervision of the first author. The authors also wish to thank Universidad Nacional Autónoma de México and Universidad Michoacana de San Nicolás de Hidalgo.

References

- [1] R. Rahgozar, H. Safari, and P. Kaviani, "Free vibration of tall buildings using Timoshenko beams with variable cross-section," in *Structures Under Shock and Impact VIII*, N. Jones and C. A. Brebbia, Eds., WIT Press, Southampton, UK, 2004.
- [2] E. Miranda and S. Taghavi, "Approximate floor acceleration demands in multistory buildings. I: formulation," *Journal of Structural Engineering*, vol. 131, no. 2, pp. 203–211, 2005.
- [3] C. L. Dym and H. E. Williams, "Estimating fundamental frequencies of tall buildings," *Journal of Structural Engineering*, vol. 133, no. 10, pp. 1479–1483, 2007.
- [4] S. Y. Chu, T. T. Soong, and A. M. Reinhorn, *Active, Hybrid, and Semi-active Structural Control: A Design and Implementation Handbook*, Wiley, New York, NY, USA, 2005.
- [5] C. H. Chang and T. T. Soong, "Structural control using active tuned mass dampers," *Journal of the Engineering Mechanics Division*, vol. 106, no. 6, pp. 1091–1098, 1980.
- [6] S. Elias and V. Matsagar, "Research developments in vibration control of structures using passive tuned mass dampers," *Annual Reviews in Control*, vol. 44, pp. 129–156, 2017.
- [7] D. De Domenico, G. Ricciardi, and I. Takewaki, "Design strategies of viscous dampers for seismic protection of building structures: a review," *Soil Dynamics and Earthquake Engineering*, vol. 118, pp. 144–165, 2019.
- [8] M. D. Symans and M. C. Constantinou, "Semi-active control systems for seismic protection of structures: a state-of-the-art review," *Engineering Structures*, vol. 21, no. 6, pp. 469–487, 1999.
- [9] M. H. Stanikzai, S. Elias, V. A. Matsagar, and A. K. Jain, "Seismic response control of base-isolated buildings using multiple tuned mass dampers," *The Structural Design of Tall and Special Buildings*, vol. 28, no. 3, Article ID e1576, 2018.
- [10] R. Rabiee and Y. Chae, "Adaptive base isolation system to achieve structural resiliency under both short- and long-period earthquake ground motions," *Journal of Intelligent Material Systems and Structures*, vol. 30, no. 1, pp. 1–16, 2019.
- [11] A. D. Matteo, T. Furtmüller, C. Adam, and A. Pirrotta, "Optimal design of tuned liquid column dampers for seismic response control of base-isolated structures," *Acta Mechanica*, vol. 229, pp. 437–454, 2018.
- [12] P. Gao, C. Xiang, H. Liu, and H. Zhou, "Reducing variable frequency vibrations in a powertrain system with an adaptive tuned vibration absorber group," *Journal of Sound and Vibration*, vol. 425, pp. 82–101, 2018.
- [13] M. H. Stanikzai, S. Elias, and R. Rupakhety, "Seismic response mitigation of base-isolated buildings," *Applied Sciences*, vol. 10, no. 4, Article ID 1230, 2020.

- [14] A. Di Matteo, C. Masnata, and A. Pirrotta, "Hybrid passive control strategies for reducing the displacements at the base of seismic isolated structures," *Frontiers in Built Environment*, vol. 5, no. 132, pp. 1–13, 2019.
- [15] J. P. Den Hartog, *Mechanical Vibration*, McGraw-Hill, New York, NY, USA, 1956.
- [16] G. B. Warburton and E. O. Ayorinde, "Optimum absorber parameters for simple systems," *Earthquake Engineering & Structural Dynamics*, vol. 8, no. 3, pp. 197–217, 1980.
- [17] F. Sadek, B. Mohraz, A. W. Taylor, and R. M. Chung, "A method of estimating the parameters of tuned mass dampers for seismic applications," *Earthquake Engineering and Structural Dynamics*, vol. 26, no. 6, pp. 617–663, 1998.
- [18] A. Kareem, "Reduction of wind induced motion utilizing a tuned sloshing damper," *Journal of Wind Engineering and Industrial Aerodynamics*, vol. 36, no. 2, pp. 725–737, 1990.
- [19] C. C. Chang and M. Gu, "Suppression of vortex-excited vibration of tall buildings using tuned liquid dampers," *Journal of Wind Engineering and Industrial Aerodynamics*, vol. 83, no. 1–3, pp. 225–237, 1999.
- [20] J.-C. Wu, M.-H. Shih, Y.-Y. Lin, and Y.-C. Shen, "Design guidelines for tuned liquid column damper for structures responding to wind," *Engineering Structures*, vol. 27, no. 13, pp. 1893–1905, 2005.
- [21] M. J. Tait, "Modelling and preliminary design of a structure-TLD system," *Engineering Structures*, vol. 30, no. 10, pp. 2644–2655, 2008.
- [22] S.-K. Lee, K.-W. Min, and H.-R. Lee, "Parameter identification of new bidirectional tuned liquid column and sloshing dampers," *Journal of Sound and Vibration*, vol. 330, no. 7, pp. 1312–1327, 2011.
- [23] K.-W. Min, J. Kim, and H.-R. Lee, "A design procedure of two-way liquid dampers for attenuation of wind-induced responses of tall buildings," *Journal of Wind Engineering and Industrial Aerodynamics*, vol. 129, pp. 22–30, 2014.
- [24] L. Rozas, R. L. Boroschek, A. Tamburrino, and M. Rojas, "A bidirectional tuned liquid column damper for reducing the seismic response of buildings," *Structural Control and Health Monitoring*, vol. 23, no. 4, pp. 621–640, 2016.
- [25] M. P. Sacks and J. C. Swallow, "Tuned mass dampers for towers and buildings," in *Proceedings of the Symposium on Structural Engineering in Natural Hazards Mitigation*, pp. 640–645, Irvine, CA, USA, 1993.
- [26] R. R. Gerges and B. J. Vickery, "Optimum design of pendulum-type tuned mass dampers," *The Structural Design of Tall and Special Buildings*, vol. 14, no. 4, pp. 353–368, 2005.
- [27] Z. Shu, S. Li, X. Sun, and M. He, "Performance-based seismic design of a pendulum tuned mass damper system," *Journal of Earthquake Engineering*, vol. 23, no. 2, pp. 334–355, 2019.
- [28] C. C. Chang and W. L. Qu, "Unified dynamic absorber design formulas for wind-induced vibration control of tall buildings," *The Structural Design of Tall Buildings*, vol. 7, no. 2, pp. 147–166, 1998.
- [29] C. C. Chang, "Mass dampers and their optimal designs for building vibration control," *Engineering Structures*, vol. 21, no. 5, pp. 454–463, 1999.
- [30] F. Ricciardelli, "A linear model for structures with tuned mass dampers," *Wind and Structures*, vol. 2, no. 3, pp. 151–171, 1999.
- [31] L. Min-Yi, C. Wei-Ling, H. Jin-Hung, and C. Chia-Ren, "Wind-induced vibration of high-rise building with tuned mass damper including soil-structure interaction," *Journal of Wind Engineering and Industrial Aerodynamics*, vol. 96, no. 6–7, pp. 1092–1102, 2008.
- [32] S. Elias and V. Matsagar, "Distributed multiple tuned mass dampers for wind vibration response control of high-rise building," *Journal of Engineering*, vol. 2014, Article ID 198719, 11 pages, 2014.
- [33] S. Elias, V. Matsagar, and T. K. Datta, "Effectiveness of distributed tuned mass dampers for multi-mode control of chimney under earthquakes," *Engineering Structures*, vol. 124, pp. 1–16, 2016.
- [34] S. Elias and V. Matsagar, "Effectiveness of tuned mass dampers in seismic response control of isolated bridges including soil-structure interaction," *Latin American Journal of Solids and Structures*, vol. 14, no. 13, pp. 2324–2341, 2017.
- [35] D. De Domenico and G. Ricciardi, "Earthquake-resilient design of base isolated buildings with TMD at basement: application to a case study," *Soil Dynamics and Earthquake Engineering*, vol. 113, pp. 503–521, 2018.
- [36] T. Balendra, C. M. Wang, and G. Rakesh, "Vibration control of various types of buildings using TLCD," *Journal of Wind Engineering and Industrial Aerodynamics*, vol. 83, no. 1–3, pp. 197–208, 1999.
- [37] I. F. Huergo and H. Hernández, "Coupled shear-flexural model for dynamic analysis of fixed-base tall buildings with tuned mass dampers," *The Structural Design of Tall and Special Buildings*, vol. 28, no. 17, Article ID e1671, 2019.
- [38] H. Bachmann, W. J. Ammann, F. Deischl et al., *Vibration Problems in Structures: Practical Guidelines*, Birkhäuser, Basel, Switzerland, 1995.
- [39] C. Christopoulos and A. Filiatrault, *Principles of Passive Supplemental Damping and Seismic Isolation*, IUSS Press, Pavia, Italy, 2006.
- [40] L. M. Sun, Y. Fujino, B. M. Pacheco, and P. Chaiseri, "Modelling of tuned liquid damper (TLD)," *Journal of Wind Engineering and Industrial Aerodynamics*, vol. 43, no. 1–3, pp. 1883–1894, 1992.
- [41] M. A. Steyer, *Multifunctionality of Distributed Sloshing Dampers in Buildings*, Master thesis, Massachusetts Institute of Technology, Massachusetts, MA, USA, 2002.
- [42] V. J. Modi and S. R. Munshi, "An efficient liquid sloshing damper for vibration control," *Journal of Fluids and Structures*, vol. 12, no. 8, pp. 1055–1071, 1998.
- [43] L. M. Sun, Y. Fujino, P. Chaiseri, and B. M. Pacheco, "The properties of tuned liquid dampers using a TMD analogy," *Earthquake Engineering & Structural Dynamics*, vol. 24, no. 7, pp. 967–976, 1995.
- [44] L. M. Sun and Y. Fujino, "A semi-analytical model for tuned liquid damper (TLD) with wave breaking," *Journal of Fluids and Structures*, vol. 8, no. 5, pp. 471–488, 1994.
- [45] T. K. Caughey, "Equivalent linearization techniques," *The Journal of the Acoustical Society of America*, vol. 35, no. 11, pp. 1706–1711, 1963.
- [46] J. J. Connor, *Introduction to Structural Motion Control*, Pearson Education, London, UK, 2003.
- [47] E. Miranda and C. J. Reyes, "Approximate lateral drift demands in multistory buildings with nonuniform stiffness," *Journal of Structural Engineering*, vol. 128, no. 7, pp. 840–849, 2002.
- [48] N. M. Newmark and W. J. Hall, *Earthquake Spectra and Design*, Earthquake Engineering Research Institute, Berkeley, California, 1982.
- [49] B. Ellis, "An assessment of the accuracy of predicting the fundamental natural frequencies of buildings and the implications concerning the dynamic analysis of structures," *Proceedings of the Institution of Civil Engineers*, vol. 69, no. 3, pp. 763–776, 1980.

- [50] B. Stafford and A. Coull, *Tall Building Structures: Analysis and Design*, Wiley, Hoboken, NJ, USA, 1991.
- [51] R. K. Goel and A. K. Chopra, "Period formulas for moment-resisting frame buildings," *Journal of Structural Engineering*, vol. 123, no. 11, pp. 1454–1461, 1997.
- [52] R. K. Goel and A. K. Chopra, "Period formulas for concrete shear wall buildings," *Journal of Structural Engineering*, vol. 124, no. 4, pp. 426–433, 1998.
- [53] A. K. Chopra, *Dynamics of Structures: Theory and Applications to Earthquake Engineering*, Pearson, New Jersey, NJ, USA, 2017.
- [54] G. C. Hart and K. Wong, *Structural Dynamics for Structural Engineers*, Wiley, Hoboken, NJ, USA, 1999.
- [55] I. F. Huergo, H. Hernández, and C. M. Patlán, "A continuous-discrete approach for pre-design of flexible-base tall buildings with fluid viscous dampers," *Soil Dynamics and Earthquake Engineering*, vol. 131, Article ID 106042, 2020.
- [56] R. Soto and S. E. Ruiz, "Influence of ground motion intensity on the effectiveness of tuned mass dampers," *Earthquake Engineering and Structural Dynamics*, vol. 28, no. 11, pp. 1255–1271, 1999.
- [57] S. E. Ruiz and L. Esteva, "About the effectiveness of tuned mass dampers on nonlinear systems subjected to earthquakes," *Transactions on the Built Environment*, vol. 23, pp. 311–320, 1996.
- [58] I. F. Huergo and H. Hernández, "Coupled-two-beam discrete model for dynamic analysis of tall buildings with tuned mass dampers including soil-structure interaction," *The Structural Design of Tall and Special Buildings*, vol. 29, no. 1, Article ID e1683, 2020.
- [59] CFE, *Manual de Diseño de Obras Cíviles: Diseño por Viento*, Instituto de Investigaciones Eléctricas, Cuernavaca, México, 2008.
- [60] G. Solari, "Gust buffeting. I: peak wind velocity and equivalent pressure," *Journal of Structural Engineering*, vol. 119, no. 2, pp. 365–382, 1993.
- [61] M. Shinozuka and C.-M. Jan, "Digital simulation of random processes and its applications," *Journal of Sound and Vibration*, vol. 25, no. 1, pp. 111–128, 1972.
- [62] G. Tamura and A. Kareem, *Advanced Structural Wind Engineering*, Springer, Berlin, Germany, 2013.
- [63] K. H. M. Bjørnland, "Wind-induced dynamic response of high rise buildings," Master thesis, Norwegian University of Science and Technology, Trondheim, Norway, 2013.
- [64] Y. Quan, M. Gu, and Y. Tamura, "Experimental evaluation of aerodynamic damping of square super high-rise buildings," *Wind and Structures*, vol. 8, no. 5, pp. 309–324, 2005.

Research Article

Energy Response Analysis of Continuous Beam Bridges with Friction Pendulum Bearing by Multihazard Source Excitations

Bing Li,¹ Bin Wang ,² Shaohua Wang,³ and Xiao Wu³

¹School of Mechanical Engineering, North China University of Water Resources and Electric Power, Zhengzhou 450045, China

²College of Engineering, Design and Physical Sciences, Brunel University London, London, UK

³School of Mechanical Engineering, Southwest Jiaotong University, Chengdu 610031, China

Correspondence should be addressed to Bin Wang; bin.wang@brunel.ac.uk

Received 11 October 2019; Revised 2 January 2020; Accepted 21 February 2020; Published 6 July 2020

Guest Editor: Vasant Matsagar

Copyright © 2020 Bing Li et al. This is an open access article distributed under the Creative Commons Attribution License, which permits unrestricted use, distribution, and reproduction in any medium, provided the original work is properly cited.

Based on the principle of conservation of energy, analytical modelling of the energy response of continuous beam bridges with friction pendulum bearing (FPB) was carried out for foundation-induced vibrations. A three-dimensional finite element analysis of a multispan continuous concrete girder bridge with FPB was established using the nonlinear time-history method to verify the accuracy of analytical modelling. The influence of the friction coefficient and isolation period of the FPB on the energy response of isolated bridge was then investigated under multihazard source excitations (e.g., El Centro and Taft waves) with different dominant periods and durations. The variations of structural response energy, sliding displacement, energy dissipation ratio, and acceleration of the isolated bridges are plotted. The results of analytical modelling and finite element simulation show good agreement. In addition, there exist particular values of the friction coefficient and isolation period of FPB, for which the structural response energy of the isolated bridges attains the minimum value. The optimal parameters of FPB are greatly influenced by seismic waves, and the friction coefficient of FPB should be increased with the increase of seismic fortification intensity. In addition, the energy dissipation capacity of FPB used in isolated bridge is excellent.

1. Introduction

Seismic isolation devices are now widely used for protection and retrofit of bridges. The purpose of the isolation devices is to insulate the dynamic movements of the super- and the substructures (e.g., the main beam and the pier of the bridge, see Figure 1), to provide a form of damping force to dissipate kinetic energy, and to reduce the relative displacement of movement between the structure components [1–3]. Due to their potential effectiveness in reducing bridge damages, isolation devices have been studied extensively for their performance. Tubaldi et al. [4] proposed a formulation for the seismic assessment of partially restrained seismically isolated (PRSI) bridges based on the complex modes superposition method. Zhang et al. [5] proposed a new isolation device FRPEIs, and it is feasible to use FRPEIs in seismic isolation of short span bridges in low seismic regions. Ismail et al. [6, 7] carried out numerical

simulation of the seismic performance of cable-stayed bridges using a Roll-N-Cage (RNC) isolator and showed that the RNC isolator is a convenient isolation system in protecting cable-stayed bridges against near-fault (NF) earthquakes. Zhong et al. [8] studied the influences of the peak ground accelerations, the principal dynamic parameters on the input energy, and the hysteretic energy ratio using lead rubber bearing as isolation devices. Different isolation designs were studied by Diceli et al. [9], Taflanidis [10], and Ates and Constantinou [11] for their effectiveness against seismic waves, including the probabilistic performance, and for applications to different bridge designs, such as for curved bridges and cable-stayed bridges. Jangid [2, 12] studied the equivalent linearization approximate method of isolated bridges using lead-rubber bearing (LRB), the results showed the yield strength of LRB, and the bidirectional interaction of bearing restoring forces had considerable effects on the seismic response of bridges.

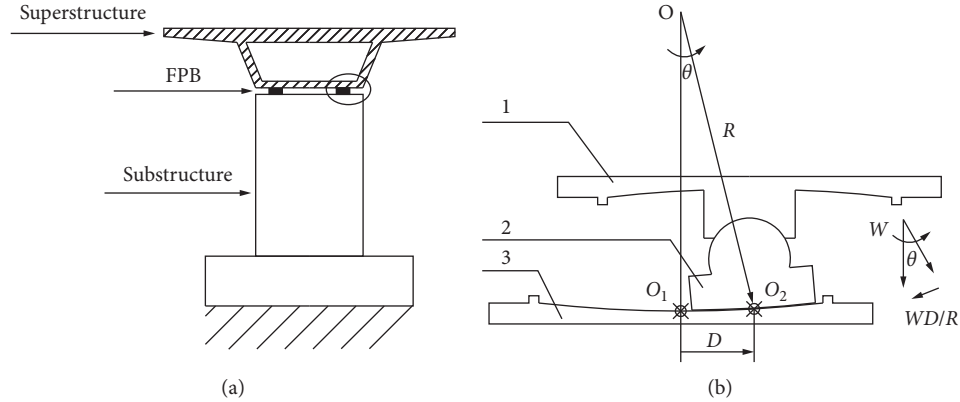


FIGURE 1: (a) Isolated bridge with 2 FPBs in view of the axial direction of the bridge. (b) Structural illustration of a FPB (circled in (a)), (1) upper support plate, (2) articulated slider, and (3) lower support plate.

Among various isolation devices, the design of friction pendulum bearing (FPB) has gained strong popularity due to its simplicity in design, effectiveness of energy dissipation, the capacity of self-returning to the original position, and low cost of construction and maintenance. A FPB utilizes a spherical surface for the contact between the super- and substructures. Such surfaces allow sliding movement between the two contacting bodies to dissipate energy through friction. The spherical profile of the contact surfaces also allows the superstructure to return to its balanced position under gravity [13]. Compared with other isolation devices, FPB has better vertical bearing capacity, energy dissipation capacity, durability, among other advantages [14, 15]. Lei et al. [16] studied the dynamic characteristics and responses of two curved bridges considering or not bearings friction sliding isolation used shaking table tests, and concluded that the isolation model curved bridge suffered less seismic damage than the seismic model curved bridge. Dicleli and Mansour [17] showed that the use of FPB can mitigate seismic forces and eliminate the need for retrofitting the substructure components of the bridge.

Several studies have been conducted for seismic response and optimization of FPB system subjected to random earthquake. Hwang et al. [18] studied the isolated regular bridges, and suggested that a bridge can be modelled as a two-degree of freedom system underground excitations. Jangid [19, 20] studied the seismic response of a multistorey building and bridge isolated by the friction pendulum system using equivalent linearization system, and they concluded that there are optimum friction coefficient and isolation period of the FPS, for which the acceleration of the top floor or deck attains a minimum value, and the optimum friction coefficient varies with the change of seismic fortification intensity. Ates et al. [21] investigated the effect of the spatially varying earthquake ground motions on the stochastic responses of isolated bridges with FPS, and a calculation method using equivalent linearization techniques for the response amplitude of isolated bridges is proposed. Eröz et al. [22, 23] investigated the effects of modelling and bridge design parameters on the seismic response of FPS-isolated bridges through a 3D analytical model with the

nonlinear time-history method. Saha et al. [24, 25] studied the response of the highway bridge isolated with a polynomial friction pendulum isolator (PFPI) and passive hybrid control system, and the result indicated that a passive supplement damper with a PFPI system is significantly reducing the seismic response of the highway bridge.

Seismic energy response can better reflect the cumulative damage of the seismic wave on isolated bridge with FPB. The review of above studies indicates that there had not been sufficiently significant information to investigate the influence of the friction coefficient and isolation period of the FPB on the energy response of isolated bridges in order to minimize the structural response energy. In this paper, we present an analytical solution for the energy and dynamic responses of continuous beam bridges with FPB under seismic wave loading. The purpose is twofold. An analytical model is a simpler tool for the design purpose, particularly at the conceptual stage. Such a model also allows for the identification of key parameters and their effects on the overall performance of the system. In addition, numerical simulations using a commercial finite element code SAP2000 [26] were carried out and compared with the results of the theoretical model, through which the energy response and parameters optimization of FPB were analyzed under multihazard source excitations with different dominant periods and durations. Results show that the analytical and numerical approaches agree well, and the outcome provides useful guidelines for optimal design of FPB.

2. Mechanical Model of Isolated Continuous Beam Bridges

2.1. The Friction Pendulum Bearing (FPB). A FPB is a sliding-based seismic isolator, which is installed between the superstructure and the substructure, as shown circled in Figure 1(a). A structural illustration of FPB is shown in Figure 1(b) where part 1 is fixed under the main bridge beam, or the superstructure, and can rotate about part 2, the articulated slider. The surfaces of part 1 and part 2 are perfectly fit with the same radius of curvature. This ensures that the superstructure remains horizontal [26] during

movement. Part 2 and part 3 are in a spherical joint with radius R where part 2 can have frictional sliding on part 3, which is fixed on the top of the pier or the substructure.

Assuming that the superstructure has a horizontal displacement D measured from its original balanced position O_1 and the corresponding angle of rotation is θ , for a small displacement assumption, the tangential component of the weight of the superstructure W becomes $W \sin \theta \approx W D/R$. This is the main restoring force to bring the superstructure back to its original position after movement. This is in the same principle of a pendulum, thus the name frictional pendulum bearing (FPB) for this type of joint. Such a joint is also called an isolation device as it dissipates the kinetic energy following seismic loading and limits the motion of the bridge upper deck.

The (tangential) force–(horizontal) displacement behavior of a FPB can be approximately described by a bilinear hysteresis model [22], as shown in Figure 2. The force–displacement hysteresis loop can be defined by equation (1) where μ is the kinetic friction coefficient and R the radius of the concave surface. The equivalent linear stiffness (k_e) is illustrated graphically in Figure 2 and defined by equation (2). The period of vibration (T_p) after the activation of an FPB isolator can be defined by equation (3) [3], where D_0 is the maximum value of horizontal displacement of FPB in the cyclic movement.

$$F = \frac{WD_0}{R} + \mu W \operatorname{sgn}(\dot{\theta}), \quad (1)$$

$$k_e = \frac{W}{R} + \frac{\mu W}{D_0}, \quad (2)$$

$$T_p = 2\pi \sqrt{\frac{R}{g}}, \quad (3)$$

For calculating the energy dissipation by the friction effect, ε_1 is defined as the equivalent damping ratio following Dicleli and Mansour [17]. A FPB can be simplified equivalently as a viscous spring damper. Letting the energy dissipation of a FPB and that of an equivalent viscous spring damper be the same in one cycle movement, where ΔE being the hysteretic energy dissipation of a FPB, the equivalent damping ratio of FPB can be obtained as given in equation (4). Details of the derivation are given in Appendix A:

$$\varepsilon_1 = \frac{\Delta E}{2\pi k_1 D_0^2} = \frac{4\mu W D_0}{2\pi D_0 ((W D_0/R) + \mu W)} = \frac{2\mu}{\pi ((D_0/R) + \mu)}. \quad (4)$$

2.2. Dynamic Equations. Two FPBs are normally installed between the superstructure and the substructure as shown in Figure 1(a), with equal distribution of the weight of the superstructure on each FPB. A bridge pier typically has less flexural rigidity in the bridge axial direction than that in the

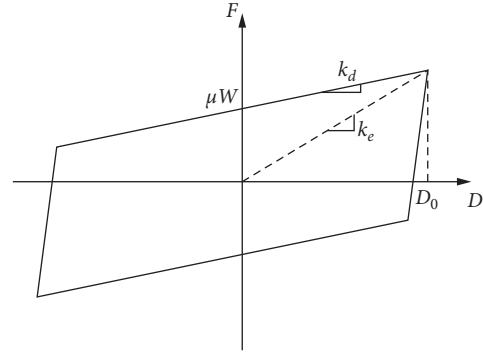


FIGURE 2: Bilinear hysteresis model.

transverse direction, and the seismic response will occur in the weaker direction. Hence, an isolated bridge can be modeled as a two-degree of freedom system in the axial direction of the bridge [5]. The main beam and pier can be described by an equivalent model shown in Figure 3. u_1 and u_2 are the displacements of the main beam and the pier relative to the ground along the bridge direction. x represents the axial direction of the bridge, and y represents the vertical direction of the bridge.

The vibration equation of the system shown in Figure 3 is given by

$$\begin{aligned} \begin{bmatrix} m_1 & 0 \\ 0 & m_2 \end{bmatrix} \begin{Bmatrix} \ddot{u}_1 \\ \ddot{u}_2 \end{Bmatrix} + \begin{bmatrix} c_1 & -c_1 \\ -c_1 & c_1 + c_2 \end{bmatrix} \begin{Bmatrix} \dot{u}_1 \\ \dot{u}_2 \end{Bmatrix} \\ + \begin{bmatrix} k_1 & -k_1 \\ -k_1 & k_1 + k_2 \end{bmatrix} \begin{Bmatrix} u_1 \\ u_2 \end{Bmatrix} = - \begin{bmatrix} m_1 & 0 \\ 0 & m_2 \end{bmatrix} \begin{Bmatrix} 1 \\ 1 \end{Bmatrix} \ddot{u}_g, \end{aligned} \quad (5)$$

where m_1 is the equivalent weight of the main bridge beam or the superstructure and m_2 is the equivalent weight of the pier or the substructure. The top of the pier and the bottom of the main beam are constrained interactively by the isolation devices or FPBs between them. k_2 is the stiffness of the pier, and c_1 and c_2 are the equivalent viscous damping coefficients of the two FPBs and pier, respectively. The energy transferred to the superstructure is mainly consumed by the FPBs; the equivalent viscous damping coefficient of FPB is much larger than that of the main bridge beam, so the equivalent viscous damping coefficient of the main bridge beam is neglected, and the assumption has little effect on the results. \ddot{u}_g is the ground acceleration by the seismic wave.

k_1 is the equivalent linear stiffness of the two FPBs (i.e., $2k_e$). As D_0 is not a known priori, for calculating k_1 using equation (2), its value can be chosen as the maximum allowable displacement of the superstructure determined by the design specification, given a conservative design, or through a finite element analysis as a function of the input energy. Detailed discussion on the latter approach using an FE analysis is beyond the scope of this paper and will be provided elsewhere [27].

Following the classical vibration analysis, we have

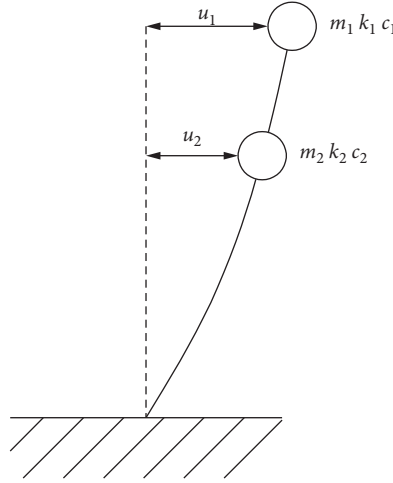


FIGURE 3: A two-degree-of-freedom system of the continuous beam bridge with 2 FPBs, showing corresponding displacements of the masses.

$$\begin{aligned}\omega_1^2 &= \frac{k_1}{m_1}, \\ \omega_2^2 &= \frac{k_2}{(m_2 + m_1)}, \\ c_1 &= 2m_1\varepsilon_1\omega_1, \\ c_2 &= 2(m_2 + m_1)\varepsilon_2\omega_2,\end{aligned}\quad (6)$$

where ω_1 and ω_2 are the fundamental frequencies of the isolated system and ε_1 and ε_2 the equivalent damping ratios of the FPB and pier, respectively. In practice, ε_2 is usually

selected as a value recommended by design codes and standards, for instance, 0.05; and ω_2 and c_2 are chosen as constants, depending on the design of the pier.

3. Energy Equations

For an isolated bridge system, energy equations can be obtained by integrating equation (5) to the relative displacements into a weak form as given in equation (7) (also see [28]). The energy of each mass is first calculated, and the energy of the whole system is then obtained by superposition:

$$\begin{aligned}\int_0^t \begin{Bmatrix} \dot{u}(t) \\ \dot{u}_2(t) \end{Bmatrix}^T \begin{bmatrix} m_1 & 0 \\ 0 & m_2 \end{bmatrix} \begin{Bmatrix} \ddot{u}_1(t) \\ \ddot{u}_2(t) \end{Bmatrix} dt + \int_0^t \begin{Bmatrix} \dot{u}_1(t) \\ \dot{u}_2(t) \end{Bmatrix}^T \begin{bmatrix} c_1 & -c_1 \\ -c_1 & c_1 + c_2 \end{bmatrix} \begin{Bmatrix} \dot{u}_1(t) \\ \dot{u}_2(t) \end{Bmatrix} dt + \\ \int_0^t \begin{Bmatrix} \dot{u}_1(t) \\ \dot{u}_2(t) \end{Bmatrix}^T \begin{bmatrix} k_1 & -k_1 \\ -k_1 & k_1 + k_2 \end{bmatrix} \begin{Bmatrix} u_1(t) \\ u_2(t) \end{Bmatrix} dt = - \int_0^t \begin{Bmatrix} \dot{u}_1(t) \\ \dot{u}_2(t) \end{Bmatrix}^T \begin{bmatrix} m_1 & 0 \\ 0 & m_2 \end{bmatrix} \begin{Bmatrix} 1 \\ 1 \end{Bmatrix} \ddot{u}_g(t) dt.\end{aligned}\quad (7)$$

Terms in the left-hand side of equation (7) represent the kinetic energy $E_K(t)$, the mass-damping and friction hysteretic energy $E_D(t)$ and $E_F(t)$, and the elastic strain energy $E_P(t)$. The right-hand side is the seismic input energy $E_O(t)$. Equation (7) can be written into equation (8), and the kinetic energy of the system and the elastic strain energy are given in equations (9) and (10):

$$E_K + E_D(t) + E_F(t) + E_P(t) = E_O(t), \quad (8)$$

$$E_K(t) = \frac{1}{2}m_1\dot{u}_1^2(t) + \frac{1}{2}m_2\dot{u}_2^2(t), \quad (9)$$

$$E_P(t) = \frac{1}{2}k_1(u_1(t) - u_2(t))^2 + \frac{1}{2}k_2u_2^2(t). \quad (10)$$

Time step $\Delta t (=t_{i+1} - t_i)$ has an important influence on the computational accuracy and efficiency; so, the appropriate Δt is selected by comparing the calculation results of different time steps in the following section. To solve the energies over a small time step Δt , the following assumptions are made within a time step:

- (1) the ground acceleration $\ddot{u}_g(t)$ and the point mass velocity $\dot{u}(t)$ vary linearly in time
- (2) Acceleration $\ddot{u}(t)$ is assumed constant, taken as the average value over Δt

While it is also possible to assume a constant value of $\ddot{u}_g(t)$ within Δt , it was found that a linear assumption actually makes calculation simpler. As long as Δt is kept small

enough, there is negligible difference between the linear and constant assumptions.

The energies can then be solved as shown in Figure 4 where the ordinate represents the velocity of the point mass, and the abscissa represents time. Within the time step from t_i to t_{i+1} , $\dot{u}(t)$ varies linearly:

$$\dot{u}(t) = \dot{u}(t_i) + \frac{\ddot{u}(t_{i+1}) + \ddot{u}(t_i)}{2} t. \quad (11)$$

Similarly, we can develop the ground acceleration $\ddot{u}_g(t)$ as

$$\ddot{u}_g(t) = \ddot{u}_g(t_i) + \frac{\ddot{u}_g(t_{i+1}) - \ddot{u}_g(t_i)}{\Delta t} t. \quad (12)$$

Integration of the seismic input energy over the time step can be carried out as

$$\begin{aligned} \Delta E_O(n) &= \sum_{j=1}^{t_{i+1}} \int_{t_i}^{t_{i+1}} m_j \dot{u}_j(t) \ddot{u}_g(t) dt \\ &= \sum_{j=1}^{\Delta t} \int_0^{\Delta t} m_j \times \left[\dot{u}_j(t_i) + \frac{\ddot{u}_j(t_{i+1}) + \ddot{u}_j(t_i)}{2} t \right] \times \left[\ddot{u}_g(t_i) + \frac{\ddot{u}_g(t_{i+1}) - \ddot{u}_g(t_i)}{\Delta t} t \right] dt \\ &= \sum_{j=1}^2 \left\{ \begin{aligned} & -m_j \dot{u}_j(t_i) \ddot{u}_g(t_i) \Delta t - \frac{m_j}{2} [\dot{u}_j(t_i) (\ddot{u}_g(t_{i+1}) - \ddot{u}_g(t_i))] \Delta t \\ & - \frac{m_j}{4} [\ddot{u}_g(t_i) (\ddot{u}_j(t_i) + \ddot{u}_j(t_{i+1}))] \Delta t^2 - \frac{m_j}{6} [(\ddot{u}_g(t_{i+1}) - \ddot{u}_g(t_i)) (\dot{u}_j(t_i) + \ddot{u}_j(t_{i+1}))] \Delta t^2 \end{aligned} \right\}. \end{aligned} \quad (13)$$

Summing up over all time steps for the total gives

$$E_O(t) = \sum_1^{n=t/\Delta t} \Delta E_O(n). \quad (14)$$

Using MATLAB [29], we can develop the energy equations for ΔE_D and ΔE_F ,

$$\begin{aligned} \Delta E_D(n) + \Delta E_F(n) &= c_1 \left\{ \dot{u}_1^2(t_i) \Delta t + \dot{u}_1(t_i) (\ddot{u}_1(t_i) + \ddot{u}_1(t_{i+1})) \frac{\Delta t^2}{2} + \frac{(\ddot{u}_1(t_i) + \ddot{u}_1(t_{i+1}))^2}{12} \Delta t^3 \right\} + (c_1 + c_2) \\ & \left\{ \dot{u}_2^2(t_i) \Delta t + \dot{u}_2(t_i) (\ddot{u}_2(t_i) + \ddot{u}_2(t_{i+1})) \frac{\Delta t^2}{2} + \frac{(\ddot{u}_2(t_i) + \ddot{u}_2(t_{i+1}))^2}{12} \Delta t^3 \right\} - 2c_1 \dot{u}_1(t_i) \dot{u}_2(t_i) \Delta t \\ & - c_1 \dot{u}_1(t_i) \frac{(\ddot{u}_2(t_i) + \ddot{u}_2(t_{i+1}))^2}{2} \Delta t^2 - c_1 \dot{u}_2(t_i) \frac{(\ddot{u}_1(t_i) + \ddot{u}_1(t_{i+1}))^2}{2} \Delta t^2 - c_1 \frac{(\ddot{u}_1(t_i) + \ddot{u}_1(t_{i+1})) (\ddot{u}_2(t_i) + \ddot{u}_2(t_{i+1}))}{6} \Delta t^3, \end{aligned} \quad (15)$$

and the mass-damping and friction hysteretic energy

$$E_D(t) + E_F(t) = \sum_1^{t/\Delta t} [\Delta E_D(n) + \Delta E_F(n)]. \quad (16)$$

In the following sections, measured earthquake wave signals are used as case studies in the model developed above for numerical solutions of the response isolated bridges with FPBs.

4. Numerical Solutions

4.1. Multihazard Source Excitations. El Centro [30] was the seismic wave signals recorded in 1940 and has been widely used in seismic response analyses. Taft [30] was another wave signal recorded in 1952. The traces of the wave signals

are shown in Figures 5 and 6, respectively, and their characteristics are given in Table 1. As case studies, the peak accelerations of the two waves were adjusted to $0.3g$ and $0.4g$, following the US bridge design code AASHTO LRFD [31] for the seismic zone four, representing two cases of the seismic fortification intensity, respectively.

4.2. Time Step. The published data on the time step of El Centro and Taft waves available by recording were 0.02 s. And the energy responses of isolated bridges with FPB in different time steps (e.g., 0.02 s, 0.01 s, 0.005 s, and 0.0025 s) were obtained; the detailed data are shown in Figure 7 and Tables 2 and 3, respectively. Figure 7 and Table 2 show the influence of time step on the time history and amplitudes of

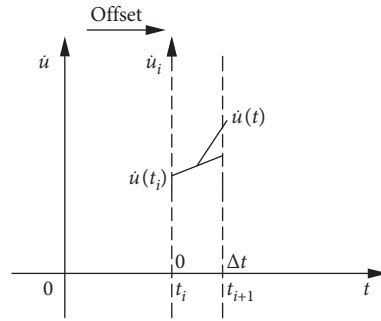


FIGURE 4: Velocity variation in time step.

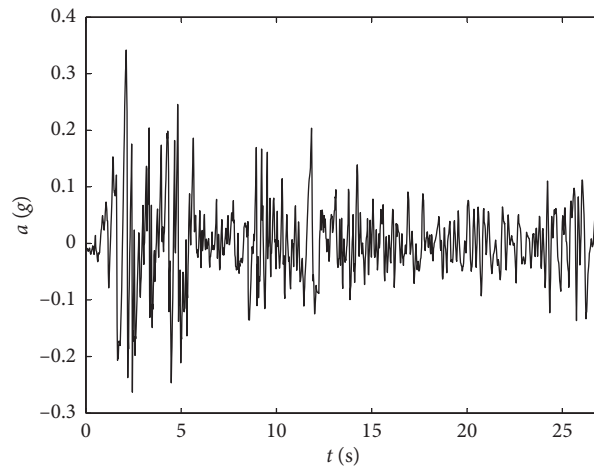


FIGURE 5: El Centro seismic wave.

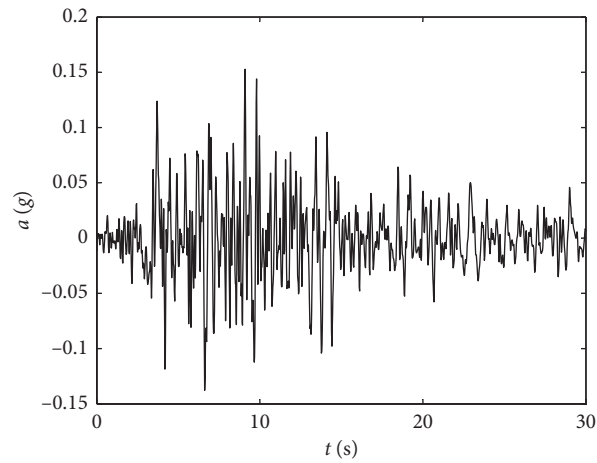


FIGURE 6: Taft seismic wave.

TABLE 1: Characteristics of seismic waves.

Wave	Peak acceleration (g) corresponding to the acceleration coefficient		Duration (s)	Dominant period of the ground motion (s)
El Centro	0.3	0.4	27	0.54
Taft			30	0.36

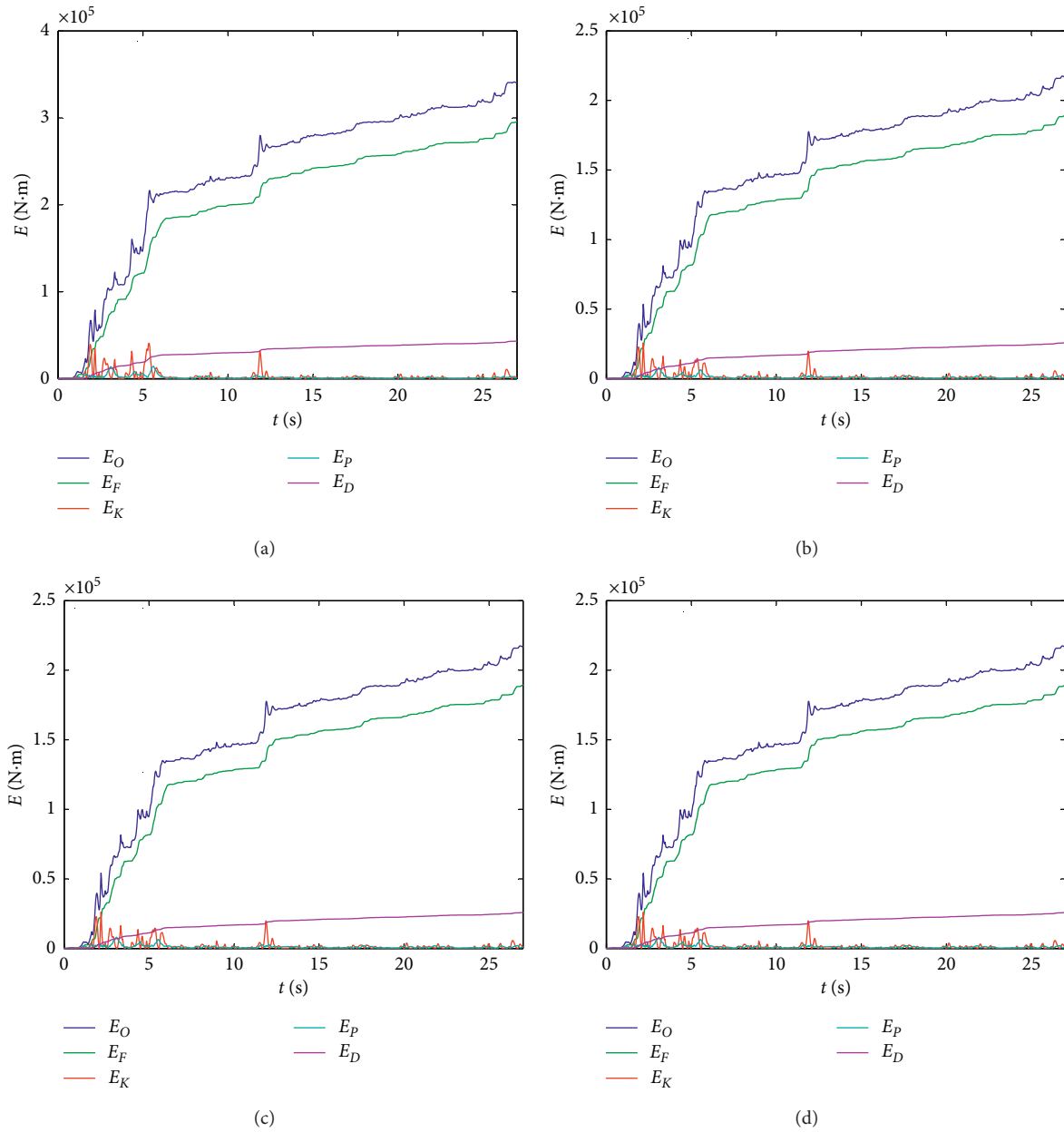


FIGURE 7: Comparison of time history of the energy response in different time steps, $T_g = 2.84$ s, $\mu = 0.05$; El Centro seismic wave; peak acceleration is $0.4g$. (a) $\Delta t = 0.02$ s, (b) $\Delta t = 0.01$ s, (c) $\Delta t = 0.005$ s, and (d) $\Delta t = 0.0025$ s.

TABLE 2: Amplitudes of energy response: the El Centro seismic wave.

Step time (s)	E_O (N·m)	E_F (N·m)	E_K (N·m)	E_P (N·m)	E_D (N·m)
0.02	341360	295510	40865	14331	43265
0.01	217500	189450	25740	8029	25831
0.005	217510	189460	25994	8033	25829
0.0025	217490	189450	26017	8033	25826

TABLE 3: Amplitudes of energy response: the TAFT seismic wave.

Step time (s)	E_O (N·m)	E_F (N·m)	E_K (N·m)	E_P (N·m)	E_D (N·m)
0.02	457200	409142	66571	22060	46828
0.01	457225	409223	66485	21966	46772
0.005	457192	409356	66495	21975	46805
0.0025	457180	409428	66485	21968	46800

the energy response under the El Centro wave with a peak acceleration of $0.4g$, respectively. The appropriate time step should be selected according to the seismic wave to ensure

the convergence and efficiency of a computational algorithm. It can be seen that the results are basically consistent when the time step is less than 0.01 s, so the time step should

be selected as 0.01 s for the loading case of El Centro. And the time step should be selected as 0.02 s for the loading case of TAFT according to Table 3.

4.3. Calculated Time History of the Energy Response. To study the energy variation over time, the time history of energy response of an FPB isolated bridge was solved using the model discussed in Section 3. The structural parameters of the bridge are given in Appendix B. In the calculation, the isolation period of the FPB was taken as 2.84 s and the friction coefficient as 0.05. Table 4 shows the kinetic parameters of the bridge system, with k_1 and c_1 being calculated by equations (2) and (5), and the peak accelerations of the seismic wave was set to $0.4g$. As the horizontal displacement D is related to the seismic wave, kinetic parameters are different in the cases of El Centro and Taft. Figure 8 illustrates the time history of the energy response.

In Figure 9, E_O is the seismic input energy obtained by the right hand side of equation (6). E_O' is the summation of the left hand terms of equation (7). The two results are virtually identical through the duration of seismic waves. It can be seen that the seismic input energy E_O , the friction hysteretic energy E_F , and the mass-damping energy E_D all increase with the duration of seismic waves. The numerical results indicate a highly effective damping effect of FPBs with around 90% of total input energy dissipated through friction (E_F to E_O).

5. Finite Element Modelling

5.1. Results of the SAP2000 Model. A finite element model was built for a four-span continuous bridge section using SAP2000 [26], a commercially available finite element code for the general structural analysis. The model is shown in Figure 9, including five piers and ten FPBs, with two FPBs on each pier. Mid-thick shell elements provided by the FE code were used for the beams and the piers. The frictional function of FPBs was modeled by the link-element available in the code. The link-element is a nonlinear element with the friction coefficient of FPB, the spherical radius of contact surfaces, and the vertical stiffness being the defined parameters. A mesh sensitivity study showed that a total of 725 elements and 855 nodes provide an appropriate model with good convergence.

5.2. Modal Analysis. Figure 10 shows the modal period and mode shape of formal six modes when the radius of the spherical pendulum bearing was set as 2 m.

Mode 1 and mode 2 were the isolation modes of the bridge structure in transverse and longitudinal direction, respectively. The radius of the concave surface of FPB was constant in both directions, so the isolation periods of mode 1 and mode 2 were the same, and the isolation period was 2.95 s. The isolation period calculated by theoretical calculation was 2.84 s according to equation (3). The results of numerical simulation and theoretical calculation were in good agreement.

TABLE 4: Kinetic parameters when $T_g = 2.84$ s, $\mu = 0.05$, and the peak acceleration is $0.4g$.

Parameters	k_1	k_2	c_1	c_2	ε_1	ε_2	ω_1	ω_2
Unit	N/ mm	N/ mm	N·s/ mm	N·s/ mm	—	—	Hz	Hz
El Centro	5283	87000	1110	753	0.336	0.05	3.15	25.5
Taft	6108	87000	1313	754	0.375	0.05	3.17	34.9

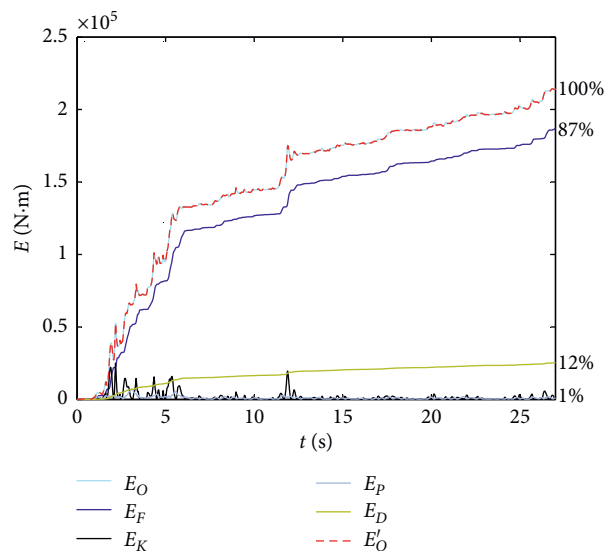


FIGURE 8: Time history of the energy response, $T_g = 2.84$ s, $\mu = 0.05$, and peak acceleration is $0.4g$; El Centro wave.

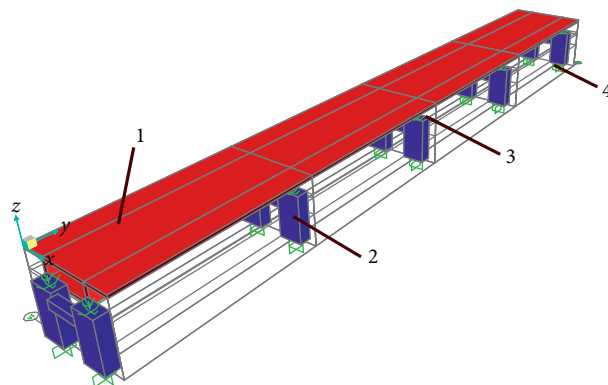


FIGURE 9: The finite element model of a four-span continuous beam bridge unit with FPBs. (1) Main bridge beam; (2) pier; (3) FPB; and (4) fixed boundary constraints to piers.

5.3. Influence of Structural Parameters on the Dynamic Responses of the Bridge. El Centro wave was used as the dynamic loading, with a peak acceleration of $0.4g$. All structural and mechanical parameters used in the FE model were the same as in the theoretical analysis.

Figures 11(a) and 10(b) show the seismic input energy in terms of the frictional coefficient of FPB when the isolation period of the spherical pendulum bearing is set as 2.46 s and

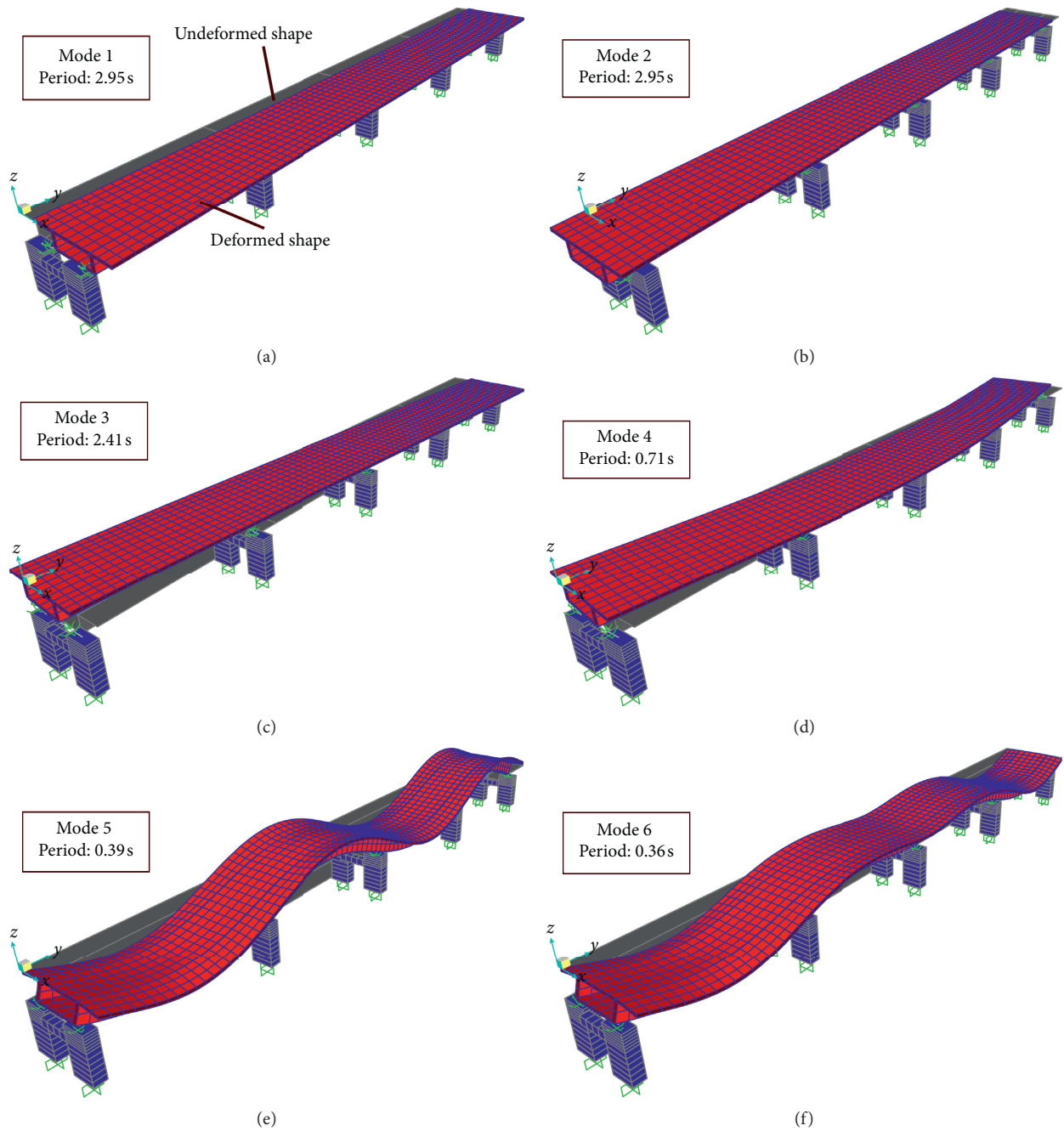


FIGURE 10: Modal periods and mode shapes when $R=2$ m.

2.84 s, respectively. The energy response of the theoretical and FEA results agrees well broadly. Figure 11 also illustrates that the input energy to the bridge increases approximately linearly with the friction coefficient under the small displacement assumption. And the isolation period appears to have only a moderate effect on the input energy.

In industrial practice, the pier stiffness k_2 is normally chosen in the range of 80–300 kN/m [32]. Taking the two range-end values (i.e., 80 and 300) as the minimum and maximum cases, Figure 12 illustrates the effect of k_2 on the response of the beam-pier system under the El Centro wave with a peak acceleration of $0.4g$.

Figures 12(a) and 12(c) show that the dynamic responses of the main beam are virtually identical under the two range-end values, i.e., not affected by k_2 . In contrast, the pier is more sensitive to k_2 (as shown in Figures 12(b) and 12(d)). It can be seen that both the displacement and the acceleration of the pier decrease when the pier becomes more rigid with a higher k_2 .

5.4. Parameter Optimization of FPB. The energy dissipation of a FPB can be described by a ratio between its friction hysteretic energy and the seismic input energy, denoted as λ ,

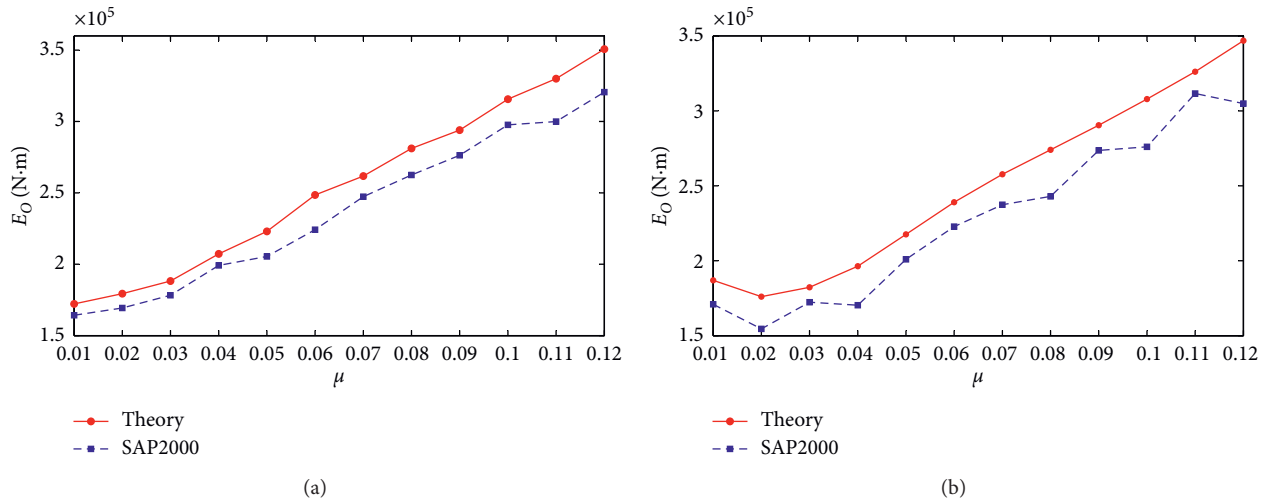


FIGURE 11: Comparison of seismic input energy between FE and analytical results. (a) $T_g = 2.46$ s and (b) $T_g = 2.84$ s.

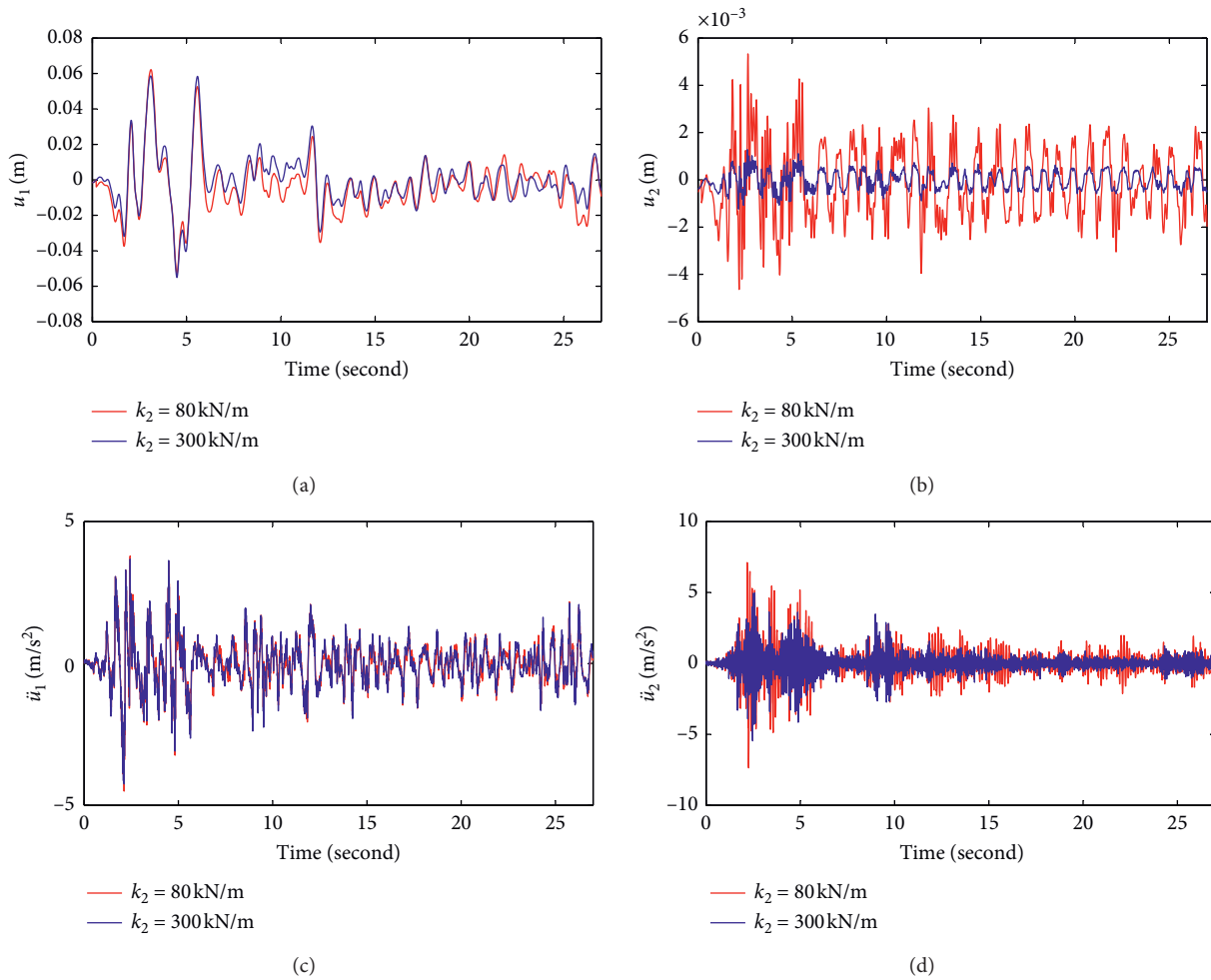


FIGURE 12: Comparison of the dynamic responses of the main beam and the pier for the minimum and maximum values of k_2 . $T_g = 2.84$ s, $\mu = 0.05$. Minimum: $k_2 = 80$ kN/m. Maximum: $k_2 = 300$ kN/m. (a) Displacement of the main beam, (b) displacement of the pier, (c) acceleration of the main beam, and (d) acceleration of the pier.

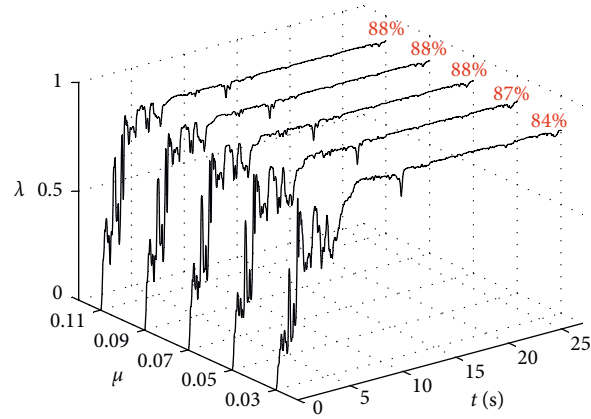
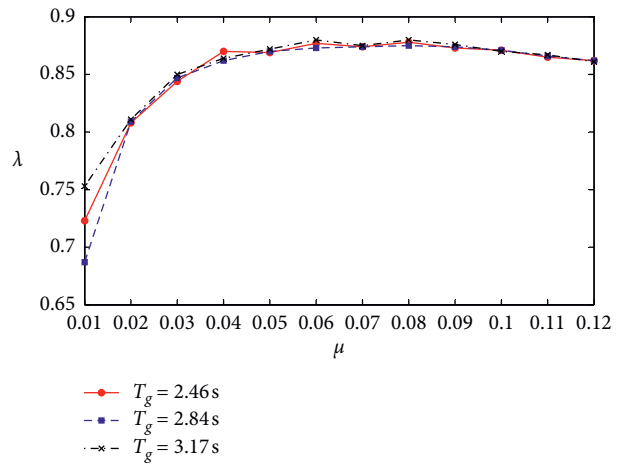
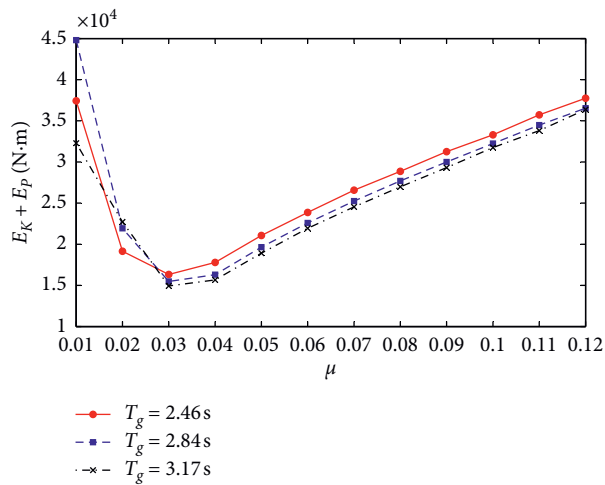
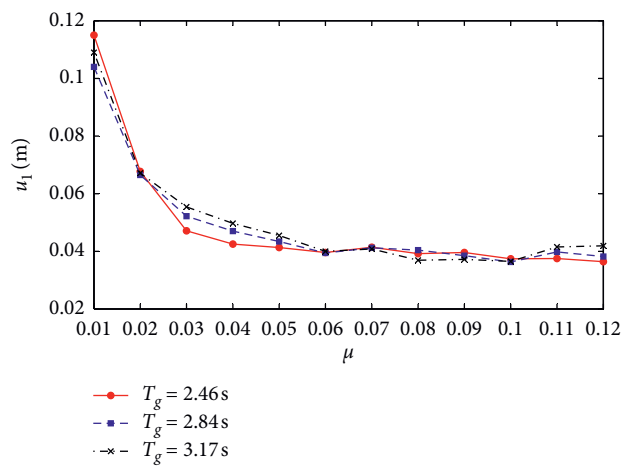
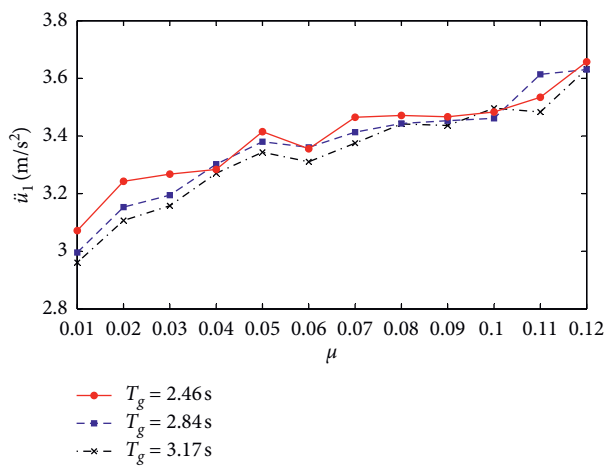


FIGURE 13: Time history of energy consuming ratio under the El Centro seismic wave, $T_g = 2.84$ s and peak acceleration is $0.4g$.



(a)

(b)



(c)

(d)

FIGURE 14: Seismic response amplitude (El Centro, peak acceleration $0.3g$). (a) Structural response energy; (b) energy consuming ratio; (c) acceleration amplitude of the main beam; (d) displacement amplitude of the main beam.

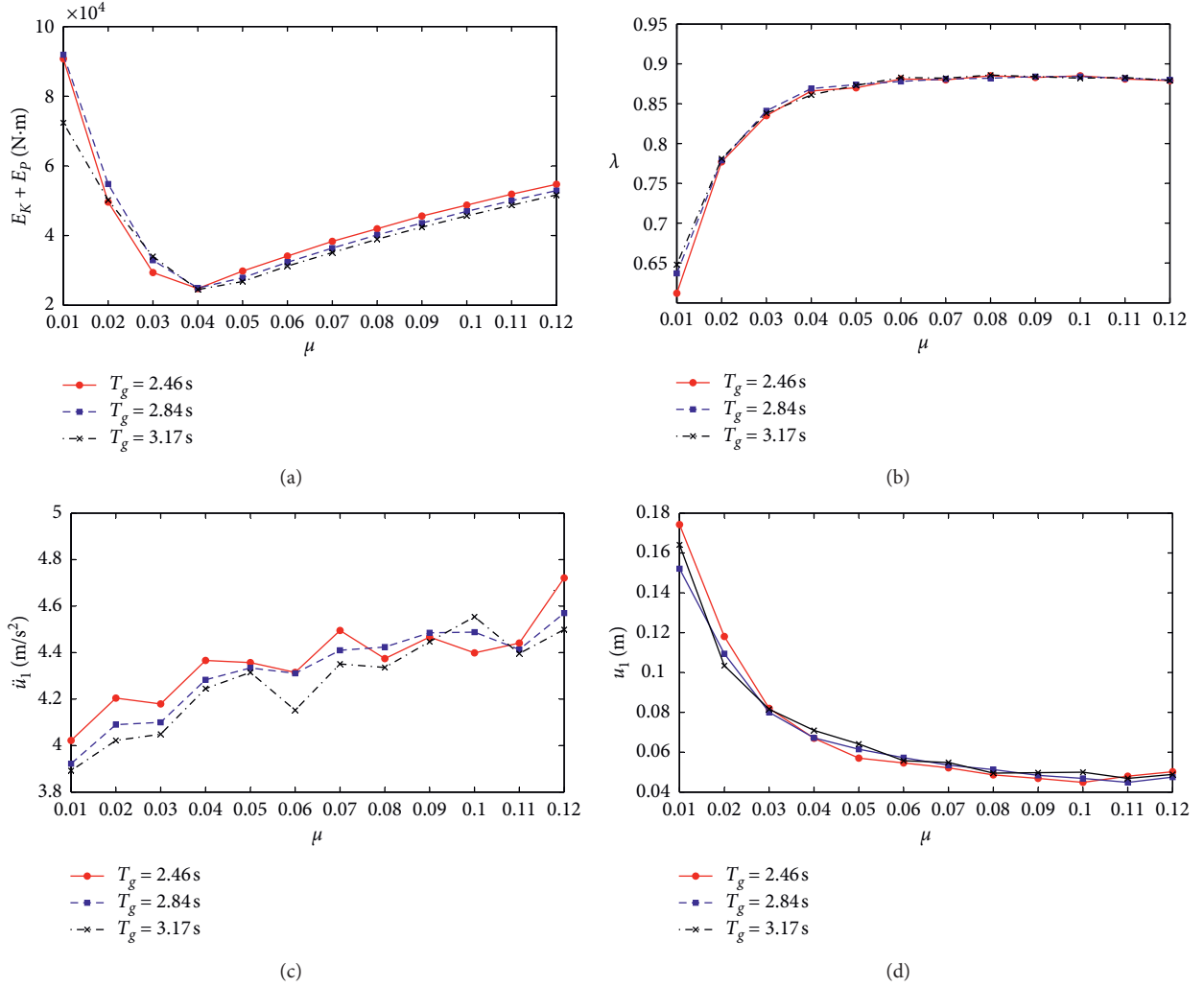


FIGURE 15: Seismic response amplitude (El Centro, peak acceleration $0.4g$). (a) Structural response energy; (b) energy consuming ratio; (c) acceleration amplitude of the main beam; (d) displacement amplitude of the main beam.

$$\lambda = \frac{E_F(t)}{E_O(t)}. \quad (17)$$

The control targets for design optimization are to minimize the structural response energy; to maximize the energy consuming ratio, thus a higher λ ; and to minimize the acceleration and displacement of the main beam. For the two loading cases of El Centro and Taft, design control parameters are discussed in more detail in the following sections based on theoretical calculations as discussed in Section 3.

5.4.1. El Centro Seismic Wave. Calculated time histories of λ are shown in Figure 13 for different friction coefficients of FPB under El Centro wave of a peak acceleration of $0.4g$. λ first increases rapidly with time and reaches a plateau value close to the full capacity of energy dissipation of FPB. The percentage of dissipation increases slightly with an increasing frictional coefficient of FPBs.

Figures 14 and 15 show the influence of the peak acceleration on the kinetic and elastic strain energy, the energy dissipation ratio, the acceleration, and the displacement of the main beam versus the friction coefficient μ . The influences of the isolation period of the FPB, T_g , are also included by three different values. It shows that in terms of the friction coefficient μ , the structural response energy, the energy consuming ratio, and the main beam acceleration do not change monotonically. There is either a maximum or minimum, allowing optimal values to be chosen for design. For instance, for a minimum structural response energy, a maximum energy consuming ratio, and for a minimum acceleration and displacement of the main beam, an optimal value of μ and R might be chosen as, respectively, $\mu = 0.03$ – 0.04 and $T_g = 3.17\text{ s}$ for the peak seismic acceleration of $0.3g$ and $\mu = 0.04$ – 0.05 and $T_g = 2.84\text{ s}$ – 3.17 s for the peak acceleration of $0.4g$.

5.4.2. Taft Seismic Wave. Similar to the loading of El Centro, Figures 16–18 illustrate the influence on the structural

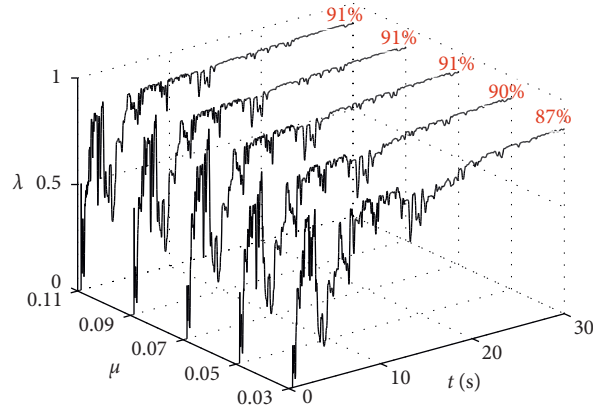


FIGURE 16: Time history response of energy consuming ratio when the Taft seismic wave $T_g = 2.84$ s and peak acceleration is $0.4g$.

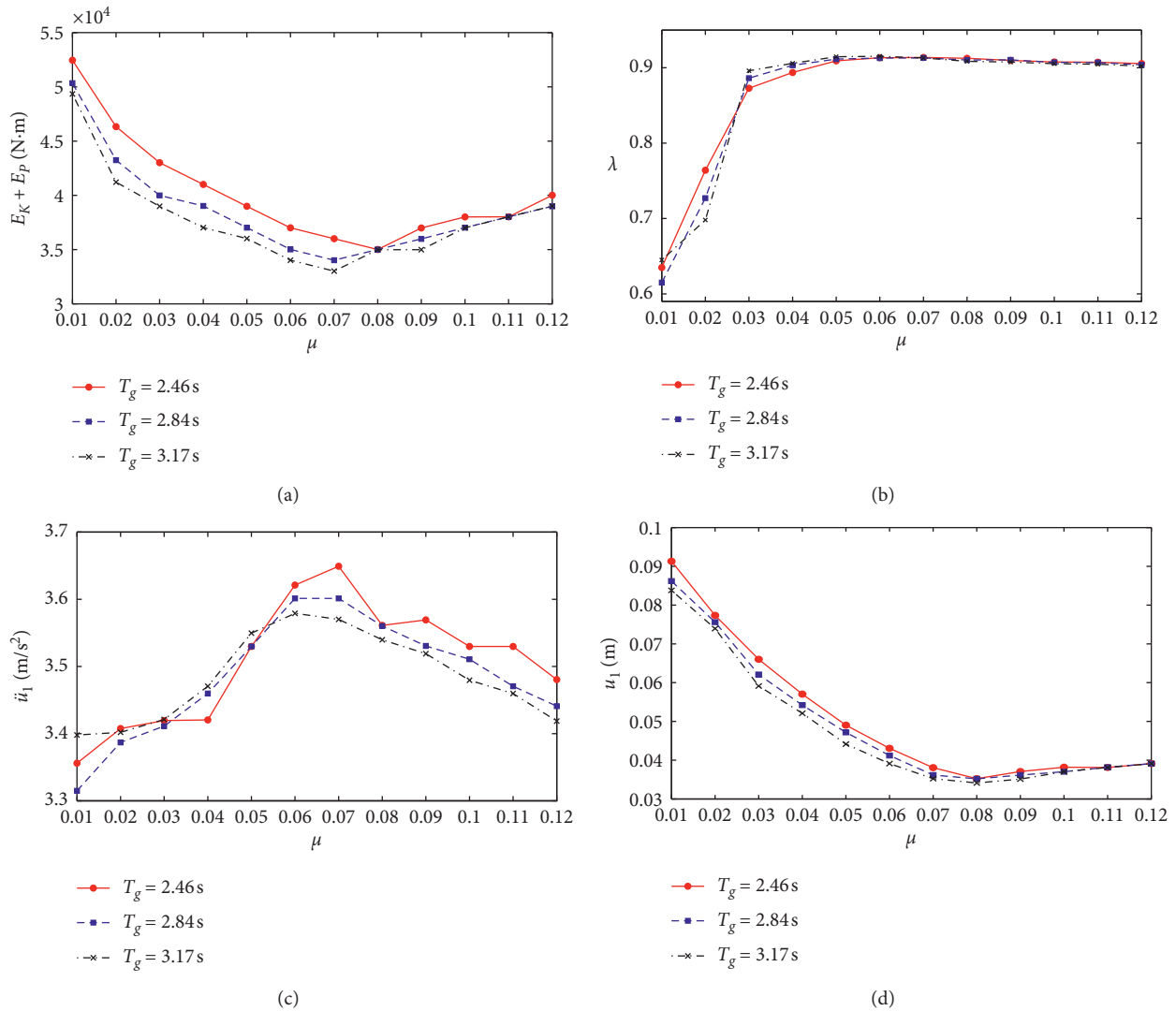


FIGURE 17: Seismic response amplitude (Taft, peak acceleration $0.3g$). (a) Structural response energy; (b) energy consuming ratio; (c) acceleration amplitude of the main beam; (d) displacement amplitude of the main beam.

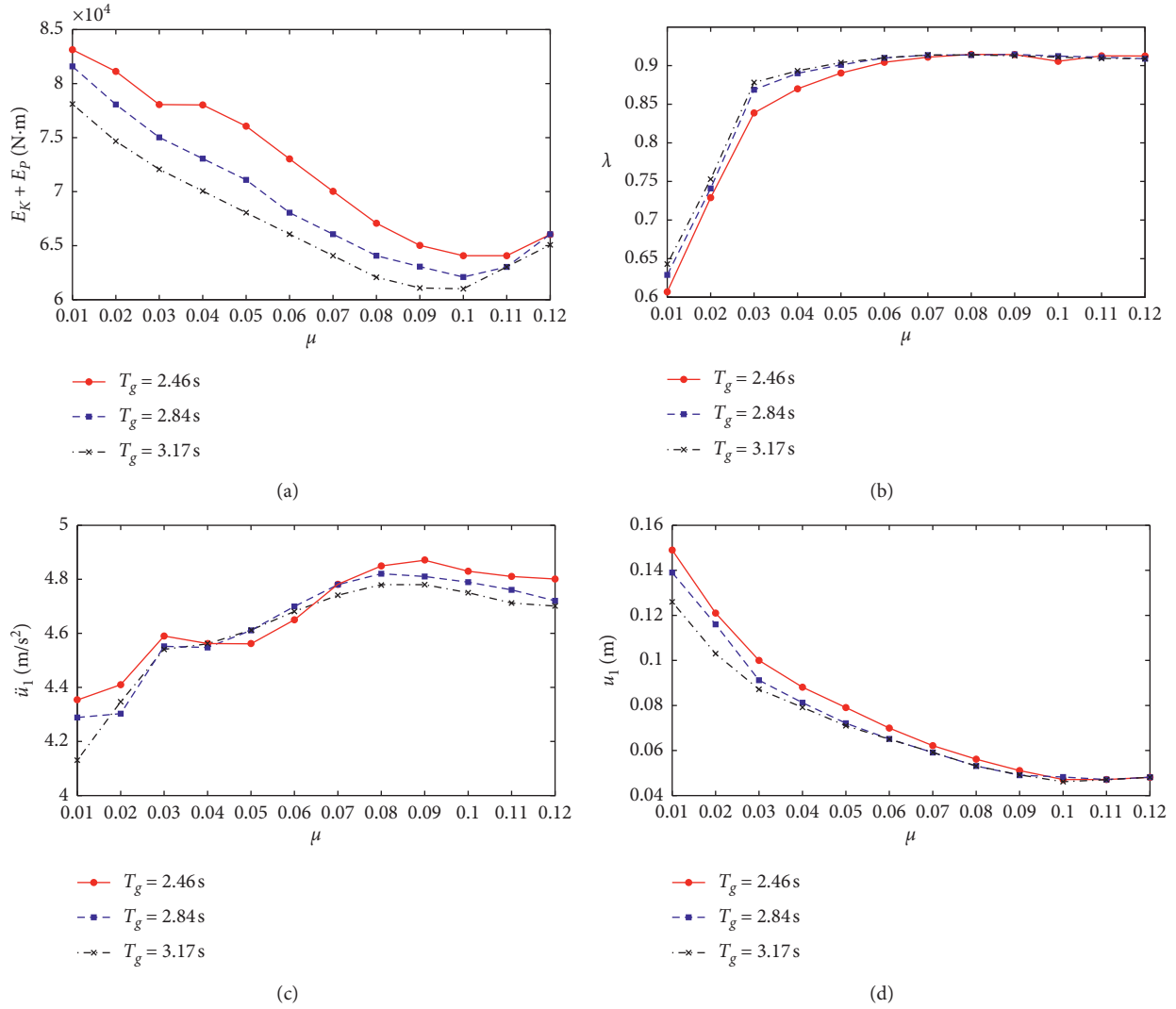


FIGURE 18: Seismic response amplitude (Taft, peak acceleration 0.4g). (a) Structural response energy; (b) energy consuming ratio; (c) acceleration amplitude of the main beam; (d) displacement amplitude of the main beam.

TABLE 5: The optimal parameters in different cases.

Parameters	Cases				
	El Centro		Taft		Sichuan
	0.3g	0.4g	0.3g	0.4g	
μ	0.03-0.04	0.04-0.05	0.06-0.07	0.09-0.1	0.04-0.06
T_g	3.17 s	2.84 s-3.17 s	3.17 s	3.17 s	3.17 s

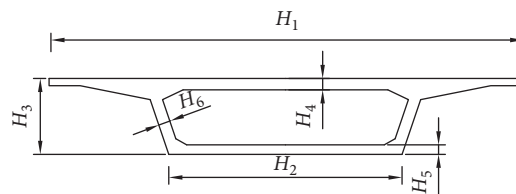


FIGURE 19: Cross section of span double line box beam.

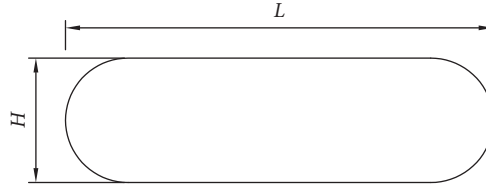


FIGURE 20: Cross section of round ended pier.

TABLE 6: Structural parameters of high-speed railway bridges.

Parameters	H_1	H_2	H_3	H_4	H_5	H_6	m_1	H	L	m_2
Unit	m	m	m	m	m	m	t	m	m	t
Values	12.4	6.12	2.00	0.30	0.25	0.45	510	1.5	6.3	142

parameters under the Taft wave with peak accelerations of $0.3g$ and $0.4g$, respectively. Following the same analyses and discussions, we may draw the conclusion that the optimal design values of FPB unit might be chosen as $\mu = 0.06-0.07$ and $T_g = 3.17$ s for the peak seismic acceleration $0.3g$ and $\mu = 0.09-0.1$ and $T_g = 3.17$ s for the peak acceleration is $0.4g$.

A further case study is given here on the Sichuan Earthquake in 2008, which was measured at 8.0 Ms. Using the seismic data available, the optimal value of the friction coefficient and the spherical radius of FPB would be chosen as $\mu = 0.03-0.05$ and $R = 2.5$ m. Table 5 summaries the optimized parameters of the friction coefficient and the spherical radius in different cases.

6. Conclusions

Based on energy balance equations of continuous beam bridges with FPBs, analytical modelling and finite element simulations were carried out. Numerical results of the theoretical analysis agree well with those of the finite element modelling. It shows that in order to control the dynamic response of bridges under seismic loading, optimal design values can be chosen for the friction coefficient and the isolation period of FPB. The following conclusions can be drawn:

- (1) The appropriate time step should be selected according to the seismic wave to ensure the convergence and efficiency of computational algorithm, and the time steps are selected as 0.01 s and 0.02 s for El Centro and TAFT waves, respectively.
- (2) The seismic input energy to the bridge structure increases with the increase of the friction coefficient of FPB, and the influence of the isolation period (2.46 s–3.17 s) on the seismic input energy to the bridge structure is less.

- (3) Selection of the optimal values of the friction coefficient μ and the isolation period T_g of FPB under different seismic loading can be based on the structural energy response and the dynamic response of the main beams. Recommended values of μ and T_g were given for the benchmark wave data El Centro and Taft. The structural energy response decreases with the increase of the isolation period of FPB.
- (4) The longitudinal stiffness of piers should be increased to the upper end of the allowable range (such as those defined in design codes/standards) in order to decrease the peak displacement and acceleration of piers.
- (5) The friction coefficient of FPB μ should be proportionally increased in line with the expected seismic fortification intensity.
- (6) The energy dissipation ratio can reach up to 90% by introducing properly designed FPBs.

The proposed analytical modelling can be used for design optimization of FPBs for seismic loading isolation in bridges, through which, design guidelines and some recommended design values have been given. It should be noted that though the theoretical modelling and finite element simulations show good agreement, further comparison with experiment results, particularly full-scale site measurement is needed. This remains the scope for future work.

Appendix

A. Derivation of Equivalent Damping Ratio

FPB can be simplified equivalently as a viscous spring damper with one-degree of freedom. Energy dissipations of FPB in one cycle is given as

$$\begin{aligned}
\Delta E' \int_0^{2\pi/\omega} c_1 \dot{x} \cdot \dot{x} dt &= \int_0^{2\pi/\omega} c_1 (D\omega \cos \omega t)^2 dt = \int_0^{2\pi/\omega} c_1 D^2 \omega^2 \cos^2 \omega t dt \\
&= \int_0^{2\pi/\omega} c_1 D^2 \omega^2 \left(\frac{1 + \cos 2\omega t}{2} \right) dt = c_1 D^2 \omega^2 \left(\frac{t}{2} + \frac{\sin 2\omega t}{4\omega} \right) \Big|_0^{2\pi/\omega} \\
&= \pi c_1 \omega D^2.
\end{aligned} \tag{A.1}$$

Following the classical vibration analysis, we have

$$\begin{aligned}
c_1 &= 2\varepsilon_1 \sqrt{k_1 m}, \\
\omega &= \sqrt{\frac{k_1}{m}}.
\end{aligned} \tag{A.2}$$

Hence,

$$\Delta E' = \pi \cdot 2\varepsilon_1 \sqrt{k_1 m} \cdot \sqrt{\frac{k_1}{m}} \cdot D^2 = 2\pi\varepsilon_1 k_1 D^2. \tag{A.3}$$

The hysteretic energy dissipation of FPB in one cycle is

$$\Delta E = 4\mu W D. \tag{A.4}$$

Let $\Delta E' = \Delta E$, we have

$$2\pi\varepsilon_1 k_1 D^2 = 4\mu W D. \tag{A.5}$$

Substituting equation (2) into equation (A.5) leads to

$$\varepsilon_1 = \frac{2\mu}{\pi(\mu + (D/R))}. \tag{A.6}$$

B. Details of an Isolated Bridge Unit Used in the Analysis

The unit structure of an isolated bridge with FPB consists of a span of the main beam and a pier. The main beam is supported by FPB, with the FPB fixed on the top of the pier. Based on a high-speed railway bridge design, the main beam span considered here is 24 m, and the height of the pier is 6 m. Figures 19 and 20 show the cross sections of main beam and the pier. The mainly structural parameters of bridges are given in Table 6, where m_1 and m_2 are the weight of the beam and the pier in metric ton.

Data Availability

All data relevant to the article will be made available upon request for research purpose.

Conflicts of Interest

The authors declare that they have no conflicts of interest.

Acknowledgments

This study was supported by the Doctoral Scientific Research Foundation of North China University of Water Resources and Electric Power and the Key Research Projects of Higher

Education Institutions in Henan (18A460004) and the International Exchanges Programme Scheme project by the Royal Society and National Natural Science Foundation of China (51811530311).

References

- [1] T. L. Karavasillis, T. Blakeborough, and M. S. Williams, "Development of nonlinear analytical model and seismic analyses of a steel frame with self-centering devices and viscoelastic dampers," *Computers & Structures*, vol. 89, no. 11-12, pp. 1232-1240, 2011.
- [2] R. S. Jangid, "Equivalent linear stochastic seismic response of isolated bridges," *Journal of Sound and Vibration*, vol. 309, no. 3-5, pp. 805-822, 2008.
- [3] A. M. Avossa, D. D. Giacinto, P. Malangone, and F. Rizzo, "Seismic retrofit of a multispan prestressed concrete girder bridge with friction pendulum devices," *Shock and Vibration*, vol. 2018, Article ID 5679480, 22 pages, 2018.
- [4] E. Tubaldi, A. Dall'Asta, and L. Dezi, "Seismic response analysis of continuous multispan bridges with partial isolation," *Shock and Vibration*, vol. 2015, Article ID 183756, 15 pages, 2015.
- [5] H. Zhang, J. Li, and T. Peng, "Development and mechanical performance of a new kind of bridge seismic isolator for low seismic regions," *Shock and Vibration*, vol. 20, no. 4, pp. 725-735, 2013.
- [6] M. Ismail, J. R. Casas, and J. Rodellar, "Near-fault isolation of cable-stayed bridges using an RNC isolator," *Engineering Structures*, vol. 56, pp. 327-342, 2013.
- [7] M. Ismail and R. Casas, "Novel isolation device for protection of cable-stayed bridges against near-fault earthquakes," *Journal of Bridge Engineering*, vol. 19, no. 8, 2014.
- [8] T. Y. Zhong, C. Y. Zhang, and F. L. Yang, "The parameter study of the seismically isolated bridge system by lead bearing based on energy analysis," in *Proceedings of the International Symposium on Seismic Engineering*, ASME, Baltimore, MD, USA, pp. 217-223, 2011.
- [9] M. Dicleli, "Seismic design of lifeline bridge using hybrid seismic isolation," *Journal of Bridge Engineering*, vol. 7, no. 2, pp. 94-103, 2002.
- [10] A. A. Taflanidis, "Optimal probabilistic design of seismic dampers for the protection of isolated bridges against near-fault seismic excitations," *Engineering Structures*, vol. 33, no. 12, pp. 3496-3508, 2011.
- [11] S. Ates and M. C. Constantinou, "Example of application of response spectrum analysis for seismically isolated curved bridges including soil-foundation effects," *Soil Dynamics and Earthquake Engineering*, vol. 31, no. 4, pp. 648-661, 2011.
- [12] R. S. Jangid, "Seismic response of isolated bridges," *Journal of Bridge Engineering*, vol. 9, no. 2, pp. 156-166, 2004.
- [13] G. Mosqueda, A. S. Whittaker, and G. L. Fenves, "Characterization and modeling of friction pendulum bearings subjected to multiple components of excitation,"

- Journal of Structural Engineering*, vol. 130, no. 3, pp. 433–442, 2004.
- [14] F. Khoshnoudian and A. Hemmati T, “Impact of structures with double concave friction pendulum bearings on adjacent structures,” *Proceedings of the Institution of Civil Engineers—Structures and Buildings*, vol. 167, no. 1, pp. 41–53, 2014.
- [15] Y.-S. Kim and C.-B. Yun, “Seismic response characteristics of bridges using double concave friction pendulum bearings with tri-linear behavior,” *Engineering Structures*, vol. 29, no. 11, pp. 3082–3093, 2007.
- [16] L. Yan, Q. Li, C. Han, and H. Jiang, “Shaking table tests of curved bridge considering bearing friction sliding isolation,” *Shock and Vibration*, vol. 2016, Article ID 6245062, 14 pages, 2016.
- [17] M. Dicleli and M. Y. Mansour, “Seismic retrofitting of highway bridges in Illinois using friction pendulum seismic isolation bearings and modeling procedures,” *Engineering Structures*, vol. 25, no. 9, pp. 1139–1156, 2003.
- [18] J. S. Hwang, K. C. Chang, and M. H. Tsai, “Composite damping ratio of seismically isolated regular bridges,” *Engineering Structures*, vol. 19, no. 1, pp. 55–62, 1997.
- [19] R. S. Jangid, “Stochastic response of bridges seismically isolated by friction pendulum system,” *Journal of Bridge Engineering*, vol. 13, no. 4, pp. 319–330, 2008.
- [20] R. S. Jangid, “Optimum friction pendulum system for near-fault motions,” *Engineering Structures*, vol. 27, no. 3, pp. 349–359, 2005.
- [21] S. Ates, D. Aydin Dumanoglu, and A. Bayraktar, “Stochastic response of seismically isolated highway bridges with friction pendulum systems to spatially varying earthquake ground motions,” *Engineering Structures*, vol. 27, no. 13, pp. 1843–1858, 2005.
- [22] M. Eröz and R. DesRoches, “Bridge seismic response as a function of the friction pendulum system (FPS) modeling assumptions,” *Engineering Structures*, vol. 30, no. 11, pp. 3204–3212, 2008.
- [23] M. Eröz and R. DesRoches, “The influence of design parameters on the response of bridges seismically isolated with the friction pendulum system (FPS),” *Engineering Structures*, vol. 56, no. 11, pp. 585–599, 2013.
- [24] A. Saha, P. Saha, and S. K. Patro, “Polynomial friction pendulum isolators (PFPIs) for seismic performance control of benchmark highway bridge,” *Earthquake Engineering and Engineering Vibration*, vol. 16, no. 4, pp. 827–840, 2017.
- [25] A. Saha, P. Saha, and S. K. Patro, “Seismic protection of the benchmark highway bridge with passive hybrid control system,” *Earthquake Engineering*, vol. 15, no. 3, pp. 227–241, 2018.
- [26] Computers and Structures. Inc., *SAP2000 Manuals*, Computers and Structures. Inc., Walnut Creek, CA, USA, 2000.
- [27] Optimization analysis of the equivalent linear model of friction pendulum bearing in preparation.
- [28] M. Bruneau and N. Wang, “Some aspects of energy methods for the inelastic seismic response of ductile SDOF structures,” *Engineering Structures*, vol. 18, no. 1, pp. 1–12, 1996.
- [29] Apple Hill Drive, *MATLAB Mathworks*, Apple Hill Drive, Natick, MA, USA, 2000.
- [30] Y. C. Kim, S. D. Xue, P. Zhuang, W. Zhao, and C. H. Li, “Seismic isolation analysis of FPS bearings in spatial lattice shell structures,” *Earthquake Engineering and Engineering Vibration*, vol. 9, no. 1, pp. 93–102, 2010.
- [31] AASHTO, *AASHTO LRFD Bridge Design Specifications*, AASHTO, Washington, DC, USA, 2005.
- [32] J. Zheng, *Chinese High-Speed Railway Bridges*, High Education Press, China, Beijing, 2008, in Chinese.

Research Article

Mitigating Large Vibrations of Stayed Cables in Wind and Rain Hazards

Hung Vo-Duy¹ and Cung H. Nguyen² 

¹The University of Da Nang-University of Science and Technology, Da Nang, Vietnam

²Department of Civil Engineering, Industrial University of Ho Chi Minh City, Ho Chi Minh City 700 000, Vietnam

Correspondence should be addressed to Cung H. Nguyen; nguyenhucung@iuh.edu.vn

Received 20 February 2020; Accepted 1 May 2020; Published 19 May 2020

Academic Editor: Vasant Matsagar

Copyright © 2020 Hung Vo-Duy and Cung H. Nguyen. This is an open access article distributed under the Creative Commons Attribution License, which permits unrestricted use, distribution, and reproduction in any medium, provided the original work is properly cited.

This paper presents an experimental investigation of stayed cable vibrations in dry-wind and rain-wind coupling hazards. To mitigate large vibrations of the cable, the use of spiral wires wrapped around the cable is proposed. By testing two cable models in a wind tunnel in dry and rain conditions for different yaw angles and wind speeds, the effectiveness of using the spiral wires to mitigate large vibrations is clarified. Finally, the paper provides a further understanding of the complex mechanism of wind-induced and rain-wind-induced vibrations. It is found that the low-frequency vortex flows in the wake play a significant role in the excitation of large responses of the cable in high wind speeds. The spiral wires dismiss these low-frequency flows and then reduce the large vibrations.

1. Introduction

Stay cables, such as members of cable-stayed bridges, are very sensitive to wind loading, leading to large oscillation amplitudes, even to collapses due to aeroelastic instability. They are also vulnerable to large vibrations due to rain-wind coupling actions. Study on aerodynamics and aeroelasticity of cables has attracted much interest for many years. It has been shown that common types of large vibrations of cables include vortex-induced vibration (VIV), galloping, and rain-wind-induced vibrations (RWIV). The studies on these topics have not only focused on understanding the physics and mechanics of the phenomena but also provided methods to mitigate the vibrations.

It is well known that the classical VIV occurs when a Von Karman vortex is shed with a frequency close to structural frequency. This resonance then results in large vibrations. For an inclined cable, an axial vortex flow exits along the cable and near the wake. It interacts and mitigates Von Karman vortex and then excites large vibrations of the cable in high wind speeds. The role of the axial vortex on large vibrations of cables and its mechanism has been investigated through pioneering studies by

Matsumoto and his colleagues [1–6]. The phenomenon related to these large amplitude vibrations of cables in dry condition was referred to as dry galloping and also considered as a special case of VIV due to the presence of the axial vortex. It has been recognised that wind flow around inclined cables as well as aerodynamic and aeroelastic behaviour of the cables is sophisticated that needs further investigations.

In the 21st century, a number of studies on dry galloping of inclined cables have been conducted in different parts of the world. In an attempt to explain the mechanism of dry galloping of inclined cables, Macdonald [7] used quasisteady theory to predict successfully the occurrence of galloping that was observed in wind tunnel tests by Cheng et al. [8]. Macdonald's study shows that drag crisis in the critical Reynolds number range causes the dry galloping. Later, quasisteady conditions for the occurrence of galloping of inclined cables were developed [9, 10]. Wind tunnel experiments on cables have been carried out to understand further the phenomenon [11–17]. Despite many efforts, the mechanism of excitation of large vibrations of cables remains unclear and therefore is deserved for further investigations.

The first report on violent vibrations of stay cables in the coupling of rain and wind actions was provided by Hikami and Shiraishi [18] based on full-scale measurement. The field observations on this phenomenon were documented later by other researchers [19–23]. Due to the nature of complexity and uncertainty in field measurement, it is difficult to clarify the mechanism of RWIV. A number of wind tunnel experiments on cable models have been conducted to understand the phenomenon. To simulate rain water on cables, fixed artificial water rivulets were attached on the cable surface [2, 24], or liquids were sprayed on the cables [25–29]. Recently, rain simulators were employed in wind tunnel to have better rainfall simulations, in which rainfall intensity can be adjusted in the tests [30, 31]. According to those studies, the existence of axial flows, water rivulets, and thin waters plays significant roles in RWIV. However, their roles as individuals or as combinations have not been clearly understood [31].

In order to mitigate large responses of stayed cables in dry and rain conditions, two main approaches have been applied in research as well as in real practices. The first method is to use one or two external damper devices attached near a cable anchorage, such as viscous dampers, fluid dampers, tuned mass dampers, tuned inerter dampers, and magnetorheological dampers. Although there are many studies on dynamic properties and effectiveness of those dampers for the mitigation of structural vibrations [32–36], very few studies are on how these dampers affect the occurrence of large vibrations of cables in winds. Nguyen and Macdonald [37] first addressed the galloping issue of a taut cable with an attached viscous damper.

In the second method, cables are wrapped with single or multiple spiral protuberance wires (helical fillets). The efficiency of this method has been shown through wind tunnel tests. For example, a series of experiments in the wind tunnel of Yokohama National University successfully used the spiral wires to reduce dry galloping [38, 39]. Larose and Smitt [27] reported an effective application of a single spiral protuberance for mitigating RWIV. Nevertheless, full-scale monitoring at Øresund Bridge reported that the use of spiral wires was not effective as initially expected [23].

The above remarks have motivated this study, in which vibrations of two cable models in dry and rain conditions were studied by means of wind tunnel tests. One of the models is a circular cylinder with smooth surface. Another is as the same as the smooth cylinder but is wrapped with spiral wires as a proposed method for mitigating large responses of the cable in dry-wind and rain-wind coupling. Rainfall was simulated through a rain simulator system, which allows controlling the rain intensity and provides better and more realistic rain modelling compared with others in the literature. Finally, mechanism of the large vibrations of the two models was investigated that provides a further understanding of the complex phenomena of wind flows which passed an inclined cable.

The paper is structured into five main sections. Section 2 presents the details of the wind tunnel testing setup and results of the measurement of the aeroelastic responses of the

two cable models in dry and rain conditions. Section 3 explains the mechanism of the large vibrations of the circular cable through the measurement of the flow field in the wake of the fixed cable. Section 4 presents the further tests on the fixed cable wrapped by spiral wires to assess the reduction of the large vibrations of the cable. Finally, critical comments are provided in Section 5.

2. Vibrations of Cables in Dry Wind and Rain Wind and Their Mitigations

2.1. Setup of Wind Tunnel Tests. Wind tunnel tests on two stay cable models were conducted in a wind tunnel of the Yokohama National University. The wind tunnel has a working section with the dimension of 1.3 m width and 1.8 m height. The maximum wind speed is about 20 m/s.

Model 1 is a plain high-density polyethylene (HDPE) tube of 158 mm diameter and 1500 mm length (Figure 1(a)). Model 2 is the same as Model 1 but is wrapped with 12 spiral protuberances (Figure 1(b)). The spiral wires were arranged with a spiral angle of 27° . The dimensions of each spiral wire are 7.5 mm width and 5 mm height.

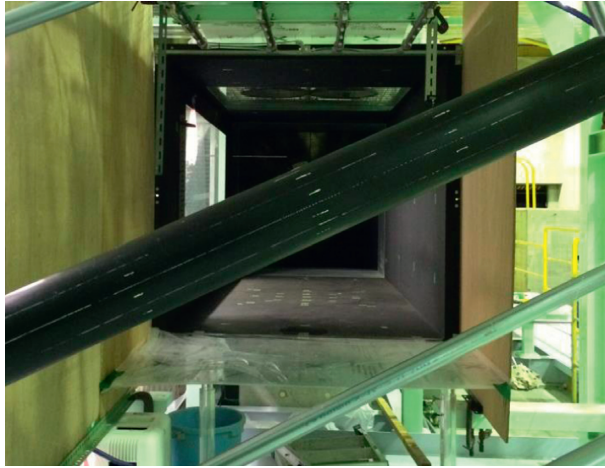
The cable models were supported by a system of springs allowing the vibrations only in vertical direction, i.e., normal to the wind flow, as one-degree-of-freedom (1DOF) system. The orientation of the cable with respect to the wind flow is determined through the angles α , β , and γ defined as in Figure 2. The angles α and β are commonly referred to as inclination angle and yaw angle, respectively. The tests were conducted for an inclination angle $\alpha = 25^\circ$ and four yaw angles $\beta = 0^\circ, 15^\circ, 30^\circ, \text{ and } 45^\circ$ in smooth wind with dry and rain conditions.

Rain was simulated by a system of water nozzles located up-front of the Model (front wind) and at the ceiling of the working section of the wind tunnel (Figure 3). The rainwater was sprayed from these nozzles to the cable models. The rain volume can be controlled through a volume adjustment system located outside the wind tunnel.

In the arrangement of measurement systems, dynamic pressure and wind speed were measured by a Pitot Tube. An accelerator system was used to capture cable vibrations in time. Each accelerometer has a rate capacity of 49.03 m/s^2 . To measure the cable vibrations, an accelerometer was mounted at each end of the cable. The vibrations were recorded for a duration of 60 seconds with the sampling frequency 50 Hz.

The structural, wind, and rain parameters used in the tests are given in Table 1. For each yaw angle β , dynamic parameters of the cable models, including the fundamental frequency f_s (Hz) and damping ratio ξ (%), were estimated from free vibration tests and showed in Table 2.

2.2. Wind-Induced Responses of the Circular Cable in Dry and Rain Conditions. Figures 4(a) and 4(b) show the reduced amplitudes, y_r , of the cable displacements versus reduced wind velocity, U_r , in dry and rain conditions, respectively, for different yaw angles. The reduced amplitude and reduced wind speed are defined as follows:



(a)



(b)

FIGURE 1: Spiral protuberance cable Model.

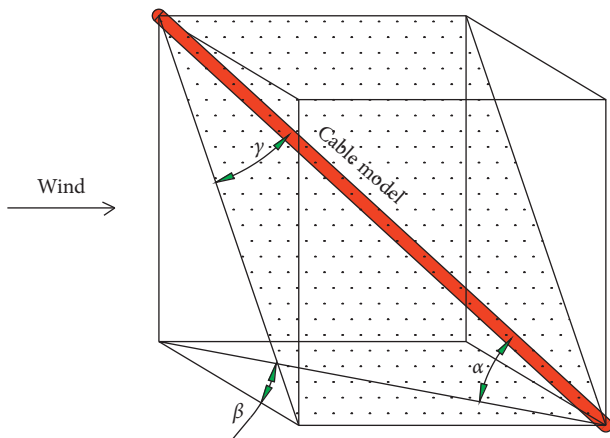


FIGURE 2: Definition of cable angles.

$$y_r = \frac{y}{D}$$

$$U_r = \frac{U}{f_s D}$$
(1)

where y , U , and f_s are the maximum amplitude (peak-to-peak displacement response, unit: m), inlet wind velocity (m/s), and structural fundamental frequency (Hz), respectively.

For dry condition, it can be seen from Figure 4(a) that the responses are generally larger for higher wind speeds. Among the four yaw angles β , the cable exposes to smallest responses for $\beta = 0^\circ$ (when wind is normal to the cable plane)

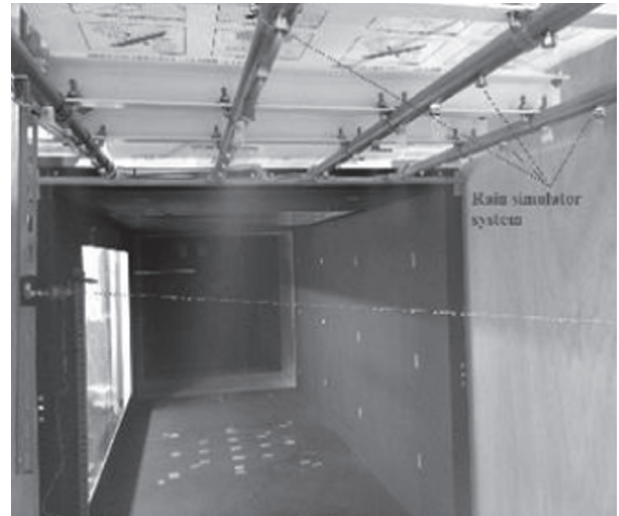


FIGURE 3: Rain simulator system.

TABLE 1: Structural, wind, and rain parameters.

Parameters	Value
Rain volume (mm/h)	40–50
Cable diameter: D (mm)	158
Effective length: L (mm)	1500
Inclination angle: α ($^\circ$)	25
Mass: m (kg/m)	9.9 (Model 1) 10.8 (Model 2)
Reynolds number	$0-2.1 \times 10^5$

TABLE 2: Dynamic parameters of cable Models for different yaw angles.

	$\beta = 0^\circ$		$\beta = 15^\circ$		$\beta = 30^\circ$		$\beta = 45^\circ$	
	f_s	ξ	f_s	ξ	f_s	ξ	f_s	ξ
Model 1 (circular)	0.9	0.16	0.9	0.14	0.86	0.16	0.86	0.16
Model 2 (spiral)	0.88	0.14	0.86	0.11	0.86	0.16	0.86	0.14

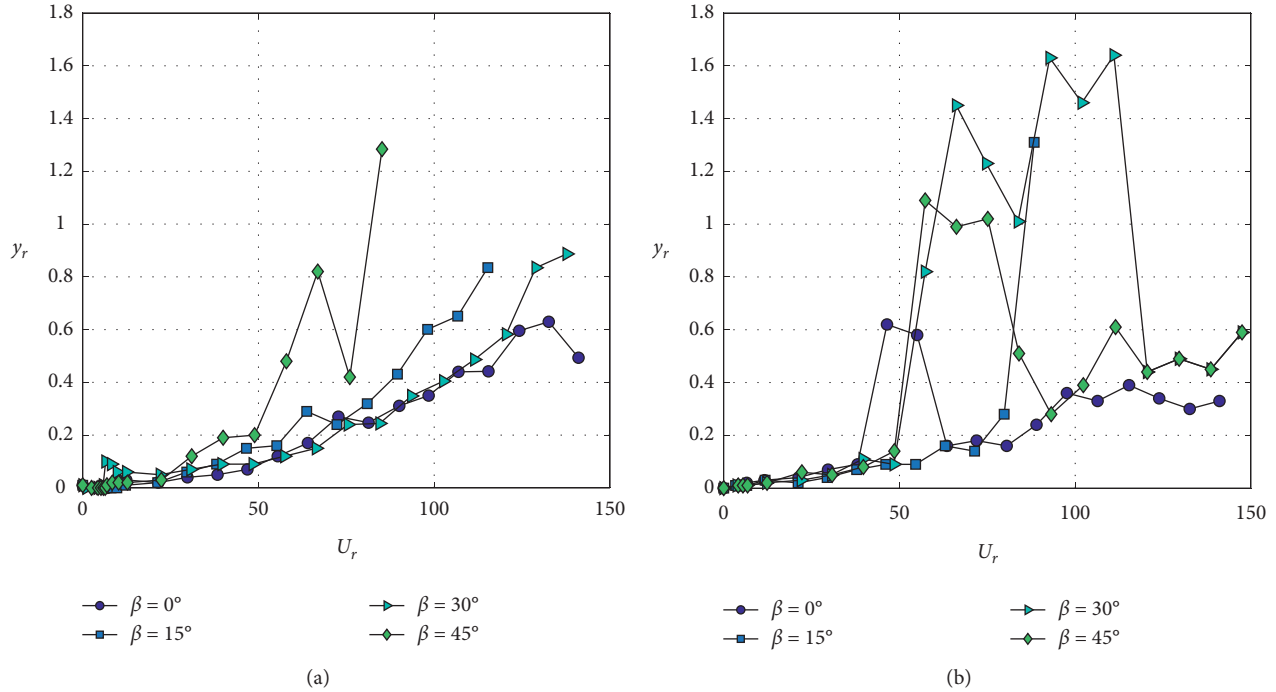


FIGURE 4: Wind-induced responses of circular cable in dry condition (a) and rain condition (b).

and largest responses for $\beta = 45^\circ$. For most of the cases, the amplitudes increase for increasing reduced wind speed. For $\beta = 45^\circ$, there is a sudden reduction of amplitude at $U_r = 76$. The reduction of amplitude is also seen for $\beta = 0^\circ$ and $\beta = 15^\circ$ but less significant. This amplitude reduction feature has been previously observed in the literature [5, 12, 17, 30]. In addition to Figure 4(a), at a given reduced wind speed, the cable does not vibrate with larger amplitudes for higher β as seen that the responses for $\beta = 15^\circ$ are larger than those for $\beta = 30^\circ$. For a range of low reduced wind speeds from 0 to 15, there is an apparent peak response for $\beta = 30^\circ$ at $U_r = 6.5$, looking similar to the classical vortex-induced vibration (VIV) due to Von Karman vortex. For other yaw angles, observation of VIV responses is not clear. This will be explained in the next section.

For rain condition, the vibration amplitudes do not always increase for increasing wind speeds. Instead, for each yaw angle, the amplitude is increasing for increased wind speed but significantly reduced at a higher wind speed as seen in Figure 4(b). These shapes of the responses are typical for rain-wind-induced vibration (RWIV) of cables as documented widely in the literature [3, 18, 24].

Comparing the responses of the cable in rain and dry condition, it reveals that, depending on the value of the reduced wind speed, the cable in wind condition can expose

larger or smaller vibration amplitudes. Taking $\beta = 30^\circ$ as an example, for $U_r = 57.3\text{--}111$, the cable vibrates violently in rain condition with amplitudes much larger, up to 4 times, than those without rain. However, for stronger wind with reduced speed higher than 111, rain can lead to reduction of cable vibrations. In summary, rain can be beneficial for the cable vibrating in high wind but significantly detrimental for the cable in a certain rain of wind speeds.

2.3. Mitigating Cable Vibrations with Spiral Wires.

Section 2.2 has shown the large vibration amplitudes of the smooth cylinder (Model (1)) in both cases with and without rain. To mitigate the large responses, 12 spiral wires were used to wrap around the smooth cable. The experimental results on the spiral cable (Model (2)) are shown below.

Figure 5 plots the reduced amplitudes of the cable with (w) and without (w/o) using spiral wires in rain and dry conditions for various yaw angles. The substantial reductions of vibration amplitudes can be seen when the cable is wrapped with the wires. This shows the efficiency of using spiral wires as a method to mitigate the cable vibrations.

Looking at the vibrations of the cable with the spiral wires, their amplitudes generally increase for increasing wind speeds, both in rain and without rain. Also, it can be

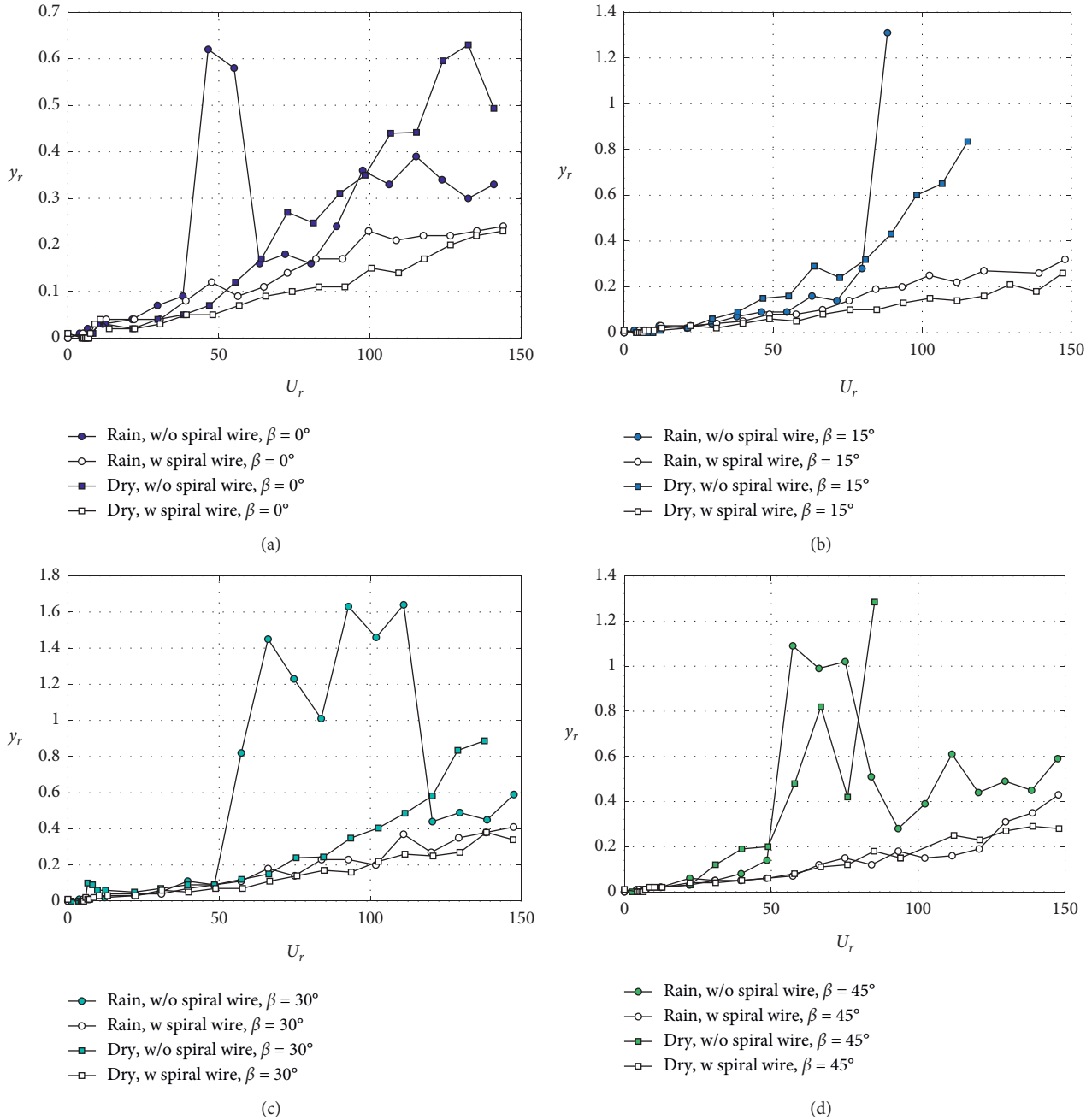


FIGURE 5: Reduced amplitudes of cable vibrations with and without using spiral wire in rain and dry condition for (a) $\beta = 0^\circ$, (b) $\beta = 15^\circ$, (c) $\beta = 30^\circ$, and (d) $\beta = 45^\circ$.

observed from Figures 5(a)–5(c) that, for yaw angles $\beta = 0^\circ$, $\beta = 15^\circ$, and $\beta = 30^\circ$, wind induces larger vibration amplitudes in rain than in dry condition. For $\beta = 45^\circ$, the vibration amplitudes in rain are larger or smaller than in dry condition, depending on the wind speed.

In addition to the vibrations of the cable with the spiral wires, particularly in rain, the variation of the amplitudes of Model 2 (with the spiral wires) against wind speeds has different pattern from those of Model 1 (without the spiral wires). The later has been discussed in the previous section in relation to Figure 4. As shown in many studies [28, 31, 40], the formation and vibration of water rivulets on the cable in

rain give rise to large amplitude vibrations of cables without spiral wires. The appearance of the spiral wires herein interrupts the oscillations of water rivulets on the cable, reducing cable vibrations and changing their patterns.

3. Mechanism of Large Amplitude Vibrations of the Circular Cable

Since the cable exposes to large amplitude vibrations as shown in Figure 4, it is important to understand the mechanism of cable vibrations in wind. For this purpose,

vertical component of fluctuating velocity in the wake of the cable is investigated through further wind tunnel tests.

In the experimental setup, the circular cable (Model 1) was statically fixed in the wind tunnel for $\alpha = 25^\circ$ and $\beta = 30^\circ$. A hot-wire anemometer was used to measure the fluctuating wind speed in the wake of the cable. As illustrated in Figure 6, it is located in the wake of the cable with the coordinates of $0.5D$ and $2D$ and varied along the cable with distances from $2D$ to $7D$, allowing the fluctuating speeds to be measured at different locations.

Due to technical difficulty in measuring the fluctuations using hot-wire anemometer in rain, only dry condition was considered during the measurements. For the interest of understanding the flow in the wake of cable in rain, readers might refer to the studies mentioned in Section 1, which used artificial rivulets.

Figure 7 shows the power spectral density (PSD) of the vertical fluctuating wind velocity in the wake along the cable at different locations X , which is a distance from the top end of the cable to the measured location, for $\alpha = 25^\circ$ and $\beta = 30^\circ$. The inlet mean wind velocities in the wind tunnel are 5 m/s (Figure 7(a)), 10 m/s (Figure 7(b)), and 15 m/s (Figure 7(c)). The reduced frequency, denoted as f_r as in the figure, is defined as

$$f_r = \frac{f_w D}{U}, \quad (2)$$

where f_w is the frequency of the vertical fluctuating velocity.

For the inlet wind speed $U = 5 \text{ m/s}$, as shown in Figure 7(a), there are slight PSD peaks at reduced frequency $f_r = 0.15$; that is, Strouhal number $St = 0.15$. Such St implies the Von Karman vortex of the circular cable [3, 5, 14], leading to the classical VIV, theoretically at a critical wind speed $U_r = 1/St = 6.67$. This explains the peak amplitude at $U_r = 6.5$ in the dynamic tests as shown in Figure 4(a), showing the excellent agreement between the theoretical prediction and experiment.

The situation changes for the inlet wind speed 10 m/s . It can be seen from Figure 7(b) that the dominant PSD peaks are at a low reduced frequency $f_r = 0.013$, equivalent to a relatively high reduced velocity $U_r = 76.9$. The appearance of this low-frequency flow weakens the Von Karman vortex as seen in Figure 7(b) and generates larger responses for higher wind speed than those for $U_r = 6.5$ (Figure 4(a)).

It can be seen from Figure 7(c) that when the inlet wind speed increases to 15 m/s , Von Karman vortex is significantly mitigated and two clear PSD peaks appear at reduced frequencies $f_{r1} = 0.009$ and $f_{r2} = 0.017$, equivalent to reduced velocities $U_{r1} = 111$ and $U_{r2} = 58.8$, respectively. To have a further insight into these peaks, Figure 8 shows the wavelet map of the fluctuating wind velocity at the location $X = 6D$, which is near the middle of the cable. The Morlet wavelet mother function was used in the wavelet transform. It can be observed that the mode associated with the reduced frequency f_{r1} is dominant between the two modes and more consistent in time. From (2), the flow at this mode has a frequency of 0.85 Hz , which is close to the structural frequency; therefore, it excites large vibrations of the cable at the high reduced wind speed U_{r1} .

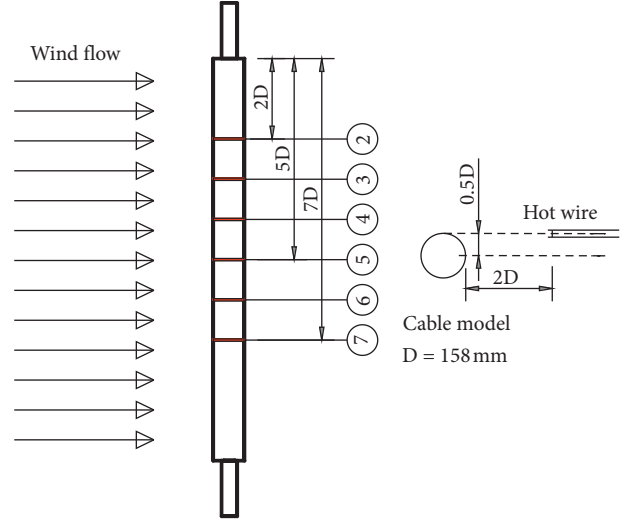


FIGURE 6: Locations of the hot-wire anemometer in the wake and along the cable.

In summary of the observations from Figures 7 and 8, it is evident that the low-frequency flows in the wake of the cable are more dominant and Von Karman vortex is weaker for higher wind speed. These low-frequency flows contain high energy at high wind speed and so excite large vibrations of the cable. The phenomenon was referred to as dry galloping, according to important investigations by Matsumoto and his colleagues with similar observations [2, 5]. These studies showed that low-frequency axial flows along the cable and near the wake are the main cause of large responses at high wind speeds. On the other hand, in the present study, the low-frequency flows are associated with vertical fluctuation. This implies three-dimensional characteristics of the low-frequency flows in the wake of the cable. This remark agrees CFD simulations of wind flow which passed a yawed cable in [41].

To have a further illustration of the dominating vortices as increasing wind speed and to summarise the mechanism of the large vibrations, Figure 9 shows the normalised PSD, denoted as S_n and given by (3), against the reduced frequency for different wind speeds:

$$S_n = \frac{\text{PSD}}{\sigma_v}, \quad (3)$$

where σ_v is the standard deviation of the vertical fluctuating wind speed in the wake.

It can be seen from Figure 9 that Von Karman vortex is apparent at low reduced wind speed. When the wind speed is increasing, this vortex is gradually suppressing. At the same time, low-frequency flows are developing and getting stronger for higher wind speeds. The low-frequency flows contain high energy that excites the vibration of the cable to higher amplitudes for higher wind speeds.

4. Mechanism of Vibration Stabilisation of the Cable with Spiral Wires

For further understanding how spiral wires can help reducing large vibrations of the cable, it is important to

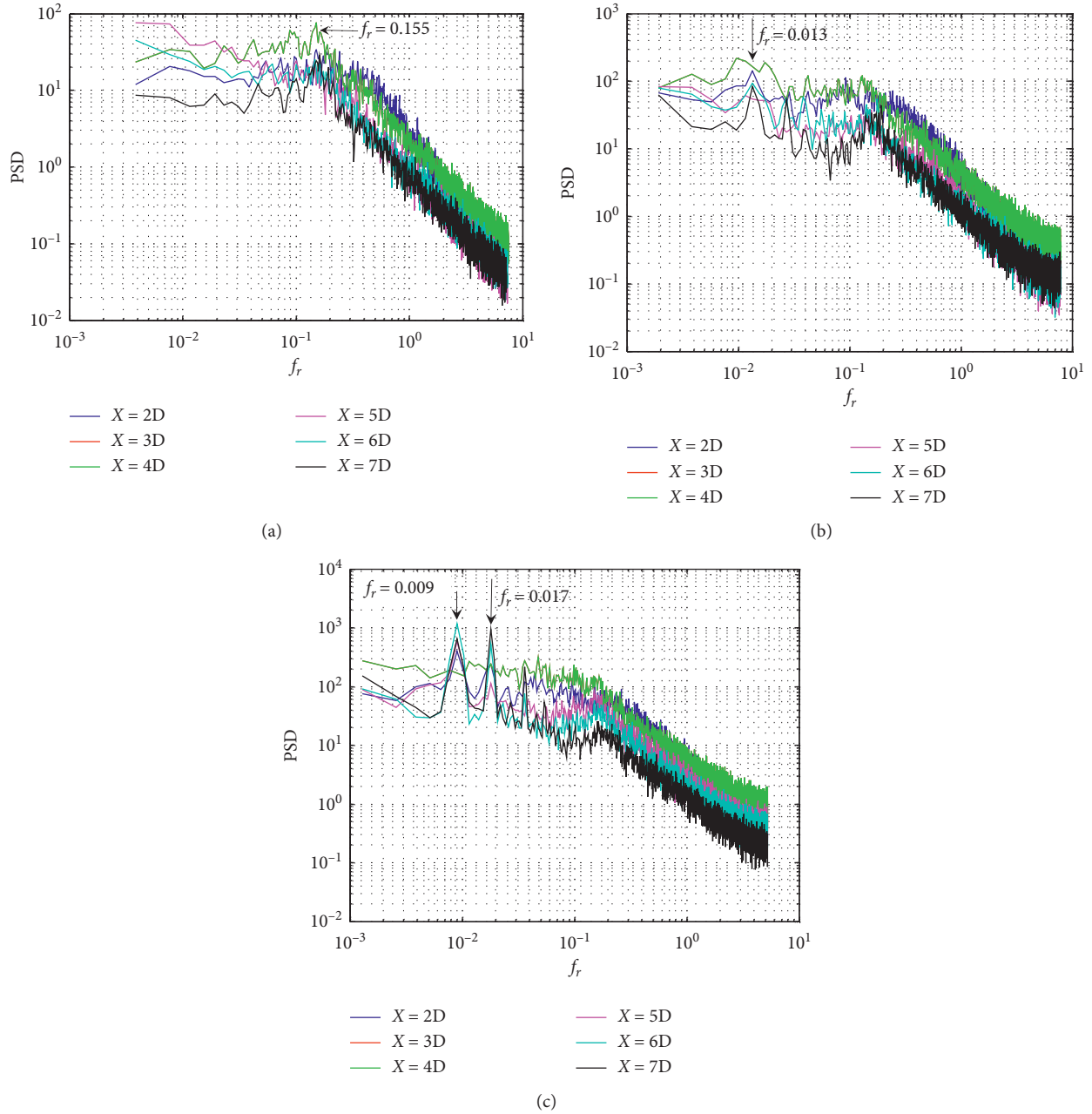


FIGURE 7: PSD of vertical fluctuating wind speeds for different locations in the wake of the cable, (a) $U = 5$ m/s; (b) $U = 10$ m/s; (c) $U = 15$ m/s.

investigate the vibration mechanism of the cable when it is wrapped with the spiral wires. For this purpose, the vertical component of the fluctuating wind speeds in the wake of Model 2 (Figure 1(b)) was measured. The experimental setup for this measurement with the use of hot wire was the same as described in Section 3, with the same inclination angle and yaw angle; that is, $\alpha = 25^\circ$ and $\beta = 30^\circ$. The inlet wind flow is smooth with the speed $U = 15$ m/s.

Figure 10 compares the spectrums of the vertical fluctuating wind speeds at the location $X = 6D$, i.e., near the middle of the cable, for Model 1 (without spiral wires) and Model 2 (with spiral wires). It can be seen that the

dominant spectrum in the low-frequency regime is significantly mitigated when the cable is wrapped with the spiral wires. As these low-frequency vortices are weakened, their energies are too low to excite large vibrations in high wind speeds.

With the presence of the spiral protuberance, the dominant spectrum associates with Von Karman vortex ($St = 0.2$). Then, the critical reduced velocity for the occurrence of Von Karman VIV is $1/St = 5$. For higher wind speeds, the vortex's frequency is different from the frequency of the cable. As a result, the VIV is diminished, showing small amplitude vibrations of the cable.

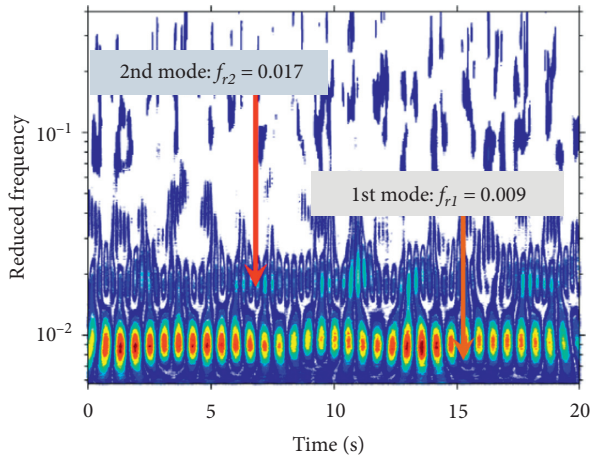


FIGURE 8: Wavelet map of the vertical fluctuating wind speed in the wake at location $X=6D$ for $\alpha=25^\circ$, $\beta=30^\circ$, and $U=15$ m/s.

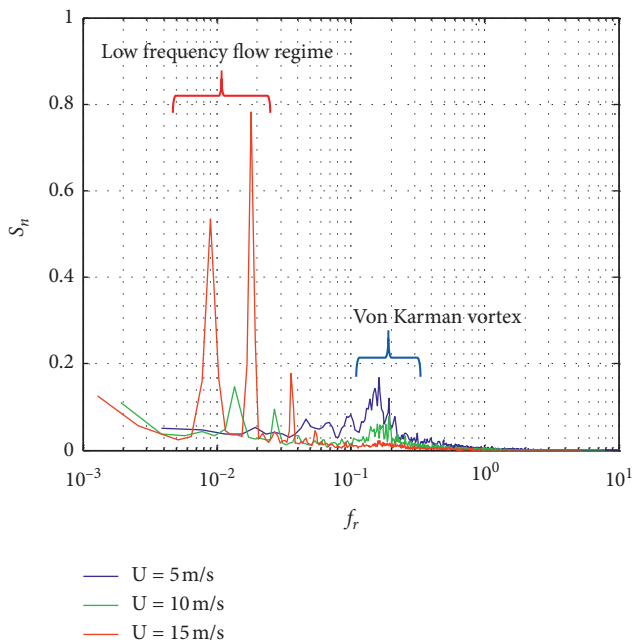


FIGURE 10: PSD of fluctuating wind speed in the wake of Model 1 (cable without the spiral wires) and Model 2 (with the spiral wires).

FIGURE 9: Normalized PSD (location $6D$, $D=158$ mm, $\beta=30^\circ$, and $\alpha=25^\circ$).

5. Conclusions

This paper studies the vibration characteristics of stayed cables in wind with and without rain through a series of wind tunnel experiments. A rain simulator system in which rain intensity can be controlled was used to simulate a more realistic rainfall and water on the cable surface. The tests were conducted for four yaw angles (0° , 15° , 30° , and 45°). Also, the use of spiral protuberance wires wrapping around the cable as a method to mitigate cable vibrations is investigated.

The tests on the smooth cable (without spiral wires) showed that, in dry condition, Von Karman VIV was apparent for yaw angle 30° and weak for other yaw angles. Meanwhile in rain condition, VIV disappeared for all

angles. In addition, for each yaw angle, RWIV with large amplitudes were observed for a range of wind speeds. These amplitudes were larger, up to 4 times, than those without rain. For higher wind speeds outside this range, the amplitudes were significantly reduced. Among tested yaw angles, for the both cases with and without rain, the cable is exposed to smaller vibration amplitudes when being normal to the wind (zero yaw angle) than when being yawed to the wind.

On the other hand, the tests on the cable wrapped with the spiral wires showed considerable reduction of vibrations amplitudes in both dry and rain conditions. Typical RWIV were then suppressed, although they had slightly larger amplitudes than in dry condition. This observation implies the role of the spiral wires in mitigating the larger responses of cable in wind hazards with and without the coupling of rain.

In an attempt to understand the mechanism of the large amplitude vibrations as well as the mechanism of mitigating such amplitudes, the vertical fluctuations in the wake of the cable models were measured. The low-frequency vortex flows were found. They play a vital role in generating large responses of the smooth cable in high wind speeds. These vortices interrupt the Von Karman vortex, shed continuously and regularly in time, and contain high energy that excites the vibration of the cable. When the spiral wires were wrapped around the cable, they dismissed the low-frequency flows and so reduced the vibration amplitudes.

Data Availability

Data used to support the findings of this study are available from the corresponding author upon request.

Conflicts of Interest

The authors declare that there are no conflicts of interest regarding the publication of this paper.

Acknowledgments

This research was funded by Vietnam National Foundation for Science and Technology Development (NAFOSTED) under Grant no. 107.04–2017.321. The authors gratefully acknowledge the support from the Department of Civil Engineering, Yokohama National University, for the wind tunnel experiments.

References

- [1] M. Matsumoto, "Aerodynamic behaviour of inclined circular cylinders-cable aerodynamics," *Wind Engineering and Industrial Aerodynamics*, vol. 33, pp. 63–72, 1990.
- [2] M. Matsumoto, N. Shiraishi, and H. Shirato, "Rain-wind induced vibration of cables of cable-stayed bridges," *Journal of Wind Engineering and Industrial Aerodynamics*, vol. 43, no. 1-3, pp. 2011–2022, 1992.
- [3] M. Matsumoto, T. Yagi, Y. Shigemura, and D. Tsushima, "Vortex-induced cable vibration of cable-stayed bridges at high reduced wind velocity," *Journal of Wind Engineering and Industrial Aerodynamics*, vol. 89, no. 7-8, pp. 633–647, 2001.
- [4] M. Matsumoto, T. Yagi, Q. Liu, Y. Oishi, and Y. Adachi, "Effects of axial flow and Karman vortex interference on dry-state galloping of inclined stay-cables," in *Proceedings of the 6th International Symposium on Cable Dynamics*, pp. 247–254, Charleston, SC, USA, September 2005.
- [5] M. Matsumoto, T. Yagi, H. Hatsuda, T. Shima, M. Tanaka, and H. Naito, "Dry galloping characteristics and its mechanism of inclined/yawed cables," *Journal of Wind Engineering and Industrial Aerodynamics*, vol. 98, no. 6-7, pp. 317–327, 2010.
- [6] T. Tanaka, M. Matsumoto, H. Ishizaki, and H. Kibe, "Dry galloping characteristic and vibration control of inclined stay cable," in *Proceedings of the First International Symposium on Flutter and its Application*, pp. 639–648, Tokyo, Japan, 2016.
- [7] J. H. G. Macdonald, "Quasi-steady analysis of 2DOF inclined cable galloping in the critical Reynolds number range," in *Proceedings of the 6th International Symposium on Cable Dynamics*, pp. 435–442, Charleston, SC, USA, September 2005.
- [8] S. Cheng, P. A. Irwin, J. B. Jakobsen, and G. L. Larose, "Divergent motion of cables exposed to skewed wind," in *Proceedings of the 5th International Symposium on Cable Dynamics*, pp. 271–278, Charleston, SC, USA, September 2003.
- [9] J. H. G. Macdonald and G. L. Larose, "A unified approach to aerodynamic damping and drag/lift instabilities, and its application to dry inclined cable galloping," *Journal of Fluids and Structures*, vol. 22, no. 2, pp. 229–252, 2006.
- [10] J. H. G. Macdonald and G. L. Larose, "Two-degree-of-freedom inclined cable galloping-Part I: general formulation and solution for perfectly tuned system," *Journal of Wind Engineering and Industrial Aerodynamics*, vol. 96, no. 3, pp. 291–307, 2008.
- [11] H. Katsuchi and H. Yamada, "Dry galloping characteristics of indented stay cables in turbulent flow," in *Proceedings of the 9th International Symposium on Cable Dynamics*, Shanghai, China, October 2011.
- [12] J. B. Jakobsen, T. L. Andersen, J. H. G. Macdonald et al., "Wind-induced response and excitation characteristics of an inclined cable Model in the critical Reynolds number range," *Journal of Wind Engineering and Industrial Aerodynamics*, vol. 110, pp. 100–112, 2012.
- [13] N. Nikitas and J. H. G. Macdonald, "Aerodynamic forcing characteristics of dry cable galloping at critical Reynolds numbers," *European Journal of Mechanics-B/Fluids*, vol. 49, pp. 243–249, 2015.
- [14] W. Ma, Q. Liu, J. H. G. Macdonald, X. Yan, and Y. Zheng, "The effect of surface roughness on aerodynamic forces and vibrations for a circular cylinder in the critical Reynolds number range," *Journal of Wind Engineering and Industrial Aerodynamics*, vol. 187, pp. 61–72, 2019.
- [15] N. Nikitas, J. H. G. Macdonald, J. B. Jakobsen, and T. L. Andersen, "Critical Reynolds number and galloping instabilities: experiments on circular cylinders," *Experiments in Fluids*, vol. 52, no. 5, pp. 1295–1306, 2012.
- [16] W. Ma, J. H. G. Macdonald, Q. Liu, C. H. Nguyen, and X. Liu, "Galloping of an elliptical cylinder at the critical Reynolds number and its quasi-steady prediction," *Journal of Wind Engineering and Industrial Aerodynamics*, vol. 168, 2017.
- [17] G. Matteoni and C. T. Georgakis, "Effects of surface roughness and cross-sectional distortion on the wind-induced response of bridge cables in dry conditions," *Journal of Wind Engineering and Industrial Aerodynamics*, vol. 136, pp. 89–100, 2015.
- [18] Y. Hikami and N. Shiraishi, "Rain-wind induced vibrations of cables stayed bridges," *Journal of Wind Engineering and Industrial Aerodynamics*, vol. 29, no. 1-3, pp. 409–418, 1988.
- [19] M. Matsumoto, "Observed behavior of prototype cable vibration and its generation mechanism," in *Proceedings of the Advances in Bridge Aerodynamics*, Balkema, Rotterdam, The Netherlands, pp. 189–211, May 1998.
- [20] J. A. Main and N. P. Jones, "Full scale measurements of stay cable vibration," in *Proceedings of the 10th International Conference on Wind Engineering*, pp. 963–970, Copenhagen, Denmark, June 1999.
- [21] A. J. Persoon and K. Noorlander, "Full scale measurements on the Erasmus Bridge after rain/wind-induced cable vibration," in *Proceedings of the 10th International Conference on Wind Engineering*, pp. 1019–1026, Copenhagen, Denmark, June 1999.
- [22] S. Kumarasena, N. Jones, P. Irwin, and P. Taylor, *Wind-Induced Vibration of Stay Cables*, Wiley, Hoboken, NJ, USA, 2007.
- [23] A. Acampora and C. T. Georgakis, "Recent monitoring of the Oresund Bridge: rain-wind induced cable vibrations," in *Proceedings of the 13th International Wind Engineering Conference*, p. 2011, Amsterdam, Netherland, July 2011.
- [24] M. Gu and Q. Lu, "Theoretical analysis of wind- rain induced vibration of cables of cable- stayed bridges," *Wind Engineering and Industrial Aerodynamics*, vol. 89, pp. 125–128, 2001.
- [25] O. Flamand, "Rain/wind-induced vibration of cables," in *Proceedings of the International Conference on Cable-Stayed and Suspension Bridges (AFPC)*, pp. 523–531, Deauville, France, October 1994.
- [26] A. Bosdogianni and D. Olivari, "Wind- and rain-induced oscillations of cables of stayed bridges," *Journal of Wind Engineering and Industrial Aerodynamics*, vol. 64, no. 2-3, pp. 171–185, 1996.
- [27] G. L. Larose and L. W. Smitt, "Rain/wind induced vibrations of parallel stay cables," in *Proceedings of the IABSE Conference, Cable-Stayed Bridges—Past, Present and Future*, Malmo, Sweden, June 1999.
- [28] N. Coesentino, O. Flamand, and C. Ceccoli, "Rain-wind-induced vibration of inclined stay cables. Part I: experimental investigation and physical explanation," *Wind Engineering and Industrial Aerodynamics*, vol. 93, pp. 79–95, 2005.

- [29] M. Gu and X. Du, "Experimental investigation of rain-wind-induced vibration of cables in 369 cable-stayed bridges and its mitigation," *Wind Engineering and Industrial Aerodynamics*, vol. 93, no. 79-95, 2005.
- [30] H. Katsuchi, H. Yamada, I. Sakaki, and E. Okado, "Wind-tunnel investigation of the aerodynamic performance of surface-modification cables," *Engineering*, vol. 3, no. 6, pp. 817-822, 2017.
- [31] Y. Ge, Y. Chang, L. Xu, and L. Zhao, "Experimental investigation on spatial attitudes, dynamic characteristics and environmental conditions of rain-wind-induced vibration of stay cables with high-precision raining simulator," *Journal of Fluids and Structures*, vol. 76, pp. 60-83, 2018.
- [32] J. A. Main and N. P. Jones, "Evaluation of viscous dampers for stay-cable vibration mitigation," *Journal of Bridge Engineering*, vol. 6, no. 6, pp. 385-397, 2001.
- [33] E. A. Johnson, G. A. Baker, B. F. Spencer, and Y. Fujino, "Semiactive damping of stay cables," *Journal of Engineering Mechanics*, vol. 133, no. 1, pp. 1-11, 2007.
- [34] W. Wu and C. S. Cai, "Theoretical exploration of a taut cable and a TMD system," *Engineering Structures*, vol. 29, pp. 962-972, 2006.
- [35] I. F. Lazar, S. A. Neild, and D. J. Wagg, "Vibration suppression of cables using tuned inerter dampers," *Engineering Structures*, vol. 122, pp. 62-71, 2016.
- [36] S. Elias and V. Matsagar, "Research developments in vibration control of structures using passive tuned mass dampers," *Annual Reviews in Control*, vol. 44, pp. 129-156, 2017.
- [37] C. H. Nguyen and J. H. G. Macdonald, "Galloping analysis of a stay cable with an attached viscous damper considering complex modes," *Journal of Engineering Mechanics*, vol. 144, no. 2, 2018.
- [38] H. Katsuchi and H. Yamada, "Wind-tunnel study on dry-galloping of indented-surface stay cable," in *Proceedings of the 11th Americas conference on wind engineering*, pp. 22-26, Puerto Rico, USA, June 2009.
- [39] H. D. Vo, H. Katsuchi, H. Yamada, and M. Nishio, "Experimental study on dry-state galloping with various wind relative angles and its countermeasures," *Journal of Structural Engineering*, vol. 60A, pp. 428-436, 2014.
- [40] H. Jing, Y. Xia, H. Li, Y. Xu, and Y. Li, "Excitation mechanism of rain-wind induced cable vibration in a wind tunnel," *Journal of Fluids and Structures*, vol. 68, no. 32-47, 2017.
- [41] D. Yeo and N. P. Jones, "Investigation on 3-D characteristics of flow around a yawed and inclined circular cylinder," *Journal of Wind Engineering and Industrial Aerodynamics*, vol. 96, no. 10-11, pp. 1947-1960, 2008.